University of California
Santa Barbara

Twin Related Domains in Polycrystalline Nickel-Base Superalloys: 3D Structure and Fatigue

A dissertation submitted in partial satisfaction
of the requirements for the degree

Doctor of Philosophy
in
Materials

by

William Carl Lenthe

Committee in charge:

Professor Tresa M. Pollock, Chair
Professor Carlos G. Levi
Professor G. Robert Odette
Professor Samantha H. Daly

January 2018

The dissertation of William Carl Lenthe is approved.

Professor Carlos G. Levi

Professor G. Robert Odette

Professor Samantha H. Daly

Professor Tresa M. Pollock, Committee Chair

October 2017

Twin Related Domains in Polycrystalline

Nickel-Base Superalloys: 3D Structure and Fatigue

by

William Carl Lenthe

Acknowledgments

No dissertation is a solitary undertaking, and this work was made possible by the generous contributions of many people. I benefited greatly from the guidance of my committee, most notably the mentorship of my advisor Professor Tresa Pollock who always has her students' best interests at heart.

The Materials Department's excellent technical staff, in particular Chris Torbet and Mark Cornish, facilitated my experimental efforts. I would also like to acknowledge the development team of DREAM.3D, especially Mike Groeber and Mike Jackson for their help and patience in familiarizing me with the software. Finally, I'd like to thank Mike Uchic for teaching me so much about 3D data collection and analysis.

I am fortunate to have shared my tenure at UCSB with a remarkable selection of students, postdoctoral researchers, and visiting scientists. My graduate school experience was personally and professionally enriched by my group mates and I feel deeply privileged to call them peers.

A series of passionate educators including Mr. Sivek, Mr. Kamin, Ms. Poodry, Ms. Croul, and Professor Vinci cultivated my curiosity and enabled my path to graduate school. Most importantly I would like to thank my parents, sisters, and wife for their enduring support and encouragement.

This work has been supported through a grant No. FA9550-12-1-0445 to the Center of Excellence on Integrated Materials Modeling (CEIMM) at Johns Hopkins University (partners JHU, UIUC, UCSB), awarded by the AFOSR/RSL and AFRL/RX.

Curriculum Vitæ

William Carl Lenthe

Education

2017 Ph.D. in Materials, University of California, Santa Barbara.

2012 B.S. in Materials Science & Engineering, Lehigh University, Bethlehem, PA.

Publications

18. **W. C. Lenthe**, M. P. Echlin, J. C. Stinville, T. Francis, and T. M. Pollock. "Twin Related Domain Statistics in a Polycrystalline Nickel Alloy". **(In Preparation)**

17. **W. C. Lenthe**, J. C. Stinville, M. P. Echlin, and T. M. Pollock. "Beam Scanning Defects in Scanning Electron Microscopy Digital Image Correlation". **(In Preparation)**

16. **W. C. Lenthe**, M. P. Echlin, A. Trenkle, M. Syha, P. Gumbsch, and T. M. Pollock. "Automatic Feature Matching of 3D Datasets". **(In Preparation)**

15. A. Polonsky, M. P. Echlin, **W. C. Lenthe**, M. Kirka, R. Dehoff, and T. M. Pollock. "Defects and 3D Structural Inhomogeneity in Electron Beam Additively Manufactured Inconel 718". *Materials Characterization.* **(Submitted)**

14. B. Bales, B. Goodlet, **W. C. Lenthe**, L. Petzold, and T. M. Pollock. "Bayesian Inference of Elastic Properties with Resonant Ultrasound Spectroscopy". *Journal of the Acoustical Society of America.* **(Submitted)**

13. W. S. LePage, A. Ahadi, **W. C. Lenthe**, Q. P. Sun, T. M. Pollock, J. A. Shaw, and S. H. Daly. "Grain Size Effects on NiTi Shape Memory Alloy Fatigue Crack Growth". *Journal of Materials Research* (2017). **(Accepted)**

12. J. C. Stinville, **W. C. Lenthe**, M. P. Echlin, P. G. Callahan, and D. Texier. "Microstructural Statistics for Fatigue Crack Initiation in Polycrystalline Nickel-Base Superalloys". *International Journal of Fracture* (2017). [**doi**]

11. L. T. Beringer, R. Harrison, **W. Lenthe**, and G. Spanos, "Assessing Progress on 3D Materials Science Closing Panel Discussion Highlights from 3DMS2016". *The Journal of The Minerals, Metals & Materials Society* 69.4 (2017), pp. 622–624. [**doi**]

10. J. C. Stinville, **W. C. Lenthe**, J. Miao, and T. M. Pollock. "A Combined Grain Scale Elastic-Plastic Criterion for Identification of Fatigue Crack Initation Sites in a Twin Containing Polycrystalline Nickel-Base Superalloy". *Acta Materialia* 103 (2016), pp. 461–473. [**doi**]

9. **W. C. Lenthe**, J. C. Stinville, M. P. Echlin, and T. M. Pollock. "Statistical Assessment of Fatigue-Initiating Microstructural Features in a Polycrystalline Disk Alloy". *Superalloys 2016* (2016), pp. 569–577. [**doi**]

8. D. W. Eastman, Z. Alam, G. Weber, P. A. Shade, M. D. Uchic, **W. C. Lenthe**, T. M. Pollock, and K. J. Hemker. "Benchmarking Crystal Plasticity Models with Miscrotensile Evaluation and 3D Characterization of René 88DT". *Superalloys 2016* (2016), pp. 813–820. [**doi**]

7. M. P. Echlin, J. C. Stinville, V. M. Miller, **W. C. Lenthe**, and T. M. Pollock. "Incipient Slip and Long Range Plastic Strain Localization in Microtextured Ti-6Al-4V Titanium". *Acta Materialia* 114 (2016), pp, 164–175. [**doi**]

6. **W. C. Lenthe**, M. P. Echlin, A. Trenkle, M. Syha, P. Gumbsch, and T. M. Pollock. "Quantitative Voxel-to-Voxel Comparison of TriBeam and DCT Strontium Titante Three-Dimensional Data Sets". *Journal of Applied Crystallography* 48.4 (2015), pp. 1034-1046. [**doi**]

5. J. E. Douglas, M. P. Echlin, **W. C. Lenthe**, R. Seshadri, and T. M. Pollock. "Three-Dimensional Multimodal Imaging and Analysis of Biphasic Microstructure in a Ti-Ni-Sn Thermoelectric Material". *APL Materials* 3.9 (2015), pp. 096107. [**doi**]

4. M. P. Echlin, **W. C. Lenthe**, and T. M. Pollock. "Three-Dimensional Sampling of Material Structure for Property Modeling and Design". *Integrating Materials and Manufacturing Innovation* 3.1 (2014), pp. 21. [**doi**]

3. S. A. Bojarski, J. Knighting, S. L. Ma, **W. Lenthe**, M. P. Harmer, and G. S. Rohrer. "The Relationship Between Grain Boundary Energy, Grain Boundary Complexion Transitions, and Grain Size in Ca-Doped Yttria". *Materials Science Forum* 753 (2013), pp. 87–92. [**doi**]

2. C. Marvel, **W. Lenthe**, and J. Logan, "Microstructural Analysis of a Silver-Plated Trombone". *Advanced Materials and Processes* 170.2 (2012), pp. 18–19. [**doi**]

1. S. A. Bojarski, S. Ma, **W. Lenthe**, M. P. Harmer, and G. S. Rohrer. "Changes in the Grain Boundary Character and Energy Distributions Resulting From a Complexion Transition in Ca-Doped Yttria". *Metallurgical and Materials Transactions A* 43.10 (2012), pp. 3532–3538. [**doi**]

Abstract

Twin Related Domains in Polycrystalline

Nickel-Base Superalloys: 3D Structure and Fatigue

by

William Carl Lenthe

Fatigue is the life limiting property of polycrystalline nickel-base superalloys used in turbine disks in the hot section of turbine engines for aerospace and power generation applications. Fabricating components through a powder metallurgy route provides enhanced properties and removes many extrinsic defects associated with fatigue crack formation, driving cracks to initiate at intrinsic microstructrual extremes. Fatigue cracks in the powder metallurgy alloy René 88DT frequently initiate in large grains that are in the tail of the size distribution and contain favorably oriented annealing twin boundaries. Fully characterizing twin boundaries and twin related domains requires 3D microstructural volumes. Datasets of 3D microstructure for René 88DT were collected by TriBeam tomography across a range of resolutions and volumes to characterize microstructure and annealing twins. Algorithms developed to analyze these datasets allow identification of strain localizing sites from 2D cross sections and the frequency of microstructural features amenable to fatigue crack initiation is statistically assessed. Twin related domain structure is quantified via network analysis and leveraged to propose a criterion for identifying fatal fatigue crack sites.

Contents

List of Figures

List of Tables

List of Algorithms

List of Acronyms and Initialisms

APB	antiphase boundary
ART	algebraic reconstruction technique
BCC	body centered cubic
CI	confidence index
CSL	coincident site lattice
DAQ	data acquisition
DCT	diffraction contrast tomography
DIC	digital image correlation
DREAM.3D	Digital Representation Environment for Analyzing Microstructure in 3D
EBSD	electron backscatter diffraction
EDM	electrical discharge machining
FCC	face centered cubic
FIB	focused ion beam
HCP	hexagonal close packed
IPF	inverse pole figure
IQ	image quality
LIPSS	laser-induced periodic surface structure
PEEM	photoemission electron microscopy
PM	powder metallurgy
PSB	persistant slip band

PVE property volume element

SEM scanning electron microscope

STO strontium titanate

UCSB University of California, Santa Barbara

Chapter 1

Introduction: Fatigue Life of Polycrystalline Disk Ni-Base Superalloys Alloys

1.1 Nickel-Base Superalloys for Gas Turbine Engines

Nickel-base superalloys are employed extensively in the manufacture of gas turbine engines for power generation and aerospace applications due to their excellent mechanical and environmental resistance properties at high temperature. Nickel-base superalloys account for ≈40–50% of engine weight, predominantly as turbine blades and disks in the hot section of the engine, as shown in figure 1.1 [1]. Modern nickel-base superalloys for the hot section of turbines can be broadly divided into two categories. Alloys for high pressure turbine blades are optimized for creep life due to their proximity to the hot gas stream. Alloys for high pressure turbine disks are optimized for fatigue life (although creep may occur in the hotter exterior regions of the disk). Low cycle fatigue occurs with

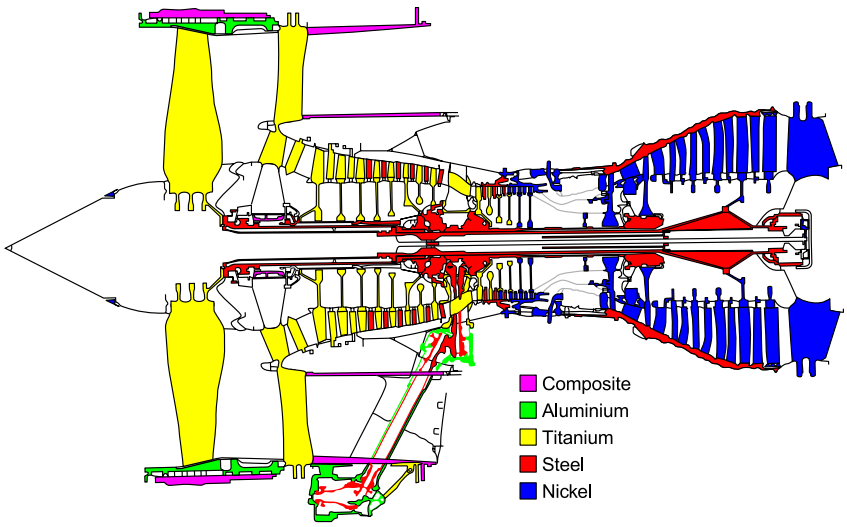

Figure 1.1: Schematic cross section of a Rolls Royce Trent 800 engine colored by material showing the extensive use of nickel alloys in the hot section. Figure reproduced from Reed [2].

flight cycles (takeoff, cruise, landing), while high cycle fatigue is most often associated with resonance. Although there are many similarities, superalloys for disk applications will be considered in this dissertation except where otherwise noted; an example of a forged disk is shown in figure 1.2. Disk alloys alone account for approximately 20% of the weight and 10% of the cost of a modern commercial aircraft engine and approximately 5% of the weight and 25% of the cost of military engines [2].

1.1.1 Chemical Composition

Superalloys are derived from the Nickel–Aluminum binary system (figure 1.3). Their composition is located within the γ/γ' phase field, with the γ phase designating an FCC solid solution and the γ' phase an ordered $L1_2$ crystal structure with a nominal composition of Ni_3Al (figure 1.4) [1, 3]. The elements C, B, and Hf are typically added as grain boundary strengtheners, Al and Cr for oxidation resistance, and refractory elements including Mo, Ta, and W as solid solution strengtheners. Generally elements partition preferentially to either the γ phase, the γ' phase, or the grain boundaries as indicated in figure 1.5 [2]. In addition to the γ and γ' phases in the Ni–Al binary system, Cr, Mo,

Figure 1.2: A disk forged from polycrystalline nickel-base superalloy. Image courtesy of Jack Schirra, Pratt & Whitney.

Table 1.1: The composition of selected PM alloys is given in weight percent. Nickel is the balance for all alloys.

Alloy	Co	Cr	Mo	W	Al	Ti	Nb	C	B	Zr	Other
René 88DT	13	16	4	4	2.1	3.7	0.7	0.03	0.015	0.03	
René 95	8	14	3.5	3.5	3.5	2.5	3.5	0.15	0.010	0.05	
RR1000	18.5	15			1.1	3.0	1.1	0.027	0.015	0.06	
IN100	15	10	3		5.5	4.7		0.18	0.014	0.06	0.90 V
Udimet 720	14.7	16	3.0	1.25	2.0	5.0		0.025	0.020	0.03	
IN-718		18	3.0		0.45	0.9	5.0	0.02	0.004		18 Fe
N18	15.5	11.5	6.5		4.3	4.3		0.02	0.015		0.5 Hf

Ti, Ta and Hf may form borides or carbides, typically at grain boundaries. Excess Cr, Mo, W, and Re may stabilize detrimental topologically close packed phases including δ and σ, though compositions are tailored to suppress their formation [1, 3]. The γ phase is stable to the melting point (≈1320–1450 °C liquidus) and γ' phase is less stable at elevated temperature with a solvus temperature typically in the range of ≈1050–1200 °C [1–3]

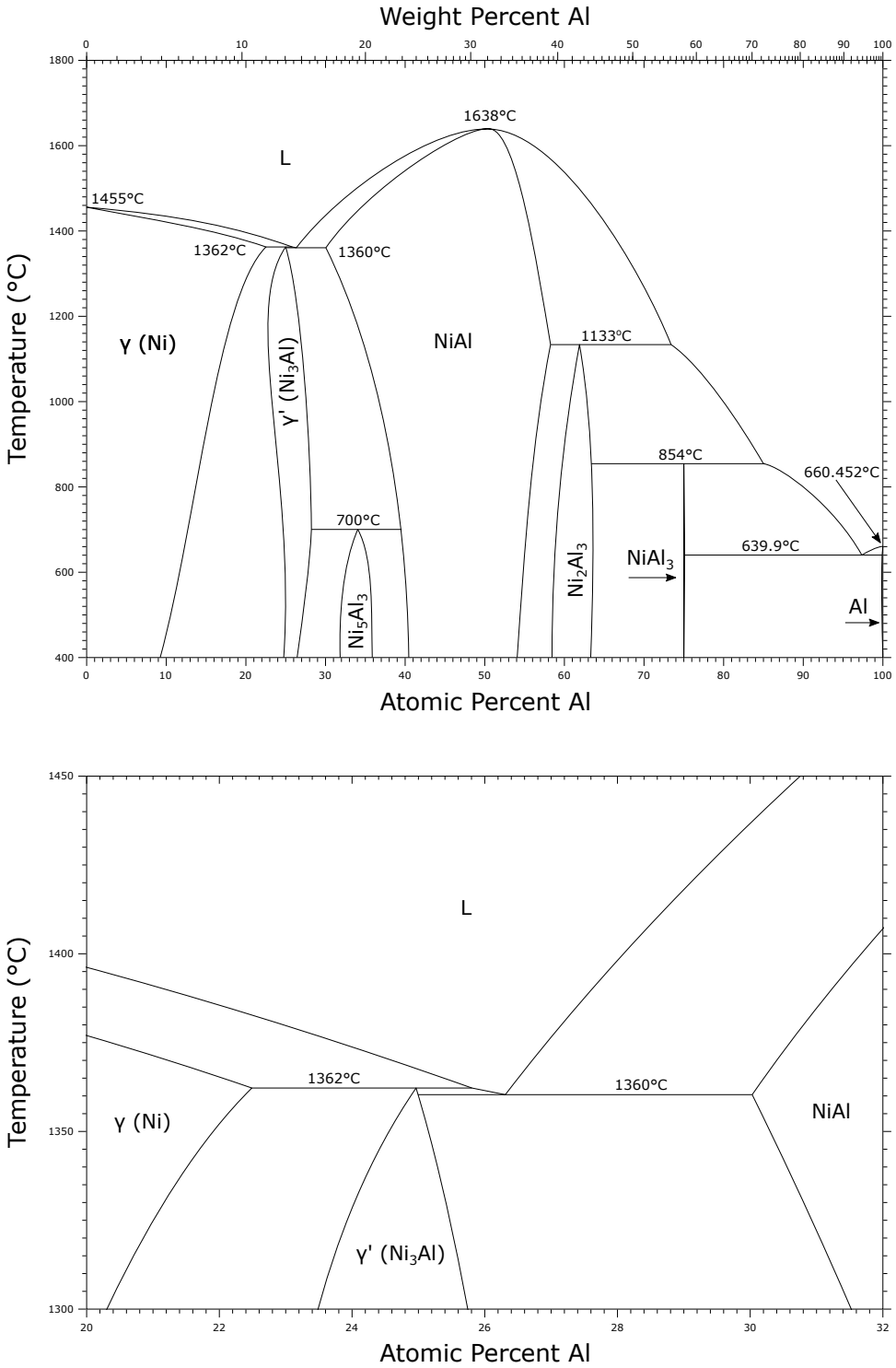

Figure 1.3: The Nickel–Aluminum binary phase diagram is shown (top) with detail for γ' invariant reactions (bottom). Figure based on data from Okamoto [4].

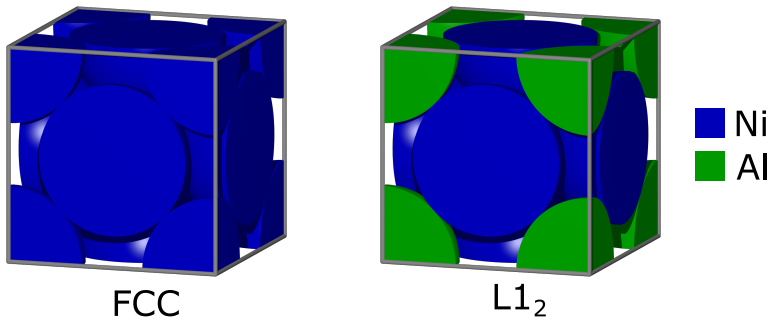

Figure 1.4: Unit cells of the γ (FCC) and γ' ($L1_2$) crystal structures are shown.

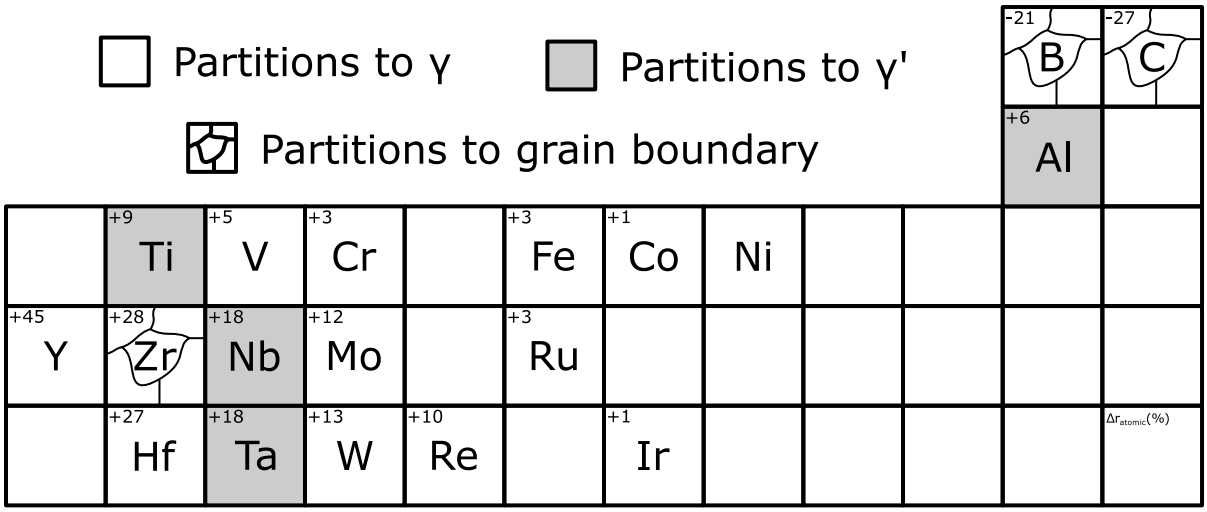

Figure 1.5: Common nickel-base superalloy alloying additions are colored by the phase they partition to, with and percent difference from the atomic radius of nickel indicated. Figure modified from Reed [2].

1.1.2 Processing

Some disk alloys are amenable to fabrication via traditional casting and forging routes. Increasing refractory content is desirable to improve high temperature strength, but increased segregation during solidification and reduced ductility make traditional processing routes infeasible [1, 2]. Alloys not amenable to traditional processing are fabricated through a PM processing route instead. An overview of both processing pathways is given below and both begin with vacuum induction melting a large ingot [3].

Cast and Wrought Alloys

In cast and wrought alloy fabrication, as solidified ingots are typically remelted to mitigate segregation, inclusions, and shrinkage cavities that form during initial solidification [3]. Vacuum arc remelting is most frequently used for secondary melting, but electro-slag remelting and electron beam cold hearth refining may also be employed [2]. The refined ingot is subsequently annealed, mechanically worked, and forged [1, 3].

Powder Metallurgy Alloys

For PM alloys the vacuum induction melted ingot is remelted and gas atomized to refine the scale of segregation [1, 3, 5]. The resulting powder is sieved to remove large metallic particles that may have coarse segregation and large non-metallic particles that would serve as crack initiation sites [1, 6, 7]. The sized powder is evacuated in steel cans then hot isostatically pressed and/or extruded to consolidate a billet which is finally isothermally forged with deformation occurring by superplastic flow [2, 8, 9]. Superplastic forging, sometimes referred to as 'Gatorizing™' in the literature, results in a fine grain size achieved through heavy working at high temperature and strain rate (e.g. extrusion just below the recrystallization temperature) [10, 11]. The refined grain structure can be superplastically deformed to strains of over 10 (1000%) allowing forging of net or near-net shape disks [10,

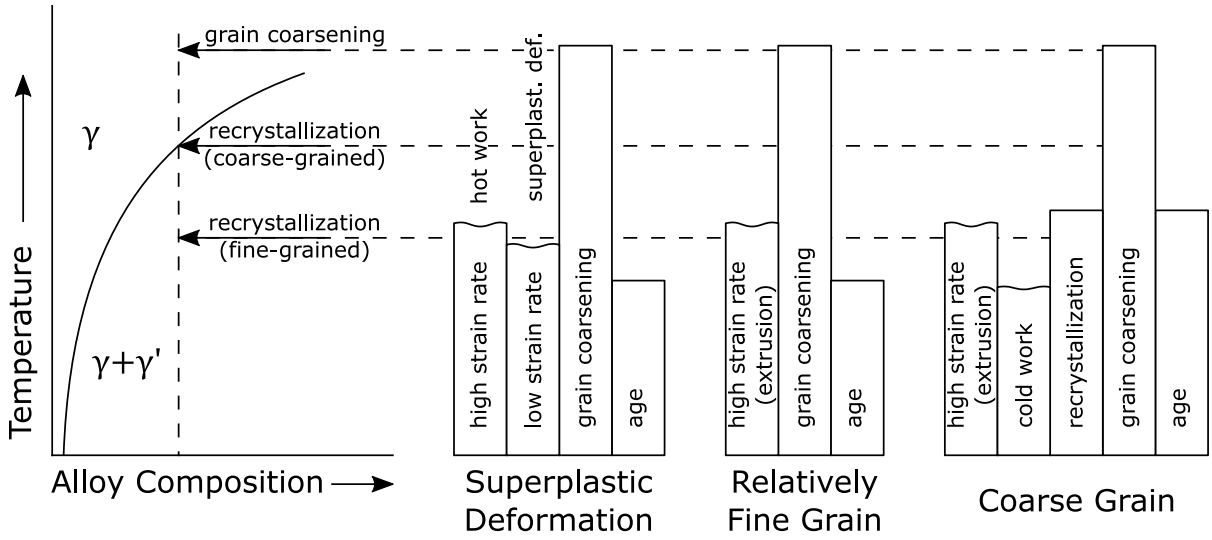

Figure 1.6: Thermomechanical processing routes for PM nickel-base superalloys are shown schematically. Figure modified from Gessinger and Bomford [10].

12]. The resulting forging undergoes a two stage heat treatment, first near or above the γ' solvus to allow grain growth and then aging below the solvus to induce γ' precipitation [8, 11, 13]. Overviews of PM themomechanical processing routes are shown in figure 1.6. This processing route enables improved performance but is considerably more expensive, particularly if smaller powder sizes, which reduce powder yields, are required [2].

1.1.3 Microstructure

Polycrystalline alloys must balance grain refinement to increase yield stress by Hall–Petch strengthening with a decrease in creep life via boundary mediated diffusion [2]. Final parts typically have an equiaxed microstructure and a grain size of 5 µm to 50 µm. Annealing twins and corresponding higher order $\Sigma 3^n$ coincidence site lattice boundaries are present in varying degrees depending on processing conditions and stacking fault energies with extensive twinning possible in some systems as shown in the electron backscatter diffraction (EBSD) map in figure 1.7. Although the formation of annealing twins is not fully understood, they can serve as fatigue crack initiation sites and are therefore of significant importance [14, 15].

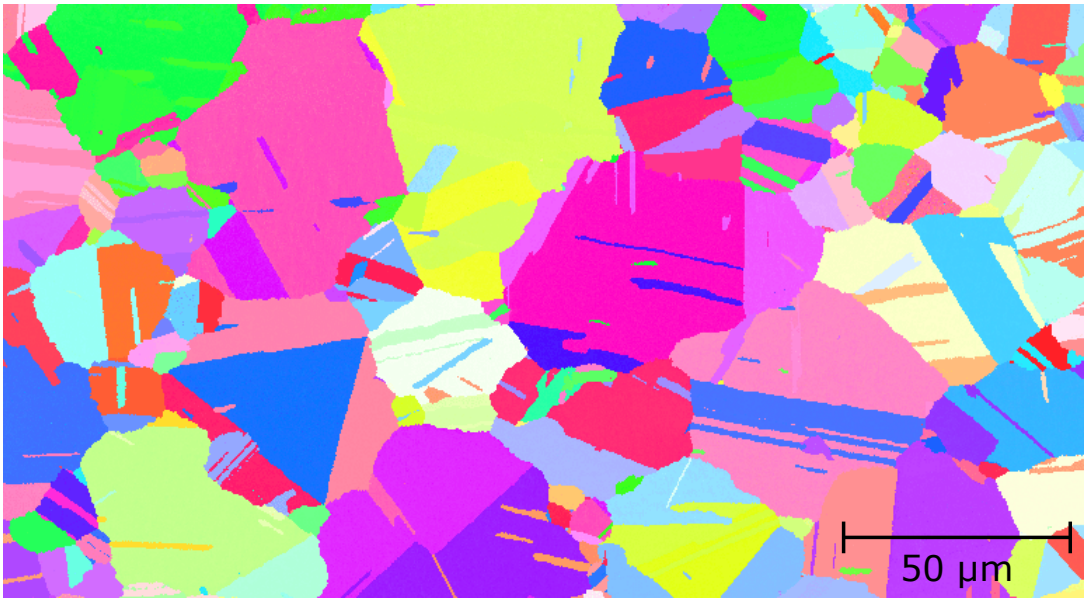

Figure 1.7: The grains of René 88DT are heavily annealing twinned as shown in this IPF colored (Z reference direction) EBSD map.

At the subgrain scale, nickel-base superalloys consist of ≈40–50% volume fraction γ' precipitates in a γ matrix (figure 1.8). The γ' particles can be categorized as primary — large 1 µm to 10 µm precipitates which restrict grain growth during processing by Zener pinning, secondary — small (≈100 nm) coherent precipitates with a spherical or cuboidal shape, or tertiary — small (≈10 nm) coherent precipitates with a spherical or cuboidal shape that are solutionized at service temperatures [3]. The shape of coherent precipitates depends on the lattice misfit $\delta = 2(a_{\gamma'} - a_{\gamma})/(a_{\gamma'} + a_{\gamma})$ [2]. Precipitates assume spherical shapes for misfit near zero and become cuboids as $|\delta|$ approaches ≈0.3%. There may only be two populations of γ' if primary precipitates are removed with a super-solvus heat treatment but the nomenclature for secondary and tertiary is unchanged.

1.1.4 Mechanical Properties

Stiffness and Strength

Nickel superalloys have a Young's modulus of ≈210 GPa, yield strength of ≈900–1300 MPa, and ultimate tensile strength of ≈1200–1600 MPa at 300 °C, with PM alloys in the

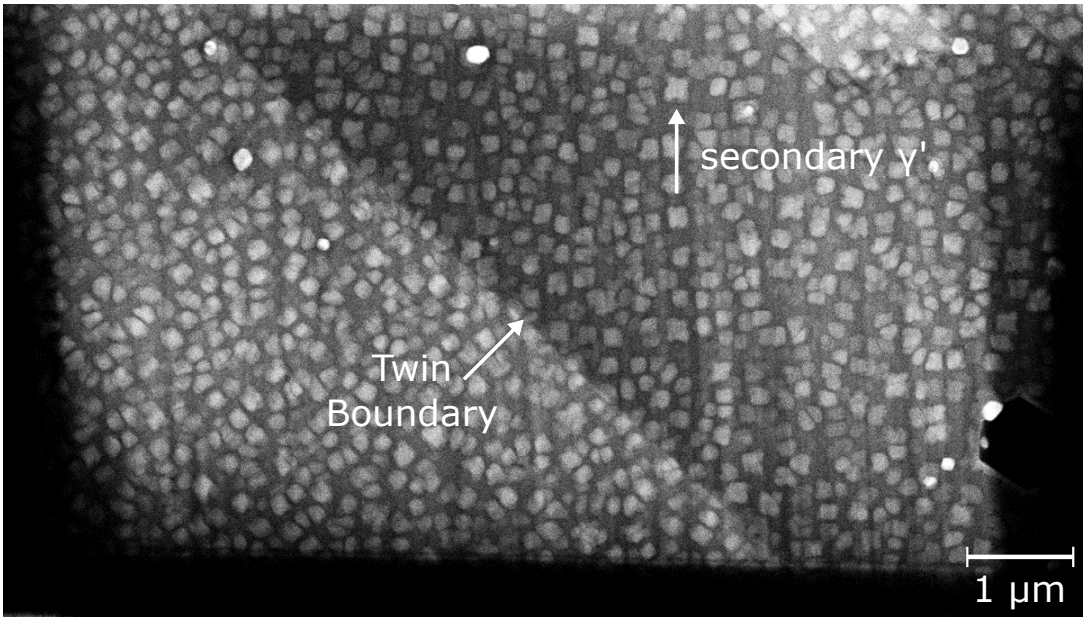

Figure 1.8: A bright field image of a René 88DT foil was collected using an SEM forward scatter detector (courtesy of J.C. Stinville). The secondary γ' precipitate structure is visible along with a twin boundary.

upper ranges [1, 3]. In addition to Hall–Petch and solid solution strengthening, the high number density and volume fraction of small coherent precipitates contributes to the high strength of nickel-base superalloys [2, 16]. Dislocations blocked by a precipitate must either shear the precipitate or Orowan-bow around it, with shearing for shorter precipitate spacings and bowing for longer spacings. A pair of $\frac{a}{2}\langle 1\bar{1}0\rangle\{111\}$ partial dislocations is required to fully shear the ordered γ' phase, with an antiphase boundary (APB) left between [2, 3]. For very small precipitates the dislocation pair may not be contained in a single precipitate (weakly coupled) but for larger precipitates the trailing dislocation enters the precipitate before the leading dislocation exits (strongly couple) [16]. The excess stress required to cut a precipitate with a leading superpartial can be roughly approximated as γ_{APB}/b. The anti-phase boundary surface energy γ_{APB} is $\approx$0.1 J/m^2 resulting in an order strengthening of $\approx$400 MPa [2]. More complete models for precipitate shearing require separate equations for the excess stress τ required to shear strongly and

weakly coupled cases, e.g.:

$$\Delta\tau_{weak} = \frac{\gamma_{APB}}{2b}\left(\sqrt{\frac{\gamma_{APB}d_s}{2T_L}}\frac{d_s}{L_s} - \frac{\pi}{4}\left(\frac{d_s}{L}\right)^2\right) \tag{1.1}$$

$$\Delta\tau_{strong} = \frac{2T_L}{\pi b L_x}\left(\frac{\pi d_s \gamma_{APB}}{2T_L} - 1\right)^2 \tag{1.2}$$

where γ_{APB} is the APB surface energy, b the burgers vector, d_s is the mean planar precipitate diameter, T_L is the dislocation line energy, L_s is the spacing between precipitates, L is the center to center distance between precipitates, and

$$L_x = \sqrt{\frac{8}{3\pi f}}d_s - d(x) \tag{1.3}$$

where f is the γ' volume fraction and $d(x)$ is the length of dislocation within a precipitate at the critical stress [16]:

$$d(x) = \frac{4T_L}{\gamma_{APB}\pi}\sqrt{\frac{d_s\gamma_{APB}\pi}{2T_L} - 1} \tag{1.4}$$

Models of polycrstalline nickel-base superalloy strength accounting for Hall–Petch effect, precipitate shearing in both strongly and weakly coupled modes, and Orowan bowing have been developed and suggest a strong effect of the anti-phase boundary energy [16]. Yield strength does not begin to decrease significantly until ≈850 °C due to the anomalous yield strength of the γ' phase.

Fatigue

Turbine components are subjected to fatigue in both the low and high cycle regimes. Typically low cycle fatigue loading arises from flight cycles and high cycle fatigue from engine resonance (kHz cycling) [1, 2]. Fatigue cracks can initiate at extrinsic non-metallic inclusions, porosity, carbides, eutectic, or within large grains [1, 2, 14, 17]. Initial crack

growth is normally transgranular with a transition to intergranular at longer crack lengths [18, 19]. Long crack growth rates follow a Paris law over wide ranges of stress intensity factor but exhibit increased lifetime variability at lower stresses. Many alloys have a threshold stress intensity factor of 8–20 MPa $m^{1/2}$, although some do not have an endurance limit [2]. Fatigue cracks generally initiate at the surface in low cycle fatigue and internally in high cycle fatigue [14, 20].

1.2 Fatigue Life of Powder Metallurgy Polycrystalline Disk Alloys

Fatigue is the life limiting property of polycrystalline nickel-base superalloys and turbine disks require a wide fatigue safety margin since failure is catastrophic [21, 22]. Fatigue cracks in cast and wrought components frequently initiate at large pores or non-metallic inclusions [17, 23, 24]. Since powder screening limits the maximum inclusion size and consolidation produces a nearly fully dense billet such extrinsic defects are uncommon in PM processed components [8]. In the absence of such large imperfections, initiation occurs at intrinsic defects making fatigue life highly microstructure sensitive and lifetime prediction challenging [1, 25, 26]. René 88DT and similar PM alloys do not exhibit an endurance limit and may not fail in service until high or very high cycle fatigue (10^5 to 10^{10} cycles) [27]. Accurate life prediction in these fatigue regimes is difficult due to high variability in number of cycles to failure (figure 1.9) [14]. Lifetime scatter arises primarily due to differences in crack initiation time and microstructurally short crack growth, which account for a majority of lifetime at lower stress amplitudes [28–30]. Because cracks spend so much of fatigue life being too short to practically detect, in service monitoring of crack growth is not feasible, further complicating lifetime prediction.

Experiments involving high and very high cycle fatigue were historically constrained by the time required for testing. Even at a frequency of 60 Hz, achieving 10^9 cycles

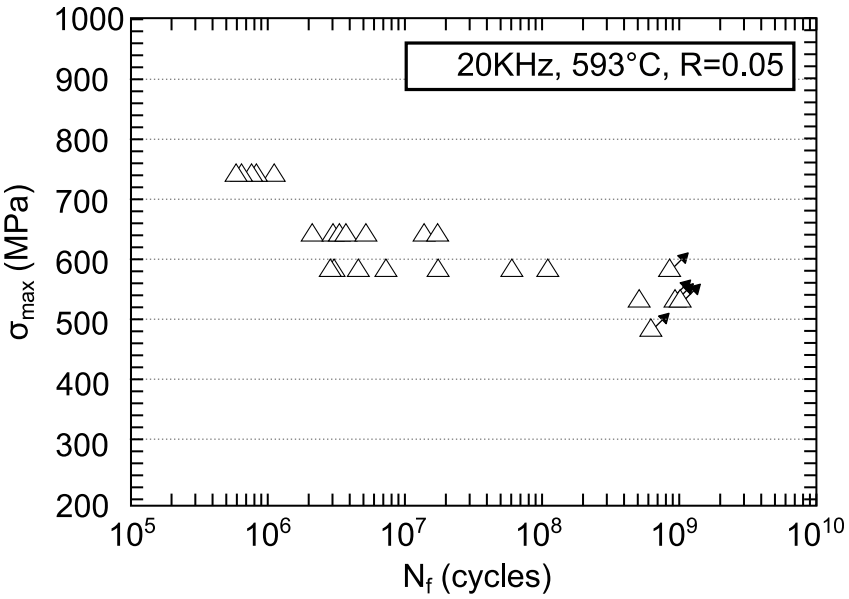

Figure 1.9: The fatigue life of René 88DT is highly variable at lower stresses (data from Miao et al. [14])

requires over 6 months. Ultrasonic fatigue at a frequency of 20 kHz allows the same test to be performed in a single day with fatigue systems and sample geometry shown in figure 1.10. Additionally, testing can accommodate elevated temperatures, matching conditions experienced during turbine operation [31]. While ultrasonic fatigue testing has existed for several decades, recent efforts have enabled in-situ detection of damage, allowing precise interruption of experiments between crack initiation and failure [32].

Fatigue cracks are generally believed to nucleate due to accumulation of dislocations. While simple systems such as copper have been most extensively studied, the fundamental mechanisms insights they provide are applicable to polycrystalline nickel alloys [35]. A grain favorably oriented for slip (high resolved shear stress) experiences plastic strain localization [36]. If the slip is irreversible, a persistant slip band (PSB) may form with dislocation glide in opposite directions on two or more parallel planes [37, 38]. With each cycle, more dislocations accumulate, forming either surface intrusions/extrusions or a dislocation pile up at an internal obstacle, e.g. a grain boundary (figure 1.11) [39, 40]. When the stress field from this induced surface roughness or dislocation pile up is

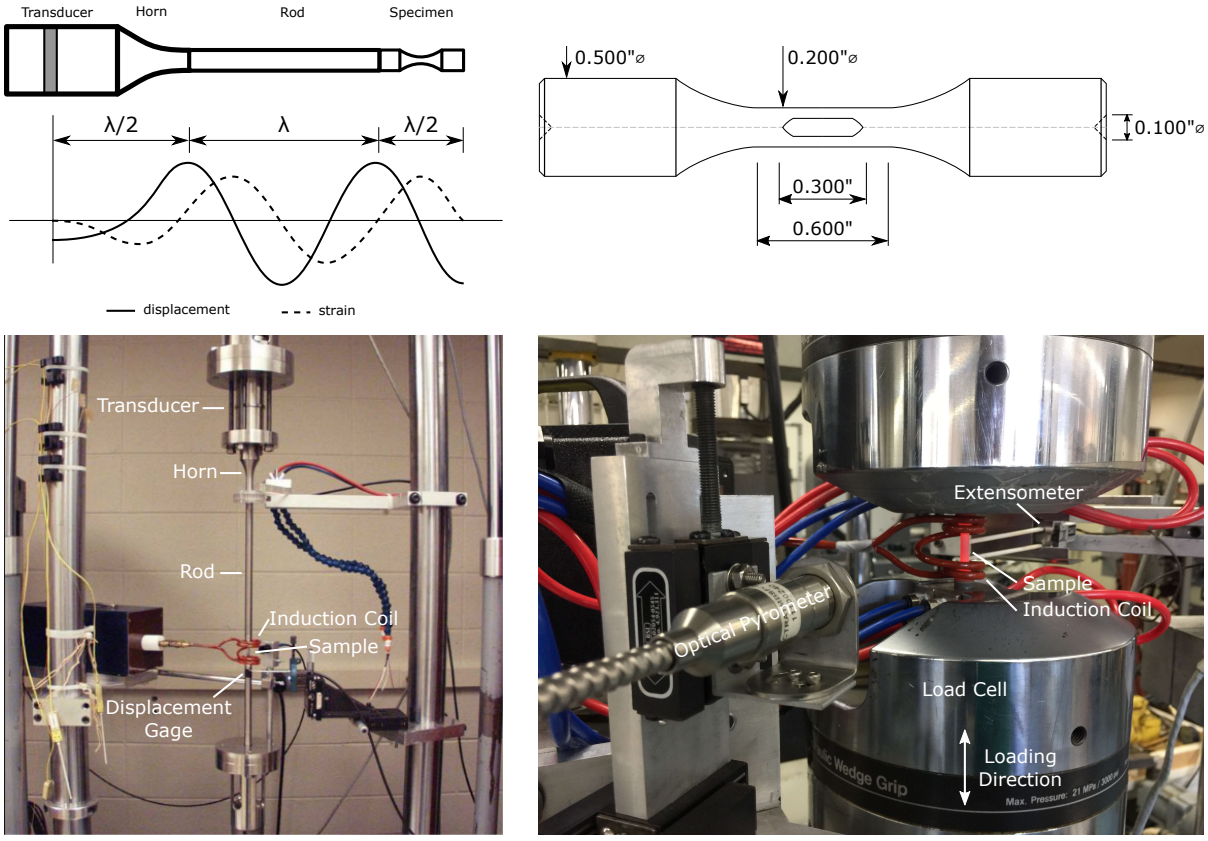

Figure 1.10: An ultrasonic fatigue system with displacement and strain profiles is shown schematically (top left, figure based on Yi et al., Copyright 2007, with permission from Elsevier [33]). The ultrasonic fatigue system uses an induction coil to heat the sample (bottom left, figure reproduced from Shyam et al. [34] Copyright 2004 by The Minerals, Metals & Materials Society. Used with permission). The specimen geometry may optionally have symmetric flats machined on opposing sides to facilitate interrupted metallography (top right). The electro-mechanical load frame used for low cycle fatigue tests can use the same sample geometry (bottom right, figure courtesy of Sean Murray).

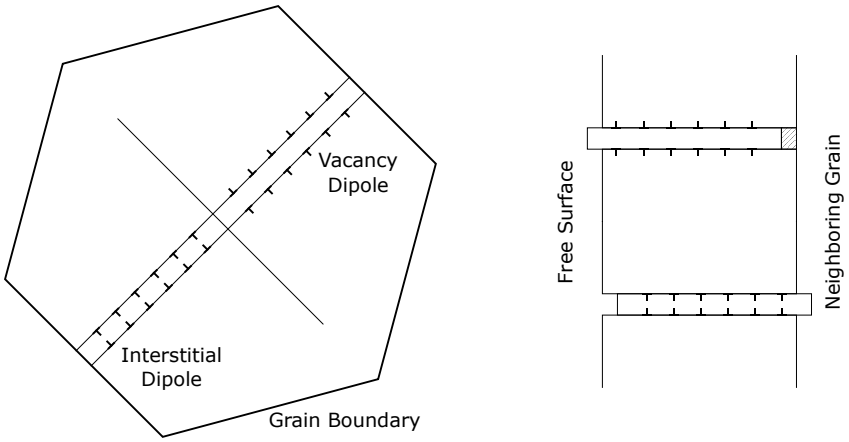

Figure 1.11: Two closely spaced parallel slip planes result in irreversible slip if alternating planes are active during loading and unloading respectively (left). Accumulated slip forms crack embryos at grain boundaries (top right) or surface intrusions/extrusions (right). Left figure republished with permission of the American Society of Mechanical Engineers from Tanaka and Mura [41]; permission conveyed through Copyright Clearance Center, Inc.

sufficient, an embryonic crack will form [41]. Although the principles of PSB formation apply to nickel-base superalloys, dislocation shearing of and bowing around precipitates cause differences in initial irreversible slip [2, 19, 42]. These microstructural differences from pure materials also create an asymmetry between the tensile and compressive yield strengths of superalloys which may play an important role in initial strain localization [19, 43].

Determination of the microstructural conditions responsible for initiation of fatal cracks is necessary for the development of an accurate model for fatigue life prediction. Additionally accurate fatigue life predictions are necessary to prevent future turbine failures [26]. The total cycles to failure n is

$$n = n_i + n_{sc} + n_{lc} \tag{1.5}$$

where n_i, n_{sc}, and n_{lc} are the number of cycles spent in crack initiation, short crack growth, and long crack growth, respectively. Variability in initiation cycles is a significant source of total fatigue life variability [44]. Identifying and characterizing regions amenable

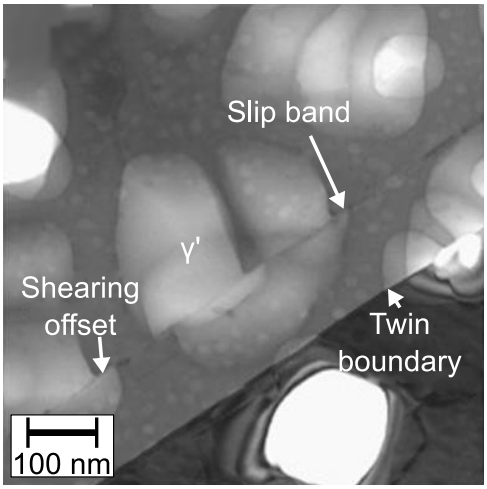

Figure 1.12: Sharp strain localization occurs near favorably oriented annealing twin boundaries. Figure reprinted from Miao et al., Copyright 2012, with permission from Acta Materialia Inc. [15].

to crack nucleation and initial propagation is a critical step in both predicting fatigue life of current materials and designing new materials with improved fatigue life. Fatigue cracks in the PM disk alloy René 88DT have recently been found to initiate due to sharp strain localization near (≈100 nm away from) annealing twin boundaries in large grains that are favorably oriented for slip (possessing a high Schmid factor) as shown in figure 1.12 [14]. Accumulation of irreversible, cyclic dislocation slip results in large incompatibility stresses, ultimately nucleating a crack. Similar investigations of low cycle fatigue behavior found high angle boundaries arrest crack growth, suggesting fatal cracks initiate in grains belonging to a larger, twin and low disoriention angle related domain [15].

1.3 Open Questions

By analyzing many observed fatigue cracks Miao et al. found that fatigue cracks in René 88DT mostly initiate near annealing twins in grains on the tail of the size distribution (at least three times larger than the average grain size) [14, 15]. They also found that the transition from initiation to short crack growth is neighborhood dependent with high

angle grain boundaries arresting crack growth. Investigating the frequency of large grains surrounded by large twin or low disorientation angle related clusters revealed that these fatal sites are a microstructural extreme with a very low frequency [15]. Quantitative structure–property relationships for fatigue life of PM polycrystalline nickel-base superalloys are lacking despite these recent insights. Some critical open questions preventing the development of such a link motivate the work of this dissertation:

1. How are annealing twins in FCC metals formed?
2. What is the structure of twin and low disorientation angle related domains?
3. How frequently do the microstructural extremes responsible for fatal crack initiation occur?
4. How large of a volume is necessary for measurement and convergence of microstructural extremes?

Chapter 2 will review the current understanding of annealing twin formation. Fully characterizing twin related domains and their connectivity requires 3D as illustrated in figure 1.13. The cases necessitating 3D microstructural data and on overview of existing methods will be discussed in chapter 3. Experimental methods and microstructural volumes collected are enumerated in chapter 4. Investigations of fatigue crack initiation and propagation are presented in chapter 5 and chapter 6 respectively.

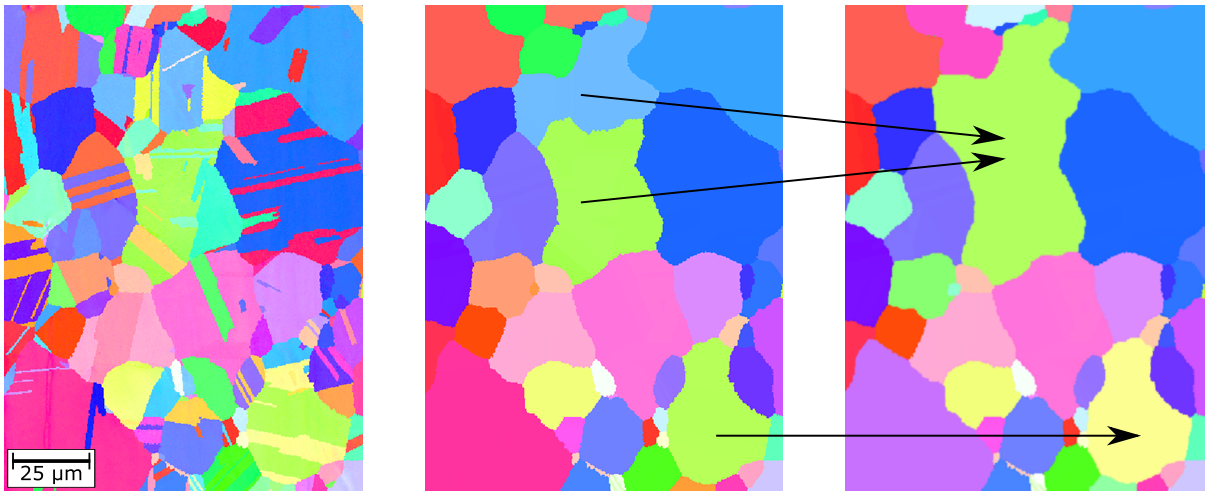

Figure 1.13: The microstructure of 2D slice René 88DT taken from within a 3D volume is shown at left. Grouping twin related domains in the 2D section (center) results in missed connections and incorrect orientation assignments compared to grouping domains in 3D and then taking a 2D section. All maps are IPF colored with Z reference direction (twin related domains are colored using the orientation of the largest volume fraction variant).

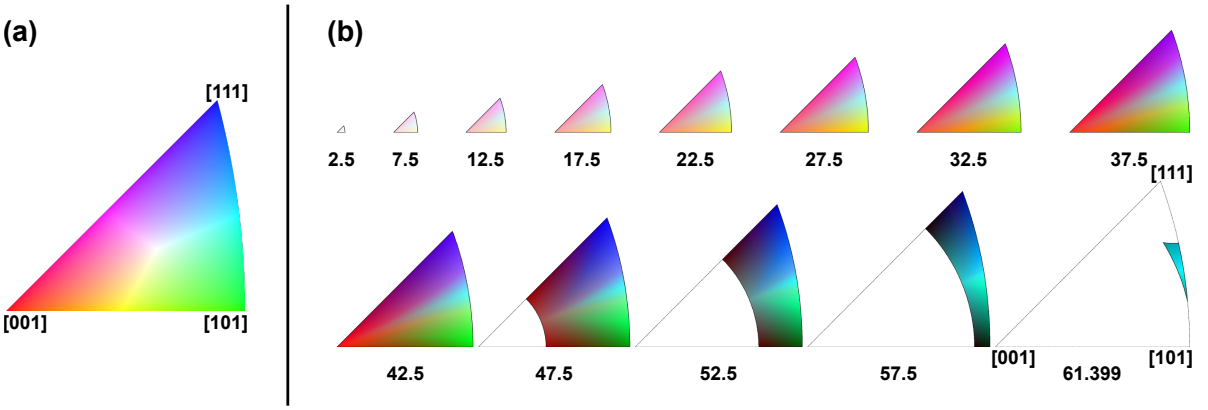

Figure 1.14: Grain and voxel orientations in this document are represented with either IPF coloring [45] (a) or disorientation coloring (b) [46] and boundary disorientations are represented with disorientation coloring. To determine the color to which an orientation maps, identify the crystallographic direction parallel to the reference direction and locate the corresponding color on the stereographic triangle. A +Z reference direction is used in this work unless otherwise specified (for 2D scan +Z corresponds to the page normal). To determine the color to which a disorientation maps, first select the stereographic triangle corresponding the disorientation angle, then locate the color at the disorientation axis. For example, to identify the disorientation color for 36.86° about [001], select the 37.5° stereographic triangle and locate the color at [001] (red). Disorientation coloring can also be used to color orientation. Orientations are colored by computing the disorientation relative to the reference frame (imposing the symmetry operators of the crystal on the reference frame). The resulting disorientation is then mapped as described above.

Chapter 2

Annealing Twin Formation in FCC Metals

Generally two crystals of the same structure are considered to have a twin orientation relationship if one is the mirror image of the other. The crystallographic plane parallel to the mirror plane is the twinning plane ({111} planes in FCC materials). Boundaries parallel to the twinning plane are coherent twin boundaries and those not parallel are incoherent twin boundaries. In FCC materials, the disorientation between a parent and its twin is a 60^o rotation about a $\langle 111 \rangle$ axis. The FCC twin relationship is illustrated in figure 2.1 and can also be understood as a reversal of the close packed plane stacking order (e.g. ABCABC to CBACBA).

Coincidence site lattices are special grain boundaries, typically denoted Σn, with a high fraction of coincident atoms $(1/n)$ [47, 48]. Coherent twin boundaries have the most dense coincident site lattice (CSL) attainable in FCC materials ($\Sigma 3$). Increasing the proportion of twin and other low Σ CSL grain boundaries can improve a wide variety of material properties including creep life, weldability, corrosion resistance, and conductivity [49, 50]. These so called 'Grain Boundary Engineered' materials can show dramatically

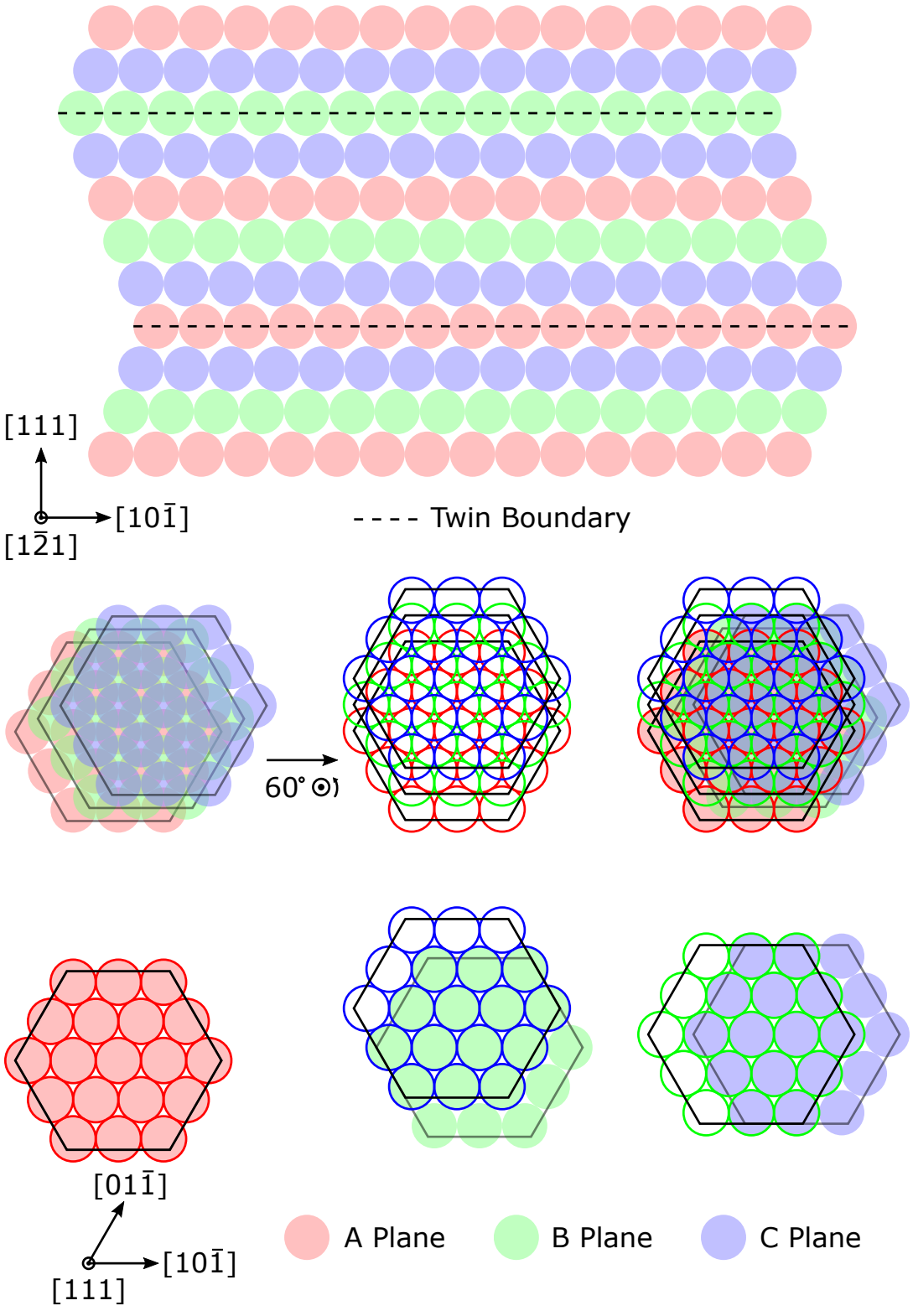

Figure 2.1: FCC twinning is a reversal of close packed plane stacking order (top) and is a 60° rotation about ⟨111⟩ axis (bottom).

improved performance and are therefore of great interest. Twins also have a strong influence over the texture that develops during recrystallization [50–54]. Annealing twins occur in many widely used material systems including Al, Cu, and Ni base alloys as well as Austenitic steels [55]. Understanding the mechanism(s) of twin nucleation is important as it may improve our ability to predict and control the density of twin boundaries.

Twins may form as the result of deformation (particularly in HCP or BCC materials with limited slip systems), solid state phase transformations, solidification, or annealing. Mechanical twins have been extensively studied and mature models developed [56, 57]. However, there is still uncertainty regarding the mechanism(s) responsible for annealing twin formation. Annealing twins (referred to simply as twins for the remainder of this document) may form during recovery, recrystallization, or grain growth [50]. Figure 2.2 shows a sequence of micrographs typical of twin formation during annealing.

2.1 Models and Theories

Proposed mechanisms for annealing twin formation are broadly divided into four categories in the literature [55, 59]: grain encounter [60–62], growth accidents [63–65], grain boundary dissociation [66, 67], and nucleation of twins by packets of stacking faults [68]. Growth accident and grain encounter require grain boundary migration, making them unsuitable mechanisms to explain recovery twins. Each of the four categories of theories are presented here chronologically with respect to first proposal of the mechanism.

2.1.1 Growth Accident

The growth accident model theorizes that twins are formed during grain boundary migration by nucleation and growth of closed packed planes with a twin boundary resulting from faulted plane nucleation [63]. The concept of an accident occurring at a migrating grain boundary was first proposed in 1926 by Carpenter and Tamura [69]. Subsequent

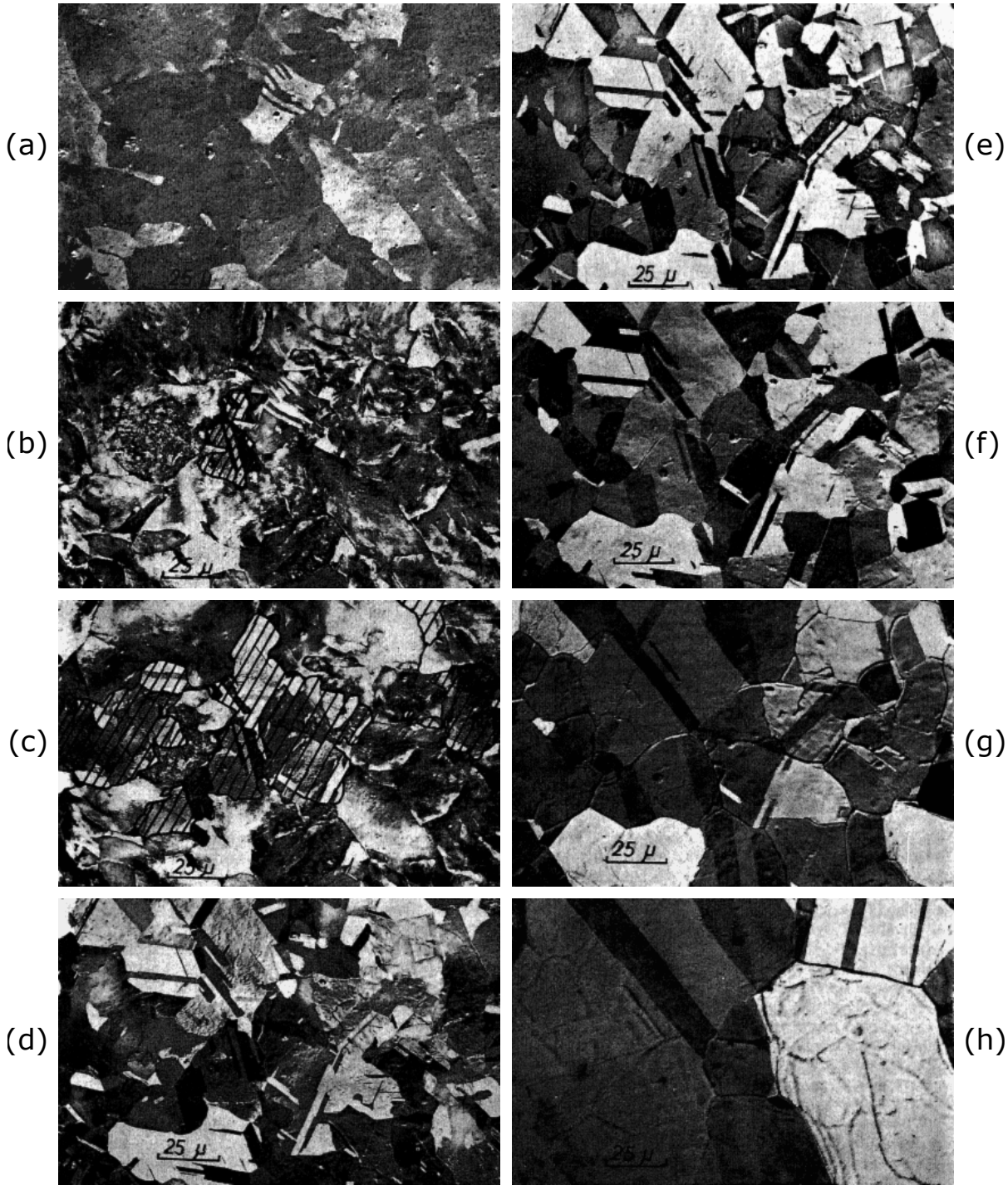

Figure 2.2: The formation of twins during annealing of copper. (a) shows the as deformed microstructure. (b)-(c) recrystallization, hatched regions are recrystallized. (d) recrystallization is complete. (e)-(h) grain growth. Figure reproduced from Gindraux and Form [58].

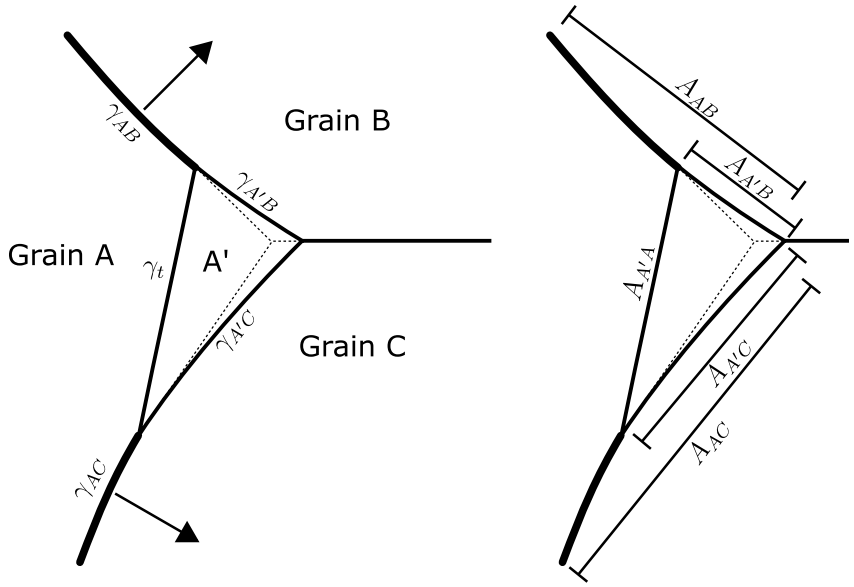

Figure 2.3: Boundary energy balance for growth accident. A′ is a twin of A. Thickness of boundaries corresponds to their energy. Left image reprinted from Fullman and Fisher [70], with the permission of AIP Publishing.

work suggested boundary energy reduction as a driving force [70]. For the geometry shown in figure 2.3, it is energetically favorable for a twin to nucleate when the energy of created boundaries is less than destroyed boundaries:

$$\gamma_t A_{A'A} + \gamma_{A'B} A_{A'B} + \gamma_{A'C} A_{A'C} = \gamma_{AB} A_{AB} + \gamma_{AC} A_{AC} \tag{2.1}$$

Relative widths of thermally grooved boundaries are supplied as evidence for such an energy minimization criterion being satisfied by corner twins (twins along a triple line with two non-twin related grains).

A more complete atomistic model was proposed by Gleiter [63]. His model is based on the idea of grain boundaries with steps on a {111} plane. Atoms are deposited at the steps, sweeping them across the surface and advancing the boundary. New {111} planes may be formed by spiral growth or 2D nucleation. Spiral growth around a dislocation of type $\frac{1}{2}[0\bar{1}1] + \frac{1}{6}[\overline{11}2] = \frac{1}{6}[\overline{1}41]$ creates a twin. A twin may also be generated by 2D nucleation of an incorrect plane (...ABC ABA CBA ...) shown schematically in

figure 2.4. An expression for the probability p that a given $\{111\}$ plane nucleates as a twin is developed:

$$p = \exp\left\{\sigma_z\left(Q - kT\ln\frac{\Delta G^o}{kT}\right)\Big/\left[kT\sigma_z - \frac{\pi kT\epsilon^2 h^2}{Q - kT\ln\frac{\Delta G^o}{kT}}\right]\right\} \tag{2.2}$$

where σ_z is the surface energy of a coherent twin boundary, Q is the activation energy for boundary migration, k is Boltzmann's constant, T is temperature, ΔG^o is the difference in Gibbs' free energy between the grains (arising from differences in curvature and/or strain energy density), ϵ is the surface energy of the $\{111\}$ step, and h is the step height. Equation 2.2 can be expressed more compactly as:

$$p = \exp\left(\frac{x}{1 - \frac{c}{x}}\right) \tag{2.3}$$

$$x = \frac{Q}{kT} - \ln\left(\frac{\Delta G^o}{kT}\right) \tag{2.4}$$

$$c = \frac{\pi\epsilon^2 h^2}{\sigma_z kT} \tag{2.5}$$

For $kT \ll Q$ this can be reduced to

$$p = \exp\left\{\left(\ln\left(\frac{\Delta G^o}{kT}\right) - \frac{Q}{kT}\right)\Big/\left(\frac{\pi\epsilon^2 h^2}{Q\sigma_z} - 1\right)\right\} \tag{2.6}$$

Although recently it has been suggested that $kT \ll Q$ is not a valid assumption, its appearance in the literature is frequent [71]. Equation 2.6 predicts a strong dependence of twin frequency on annealing temperature [63]. This is generally not borne out in experimental observations of twin density, which led to the development of an alternate model by Mahajan et al. Their model is based on twins nucleating at $\{111\}$ steps in migrating boundaries and suggests if the driving force for migration is large, the boundary creates more twins per distance traversed:

$$\Delta N \propto (\Delta D)\, F \tag{2.7}$$

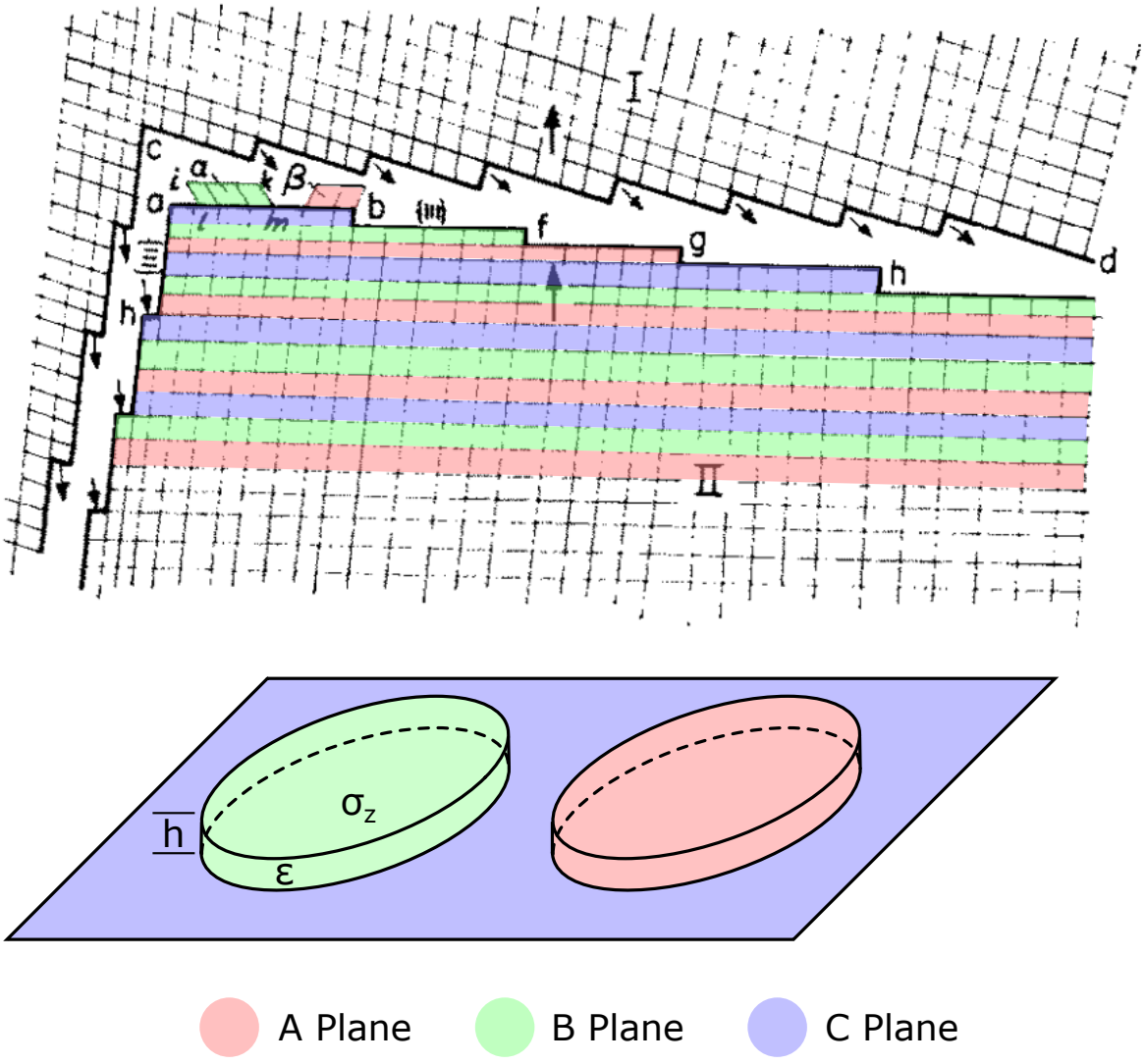

Figure 2.4: Formation of twin by 2D nucleation in the growth accident model. Grain II is growing at the expense of grain I. A new {111} plane may nucleate in a faulted position (top left colored plane), creating a twin boundary, or correctly (top right colored plane) continuing normal growth (top). Detail of the nucleated planes is labeled with equation parameters (bottom). Top figure reprinted from Gleiter et al., Copyright 1969, with permission from Elsevier [63].

where ΔN is the change in twin density (per grain), ΔD is a grain size change (and therefore a measure of boundary migration distance), and F is the driving force for migration [64, 65]. Twin density is phenomenologically found to take the form

$$\frac{p}{p_o} = \frac{D_o}{D} \log \frac{D}{D_o} \tag{2.8}$$

where p_o and D_o are normalization constants and D is grain size. The parameter p_o is directly proportional to average grain boundary energy and inversely to twin boundary energy.

It has been recently demonstrated that Gleiter's 'full' equation (Equation 2.2) has only a weak temperature dependence [72]. One subtle difference between the theories of Gleiter and Mahajan et al. is in regard to the orientation of the twin formed with respect to the boundary. In Gleiter's model steps are *between* {111} planes. As a result the nucleated twin has its coherent boundary parallel to the migrating boundary. In the model of Mahajan et al. the steps *are* {111} planes, which results in the nucleated twin's coherent boundary being perpendicular to the grain boundary.

2.1.2 Grain Encounter

Grain encounter is conceptually the simplest model, suggesting that a twin boundary is formed when two grains with a twin orientation relationship impinge during grain growth as shown schematically in figure 2.5 [60–62]. For uniform 14-sided grains in an FCC material as much as 1.4% of encounters will form twins in an untextured material; this can be up to an order of magnitude higher in a strongly textured one [62, 73].

2.1.3 Stacking Fault Packets

Dash and Brown observed twins at grain boundaries shortly after their formation during recrystallization [68]. Their investigation suggested twins nucleate as stacking faults or

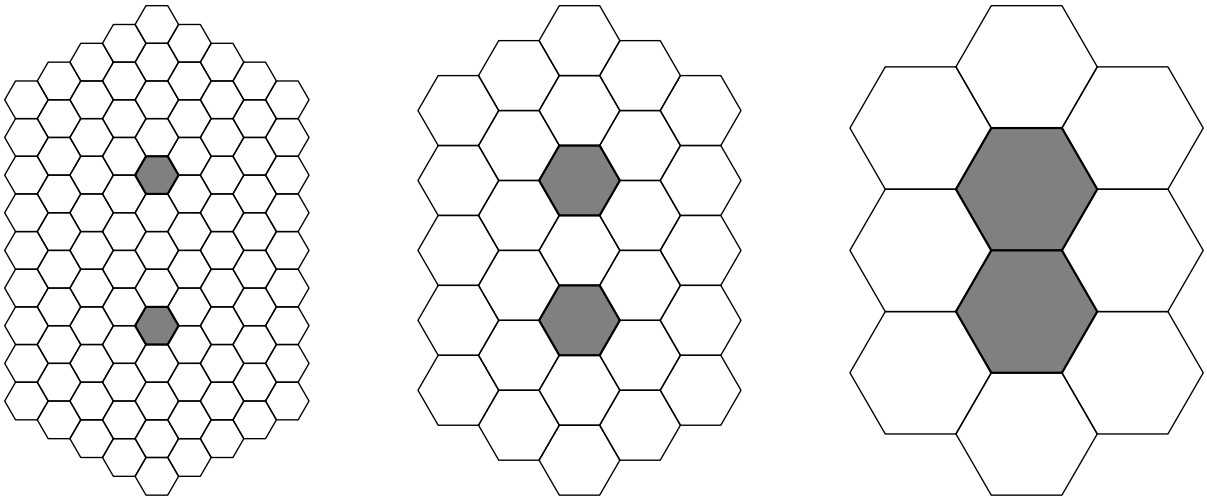

Figure 2.5: A schematic of the grain encounter mechanism is shown. The shaded grains have a twin misorientation and a twin boundary created by impingement during grain growth.

packets of stacking faults. A surface energy analysis for a half disk shaped nucleus yields a critical twin radius

$$r = -\frac{np}{2E_t}\left[\frac{2}{\pi}(E_{BC} - E_{AB}) + E_n\right] \tag{2.9}$$

where np is the thickness, p is the spacing of 111 planes, r is the radius, E_t is the energy of the twin boundary, E_n is the energy of the incoherent boundary, and E_{BC}, E_{AB} are the energies of the corresponding grain boundaries shown in figure 2.6.

2.1.4 Boundary Dissociation

The boundary dissociation model was first proposed by Meyers and Murr in 1978. It is unique in that the "nucleation boundary" can be stationary [66]. If 2 adjacent grains are near a twin orientation but are not joined by a twin boundary, the grain boundary may dissociate into a coherent and incoherent boundary as depicted in figure 2.7. This is energetically favorable when

$$\gamma_{TB}A_{TB} + \gamma_{tb}A_{tb} < \gamma_{gb}A_{gb} \tag{2.10}$$

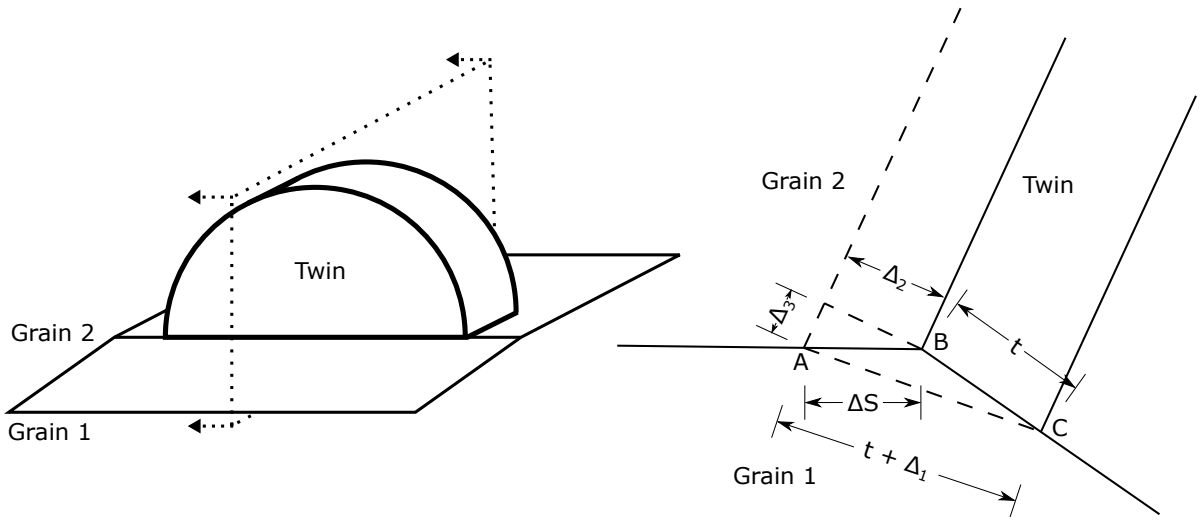

Figure 2.6: A half disk twin (left) is shown in cross section (right). Dashed lines represent the shape of the twin after growth due to the triple junction moving from point B to A. Right figure reprinted from Dash and Brown, Copyright 1963, with permission from Elsevier [68].

where TB, tb, and gb indicate the coherent twin, incoherent twin, and grain boundaries, respectively. Estimates for γ_{TB}, γ_{tb}, and γ_{gb} in Nickel are $0.0336\,\mathrm{Jm}^{-2}$, $0.497\,\mathrm{Jm}^{-2}$ (half of γ_{gb}), and $0.994\,\mathrm{Jm}^{-2}$ respectively. Twins may also nucleate in an analogous fashion when neighboring grains form a special (low energy) boundary after dissociation. Grain boundary ledges are considered an important feature for nucleation due to their ability to emit dislocations and stacking faults. Twins may grow by movement of the grain boundary or of the incoherent twin boundary. It is suggested that the driving force for incoherent twin boundary migration, depicted in figure 2.8, is adoption of a lower energy 'habit plane' [66]. However, differences in stored strain energy may be more significant during recrystallization. Subsequent work by Goodhew determined that several dissociations are possible, including: $\Sigma 9 \rightarrow \Sigma 3 - \Sigma 3$, $\Sigma 11 \rightarrow \Sigma 3 - \Sigma 33$, and $\Sigma 99 \rightarrow \Sigma 3 + \Sigma 33$ [67]

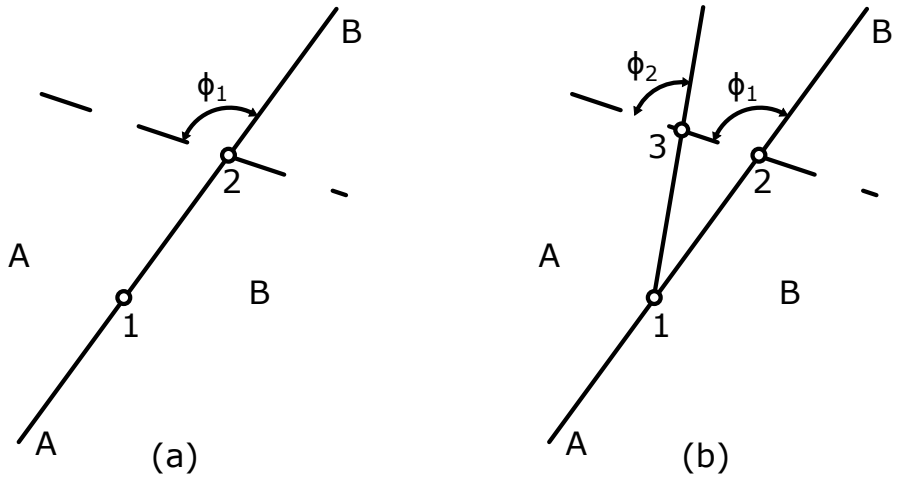

Figure 2.7: Grains of twin relationship (a) before and (b) after dissociation. In (a) segment $\overline{12}$ is a normal grain boundary due to inclination. In (b) segment $\overline{12}$ is an incoherent twin boundary and segment $\overline{23}$ a coherent twin boundary. Figure reprinted from Meyers and Murr, Copyright 1978, with permission from Elsevier [66].

2.2 Experimental Observations

2.2.1 Twin Density

Extensive experimental studies have been performed on twin density in an attempt to determine the influence of various factors on twinning frequency. Most experiments measuring twin density involve performing a series of thermomechanical treatments on a material and subsequently measuring twin density via standard metallographic techniques [64, 71, 74–78] or electron backscatter diffraction [54, 79, 80]. Several investigations have been performed in-situ via photoemission electron microscopy (PEEM) [58, 81, 82]. An assessment of this work reveals twin frequency is related inversely to stacking fault energy and directly to grain boundary energy [70, 81, 82]. However, there are conflicting results regarding the influence of most other factors including grain size, annealing temperature, and prior strain. For example, investigators claim that the occurrence of twins is directly [54, 76] or inversely [82, 83] related to grain size. Such ambiguity is due

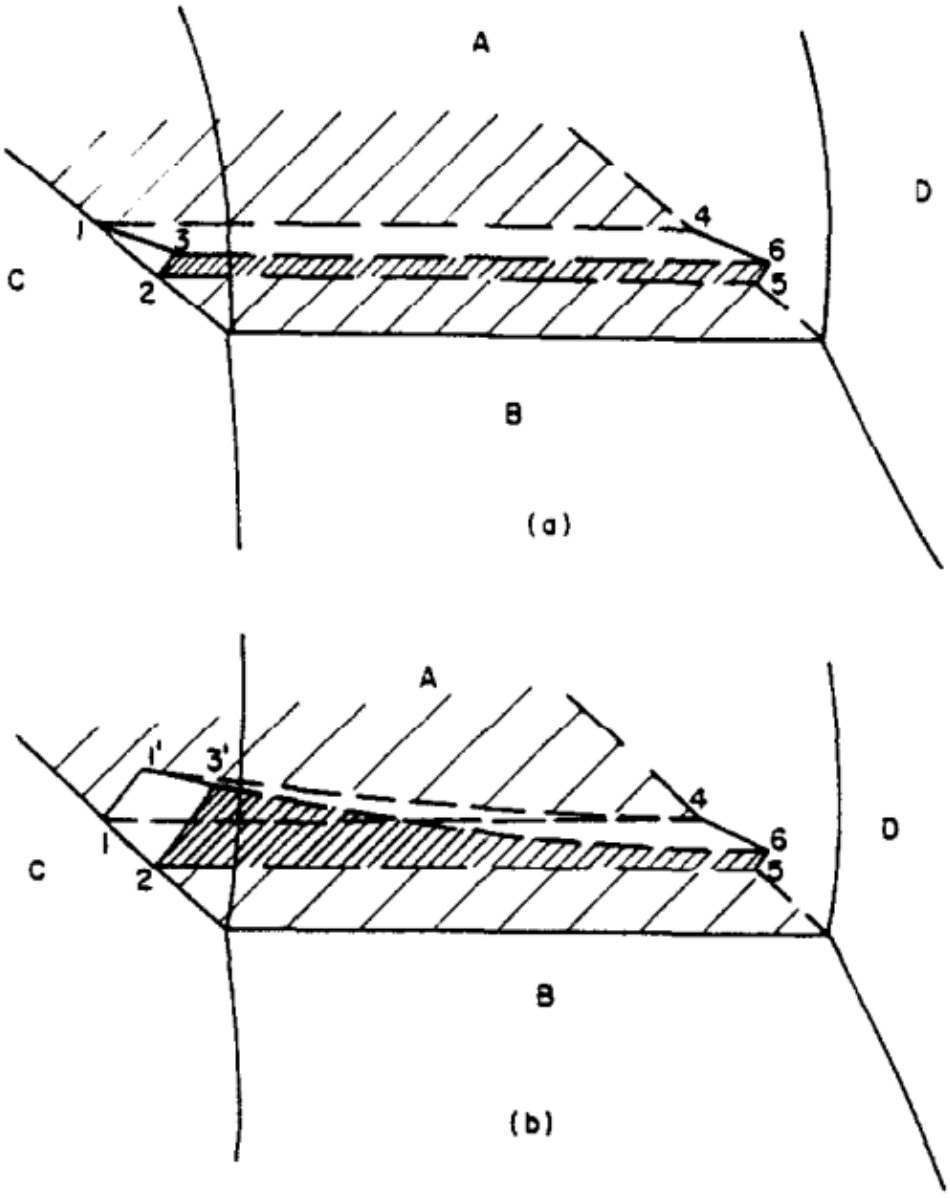

Figure 2.8: 3D representation of boundary dissociation. The twin nucleus is shown in (a). $\overline{1245}$ was the original boundary, $\overline{1346}$ is the incoherent twin boundary, $\overline{2356}$ is the coherent boundary. The incoherent boundary rotates to adopt a lower energy 'habit' plane, propagating the twin. Figure reprinted from Meyers and Murr, Copyright 1978, with permission from Elsevier [66].

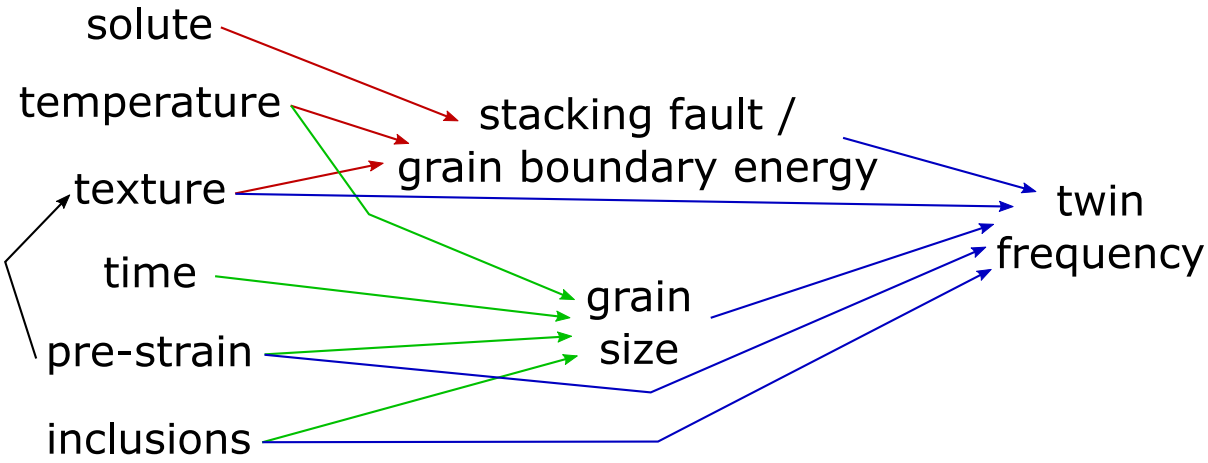

Figure 2.9: Factors influencing annealing twin frequency are shown schematically. Figure based on Charnock and Nutting [81].

to several issues. Annealing twins may form during recovery, recrystallization, and/or grain growth; potentially with varying mechanism(s) for twin formation active during each stage [50]. The factors controlling the processes are highly interrelated, as shown in figure 2.9, making variable isolation difficult. Twins may frequently be created and annihilated simultaneously [58]. With the exception of in-situ experiments it may be impossible to distinguish twins formed during different stages of annealing. Variations in the method used to report twin density further exacerbate the difficulty in comparing results from multiple studies.

Twin Density Measurements

Twin densities for 2D sections have been reported as the number of coherent twin interfaces: per grain (N_G), per area (N_A), or intersecting a line of given length (N_L) [82]. Comparing densities reported by different metrics is problematic as illustrated by a change in grain size: for two grains with the same number of twins N_G but different volumes, N_A will be greater for the smaller grain. The correct measure of twin density is m^{-1} ($\frac{area}{volume}$ analogous to dislocation density as $\frac{length}{volume}$). This makes N_L the most appropriate 2D measure of twin density as it can be directly related to density with standard methods of stereology. Neither N_G or N_A are rigorous since they are measures of $\frac{\#}{area}$

(or $\frac{\#}{volume}$) not $\frac{length}{area}$ (or $\frac{area}{volume}$) [55, 82]. Experiments using EBSD can report density as area fraction of twin boundaries, allowing direct measurement of density (twin boundary area per volume in m^{-1}) [80]. Twin density is sometimes measured as volume fraction of twins, which requires an assumption about which part of a grain twinned and which is the parent orientation. Any metric can be rigorously calculated from 3D microstructural data, but density (m^{-1}) is most practical since it can be compared directly with N_L. N_L is the best metric when comparing densities with predictions of the growth accident model since it is directly proportional to p in Equation 2.2 and Equation 2.8.

Grain Size

Annealed grain size is perhaps the most challenging variable of the factors influencing twin density as evidenced by repeatedly conflicting observations. Growth models predict that twin density (p) is either monotonically decreasing with increasing grain size [63] or has a peak for very small grain sizes [64]. Comparing only studies reporting density with the same metric clarifies the situation in part. Measurements of N_G and percent twin boundary area generally report an increase in density with increasing grain size [54, 55, 65, 76, 78, 80]. Measurements of N_A report a decrease in density with increasing grain size [71, 82]. However numerous experiments yield complex behavior (no monotonic dependence) [64, 75, 79, 81, 83]. Several attempts have been made to reconcile the discrepancy using normalized grain size and generally show an inverse dependance of twin density on grain size [71, 75, 81]. An example by Pande normalizing both twin density and grain size to compare across material systems is shown in figure 2.10.

Several attempts have been made to reconcile the discrepancy using normalized grain size, with an example by Pande normalizing twin density and grain size to compare across material systems as shown in figure 2.10 [71, 75, 81].

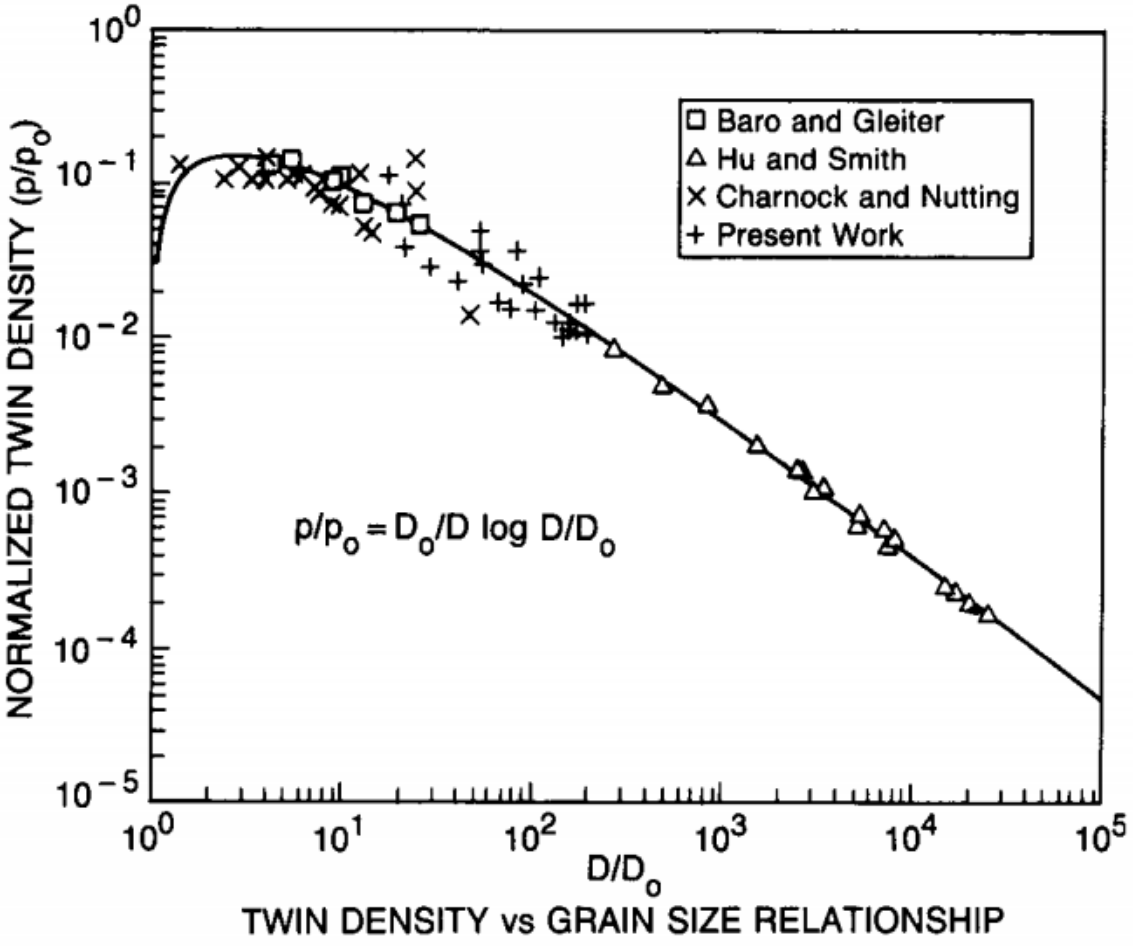

Figure 2.10: Twin boundary density is plotted against grain size. Line is based on Mahajan growth accident model (Equation 2.8). It is important to note that the fit may appear better than it is due to different experiments interrogating different grain size ranges. Figure reproduced from Pande et al. [64] with permission of Springer, copyright 1990 The Metallurgical Society of AIME.

Annealing Temperature

Many twin density investigations involve either isochronal or isothermal annealing, making it difficult to isolate the effects of temperature from grain size. Gleiter's model contains a temperature dependence while that of Mahajan et al. does not (Equation 2.2, Equation 2.8). It has been shown that when Equation 2.2 is evaluated for realistic thermodynamic values it predicts twin density is only a weak function of temperature [71, 72]. Studies of brass, comparing grains of similar size show little or no temperature dependence [76, 81]. There is no clear trend for copper with observations of temperature independent behavior and an increase in twin frequency with temperature [58, 63, 64, 77].

Prior Strain

Prior strain influences twin formation by increasing dislocation density, altering texture, changing initial grain size, and increasing the driving force for boundary migration. The influence of strain is contained within the ΔG^o term of Gleiter's treatment and D_o in the treatment of Mahajan et al. Studies of strain exhibit a linear dependence of twin density with ϵ/d_i for strains of 10% to 40% [82]. The effect is strong in copper and relatively weak in nickel [82]. Studies over a wider strain range suggest that a peak in twin density is eventually reached with increasing strain [71, 78, 81].

Other Factors

Other factors which can influence twin density include stacking fault energy, grain boundary energy, dopants, texture, and boundary speed [75, 81]. It is generally accepted that the energy of coherent twin boundaries is directly related to stacking fault energy with the relationship $\gamma_{TB} \approx \gamma_{SFE}/2$ because two adjacent twin boundaries form an intrinsic stacking fault as shown in figure 2.11 [71, 72]. Twin boundary and grain boundary energy are accounted for in the growth accident models of both Gleiter and Mahajan et

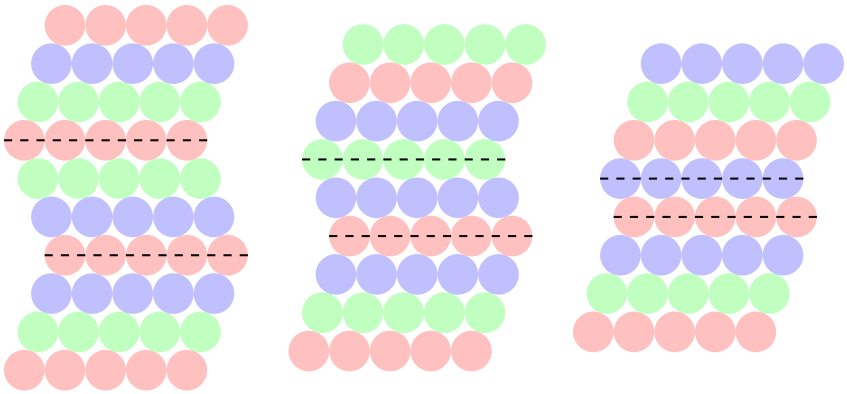

Figure 2.11: The relationship between coherent twin boundary energy and stacking fault energy is illustrated with increasingly thin twins. Two coherent twin boundaries on adjacent {111} planes is equivalent to an intrinsic stacking fault.

al. with $\Delta G^o \propto \gamma_{gb}$ and $\sigma_z = \gamma_{tb}$ in Equation 2.2 and $p_o \propto \gamma_{gb}/\gamma_{tb}$ in Equation 2.8. Consistent with a growth accident model, it is widely accepted that increasing stacking fault energy (and therefore twin boundary energy) decreases twin frequency [55, 81, 82]. Similarly, increasing the ratio of grain to twin boundary energy promotes twin formation [55, 81]. Doping may influence twin formation due to solute segregation, but few studies have been performed. In general increasing the concentration of boron inhibits twin formation [78]. There may be a minimum in twin density for moderate doping (≈150 ppm) [75]. Increasing the speed of boundary migration appears to increase twin density [64, 76].

2.2.2 Twin Morphology

Many authors attempt to classify twins by their morphology with typical categories shown in figure 2.12. Some even rule out formation theories based on observed shapes [59, 65]. To date, very limited work has been done using 3D twin morphology. These studies found many twins had complex shapes, an example of which is shown in figure 2.13, that could not be classified into the simple categories often used [84, 85]. In figure 2.14, a 3D twin with a simple shape is sectioned with various planes showing multiple 2D shapes.

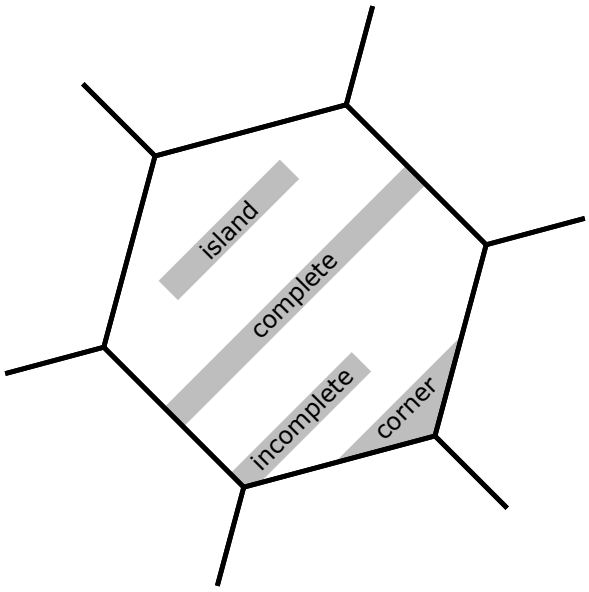

Figure 2.12: Observed Twin Morphologies are illustrated schematically with island, complete, incomplete, and corner twins typically classified by grain boundary adjacency.

2.2.3 Other Observations

Gastaldi and Jourdan first observed in-situ twin growth via X-ray tomography. They determined the shape of twins shortly after nucleation is based on the shape of the grain in which they form [86]. Meyers and Murr noted grain boundary ledges emitting stacking faults and dislocations [66]. Field et al. discovered that imposing shear stress during annealing increased twin density, suggesting that large residual stresses may have a similar effect [87]. Song et al. observed fast moving random grain boundaries by repeatedly interrupting recrystallization of lead [88]. Figure 2.15 shows an example in which a random boundary dissociates into a $\Sigma 3^n$ type boundary (frequently $\Sigma 3$) and another random grain boundary.

2.2.4 Simulations

More recently it has become possible to probe twin formation through simulation. Molecular dynamics-based simulation of annealing copper suggests nucleation of twins at mi-

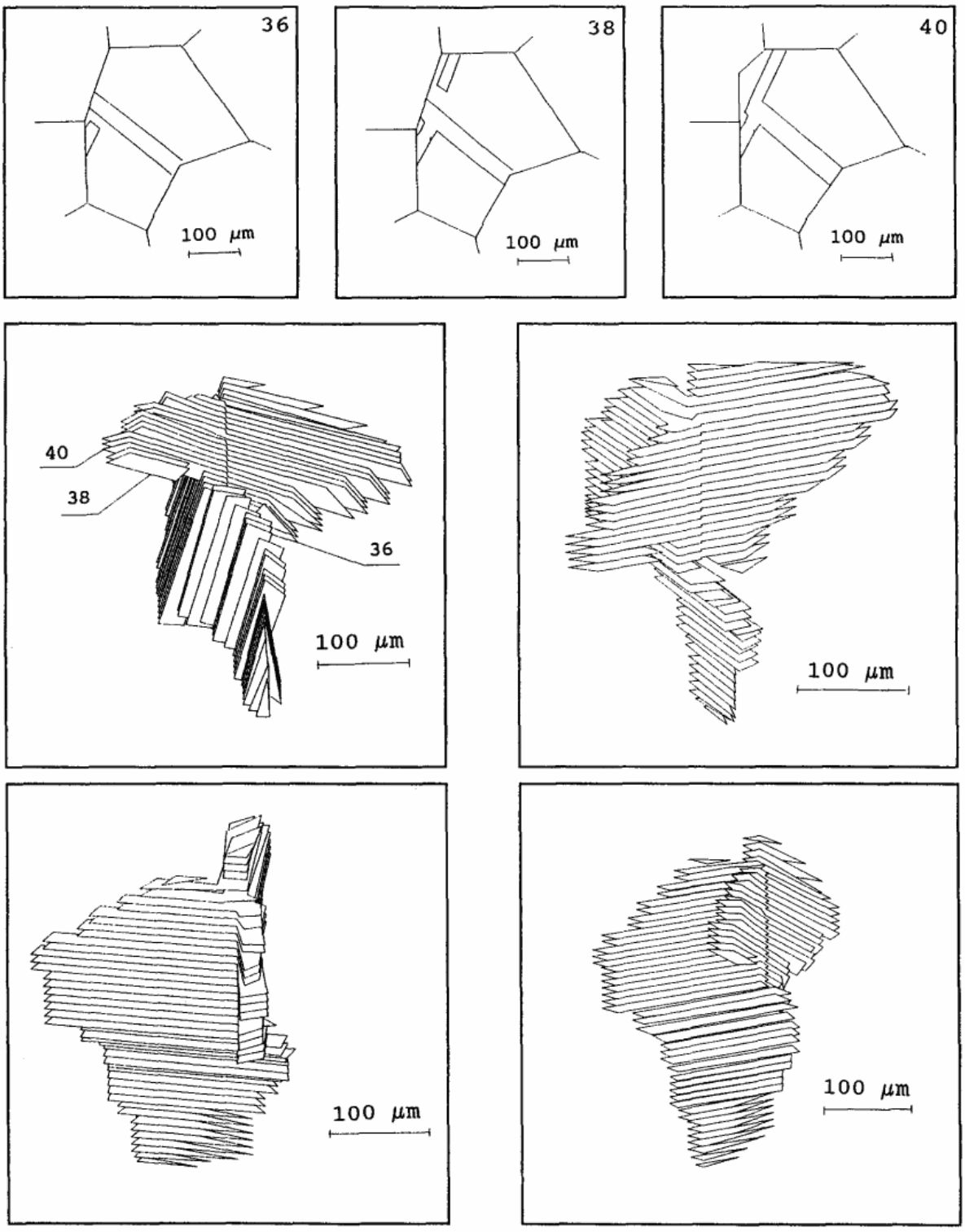

Figure 2.13: The 3D reconstruction of a twin is shown. Serial sectioned by mechanical polishing. Number refers to slice number. Figure reprinted from Bystrzycki et al., Copyright 1993, with permission from Elsevier [85].

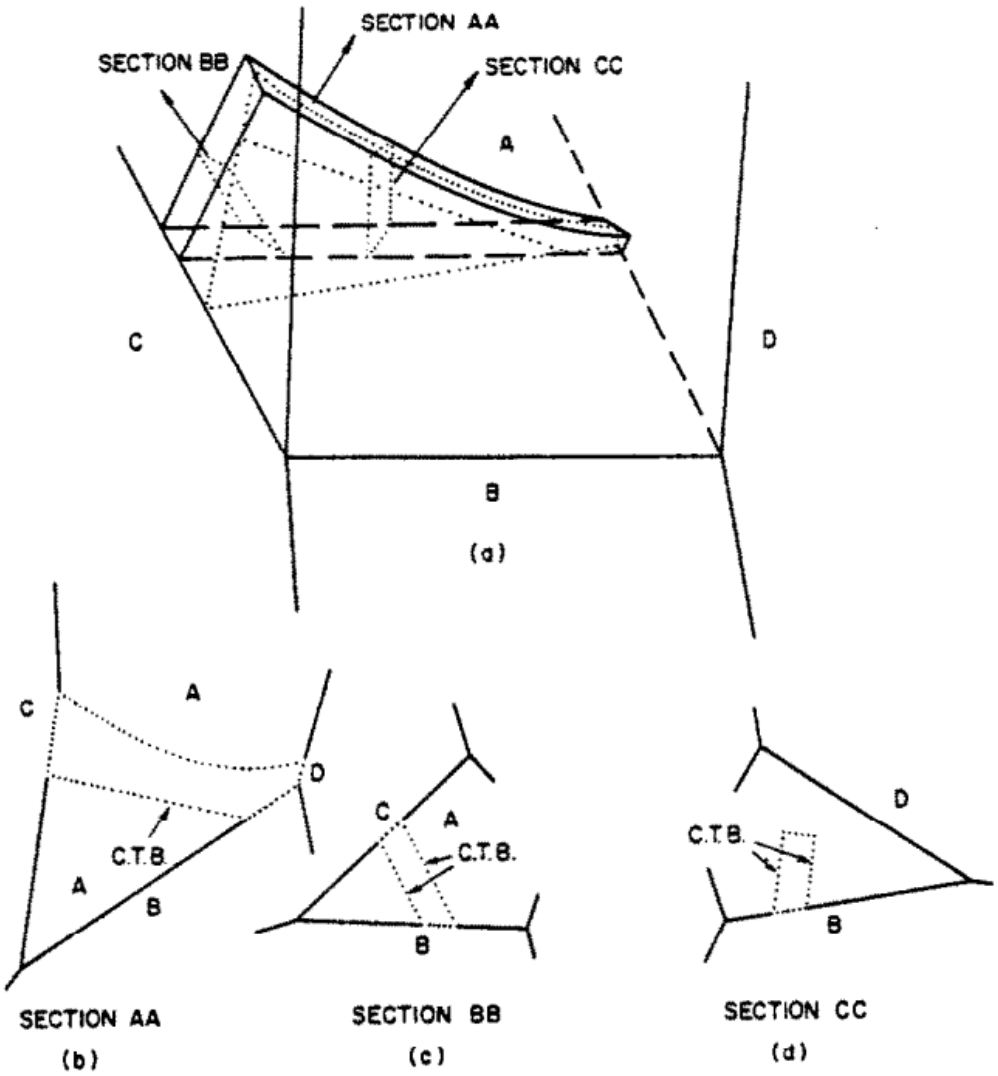

Figure 2.14: Several cross sections of a twin are shown. Even s twin with a simple 3D morphology can have different appearances depending on the sectioning plane. Not depicted: a section through the 'tip' of the twin would appear as an island twin. Figure reprinted from Meyers and Murr, Copyright 1978, with permission from Elsevier [66].

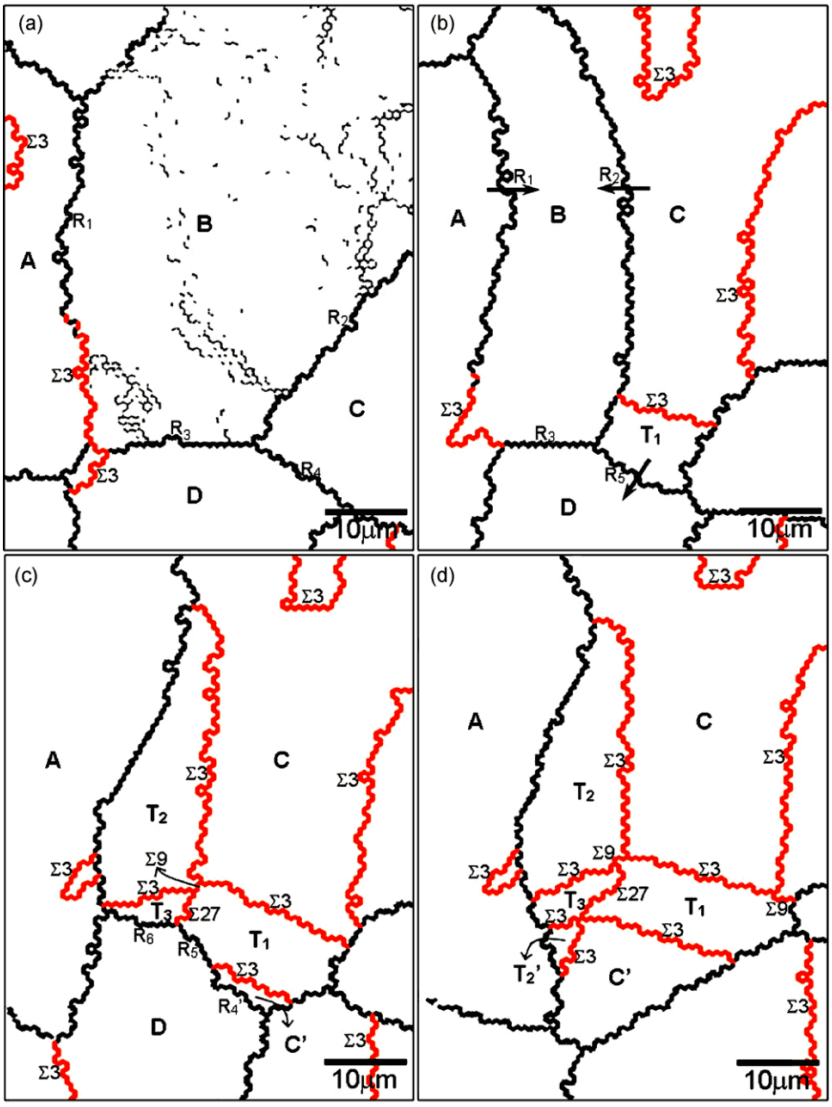

Figure 2.15: The experimental observation of formation of a twin boundary by a migrating random boundary is shown. Red boundaries are $\Sigma 3^n$ type. Thin black lines are low angle boundaries. Thick black lines are random high angle boundaries. Grain B is unrecrystallized. Figure reprinted from Song et al., Copyright 2007, with permission from Elsevier [88].

grating boundaries. It was found that the number of twins produced was proportional to the distance of migration [89]. Twins nucleated from boundaries as Shockley partials, frequently from ledges or triple points. A linear increase in N_G is observed with increasing grain size. A similar trend is observed for annealing temperature but it is difficult to draw conclusions because annealing was isochronal and grain sizes are only reported for one temperature. A similar study of fivefold twin formation in nanocrystalline copper revealed emission of Shockley partial dislocations from grain boundaries (consistent with similar simulation of mechanical twin formation) [90].

Chapter 3

3D Microstructural Data Collection Techniques

Although many microstructural properties can be inferred from statistics on planar section using stereology, there are several important exceptions relevant to fatigue life:

1. Connectivity generally can not be characterized in 2D [91].
2. Complex shapes [92] or anisotropy [93] may be impossible to quantify or require an impractically large number of random sections [92].
3. Grain boundary character requires coupled measurements of orientation and boundary inclination [94].
4. Full 3D information about specific microstructural sites can not be characterized in 2D, e.g. the grain structure surrounding a crack or a specific crack path.

To fully capture the relevant microstructural features relevant to fatigue life, 3D volumes are necessary [95]. Although there are a variety of 3D acquisition techniques, most fall into one of two broad tomographic categories. Serial sectioning tomography 'stacks' multiple slices from the sample to build a reconstruction [96]. In computed tomography, ra-

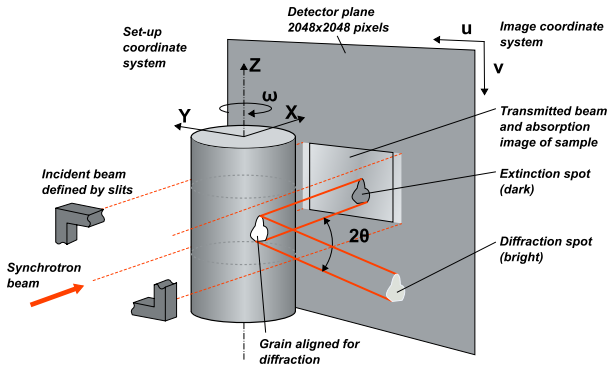

Figure 3.1: X-ray DCT experiments are performed by irradiating a sample with a beam defined by apertures or slits in the beamline. The sample is rotated in increments of ω=0.05°, around the z-axis. Extinction and diffraction spots simultaneously appear and disappear on the transmitted beam region of the detector (center of detector) and in the surrounding area (diffraction spots). Figure based on Ludwig et al. [102], reprinted with the permission of AIP Publishing.

diation is used to collect 2D projections (*tomograms*) of the sample over a range of angles [97]. X-rays are most commonly employed, but any radiation with appropriate sample absorption is possible. Tomograms containing absorption contrast are reconstructed using the Radon transform or an equivalent algorithm [98]. In crystalline materials, grain average orientations can be determined via diffraction contrast by indexing Friedel pairs as shown in (figure 3.1) [99, 100] or using a forward model [101].

While all tomographic methods have distinct strengths and weaknesses, destructive serial sectioning techniques generally encompass the length scales and contrast mechanisms most appropriate for the features relevant to fatigue of René 88DT (figure 3.2) [14, 15, 103] with mechanical serial sectioning and femtosecond laser tomography achieving the best balance of spatial resolution and accessible volumes. In serial sectioning experiments, a thin layer of the sample is removed and the exposed surface subsequently probed. These steps are repeated, taking care to interrogate a consistent region and maintain a removal rate that is uniform across slices and the sample surface [104]. Performed manually, these experiments are exceedingly difficult and time consuming, rendering collection of such data nontrivial [93]. Recently, considerable effort has enabled automation of the collection process [103]. The Air Force Research Laboratory developed an automated sys-

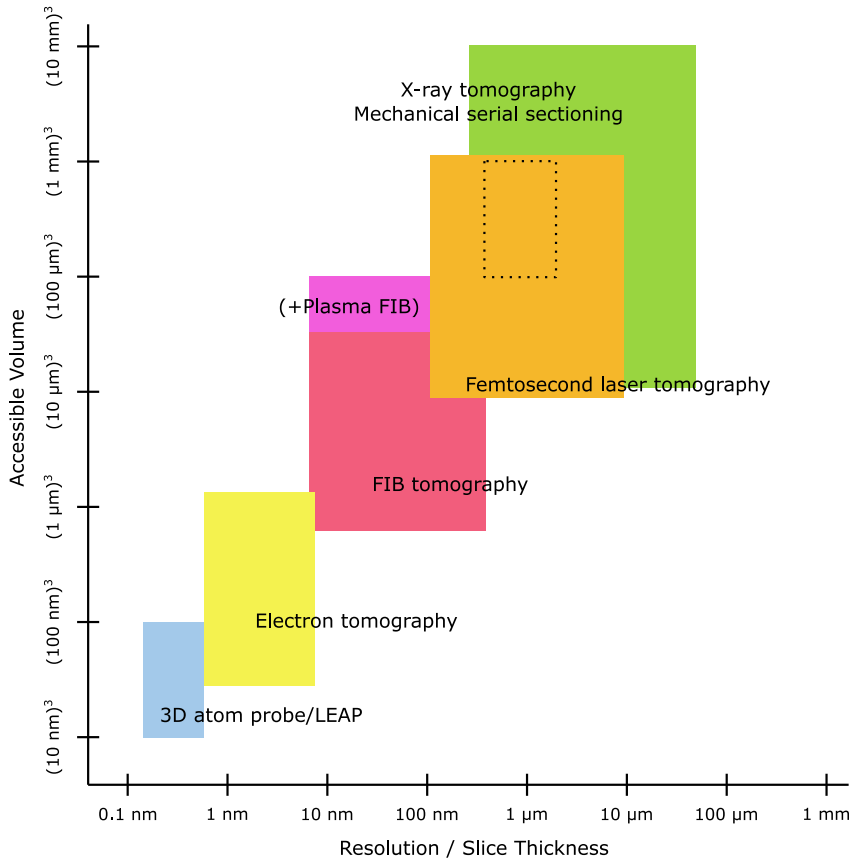

Figure 3.2: Accessible volume of a given tomographic technique generally scales with resolution. The dashed outline represents the region relevant to fatigue crack initiation and early crack growth. Figure modified from Uchic et al. [108].

tem employing mechanical polishing followed by imaging with light optical or scanning electron microscopy, as shown in figure 3.3 [105]. Similarly, the TriBeam system, shown in figure 3.4 and discussed further below, was developed at the University of California, Santa Barbara (UCSB) [106]. These systems can produce data in days or weeks with little or no human intervention, replacing months of labor [107].

Although often overlooked, the parallel development of environments for performing reconstructions [110] is equally important. The first 3D reconstructions were physically constructed of wire, cardboard, etc. Improved computational power has made it possible to construct computer models and produce digital renderings [111]. In both cases segmentation of the microstructure has historically been performed manually, a labor intensive and subjective process [112]. Although a wide variety of fairly mature soft-

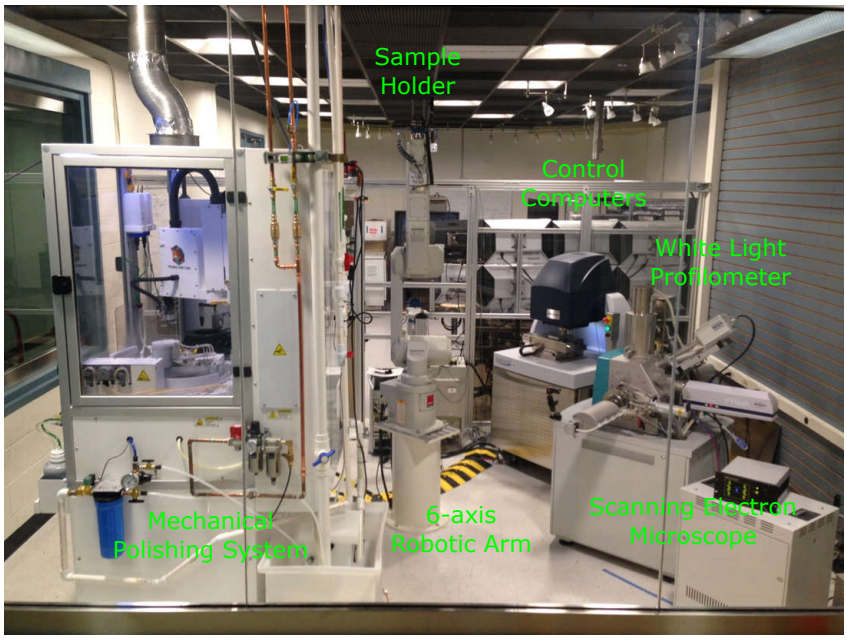

Figure 3.3: The LEROY serial sectioning system at the Air Force Research Laboratory uses a robotic arm move the sample between a mechanical polishing system with an integrated light optical microscope and other instruments (photograph courtesy of Michael Uchic).

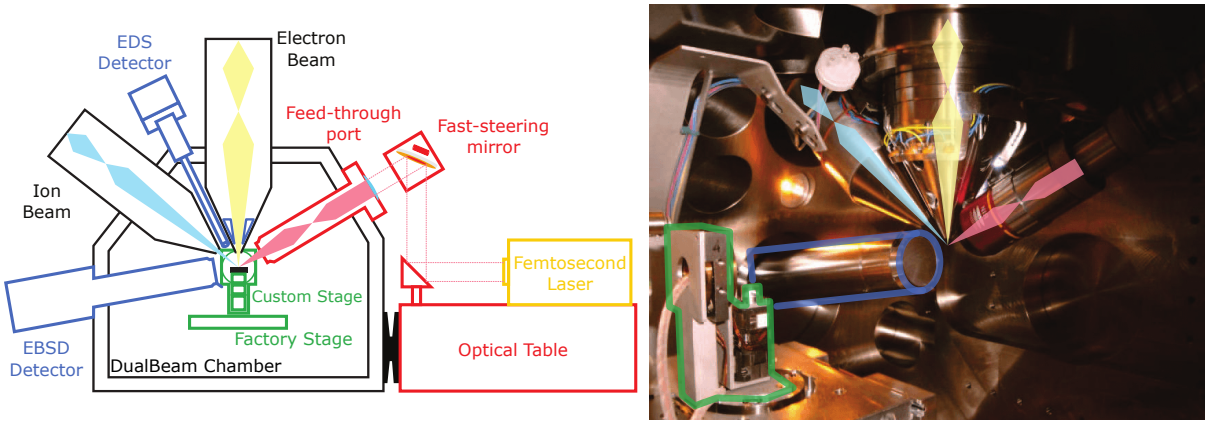

Figure 3.4: The TriBeam system developed at UCSB couples a femtosecond laser with a FIB-SEM for rapid material removal. Image reprinted from Materials Characterization, 100, M.P. Echlin, M. Straw, S. Randolph, J. Filevich, and T.M. Pollock, The TriBeam system: Femtosecond Laser Ablation in-situ SEM, 1–12, 2015, with permission from Elsevier [109].

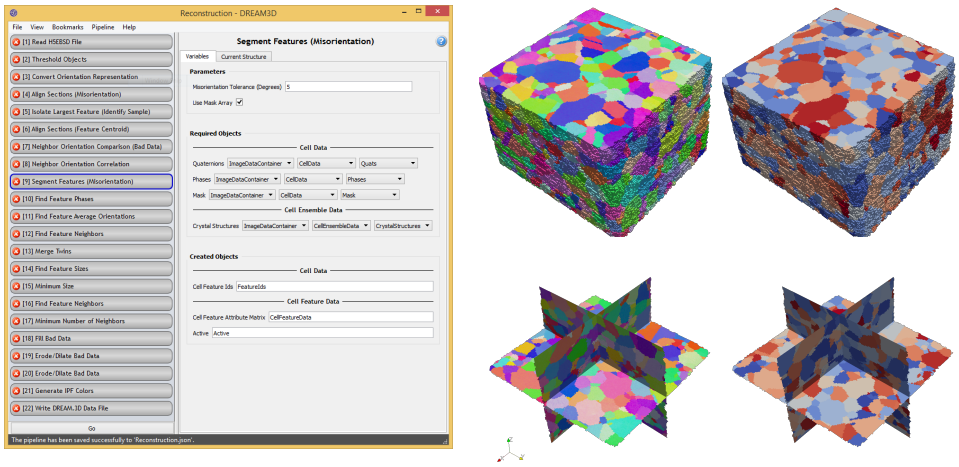

Figure 3.5: A reconstruction pipeline in the DREAM.3D software package (left) creates a file which can be used render the dataset in ParaView or other visualization software. A small volume of IN100 collected by focused ion beam serial sectioning and EBSD [104] is IPF colored (center) and uniquely colored by grain number (right). The dataset dimensions are ≈45 µm × 50 µm × 30 µm at a resolution of 0.25 µm × 0.25 µm × 0.25 µm.

ware exists to process 2D datasets, dedicated packages for reconstruction and analysis of 3D microstructure volumes did not exist until very recently [113]. New tools, including Digital Representation Environment for Analyzing Microstructure in 3D (DREAM.3D), have drastically reduced the barriers associated with performing reconstructions [114]. Once a dataset has been imported into DREAM.3D, a preliminary reconstruction can be performed in a single day, with an example shown in figure 3.5. Quantitative microstructural descriptors such as grain size distribution can be computed trivially once a reconstruction is complete [115].

3.1 The TriBeam System

The TriBeam system developed at UCSB couples a femtosecond laser with a FIB-SEM to enable rapid in-situ material removal via laser ablation [106]. The 780 nm chirp pulse amplified titanium-sapphire laser with a 1000 Hz repetition rate is introduced into the SEM vacuum chamber though a custom optical pass through port. The ultrashort laser

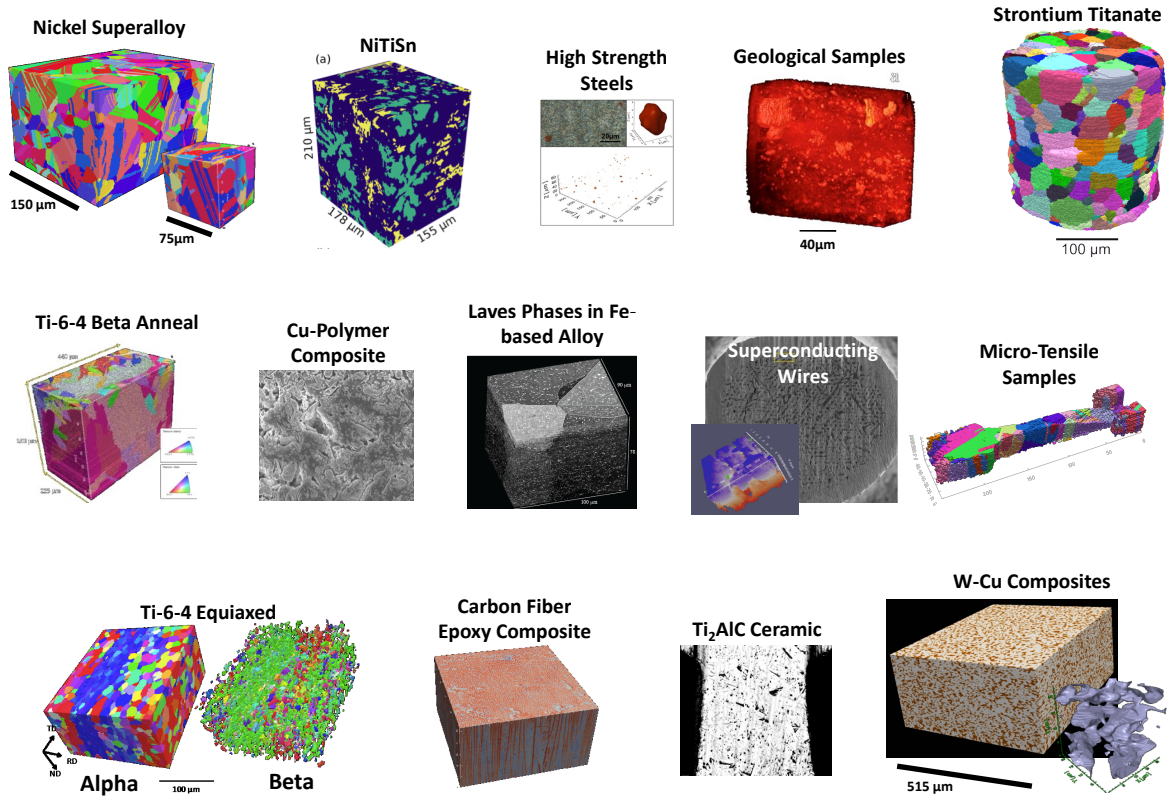

Figure 3.6: Reconstructions of a variety of material systems sections with femtosecond laser tomography are shown. Compilation courtesy of McLean Echlin.

pulses of approximately 120 fs to 150 fs result in material interactions that are fast compared to the timescale of thermalization, allowing ablation without local melting. A wide variety of materials systems including metals, ceramics, polymers, and composites have been successfully interrogated by TriBeam tomography, with example reconstructions shown in figure 3.6 [116–119].

A 5 axis (x, y, z, tilt, rotation) piezoelectric sub-stage is used so the sample can be rotated between laser, FIB, and EBSD positions without breaking vacuum. To machine, the laser is scanned across and parallel to the sample surface using a fast steering mirror. Slice thickness are controlled by incrementing the sample up into the beam with an Attocube™ piezoelectric stage. A 3x or 10x microscope objective focuses the 5 mm beam to a 25 µm or 5 µm spot size, respectively, and discrete pulses are placed at 80% overlap with 200–1000 passes used per slice.

3.1.1 Laser Damage

Laser machined surfaces display laser-induced periodic surface structure (LIPSS) with a wavelength on the order of the laser wavelength and amplitude from tens to hundreds of nm, depending on the material system. The morphology of LIPSS depends on laser polarization with a typical structure for the TriBeam's S-polarized (linearly polarized with the electric field oscillating parallel to the sample surface) laser beam shown in figure 3.7. Since the Gaussian beam is scanned parallel to the sample surface, the exposed surface is machined near the ablation threshold, resulting in minimal damage. Some materials, including nickel, copper, and strontium titanate exhibit a thin (less than 200 nm) region of increased dislocation density and machined silicon has an approximately 40 nm amorphous layer [120, 121]. In some cases, including nickel and tantalum, the surface quality is sufficient for direct EBSD data collection. Increased dislocation density or surface roughness from larger amplitude LIPSS may reduce pattern quality, but briefly FIB milling at glancing angle machines away the damaged layer and flattens surface roughness, resulting in surface quality suitable for EBSD mapping in all materials system investigated [121].

3.1.2 Accessible Length Scales and Volumes

The volume that can be easily collected in the TriBeam system is approximately 800 µm × 800 µm × 1500 µm. The lateral size is limited by how far the beam can be scanned before clipping or becoming distorted (a function of beamline geometry and optics) as shown in and sample depth is limited by depth of focus of the objective lens as shown in figure 3.8. Height is limited by the actuator travel range. Larger volumes could be achieved by modifying the laser beamline, changing the sample stage, or using multiple machining steps if needed. Material removal rates are 5 to 6 orders of magnitude faster than FIB machining with a 5 µm thick slice easily ablated from the 800 µm × 800 µm ac-

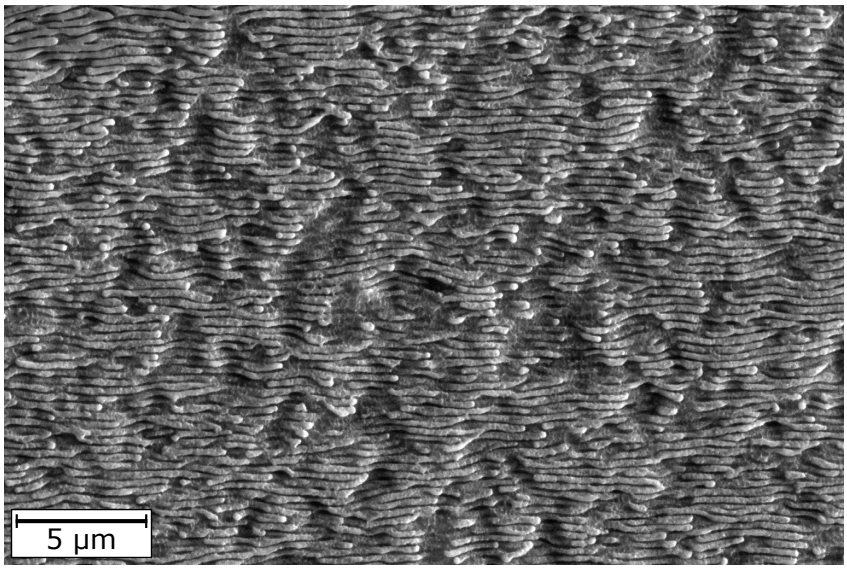

Figure 3.7: A representative laser induced periodic surface structure on a steel sample machined in the TriBeam system is shown. The laser beam propagated from the bottom to the top of the image and was scanned left to right. Image courtesy of McLean Echlin.

cessible surface area in under 2 minutes of machining. Although machining bulk samples is possible, a pedestal sample geometry is frequently used to mitigate redeposition of the large volumes of removed material, as shown in figure 3.9. Typically a series of pedestals is machined to facilitate experimental set up.

Slice resolution is limited by a combination of actuator precision and LIPSS amplitude, with typical values of 500 nm to 5 µm. Lateral resolution is theoretically limited by the resolution of the microscope, but in practice constraints on acquisition time dictate resolution limits, particularly if orientation or chemical information are collected; even with a modern EBSD camera collecting 800 patterns per second capturing an 800 µm × 800 µm × 800 µm volume with 1 µm resolution requires over a week.

3.1.3 System Developments

Considerable effort was devoted to improving the TriBeam system in the course of this research project with a focus on the software framework. The original TriBeam system relied on a combination of macros in the microscope software's scripting language and in a

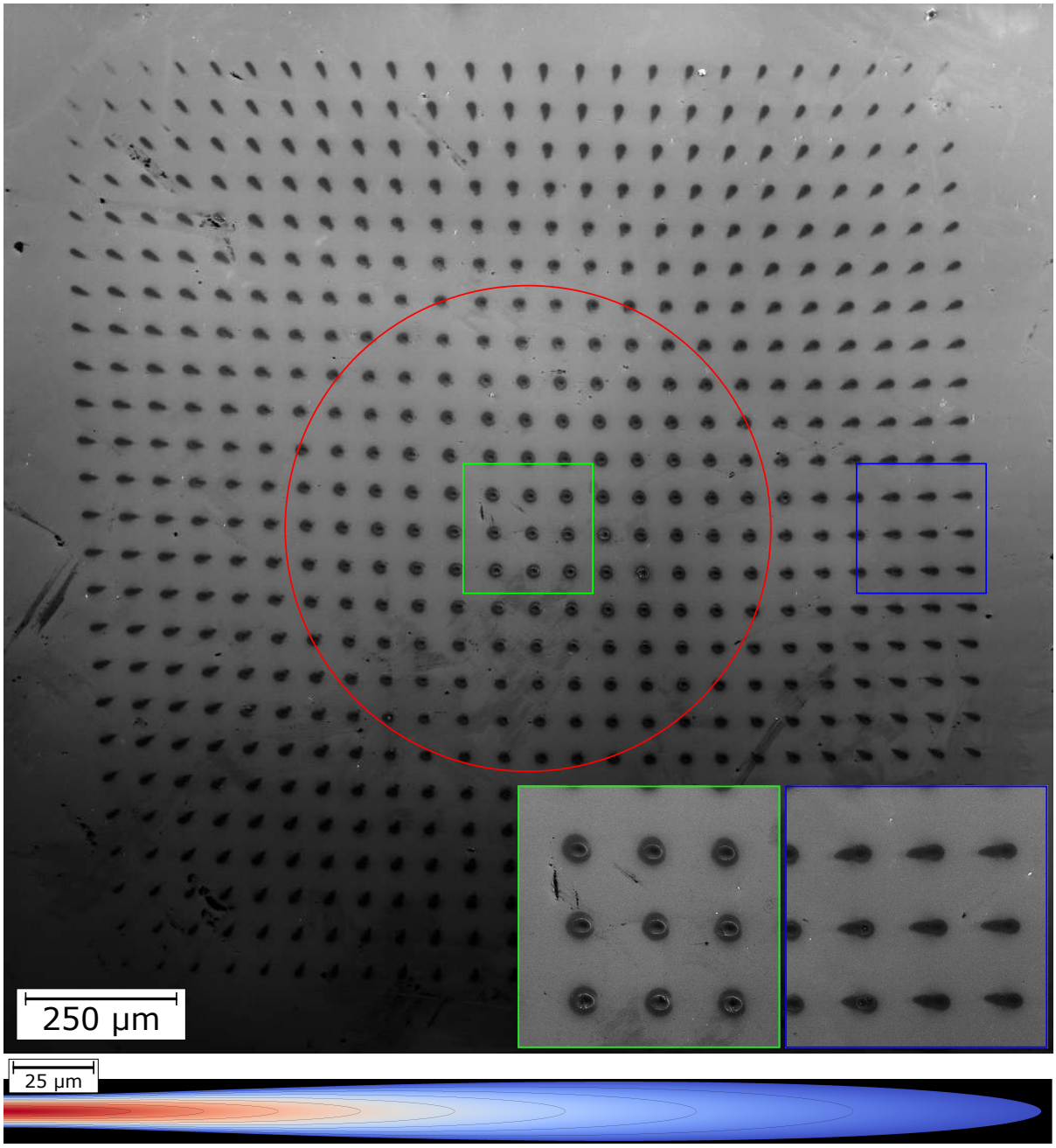

Figure 3.8: A 1.5 mm × 1.5 mm grid of single laser pulses machined with the beam direction normal to the surface shows distortion and clipping near the edges and corners of the grid respectively (top). The red circle indicates an 800 µm field of view. A simulation of beam intensity for a Gaussian 5 mm diameter 780 nm beam focused through a 54 mm focal length lens is shown below [122]. The left edge of the simulation is the focal plane with coloring and isocontours logarithmically spaced (Blue is 1% of incident beam intensity and red is 32% of incident beam intensity).

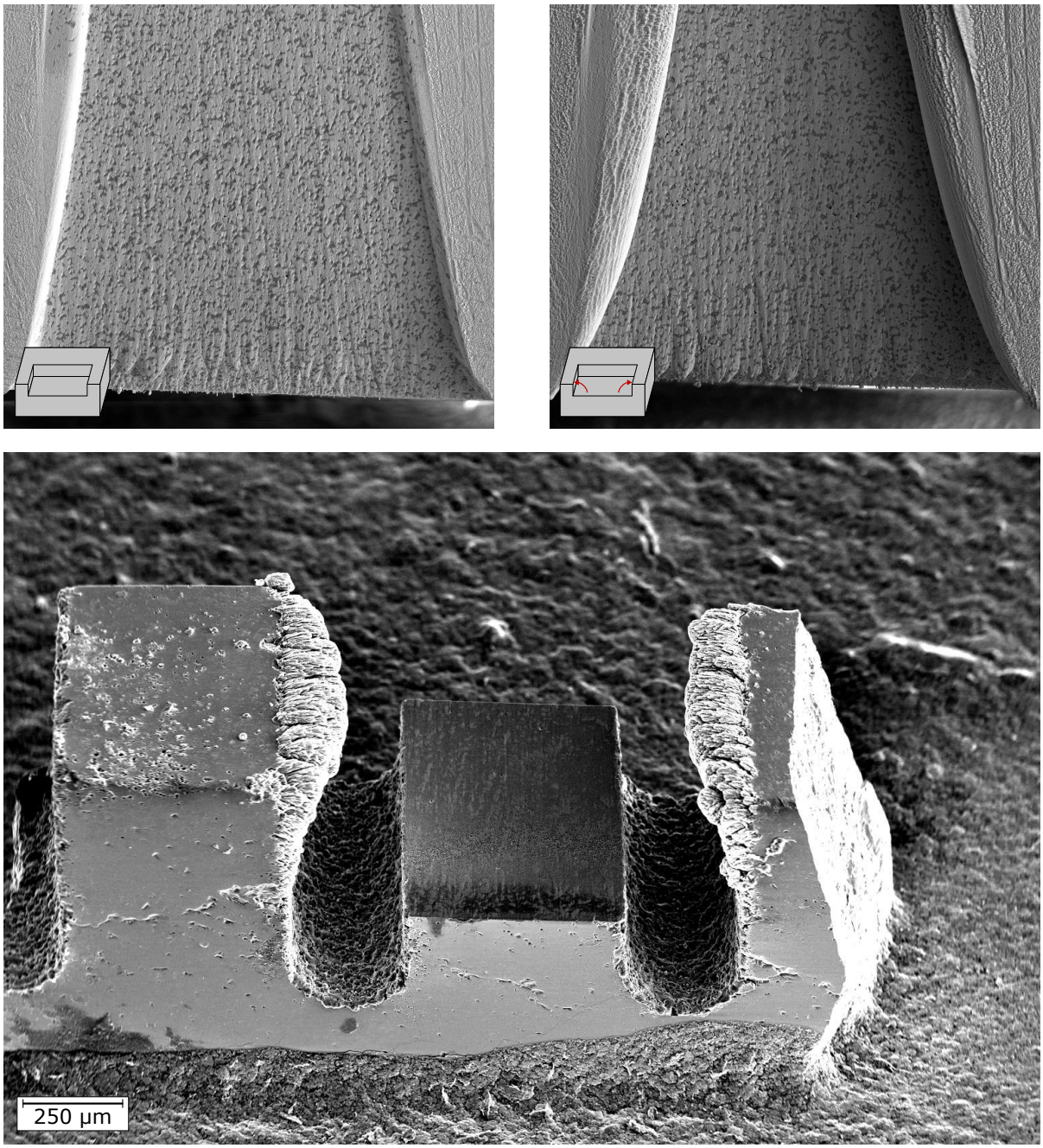

Figure 3.9: Machining into the corner of a bulk sample is possible as shown in a Cu-W composite sample (upper left). Ablated material redeposits on surfaces within line of sight causing lobes to obstruct the surface after many slices (upper right), resulting in detector shadowing. Using samples with a pedestal geometry helps to mitigate the problem as seen in a NiTiSn sample (bottom). The pedestal shown was machined in 137 2 µm thick slices with each slice requiring 500 laser passes and taking 90 s. Images courtesy of McLean Echlin.

freeware scripting language to automate mouse clicks. The current iteration implements a C++ class for each hardware component to wrap multifunction data acquisition (DAQ) and hardware specific library commands in a common framework. The resulting code base allows the logic controlling an experiment to be compact and easily interpreted (e.g. `beamlineShutter.open()` instead of a sequence of text commands exchanged over a virtual serial connection to control laser insertion into the chamber). Experiments are run using a command line program with parameter studies and other experimental set-up aided by a program with a graphical user interface to control the laser beamline, electron polepiece shutter, and scan generation.

The command line program to run an experiment accepts a plain text file of key-value pairs (INI format) describing the parameters of each step. All experiment metadata is automatically recorded to a HDF5 file for archiving and each piece of metadata includes the corresponding slice number and a timestamp [123]. Each experiment start including a copy of the configuration file and the software version used (git commit hash) is recorded to the log. Encoder positions are measured before and after each move, laser beam power and lamp current before and after each cut, and electron beam current before and after each EBSD scan. These data are also used to provide closed loop controls (e.g. laser power is automatically adjusted before each slice and the experiment stopped if the power is not within a user defined tolerance). These controls are complemented by robust error checking, greatly improving experiment stability and data quality. All errors are logged as metadata and emailed to researchers. Researchers are also emailed with periodic experiment updates.

Chapter 4

3D Dataset Collection and Reconstruction

In this chapter the process of dataset reconstruction, including algorithms used are reviewed. New algorithms for quantitatively fusing two datasets of the same volume are presented and applied to validate the TriBeam tomography technique against diffraction contrast tomography. Finally, an overview of the René 88DT datasets collected for this research program are presented with details of the reconstruction process given for each dataset.

4.1 Dataset Reconstruction

Dataset collection is only the first phase of a typical TriBeam dataset workflow, with reconstruction and analysis constituting the majority of required effort as shown in figure 4.1. Dataset reconstruction was primarily performed in the open source DREAM.3D software package with algorithms developed or augmented as needed. Reconstruction consists of four main steps which are generally, but not always, performed sequentially:

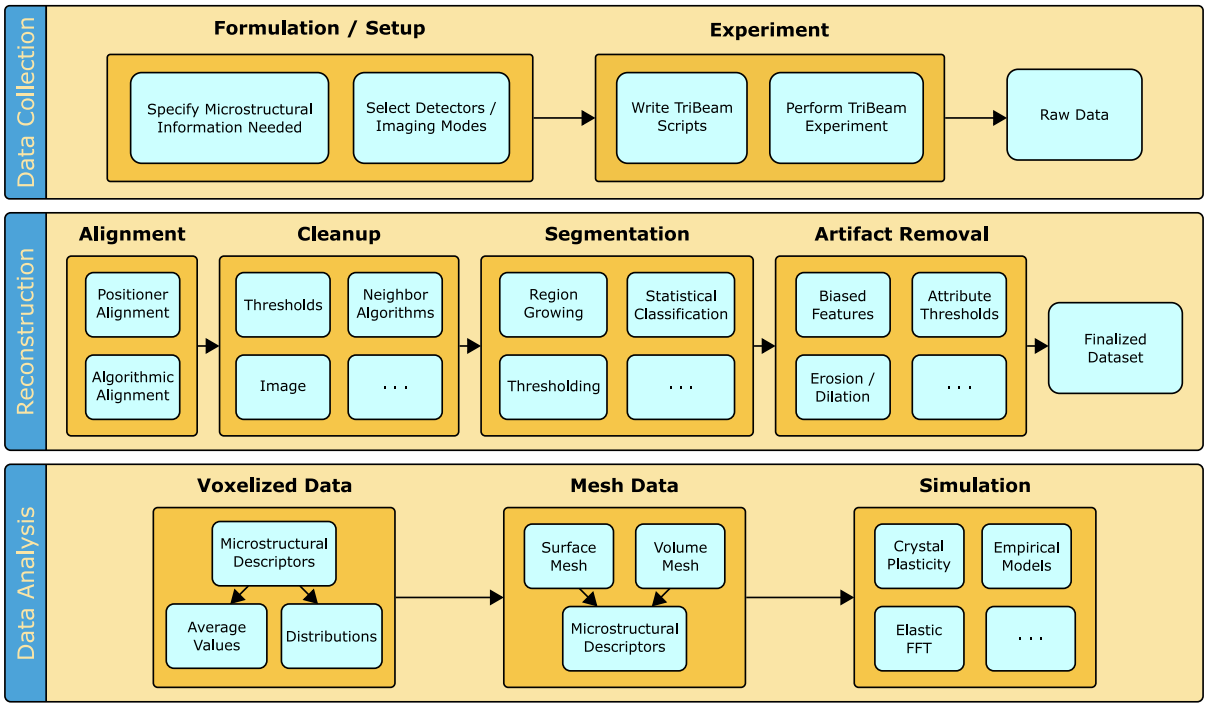

Figure 4.1: The typical TriBeam dataset workflow is depicted.

1. Slice registration / alignment
2. Voxel level cleanup
3. Feature segmentation
4. Artifact removal

The algorithms used in this process are generally determinate and therefore inherently less subjective than manual segmentation. Unfortunately, the selection of parameters required is frequently performed by rule of thumb (e.g. a segmentation tolerance of 1–5° or adjusted until the results 'look right'), with robust selection an area of open research.

4.1.1 Alignment

Since actuator positions are recorded for each slice of a dataset collected on the TriBeam system, a coarse alignment can often be performed using available position logs. Drift during long EBSD acquisitions, thermal expansion, and changing electron beam

conditions in practice require an additional alignment step. Registration algorithms generically attempt to maximize an overlap metric by modifying transformation parameters according to an optimization technique. For 3D microstructural volumes the overlap metric is typically average disorientation angle for orientation data or (normalized) cross-correlation for scalar data. Generally a simple translation transformation is used, although higher order transformations are possible. Three main slice alignment routines were used to reconstruct datasets in this work. Each algorithm computes all slice to slice shifts, subtracts a linear background to prevent shearing, then applies shifts using nearest neighbor interpolation.

Disorientation alignment computes shifts resulting in the highest fraction of overlapping voxels with the same orientation (within a user described tolerance, typically 5°) in a search window (typically ±3 voxels) as described in algorithm 4.1. Scalar alignment computes shifts to maximize normalized cross-correlation of a scalar array (e.g. image quality) using phase correlation as described in algorithm 4.2. Grain centroid alignment computes the least square shifts to align grain centroids as described in algorithm 4.3.

4.1.2 Cleanup

Poor diffraction quality, stray phases, pseudo-symmetry (the systemic mis-indexing of points to an orientation with a nearly symmetric pattern), or scan regions outside the sample may lead to noise or mis-indexed EBSD points as shown in figure 4.2 [124]. Noise at the voxel level is typically identified by thresholding on a measure of diffraction or indexing quality (e.g. image quality or confidence index respectively). More sophisticated approaches consider the orientation of a voxel with respect to its neighbors. Bad voxels may have their values replaced with those from neighboring voxels or simply be excluded from segmentation and subsequently removed with segmentation artifacts. The later approach is generally preferred in this work since consolidating cleanup to a single step reduces the number of reconstruction parameters.

Algorithm 4.1: An algorithm to compute alignment between adjacent slices using orientation is given [114].

```
Data: Phase (p) and orientation (q) of 2 adjacent slices (i and j)
Result: Shift to align slices
shift ← (0, 0)
metric ← 0
foreach −k ≤ Δx ≤ k do
    foreach −k ≤ Δy ≤ k do
        n ← 0
        m ← 0
        foreach x do
            foreach y do
                if p_i(x,y) = p_j(x + Δx, y + Δy) then
                    if disorientation(q_i(x,y), q_j(x + Δx, y + Δy)) < θ_tol then
                        n ← n + 1
                    end
                end
                m ← m + 1
            end
        end
        if n/m < metric then
            shift ← (Δx, Δy)
            metric ← n/m
        end
    end
end
```

Algorithm 4.2: An algorithm to compute alignment between adjacent slices using phase correlation of a scalar array is given.

Data: Scalar (s) of 2 adjacent slices (i and j)
Result: Shift to align slices
$G_i \leftarrow$`FourierTransform(`s_i`)`
$G_j \leftarrow$`FourierTransform(`s_j`)`
foreach x **do**
  foreach y **do**
    R$(x,y) \leftarrow G_i(x,y)G_j^*(x,y)$
    R$(x,y) \leftarrow \frac{\mathrm{R}(x,y)}{|\mathrm{R}(x,y)|}$
  end
end
$r \leftarrow$`Real(InverseFourierTransform(`R`))`
metric$\leftarrow 0$
foreach x **do**
  foreach y **do**
    if $r(x,y) >$metric **then**
      metric $\leftarrow$ r(x,y)
      shift $\leftarrow (x,y)$
    end
  end
end

Algorithm 4.3: An algorithm to compute alignment between adjacent slices using matched points is given.

Data: Slice centroids for grains of 2 adjacent slices (i and j) and flag for grains touching edge of slice
Result: Shift to align slices
n$\leftarrow 0$
shift $\leftarrow (0,0)$
foreach *grain* **do**
  if *not* surface(*grain,i*) *and not* surface(*grain,j*) **then**
    shift$\leftarrow$shift$+$centroids(*grain,i*)$-$centroids(*grain,j*)
    n$\leftarrow n+1$
  end
end
shift $\leftarrow \frac{\text{shift}}{n}$

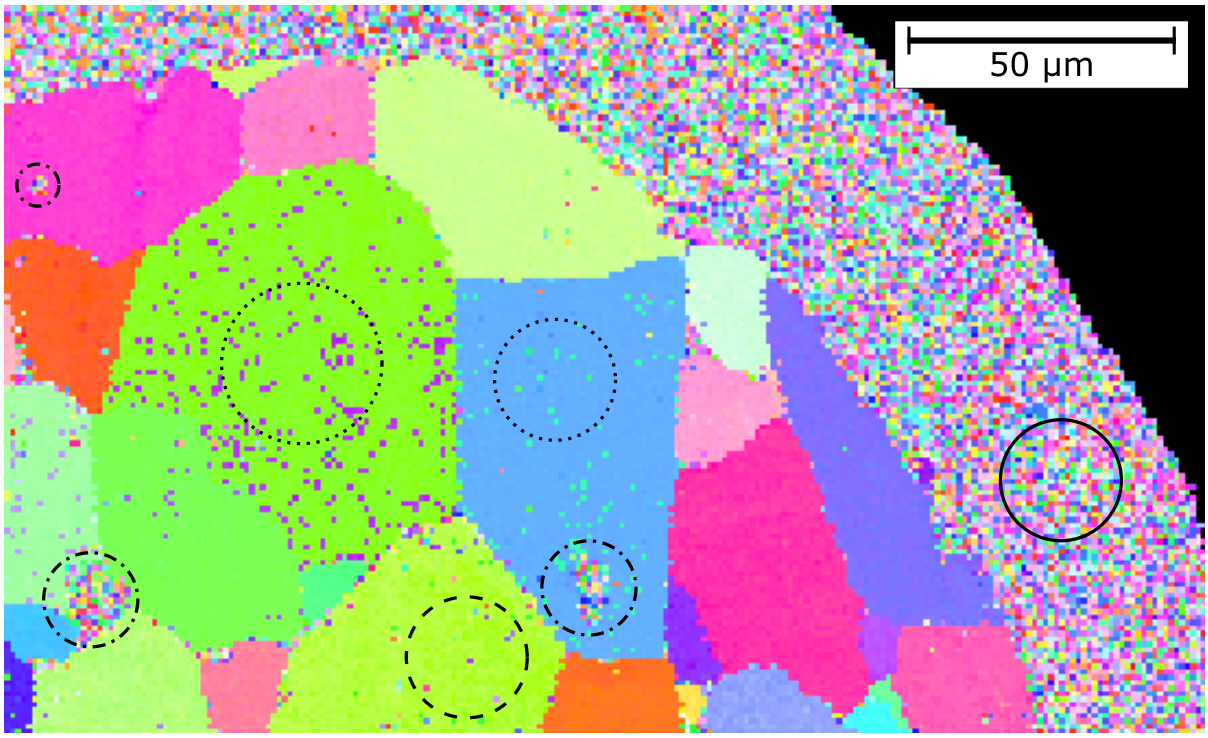

Figure 4.2: Noise in an EBSD map may arise from poor diffraction quality due to porosity (dash-dot circles), systemic mis-indexing e.g. pseudo-symmetry (dotted circles), scanning outside the sample (solid circle), or random noise (dashed circle).

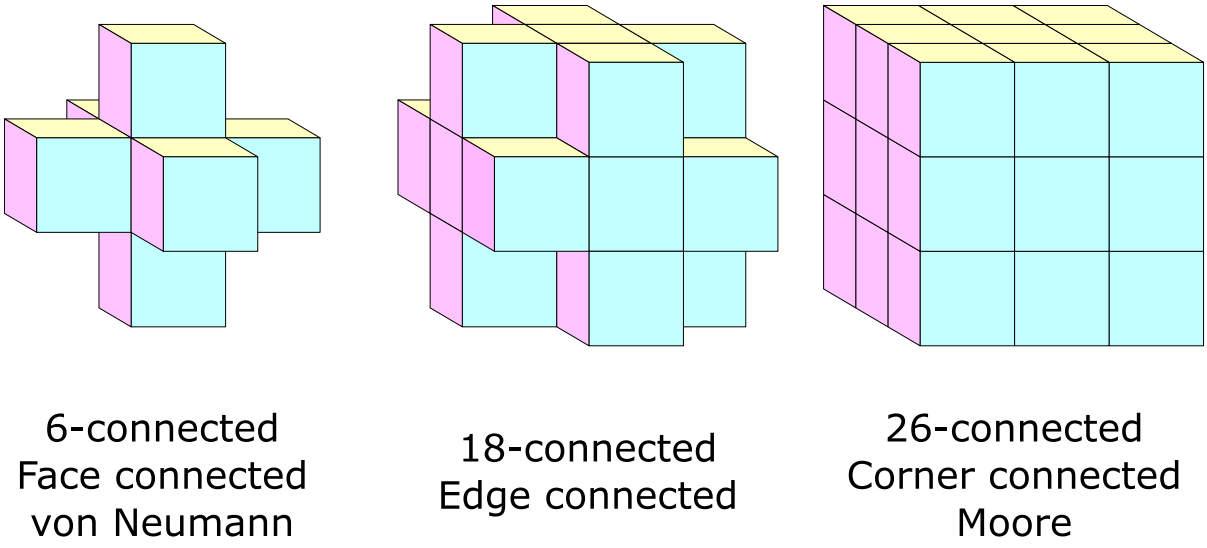

Figure 4.3: 3D voxel neighbors can be defined by shared faces, edges, or corners.

4.1.3 Segmentation

Although accurate segmentation of scalar datasets is a significant challenge, most Tri-Beam datasets include orientation data which provide some significant benefits. Orientation data are generally segmented by growing through low disorientation (1° – 5°) neighbors as described in algorithm 4.4. Segmented grains are grouped into twin related domains using essentially the same algorithm growing through twin (or nearly twin) related neighboring grains instead of low disorientation neighboring voxels. Both algorithms require a selection of connectivity type. Typically a von Neumann neighborhood is used, but other choices are possible (figure 4.3).

4.1.4 Artifact Removal

Misindexed voxels or grains too small to be well resolved frequently result in stray grains in the as segmented dataset. Artifact grains are generally identified by thresholding on size, aspect ratio, or another morphological metric and grouped with noise voxels flagged prior to segmentation. These 'bad' regions of the segmentation may be cleaned by assigning voxels to neighboring grains using erosion. Porosity and un-indexed phases

Algorithm 4.4: An algorithm to segment grains using orientation is given [114].

```
Data: Phase and orientation on a voxel grid and a neighborhood type
Result: Labeled voxel grid
numLabels ←0
foreach voxel do
    labels(voxel)←0
end
foreach voxel do
    if labels(voxel) is 0 then
        seed←voxel
        numLabels ←numLabels +1
        labels(seed)←numLabels
        push(stack,seed)
        while stack is not empty do
            voxel←top(stack)
            pop(stack)
            foreach neighbor(voxel) do
                if labels(neighbor) is 0 then
                    if phase(seed) is phase(voxel) then
                        if disorientation(seed, voxel)< θ_tol then
                            labels(neighbor)←numLabels
                            push(stack,neighbor)
                        end
                    end
                end
            end
        end
    end
end
```

are maintained by excluding large contiguous groups of unassigned voxels or performing coupled erosion and dilation operations.

4.2 Technique Validation

A volume previously interrogated by X-ray diffraction contrast tomography was collected using TriBeam tomography to validate the techniques against each other. Sample preparation and DCT data collection and reconstruction were performed by collaborators at Karlsruhe Institute of Technology [125, 126]. Datasets were collected from strontium titanate (STO), a model system used to study grain growth in ceramic perovskites.

4.2.1 Sample Preparation and Dataset Collection

$SrCO_3$ and TiO_2 with a Sr/Ti ratio of 0.996 were mixed and calcined to create $SrTi0_3$ powder [117]. The powder was pressed and sintered at 1600 °C in an oxygen atmosphere before mechanically grinding to a 320 µm cylindrical pedestal [125, 127, 128]. The sample was annealing for 2 hours at 1600 °C to grow grains before imaging with DCT at the materials science beamline ID11 of the European Synchrotron Radiation Facility. Diffraction tomograms were collected every 0.05° using a 36 keV beam with a 0.7 µm resolution detector 3.23 mm from the sample. A crystallographic indexing scheme adapted for perovskite materials was used to index diffraction spots [102]. Grain morphology was reconstructed using the algebraic reconstruction technique (ART) [129]. Finally grains were isotropically dilated to create a space filling model of the grain structure [130].

The STO sample was subsequently serially sectioned using the TriBeam system [106, 109]. 312 1 µm thick slices were cut across the entire cylinder using a laser beam attenuated to 80 mW. To section, each laser machined slice was subsequently ion milled at a 21° glancing angle using a 30kV, 30nA Ga^+ ion beam to a depth of approximately 100 nm and then then with a 5kV, 13nA beam to a depth of approximately 50 nm. EBSD

patterns were collected across the entire surface with a 1 µm resolution hexagonal grid, a 25 kV electron beam, and 4×4 camera binning.

EBSD scan data were resampled on a square grid and a tilt correction applied to account for a 5° deviation in cut angle from the cylinder axis normal plane. The EBSD scans were stacked into a 3D data container with rotations of 180° about [010] and 90° about [001] applied to the sample and orientation reference frames respectively to account for manufacturer definitions. A mask was applied to define the boundary of the sample pedestal by thresholding voxels with a confidence index greater than 0.01 and an image quality [131] greater than 200. The mask was dilated to fill in all pores and include pedestal edge data. EBSD slices were aligned along the z-direction by maximizing voxels within a 5° disorientation angle tolerance (relative to the previous slice). Grains were defined from the aligned dataset using a 1.5° segmentation tolerance. Grains below 125 voxels in size or having fewer than 3 neighbors were removed and surrounding grains dilated in order to restrict the analysis to only grains which were substantially above the spatial resolution (step size) of the EBSD data collected.

4.2.2 Data Fusion Algorithms

Both the X-ray and TriBeam dataset reconstructions have an orientation reference frame (the coordinate system in which orientations are expressed) and a sampling grid. The orientation reference frames and sampling grids may not correspond. Without aligning both between the reconstructions, only ensemble properties, such as grain size distribution, can be compared. To facilitate direct quantitative comparisons on a grain and voxel scale, the two datasets must have their orientation reference frames aligned and be fused onto a single shared sampling grid. Fusion begins by coarsely aligning datasets using several matching grain pairs manually identified from the datasets. Grain pair centroids and average orientations are used to align both the dataset sampling grids and orientation reference frames respectively. Grain pairs are next automatically identified in the

coarsely aligned volume. These steps are iterated until no new grain pairs are identified as schematically depicted in figure 4.4. For each iteration, the transformations are combined and the total transformation applied to the original volume to avoid generation of artifacts from repeated nearest neighbor interpolation as shown in figure 4.5. Each step in this iterative dataset fusion framework is detailed in figure 4.4.

Grain Pair Identification

The algorithms used to register the sampling grids and orientation reference frames require pairs of grains matched between the DCT and TriBeam dataset as input. Consequentially, several grain pairs were initially manually selected to initialize the alignment loop. In large datasets, pairs may not be distinguished readily by morphology alone and orientation based coloring will not correlate between datasets with unaligned reference frames. However, grain boundary surface meshes can be colored by their disorientations [46], which are relative between crystal reference frames. This mitigates the need for prior orientation reference frame alignment, and grain pairs are easily identified by boundary color as shown in figure 4.6.

Register & Align Sampling Grid

Aligning two sampling grids requires selection of a feature or group of features to make coincident. Grain centroids were chosen as the alignment target since they can be robustly determined by both techniques. Grains not fully contained in both volumes were excluded to avoid bias. The least squares affine transformation $[T]$ mapping centroids in dataset

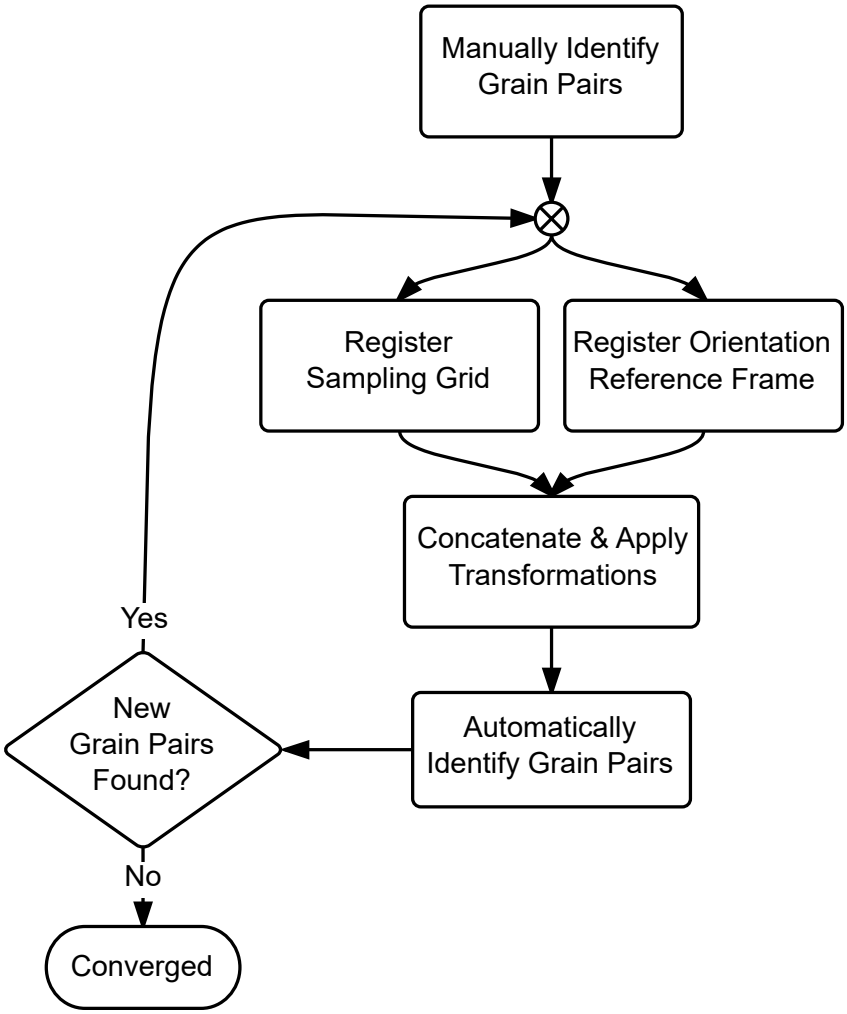

Figure 4.4: A flow chart outlining the alignment process with boxes representing algorithms and diamonds representing a loop condition is shown. A set of grain pairs are identified to initialize the alignment loop. The transformations necessary to align the sampling grids and orientation reference frames are computed independently. The datasets are then coarsely aligned, enabling automatic identification of matching grain pairs. Since grain pairs are the input for computation of both transformations, the alignment has converged when no new pairs are identified. The algorithms used in this workflow for registration could easily be replaced or modified to accept various other data or feature types for alignment.

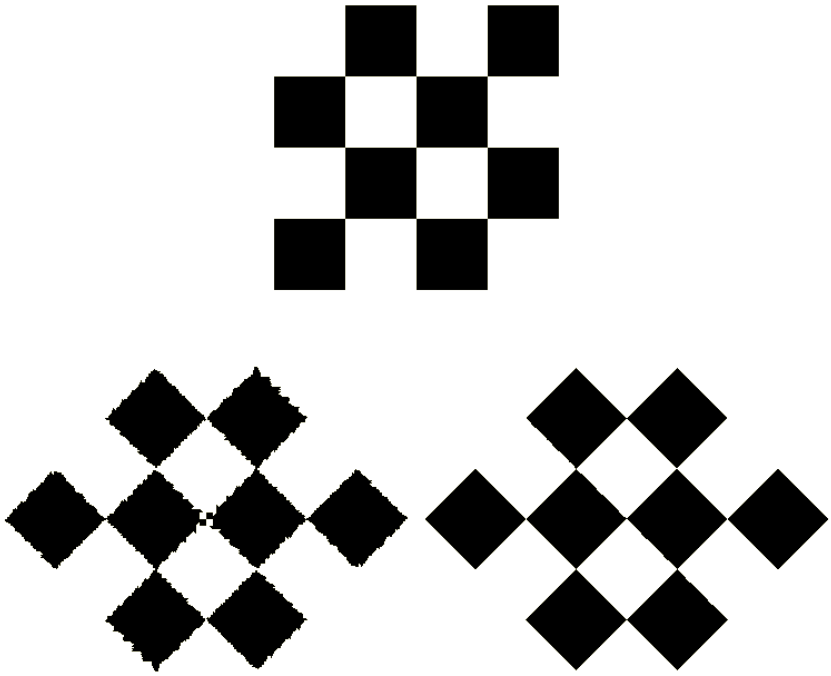

Figure 4.5: An example of artifacts introduced by repeated interpolation is shown. In nearest neighbor interpolation the value of each pixel in the resampled image is taken from the closest pixel in the transformed image. The original image (top) was rotated by 45° in 5° increments with nearest neighbor interpolation resulting in extensive artifacts (bottom left). The same transformation introduces comparatively few artifacts when performed in one step (bottom right).

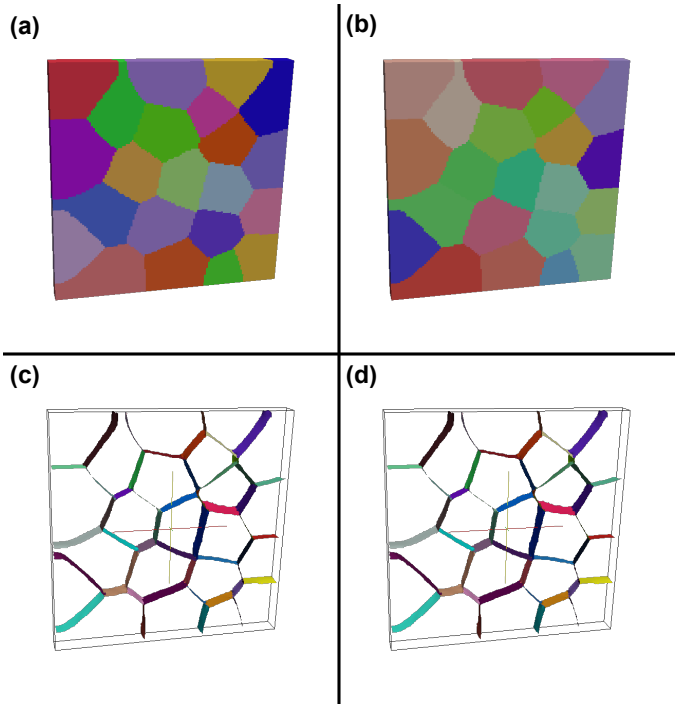

Figure 4.6: A small synthetic volume is shown with IPF coloring (a). An arbitrary rotation is applied to the orientation reference frame (b), altering the IPF colors. A grain boundary surface mesh is generated using the MultiMaterial Marching Cubes algorithm and subsequently Laplacian smoothed [132]. The mesh is colored by boundary disorientation in the original (c) and rotated (d) orientation reference frames. Since disorientations are relative in a crystal frame, the coloring is consistent, making identification of matching grains straightforward. Color legends are available in figure 1.14.

B to those in dataset A is computed:

$$
\begin{aligned}
[T]_{4x4} &= A^T_{4xn} B_{nx4} \left(B^T_{4xn} B_{nx4} \right)^{-1} \\
A &= \begin{bmatrix} a_1^x & a_1^y & a_1^z & 1 \\ a_2^x & a_2^y & a_2^z & 1 \\ \vdots & \vdots & \vdots & \vdots \\ a_n^x & a_n^y & a_n^z & 1 \end{bmatrix} \\
B &= \begin{bmatrix} b_1^x & b_1^y & b_1^z & 1 \\ b_2^x & b_2^y & b_2^z & 1 \\ \vdots & \vdots & \vdots & \vdots \\ b_n^x & b_n^y & b_n^z & 1 \end{bmatrix}
\end{aligned}
\tag{4.1}
$$

where $(a_i^x,\ a_i^y,\ a_i^z)$ is the centroid of grain i in dataset A. The transformation calculation may be modified to restrict degrees of freedom or introduce centroid weighting [133], for example the grain volume weighted least squares similarity transform. To merge both datasets onto a single grid, the transformation is applied to dataset B and the transformed volume resampled on the sampling grid of dataset A, using nearest neighbor interpolation. A schematic showing the transformation of a dataset B to the sampling grid of Dataset A is shown schematically in figure 4.7 with a detailed description provided in algorithm 4.5.

Register & Align Orientation Reference Frame

The rotation between two orientation reference frames cannot be determined by a single orientation pair due to crystal symmetry, as shown in figure 4.8. The rotation between a given pair can be expressed in a different way for each crystal symmetry operator:

$$T_i = g_1 * O_i^{sym} * g_2^{-1} \tag{4.2}$$

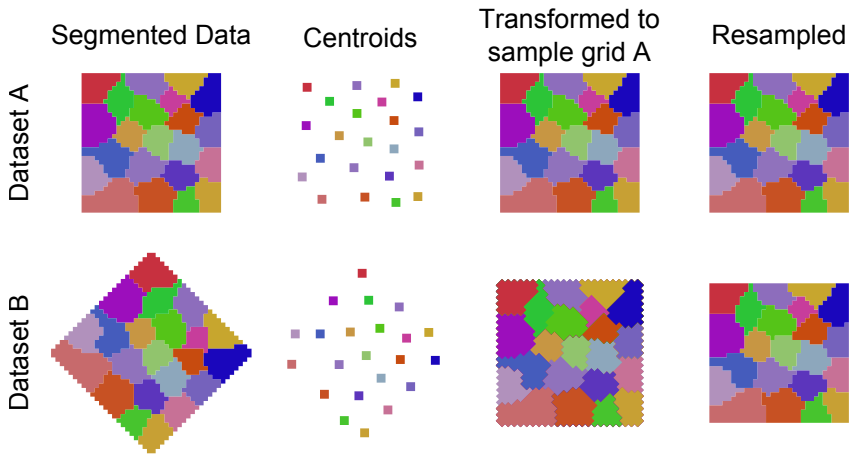

Figure 4.7: Two synthetic datasets, denoted A and B, are collected from the same hypothetical sample with different sampling grids. Grain centroids are calculated for both datasets. Pairs of matched grains are used to determine the transformation between A and B, then dataset B is resampled on the sampling grid of dataset A as described in algorithm 4.5. An IPF color legend is available in figure 1.14.

Algorithm 4.5: An algorithm to compute the rotation between sampling grids of two datasets, A and B, is provided. The centroid of grain i in datasets A and B is denoted (a_i^x, a_i^y, a_i^z) and (b_i^x, b_i^y, b_i^z) respectively. The least squares affine transformation T is computed and used to map dataset B to A with nearest neighbor interpolation.

Data: 2 voxel datasets A and B to align and list of corresponding points
Result: Dataset A and B fused on the sampling grid of dataset A

$$[A] \leftarrow \begin{bmatrix} a_1^x & a_1^y & a_1^z & 1 \\ a_2^x & a_2^y & a_2^z & 1 \\ \vdots & \vdots & \vdots & \vdots \\ a_n^x & a_n^y & a_n^z & 1 \end{bmatrix}$$

$$[B] \leftarrow \begin{bmatrix} b_1^x & b_1^y & b_1^z & 1 \\ b_2^x & b_2^y & b_2^z & 1 \\ \vdots & \vdots & \vdots & \vdots \\ b_n^x & b_n^y & b_n^z & 1 \end{bmatrix}$$

$[T] \leftarrow A^T(B^TB)^{-1}$ **foreach** *voxel in dataset A* **do**
  $x \leftarrow (\mathsf{centroid}(voxel), 1)$
  $x' \leftarrow [T]^{-1}x$ voxel$\leftarrow\mathsf{data}(voxel\ nearest\ x^prime)$
end

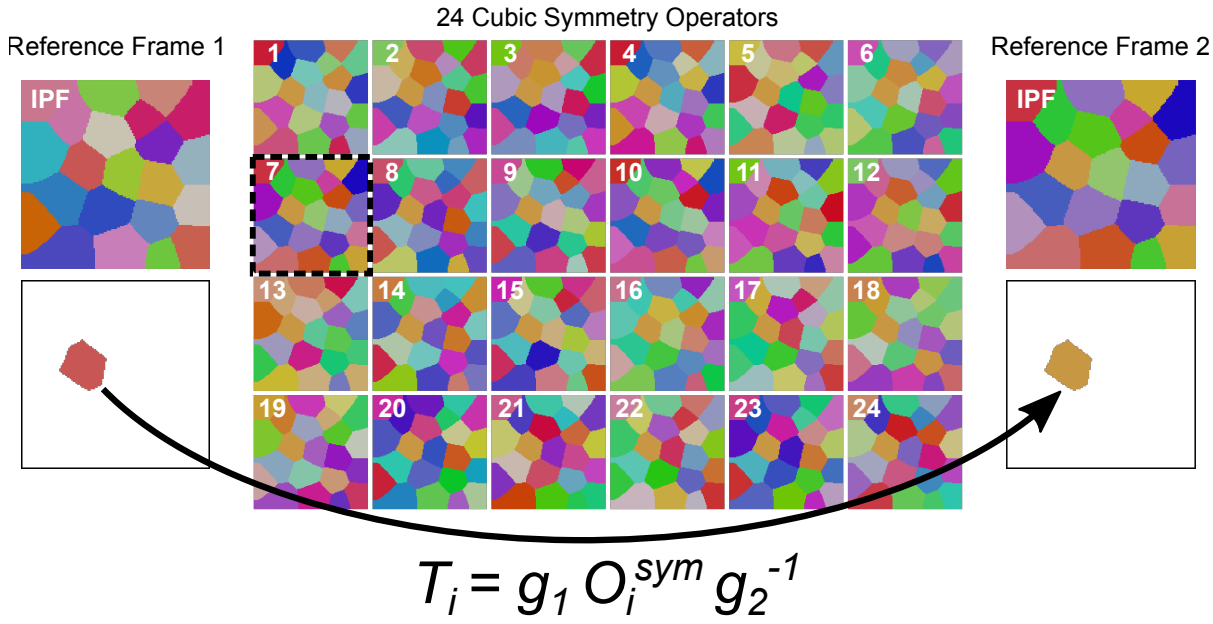

Figure 4.8: A small synthetic dataset with orientations in two reference frames is shown in the top left (reference frame 1) and right (reference frame 2). The rotation between a single matched pair of grains (the red and orange pair shown in the bottom left and right) can be expressed in a different form for each crystal symmetry operator. The result of applying each of these transformations, T_i, to reference frame 1 is shown in the center. Notice that the red/orange pair from which T_i has been computed matches reference frame 2 for every case. However, the remaining grains are only aligned with the orientations in reference frame 2 for T_7.

where T_i is the orientation reference frame transformation, g_1 and g_2 are grain orientations for a matched pair in two different reference frames, and O_i^{sym} is a symmetry operator. With multiple grain pairs, each potential rotation can be checked against other pairs to select the permutation resulting in the lowest disorientation angle for all other pairs. To determine the rotation required to align sample reference frames, this procedure is performed for each pair of grains and the resulting rotations averaged as described in algorithm 4.6.

Automatic Feature Matching and Iterative Alignment

Once a single alignment loop (figure 4.4) has been completed using manually selected grain pairs, the correspondence is sufficient for automated identification of additional

Algorithm 4.6: An algorithm to compute the rotation between crystal orientation reference frames of two datasets, A and B, is provided. The rotation is applied to the reference frame of dataset B to align it with the reference frame of dataset A.

Data: A list of matched grain pairs (grain A_i corresponds to grain B_i) and their average orientations
Result: Rotated to align orientation refernce frame of B with A
foreach *grain pair* i **do**
  $g_i \leftarrow$rotation from B_i to A_i
  foreach *symmetry operator* **do**
    $g_i' \leftarrow$equivalent rotation apply g_i' to all other orientation pairs **foreach** *other grain pair* j **do**
      $g_j \leftarrow$ rotation from B_j to A_j **foreach** *symmetry operator* **do**
        $g_j' \leftarrow$equivalent rotation $\epsilon \leftarrow angle(g_j')$
      end
      $\theta \leftarrow \min \epsilon$
    end
    $\phi \leftarrow \bar{\theta}$
  end
  $g \leftarrow g_i(\min \phi)$
end
return $\bar{g}$

pairs. The Jaccard index ($A_i \cap B_j / A_i \cup B_j$ where A_i and B_j are the volumes of grain i and j in dataset A and B respectively and $\cap$ and $\cup$ denote volume intersection and union respectively), is computed for every possible pair of grains between the datasets as a similarity metric [134]. Cosine similarity ($A_i \cap B_j / \sqrt{A_i B_j}$), Sørensen–Dice coefficient ($2A_i \cap B_j / (A_i + B_j)$), or other binary similarity coefficients may be substituted for Jaccard index [135–137]. Grains are subsequently matched by descending metric value using a 'greedy' (incrementally instead of globally optimum) algorithm described in algorithm 4.7. An optimal assignment algorithm described in algorithm 4.8 may be used instead, but has complexity scaling of n^3 or n^4 depending on implementation compared to $n \log n$ for the greedy algorithm. If the orientation reference frames are aligned, an additional orientation match requirement can be imposed for pair assignment. A schematic of the process and detailed description are provided in figure 4.9 and algorithm 4.9 respectively.

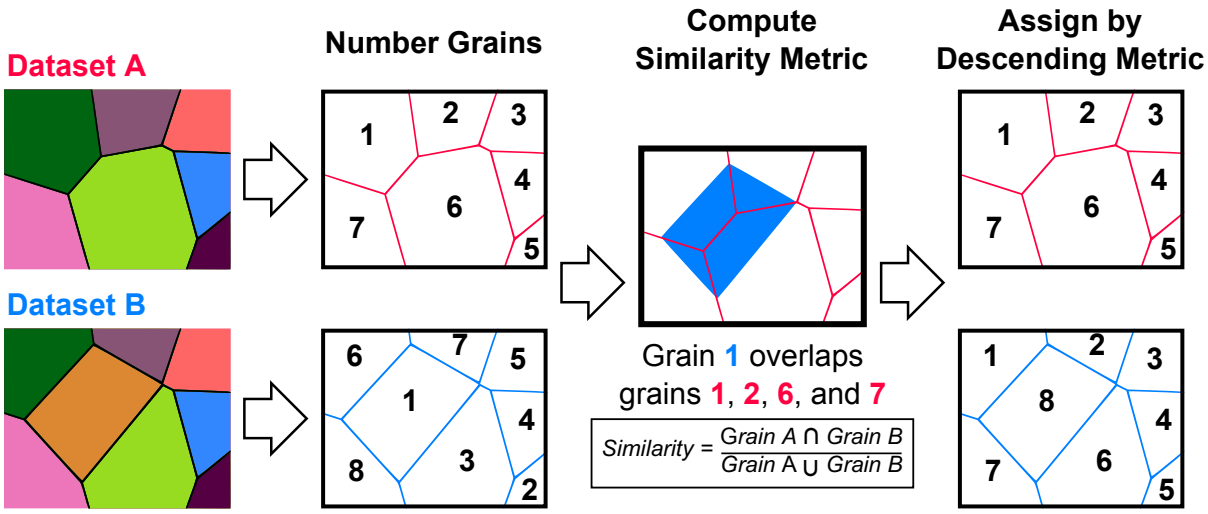

Figure 4.9: The algorithm used to match grains between datasets is demonstrated for a simple example. Two synthetic datasets A and B are shown, one containing an additional grain. The grains in each dataset are randomly numbered and then a similarity metric is calculated between all possible grain pairs. Pairs are subsequently matched by descending similarity. The similarity metric employed may be altered, allowing optimization of matching for different features. The details of this algorithm are described in algorithm 4.9.

Identification of matching grain pairs closes the alignment loop allowing iteration. Since both the sampling grid and orientation reference frame alignment algorithms are uniquely dependent upon the grain pairs considered, convergence occurs when refining the alignment provides no new matched pairs. Alignments for both sampling grid and orientation reference frames are performed iteratively, and sampling grid alignment requires nearest neighbor interpolation. Repeated interpolation may introduce artifacts as seen in figure 4.5. In order to minimize these artifacts, transformations from consecutive alignment steps are combined and applied to the original volumes in a single interpolation step.

Subsequent Developments

Manual identification of grain pairs to seed the alignment loop is by far the most labor intensive and time consuming component of dataset fusion. The concept of identifying pairs visually based on neighbor disorientation has been subsequently implemented algo-

Algorithm 4.7: An algorithm to greedily assign pairs in a bipartite graph is given.

Data: Edges of weighted bipartite graph with two vertex sets A and B
Result: A greedy minimum weight matching between A and B
sort edges by weight **foreach** *edge* $E_{i,j}$ **do**
    if A_i *and* B_j *are unassigned* **then**
        $A_i \leftarrow B_j$
    end
end

Algorithm 4.8: The Kuhn–Munkres or Hungarian algorithm for perfect minimum weighted bipartite graph assignment is given [138, 139].

Data: Weighted bipartite graph of two vertex sets A and B as a matrix of weights
Result: Minimum weight perfect assignment between A and B
uncover all rows and columns
subtract minimum row element from each row
subtract minimum column element from each column
cover each column containing a zero
1 **while** *uncovered columns exist* **do**
    while *an uncovered zero exists* **do**
        prime the uncovered zero
        if *there is a starred zero in the row of the primed zero* **then**
            uncover the column of the starred zero and cover its row
        else
            while *a starred zero exists in the current column* **do**
                move to the starred zero in current column
                move to the primed zero in current row
            end
            unstar each starred zero and star each primed zero
            uncover all rows and columns
            cover all column with starred zeros go to **1**
        end
    end
    find the minimum value uncovered element
    add the minimum value uncovered element to each covered row and subtract it from each covered column
end
return *indices of starred zeros*

Algorithm 4.9: An algorithm to match grain ID numbers of two datasets, A and B, is provided. An overlap metric is assigned for each possible grain pair, and grains in B are matched to grains in A by descending metric value.

Data: Two sets grain IDs (A and B) describing similar grains on the sample sampling grid and optionally their phases and average orientations
Result: ID assignments such that A_i and B_i correspond to the same grain.
foreach *grain* A_i *in dataset* A **do**
  foreach *grain* B_j *in dataset* B **do**
    $m \leftarrow \frac{A_i \cap B_j}{A_i \cup B_j}$
    if $m < m_{tol}$ **then**
      if *orientation provided* **then**
        if `phase(`A_i`)` *is* `phase(`B_j`)` **then**
          $\theta \leftarrow$disorientation(A_i,B_j)
          if $\theta < \theta_{tol}$ **then**
            pairs$\leftarrow${pairs,(i,j,m)}
          end
        end
      else
        pairs$\leftarrow${pairs,(i,j,m)}
      end
    end
  end
end
Match pairs using greedy (algorithm 4.7) or optimum (algorithm 4.8) assignment

rithmically as described in algorithm 4.10. This algorithm is able to successfully identify grain pairs with no prior alignment or manual intervention.

4.2.3 Dataset Fusion

Visualizations of the reconstructed DCT and TriBeam 3D datasets, prior to merging, are shown in figure 4.11 using disorientation coloring [46]. This coloring was chosen for convenience so that grains close in orientation space are also close in coloring. The TriBeam dataset is larger than the DCT dataset along the z-axis because more of the sample pillar volume was sampled during the TriBeam tomography experiment. Matching grain pairs by morphology alone is difficult and orientation coloring cannot be leveraged since the orientation reference frames are unaligned. However, since boundaries are colored by disorientation, pairs are identifiable readily as shown in figure 4.12. A cubic disorientation coloring legend and instructions for its use are available in figure 1.14. Disorientation coloring exists for most Laue groups, allowing this technique to be used for a wide variety of material systems [46]. The grains used to seed the alignment are shown in figure 4.13 and the resulting aligned and merged datasets are shown in figure 4.14. The transformation necessary for alignment of the orientation reference frames was the axis angle pair $[0.3953, -0.9183, -0.0183]$ 3.1372 rad, or approximately 180° about [100] followed by 135° about [001], which is consistent with the sample being inverted between tomography experiments with a rotation about the pedestal axis. The affine transformation required to align the sampling grids was:

$$\begin{bmatrix} -0.733 & -0.783 & -0.058 & -104.3 \\ -0.714 & -0.724 & 0.049 & -76.5 \\ 0.035 & 0.093 & -1.023 & -100.3 \\ 0 & 0 & 0 & 1 \end{bmatrix}$$

Algorithm 4.10: An algorithm for neighbor disorientation based grain matching is given.

Data: Phase, orientation, and grain morphology of 2 datasets
Result: Grain matching between dataset
foreach *dataset* $X : \{A, B\}$ **do**
  foreach *grain* X_i **do**
    foreach *neighbor* X_j **do**
      $\mathrm{v}_{x,i} \leftarrow$`disorientation(`$X_i$, X_j`)`
      $\mathrm{s}_{x,i} \leftarrow$`surfaceArea(`$X_i$, X_j`)`
    end
  end
end
foreach *grain* A_i *in reference dataset* **do**
  foreach *grain* B_j *in moving dataset* **do**
    if `phase(`A_i`)` *is* `phase(`B_j`)` **then**
      foreach *neighbor* A_m *of* A_i **do**
        foreach *neighbor* B_n *of* B_i **do**
          if `phase(`A_m`)` *is* `phase(`B_n`)` **then**
            metric $\leftarrow 1 - \mathrm{v}_{A,m} \cdot \mathrm{v}_{B,n}$
          else
            metric $\leftarrow 1$
          end
        end
      end
      determine optimum neighbor assignment using algorithm 4.8
      foreach *neighbor* **do**
        if *assigned* **then**
          weight $\leftarrow$ weight $+ (\mathrm{s}_{A,m} + \mathrm{s}_{B,n}) *$ metric
        else
          weight $\leftarrow$ weight $+ \mathrm{s}_{X,m}$
        end
      end
      if weight $<$*threshold* **then**
        edge $\leftarrow$(A_i,B_j,weight)
      end
    end
  end
end
apply greedy assignment (algorithm 4.7)

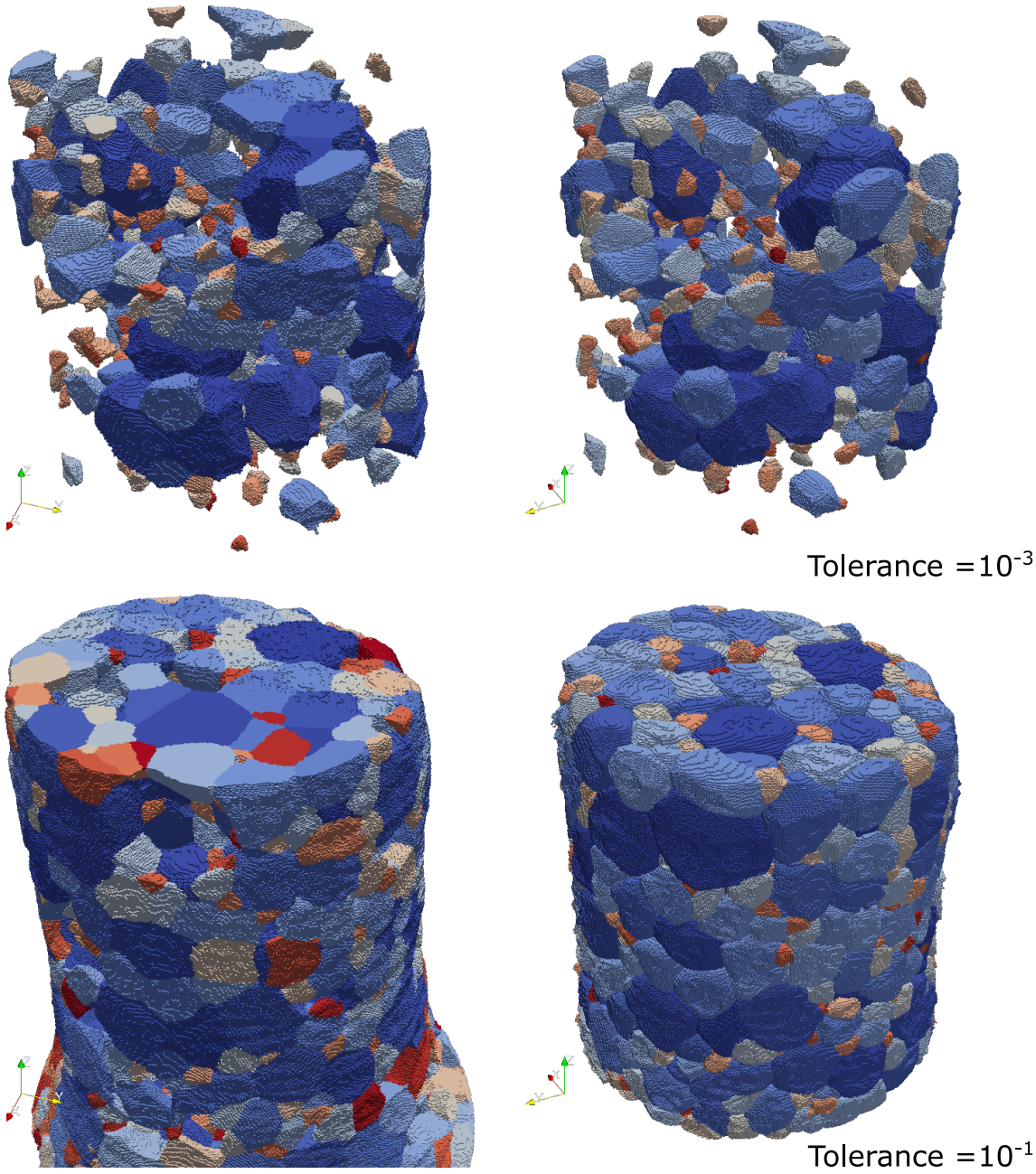

Figure 4.10: Two DCT time steps of a STO grain growth are colored by grain ID after matching using neighbor disorientation, as described in algorithm 4.10. Only grains with a match assigned between the first time step (left) and second time step (right) are shown. When a small tolerance is used (top) no incorrect matches are apparent and significantly more pairs than required to seed the fusion loop are found. When a larger tolerance is used (bottom), incorrectly matched pairs are visible. Datasets courtesy of Peter Gumbsch (unpublished work).

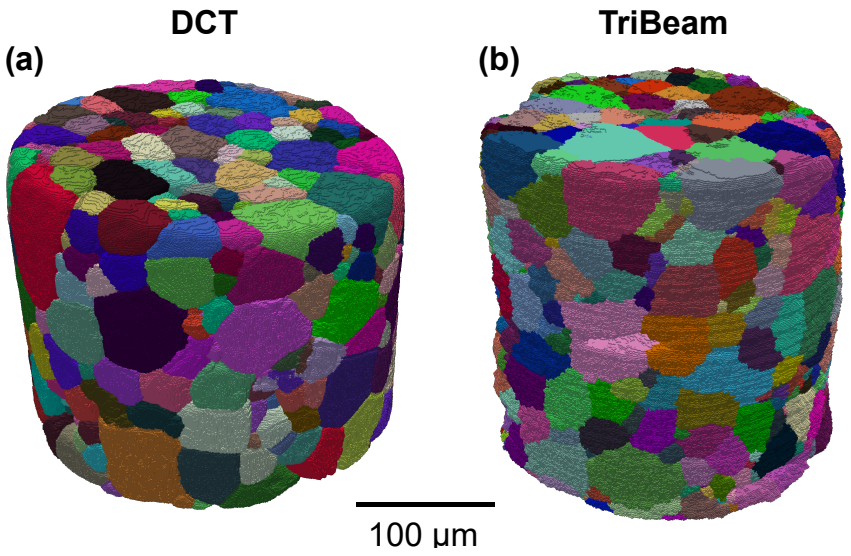

Figure 4.11: Reconstructions of the STO sample using data collected from the DCT experiment (a) and the TriBeam experiment (b) are shown. Grains are colored by their average orientation using a disorientation coloring scheme [46]. To color orientations with this scheme disorientations are computed with respect to identity. The orientation reference frames are not aligned, making selection of matching grain pairs difficult, even with the sampling grids coarsely aligned. Only careful morphological comparison can be used for matching. A disorientation color legend is available in figure 1.14.

Extracting the rotation component of the affine transformation using singular value decomposition yields $[0.3886, -0.9208, -0.0332]$ 3.0934 rad, a difference of 1° in axis and 2.5° in angle from the rotation required to align the orientation reference frames.

4.2.4 Fusion Quality

Three primary algorithms were used to combine the tomography datasets, addressing alignment of the orientation reference frame, alignment of the sampling grid, and matching of grain pairs. For each algorithm a metric was selected to appraise performance.

The difference in centroid position of matched grain pairs is used as the metric for the sample alignment algorithm. A plot of the distance between the centroid positions for matched grain pairs in the DCT and TriBeam datasets is shown in figure 4.15. A small number of edge grains have displacements that are greater than 3–4 µm due to a difference in the sensitivity of the tomography techniques to grains at the sample surface.

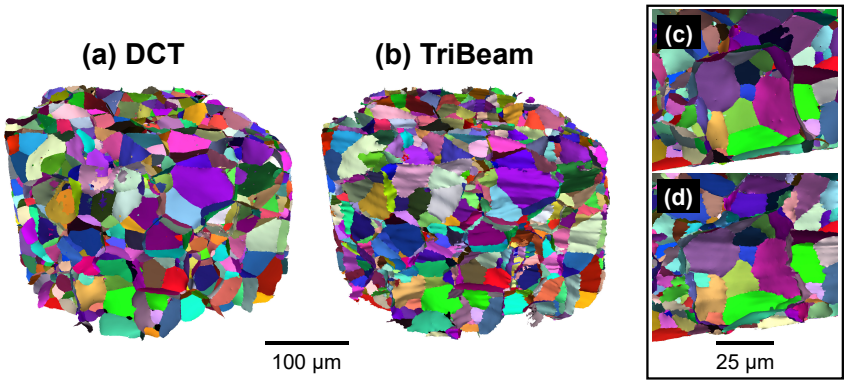

Figure 4.12: Grain boundary surface meshes of the DCT (a) and TriBeam (b) datasets are colored by Patala's disorientation coloring scheme (legend available in figure 1.14). This representation enables manual selection of grain pairs prior to alignment of the orientation reference frames as shown schematically in figure 4.6. Higher magnification images of the grain boundaries from one corresponding grain pair are shown in (c) and (d) respectively.

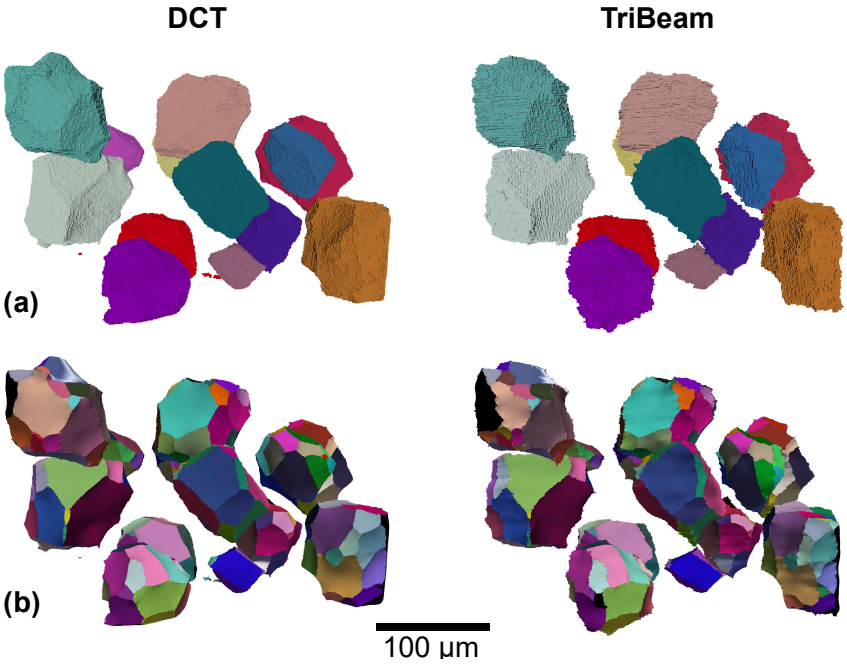

Figure 4.13: Manually selected grain pairs from the DCT and TriBeam datasets are colored by grain average orientation (a) and boundary disorientation (b) after alignment. These grains were manually identified as described and used to initialize the alignment loop shown in figure 4.4. A disorientation color legend is available in figure 1.14.

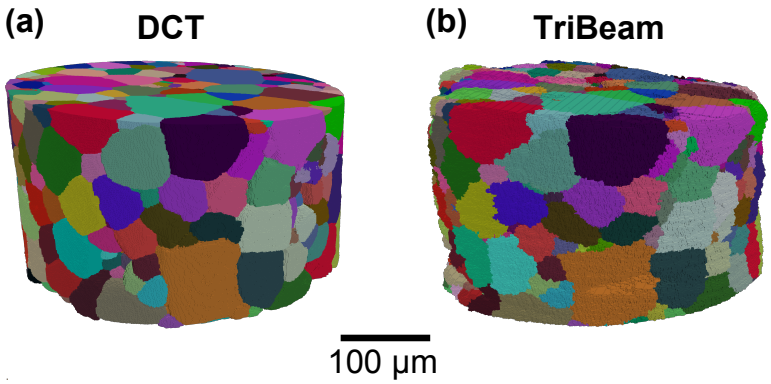

Figure 4.14: Reconstructions of the DCT and TriBeam datasets are shown after alignment is complete. The two datasets are merged into one data container and grains matched so that data at any voxel or for any grain can be simultaneously probed from both tomography datasets. The dataset is colored by disorientation with a legend available in figure 1.14.

The average of the centroid displacements in the x, y, and z positions are centered at 0.

The difference in orientations between matching grain pairs in the two final time step tomography datasets was used to assess the alignment of the orientation reference frames. Figure 4.16 shows the difference in average orientation for each grain pair between the DCT and TriBeam tomography experiments. Most of the matched grain pairs have a difference that is between 0.25° and 0.75°, and all grain pairs have a difference less than 2.5°. There is a peak in orientation difference at 0.5°.

The similarity metric ($A_i \cap B_j / A_i \cup B_j$) of matched grain pairs was selected to evaluate automated grain matching. Figure 4.17 shows the distribution of similarity metrics observed. Most grain pairs have an overlap metric between 0.7 and 0.9. Pairs with a small similarity metric generally correspond to grains that are fully contained in one volume but only partially captured by the other.

Voxel Level Dataset Comparison

Accurately aligning the sampling grids allows for direct comparisons on a voxel-by-voxel basis. This type of analysis is useful to make grain independent comparisons, such as

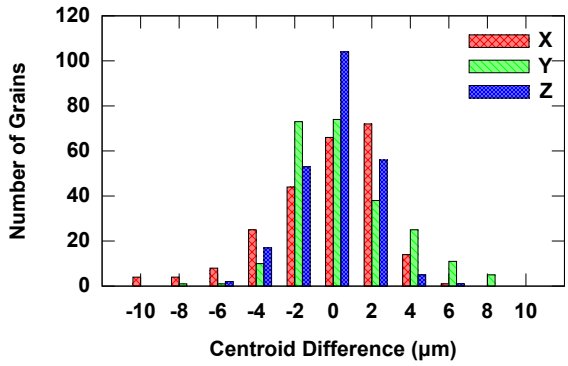

Figure 4.15: A histogram of difference in TriBeam centroid positions relative to corresponding DCT centroids is shown. The average of all the centroid positions along each primary axis is 0.

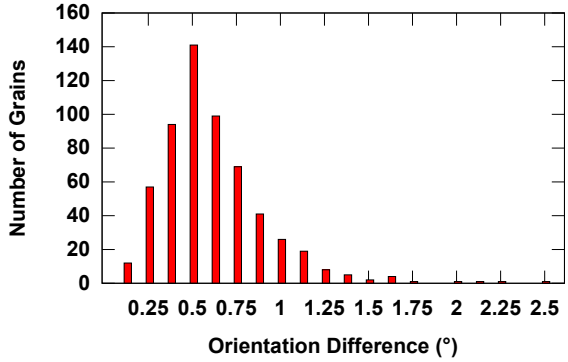

Figure 4.16: A histogram of disorientation angle between matched grain pairs in the DCT and TriBeam tomography datasets is shown. Most grain pairs exhibit an angle of between 0.25° and 0.75°.

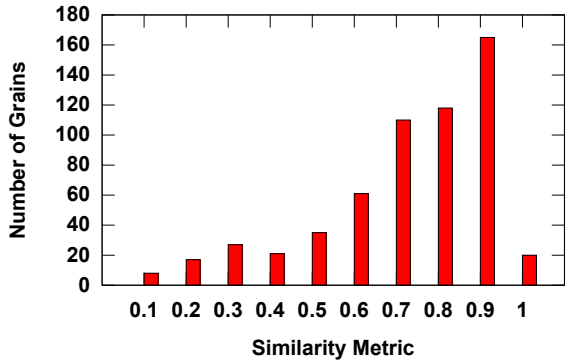

Figure 4.17: A histogram of the similarity metric ($A_i \cap B_j / A_i \cup B_j$) for all matched grain pairs between the DCT and TriBeam datasets is plotted. The lowest similarity metric values correspond to grains that were not fully contained in the overlapping tomography dataset volume.

orientation gradients, boundary locations, and measures of reconstruction or confidence. The reconstructions of DCT and TriBeam datasets have been sliced orthogonally in figure 4.18 to show the relative spatial positions of the identical grains. Voxels for which the disorientation angle between the two datasets is below 5° are transparent. Voxels with a higher angle are displayed using the disorientation coloring scheme described earlier [46]. Therefore, the colored regions indicate differences in orientation assignment between the DCT and TriBeam reconstructions that have a disorientation greater than 5°, accounting for 20% of the voxels. Half of these voxels correspond to boundary discrepancies with a typical thickness of 1–3 µm, and the balance of the voxels arises from unresolved grains in the DCT reconstruction.

Direct Grain to Grain Comparison

The grains in each dataset were matched using a grain numbering algorithm for continuous voxel regions which shared orientations within a 5° tolerance. Of particular interest are the unique grains, which only exist in one of the two datasets and were not matched. Visualizations of the grains that are unique to either the DCT or TriBeam dataset are shown in figure 4.19. Unique grains detected by the TriBeam were plotted in figure 4.20. The unique grains resolved by TriBeam are predominantly either (1) larger and located at the sample surface or (2) smaller grains below the resolution limit of this DCT reconstruction. Slices from the merged 3D datasets were made, showing examples of cases (1) and (2) in figure 4.21. From the merged dataset volume, 159 unique grains were found exclusively in the TriBeam dataset (of 741 total grains), which can be attributed to either being below the DCT reconstruction's resolution limit, apparent in figure 4.22, or high aspect ratio grains on the sample exterior.

The unique grains in the DCT dataset predominantly share at least one low angle grain boundary (below 1.5°) with a neighboring grain. EBSD data collected by the TriBeam technique at these low angle boundaries were not segmented into individual grains

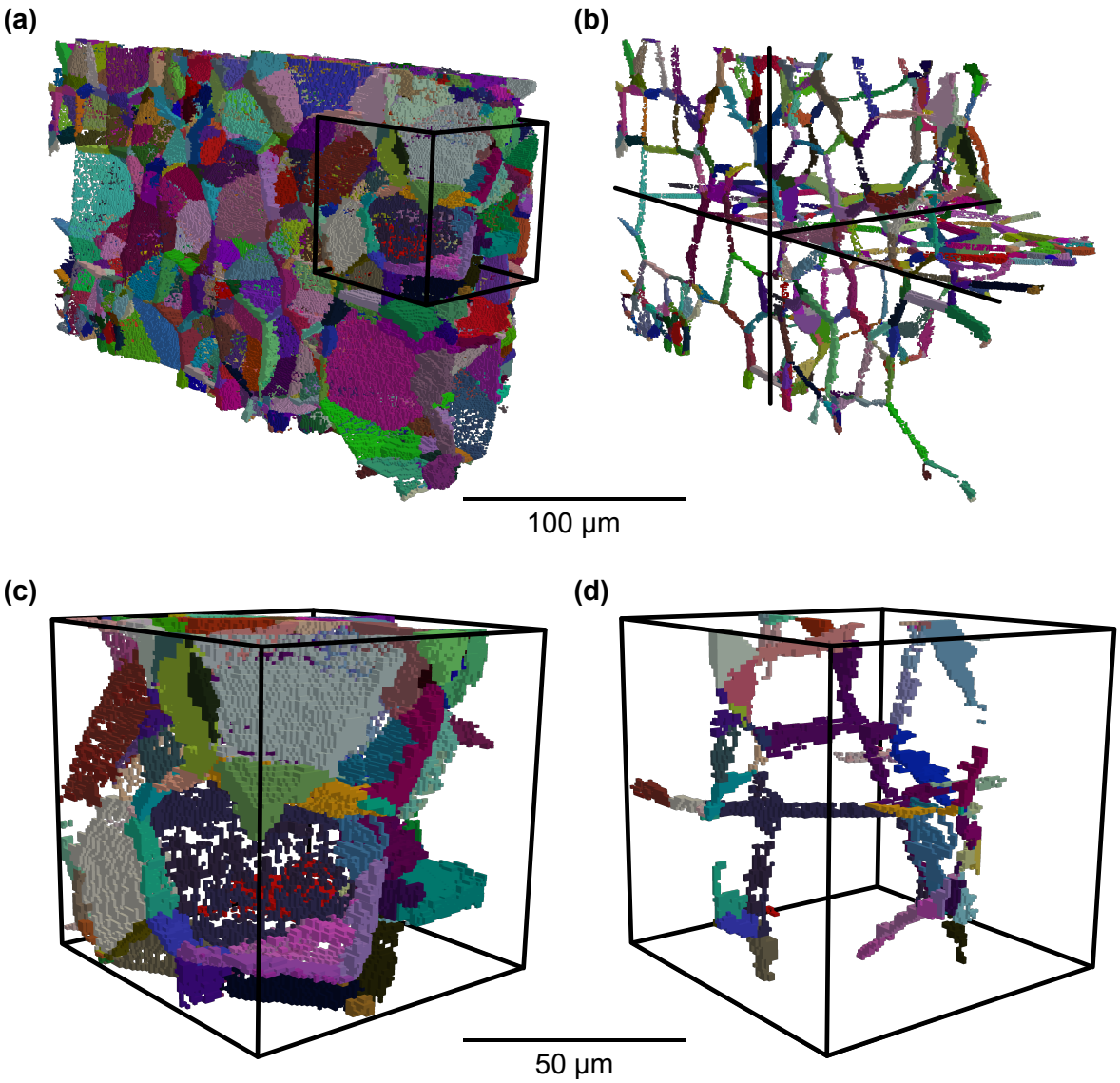

Figure 4.18: A grain difference map is rendered for half the pedestal (a) and three 2.8 µm thick orthogonal sections (b). For each voxel, disorientation is computed between the orientation of the assigned DCT grain and the average orientation of the assigned TriBeam grain. If the disorientation angle is below 5° the voxel is transparent, otherwise it is colored by disorientation. A higher magnification of the inset indicated in (a) is shown in (c) with corresponding orthogonal sections in (d). Colored regions with a perforated appearance, e.g. the dark blue face in (c), indicate voxel level agreement in grain boundary location between the two datasets. A disorientation color legend is available in figure 1.14.

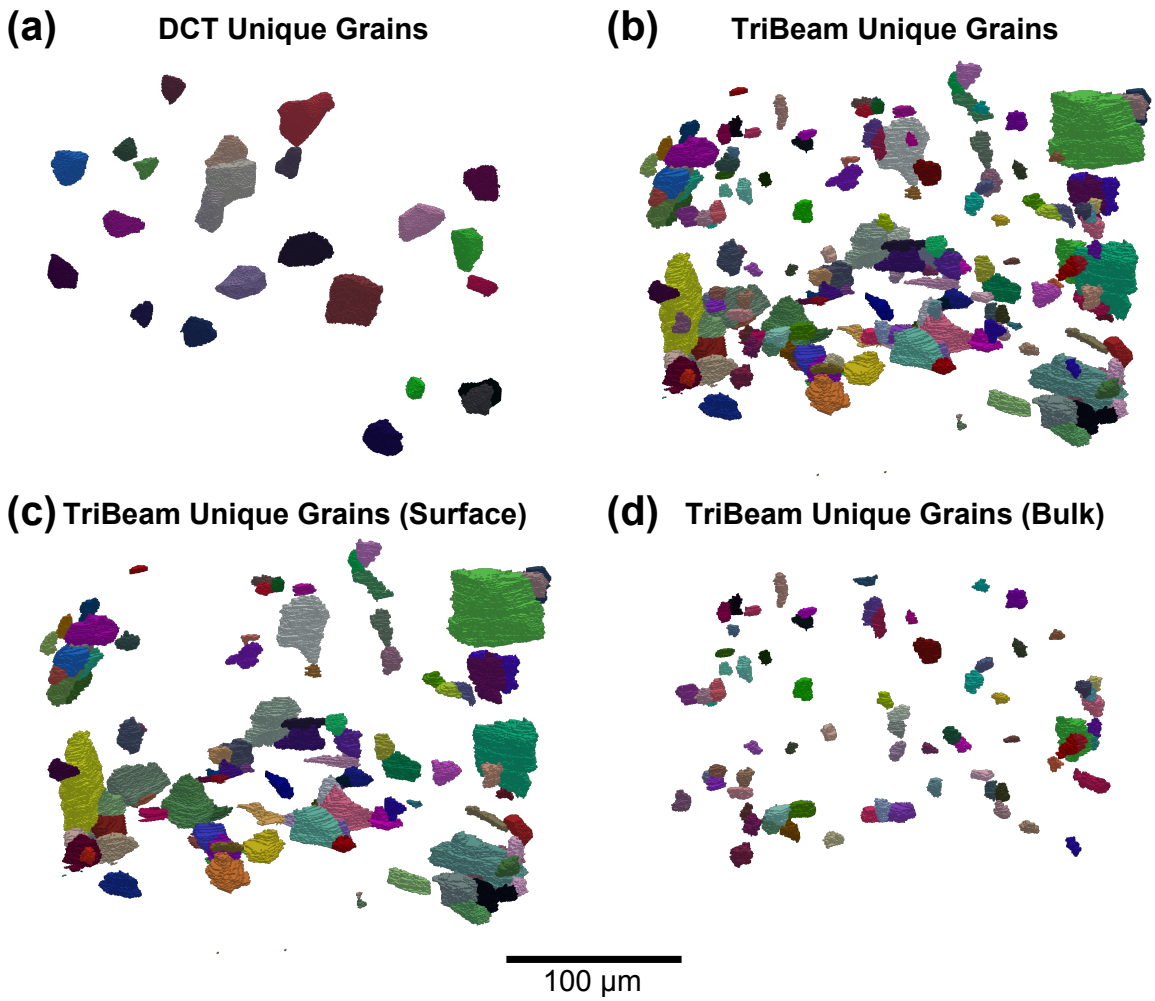

Figure 4.19: Unique grains in the DCT (a) and TriBeam (b) datasets are shown. The total volume of the unmatched TriBeam grains (b) comprises 3.8% of the matched volume. Most unmatched grains in the DCT dataset correspond to segmentation errors in the TriBeam volume. If two grains are erroneously merged during TriBeam segmentation, one will be left unpaired in the DCT volume. Most unmatched grains in the TriBeam dataset are unresolved in the DCT dataset. Unique grains in the TriBeam dataset which touch the surface (c) may be larger but are generally thin in the radial direction. Internal grains (d) are predominantly small and equiaxed. A disorientation color legend is available in figure 1.14.

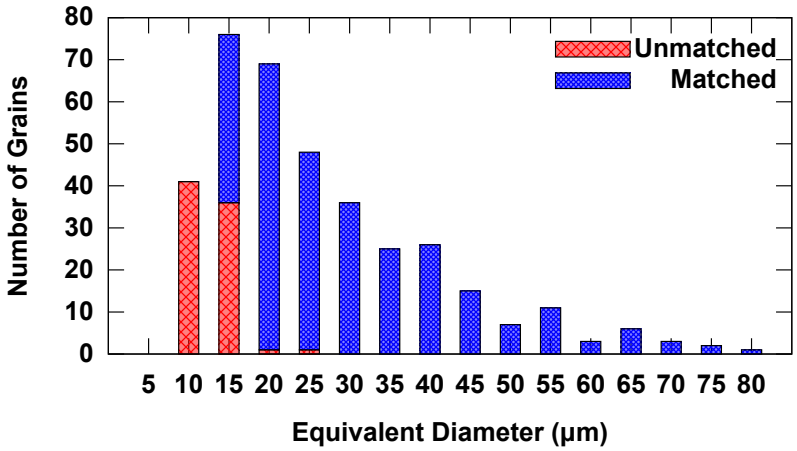

Figure 4.20: A histogram of equivalent diameter for grains reconstructed in TriBeam dataset is shown. The majority of the unmatched grains do not exist in the DCT dataset, presumably because too few diffraction spots were available for DCT reconstruction. These cases may correspond to spot overlap or resolution limits.

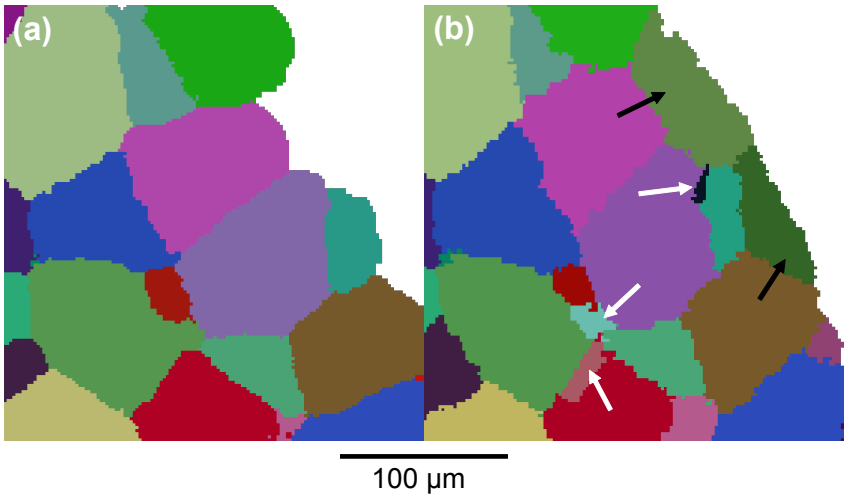

Figure 4.21: The same region is colored by grain average orientation for the DCT (left) and TriBeam (right) datasets. Very small internal or thin surface grains, indicated by white and black arrows respectively, are often unresolved in the DCT reconstruction. A disorientation color legend is available in figure 1.14.

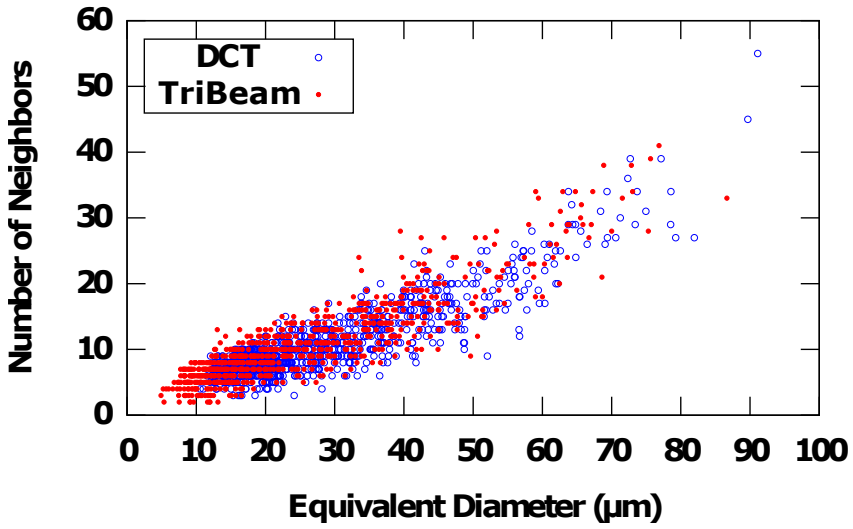

Figure 4.22: Equivalent diameters for all grains in the DCT and TriBeam datasets are plotted against their number of neighbors. The spatial resolution of the TriBeam extends below that of the DCT technique for the experimental parameters used. On average, matched DCT grains have a 0.2 µm larger equivalent diameter and 0.74 fewer neighbors than their TriBeam counterparts. The grains from the TriBeam dataset that are unmatched and have an equivalent diameter less than 12 µm account for only 0.35% of the total matched volume. This result is consistent with merging small, unresolved grains into their neighbors.

due to the variability in orientation measurements. However, the implementation of additional grain boundary definition (segmentation) algorithms may enable more accurate reconstruction of subgrains for this dataset. EBSD measurement variability can be introduced by a wide range of factors, including diffraction pattern indexation, EBSD camera binning and exposure times, spread in energy of electrons used in diffraction, surface roughness, intrinsic grain orientation substructure, and electron beam sampling volume effects. Examples of grains that were not segmented and matched to a grain in the DCT dataset are shown in figure 4.23. Of the 606 total grains collected by DCT from the merged dataset volume, 24 unique grains were found only in the DCT dataset, mostly having low angle grain boundaries.

Overall the fused datasets have excellent agreement. The TriBeam system is able to accurately capture grain morphology without any serious artifacts introduced by the alignment and reconstruction process. The flood fill segmentation algorithm used to

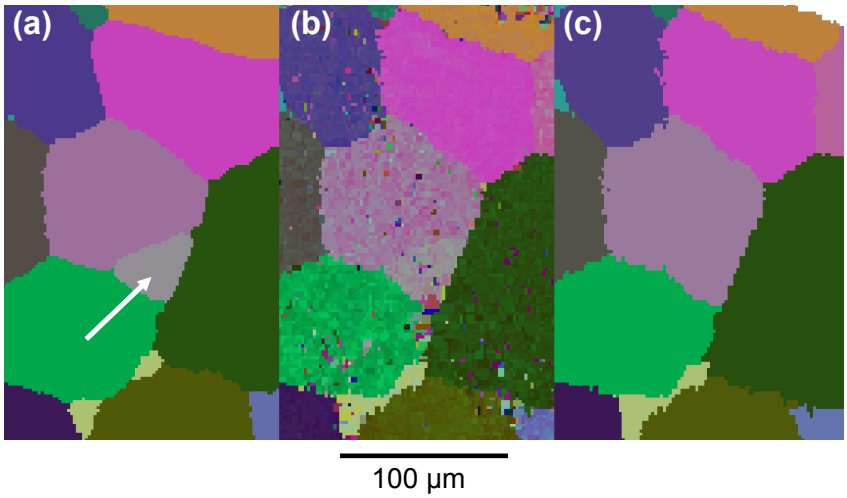

Figure 4.23: The same region is colored by DCT grain average orientation (a), TriBeam voxel orientation (b), and TriBeam grain average orientation (c). The EBSD segmentation algorithm erroneously merges neighboring grains with a low disorientation connection (below 1.5°). A disorientation color legend is available in figure 1.14.

segment grains may join neighboring grains with a low disorientation angle. Loss of low angle ($\lessapprox 5°$) boundaries may be significant for some materials and properties but should generally be acceptable when studying mechanical properties including fatigue behavior.

4.3 3D René 88DT Datasets Collected

The algorithms described and developed above were used to reconstruct a variety of René 88DT material volumes with development and application of additional algorithms for analyzing and quantifying the twin microstructure discussed in chapter 5 and chapter 6. Five 3D EBSD datasets of René88DT have been collected by TriBeam tomography with details of collection and reconstruction given below. A list of datasets including dimensions and resolution is shown in table 4.1. Unless otherwise noted all datasets were collected in collaboration with Dr. McLean Echlin using fatigue samples provided by Dr. Jean-Charles Stinville [119].

In general dataset size and resolution were balanced to keep total acquisition time on the order of 3 days (typically 15 to 30 minutes per slice). Data sets cover a range

Table 4.1: René 88DT datasets collected are listed.

Name	Resolution (µm)	Size (voxels)	Dimensions (µm)	References
Twin Scale	$0.10 \times 0.10 \times 0.50$	$742 \times 993 \times 140$	$60 \times 70 \times 70$	[119]
Grain Scale	$0.30 \times 0.30 \times 0.75$	$802 \times 482 \times 199$	$240 \times 145 \times 130$	—
Crack	$0.30 \times 0.30 \times 0.75$	$429 \times 757 \times 127$	$120 \times 200 \times 90$	—
Microtensile	$0.25 \times 0.25 \times 1.00$	$244 \times 1094 \times 33$	$20 \times 175 \times 20^*$	[140]
Inclusion	$0.55 \times 0.55 \times 0.75$	$534 \times 802 \times 143$	$400 \times 600 \times 105$	—

*gauge

of volumes but generally have similar voxel counts as a result of this balance. Energy dispersive X-ray spectroscopy and back scatter electron imaging have not been leveraged in these datasets owing to the small degree and length scale of chemical segregation. Both EBSD patterns and secondary electron images were captured for all datasets, but generally secondary electron imaging was only exploited to monitor laser cut quality with EBSD data being preferred for reconstruction due to ease of segmentation. In-plane imaging resolution and slice thickness were generally scaled together to avoid collecting datasets with extremely high aspect ratio voxels. The following sections provide additional detail on each of the datasets collected. Chapter 5 and chapter 6 focus on analysis of the datasets.

4.3.1 Twin Scale Dataset

This dataset was collected at a higher resolution over a smaller volume to characterize the twin boundaries. A 10 mm × 5 mm × 1 mm sample was sectioned from a plate of René 88DT using wire electrical discharge machining (EDM). A series of 600 µm wide pedestals were fabricated with wire EDM and then mechanically polished to 600 µm thick creating a series of 600 µm × 600 µm pedestals. A single pedestal was destructively sectioned via femtosecond laser ablation in the TriBeam system. The laser was attenuated to 40 mW and 500 nm slices cut. After each cut a 100 µm wide region was cleaned with a 15 nA Ga^+ FIB with a 30 kV accelerating voltage at a glancing angle of 3°. An example of the resulting exposed surface is shown in figure 4.24. EBSD was collected

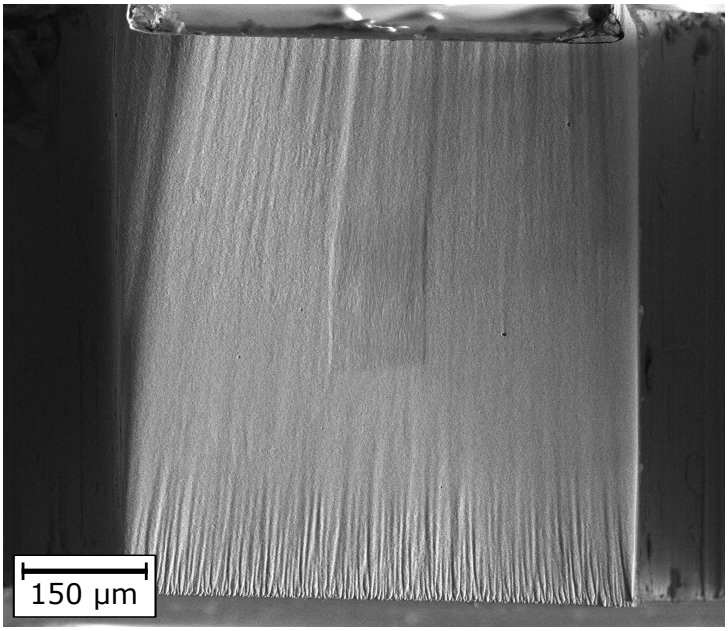

Figure 4.24: A representative exposed surface (slice 70) of the twin scale dataset is shown with the FIB cleaned region visible in the center.

from a 75 µm × 100 µm area within the cleaned region using a 25 kV electron beam, 8 × 8 camera binning, and a 100 nm step size. A total volume of 75 µm × 100 µm × 104 µm was collected from 139 ablated slices. Collection of each slice required 40 minutes of instrument time with 24 minutes of EBSD acquisition time accounting for the majority.

Good voxels were selected by thresholding confidence index greater than 0.05, image quality greater than 1000, and fit less than 2.8 and sections aligned by orientation using a 5° tolerance. Grains were segmented with a 2° tolerance and those smaller than 25 voxels removed by isotropic neighbor dilation. The resulting reconstruction contains 1971 grains and is shown in figure 4.25.

4.3.2 Grain Scale Dataset

This dataset was collected at a moderate resolution over a larger volume to characterize the structure of twin related domains. A 10 mm × 5 mm × 1 mm sample was sectioned from a plate of René 88DT using wire EDM. A series of 600 µm wide pedestals were fabricated with wire EDM and then mechanically polished to 600 µm thick creating a

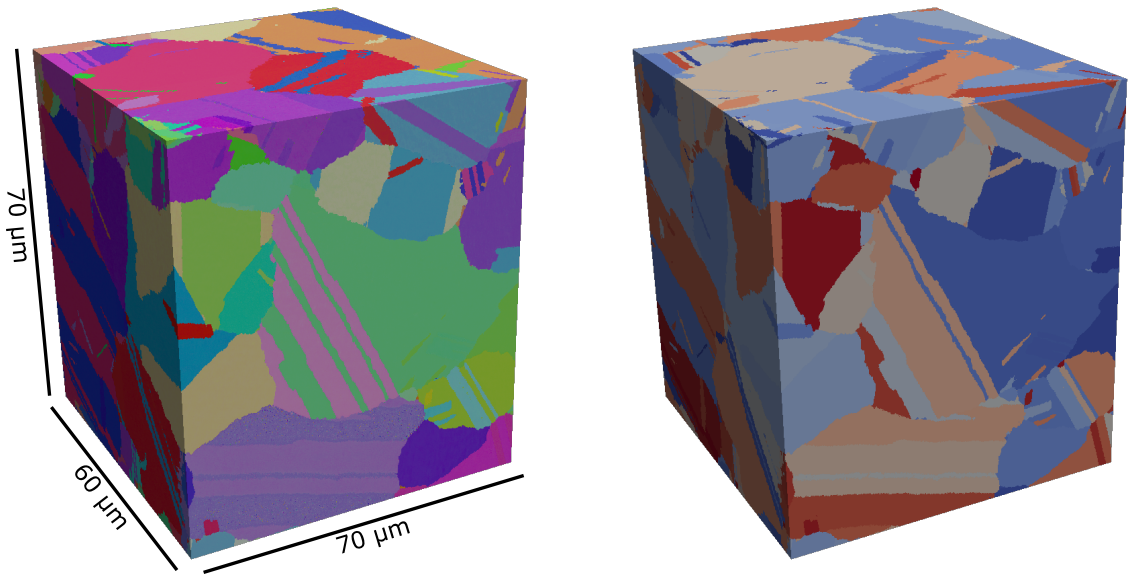

Figure 4.25: The twin scale dataset is rendered using IPF color (left) and random grain ID (right).

series of 600 µm × 600 µm pedestals. The laser was attenuated to 40 mW and 750 nm slices cut. After each cut a 250 µm wide region was cleaned with a 15 nA Ga^+ FIB with a 30 kV accelerating voltage at a glancing angle of 3°. An example of the resulting exposed surface is shown in figure 4.26. EBSD was collected from a 240 µm × 145 µm area within the cleaned region using a 25 kV electron beam, 8 × 8 camera binning, and a 300 nm step size. A total volume of 240 µm × 145 µm × 130 µm was collected from 199 ablated slices. Collection of each slice required 40 minutes of instrument time with 30 minutes of EBSD accounting for the majority.

Grains were segmented with a 2° tolerance and those smaller than 75 voxels removed by isotropic neighbor dilation. Twin related domains were grouped with a 5° tolerance on both disorientation axis and disorientation angle. Slices were aligned using twin related domain centroids. The aligned dataset was next resegmented with a 5° disorientation tolerance and grains smaller than 75 voxels removed by isotropic neighbor dilation. Finally

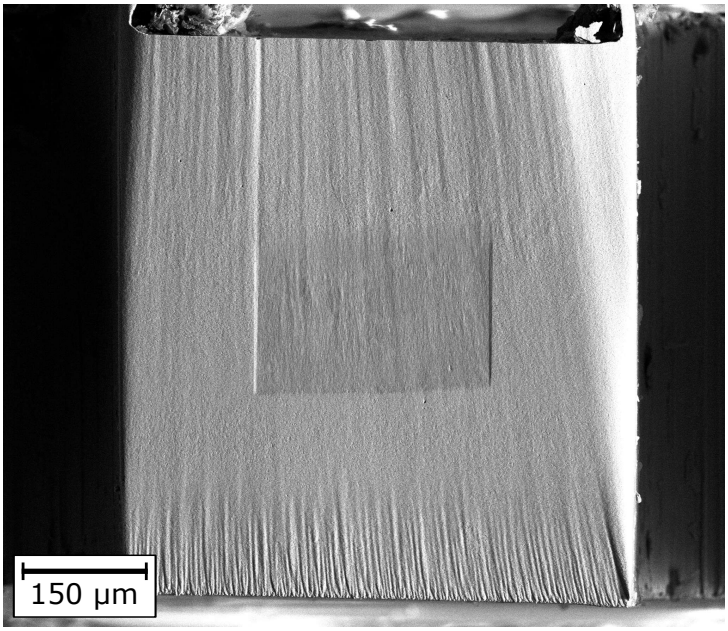

Figure 4.26: A representative exposed surface (slice 100) of the grain scale dataset is shown with the FIB cleaned region visible in the center.

twin related domains were grouped with a 5° tolerance on both disorientation axis and disorientation angle. The resulting reconstruction contains 7402 grains and 1101 twin related domains and is shown in figure 4.27.

4.3.3 Crack Dataset

This dataset was collected around a crack in an interrupted fatigue experiment to characterize crack path. A double flat sample was fatigued at 1 Hz at 20 °C with a peak load of 758 MPa and fully reversed loading. The sample was interrupted at 80% of fatigue life and a disk cut from the gauge section by wire EDM as shown in figure 4.28. A pedestal was cut from the disk and polished on all four large faces to a 600 µm × 600 µm cross section. The laser was attenuated to 40 mW and 750 nm slices cut. After each cut a 250 µm wide region was cleaned with a 15 nA Ga^+ FIB with a 30 kV accelerating voltage at a glancing angle of 3°. An example of the resulting exposed surface is shown in figure 4.26. EBSD was collected from a 120 µm × 200 µm area within the cleaned region using a 25 kV electron beam, 8×8 camera binning, and a 300 nm step size. A total

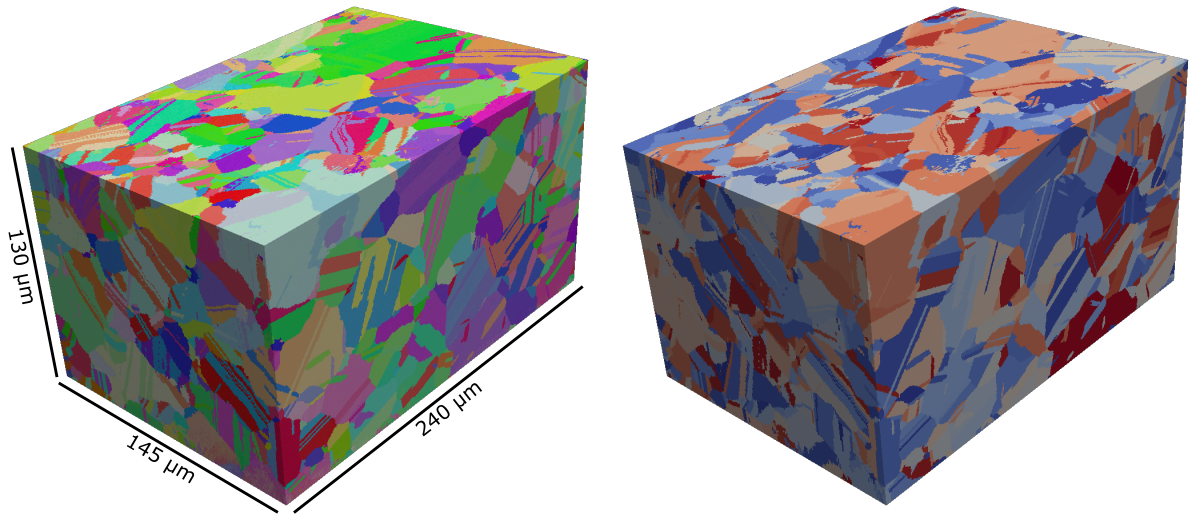

Figure 4.27: The grain scale dataset is rendered using IPF color (left) and random grain ID (right).

volume of 120 µm × 200 µm × 90 µm was collected from 127 ablated slices. Collection of each slice required 53 minutes of instrument time with EBSD accounting for 28 minutes.

Grains were segmented with a 2° tolerance and those smaller than 75 voxels removed by isotropic neighbor dilation. Twin related domains were grouped with a 5° tolerance on both disorientation axis and disorientation angle. Slices were aligned using twin related domain centroids. The aligned dataset was next resegmented with a 5° disorientation tolerance and grains smaller than 75 voxels removed by isotropic neighbor dilation. Finally twin related domains were grouped with a 5° tolerance on both disorientation axis and disorientation angle. The resulting reconstruction contains 3465 grains and 565 twin related domains and is shown in figure 4.30.

4.3.4 Microtensile Dataset

This dataset was collected from a microtensile bar provided by David Eastman (Johns Hopkins University) to provide input for a crystal plasticity simulation [141]. Microtensile bars were roughly machined from a 20 µm thick foil with a femtosecond laser and the

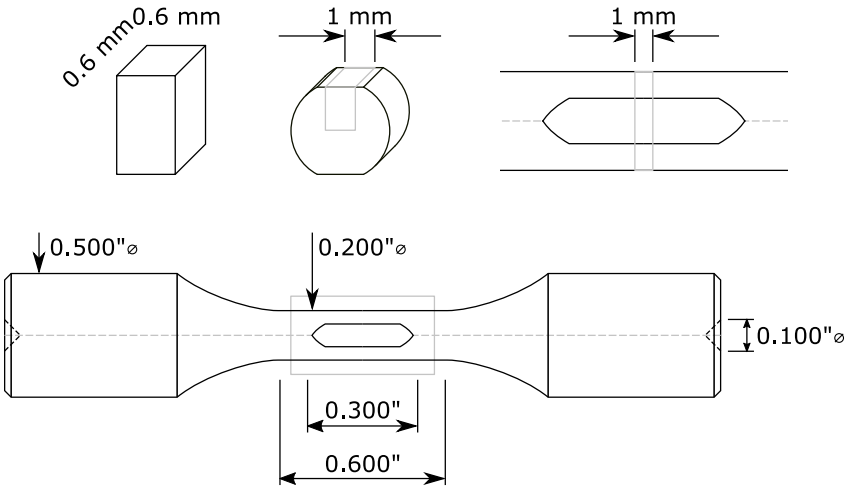

Figure 4.28: A small pedestal (top left) was cut from a disk (top center) cut from the gauge section (top right) of an interrupted fatigue sample (bottom) using wire EDM.

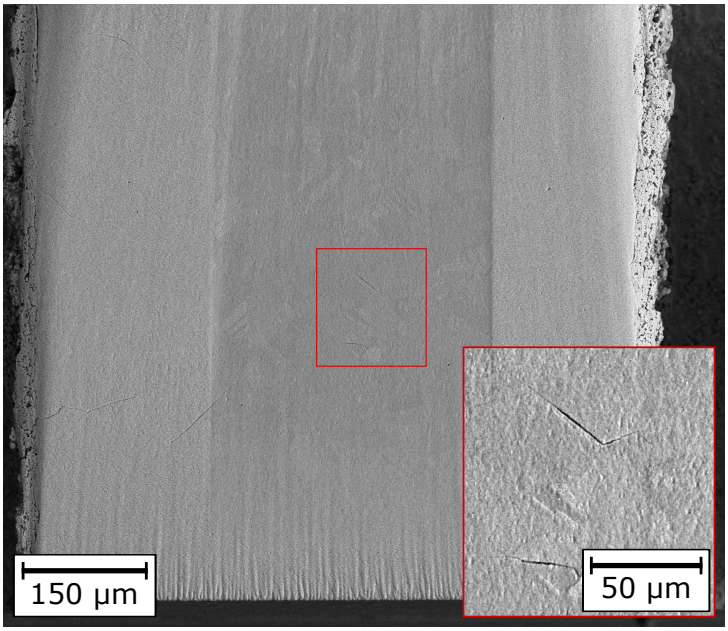

Figure 4.29: A representative exposed surface (slice 20) of the crack dataset is shown with the FIB cleaned region visible in the center. The inset shows detail around the captured cracks.

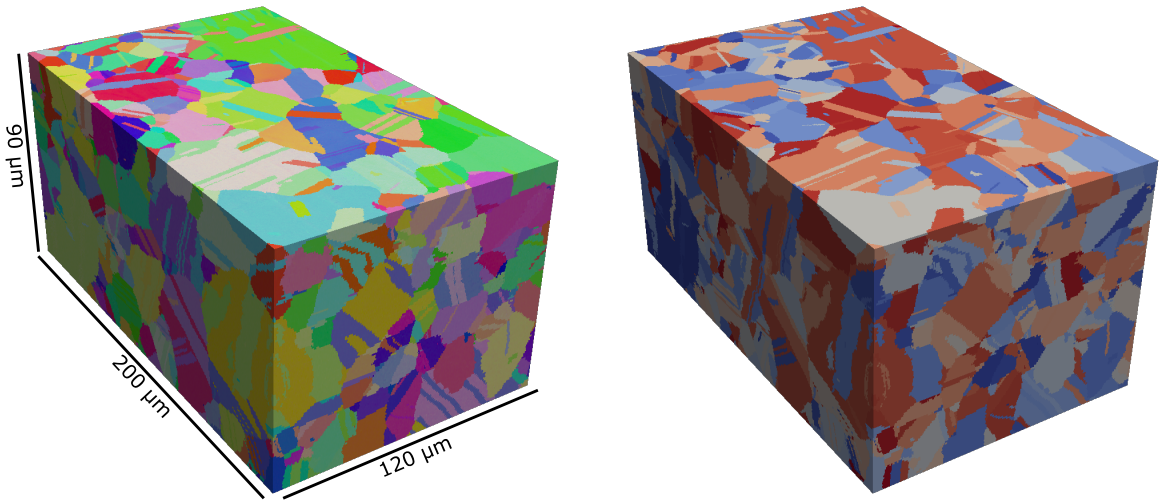

Figure 4.30: The crack dataset is rendered using IPF color (left) and random grain ID (right).

final shape cut using a Ga^+ FIB [140]. The bar was machined parallel to the gauge section to mitigate beveling as shown in figure 4.31 with the laser attenuated to 78 mW and 1 µm thick slices cut. EBSD was collected from the entire exposed surface using a 25 kV electron beam, 8×8 camera binning, and a 250 nm step size. A total volume of 60 µm × 240 µm × 20 µm was collected from 34 ablated slices, fully capturing the 20 µm × 20 µm × 175 µm gauge section. Collection of each slice required 13 minutes of instrument time with 10 minutes of EBSD accounting for the majority.

Good voxels were selected by thresholding confidence index greater than 0.05 and image quality greater than 3000. The sample was identified as the largest contiguous group of voxels and holes in the sample mask filled. Sections aligned by orientation using a 5° tolerance and grains were segmented with a 1° tolerance. Grains smaller than 64 voxels removed by isotropic neighbor dilation. The resulting reconstruction contains 293 grains and is shown in figure 4.33.

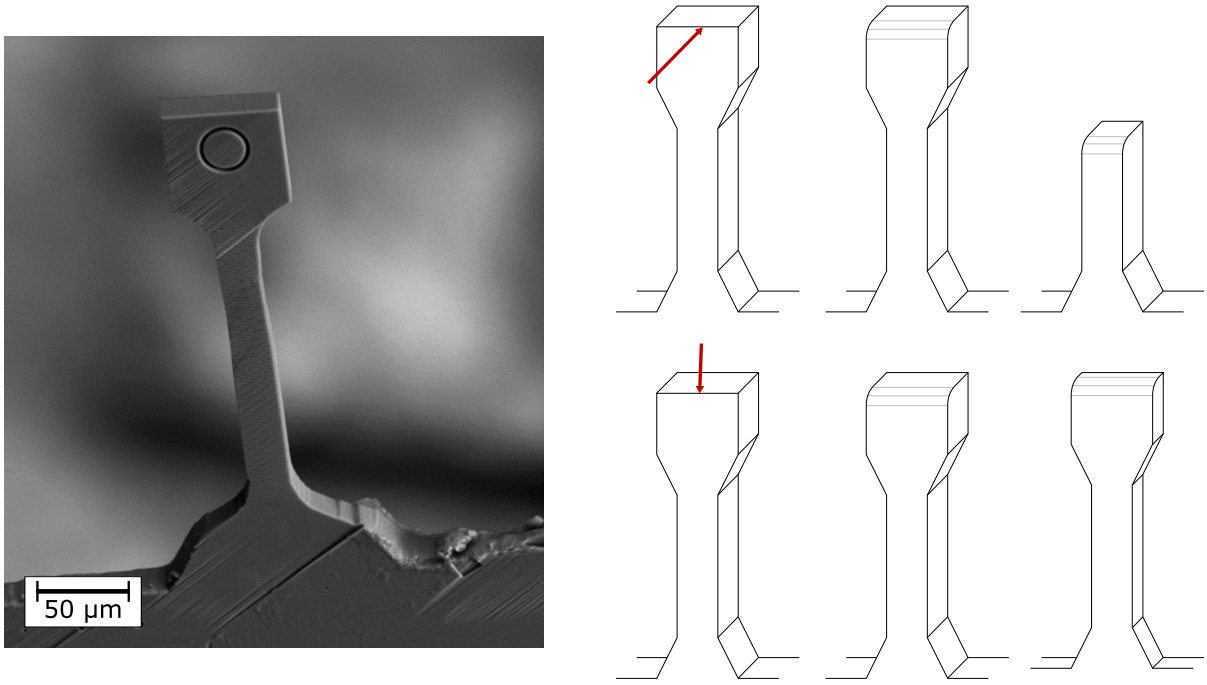

Figure 4.31: A small amount of beveling near the leading edge of the laser machined surface is insignificant for bulk samples, but represents a significant fraction of the small gauge microtensile bar (left) if machined perpendicular to the gauge (top right). Machining parallel to the gauge restricts beveling to the grip (bottom right)..

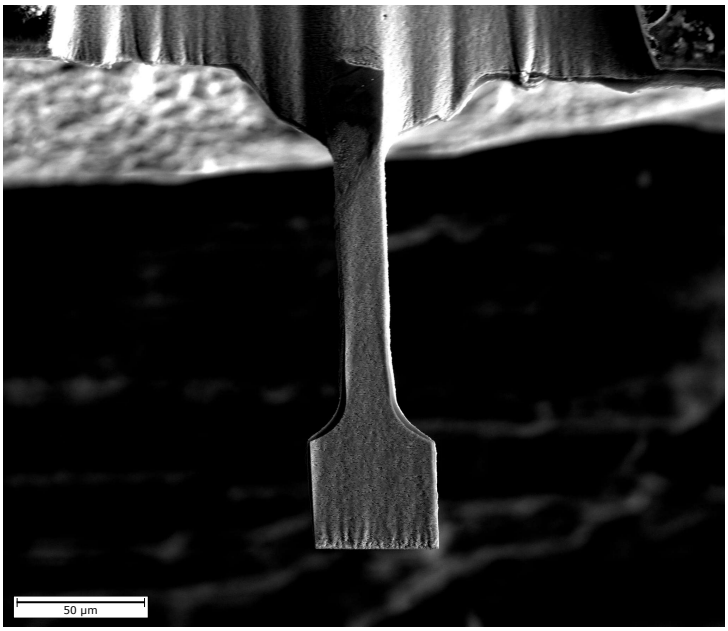

Figure 4.32: A representative exposed surface (slice 14) of the microtensile dataset is shown.

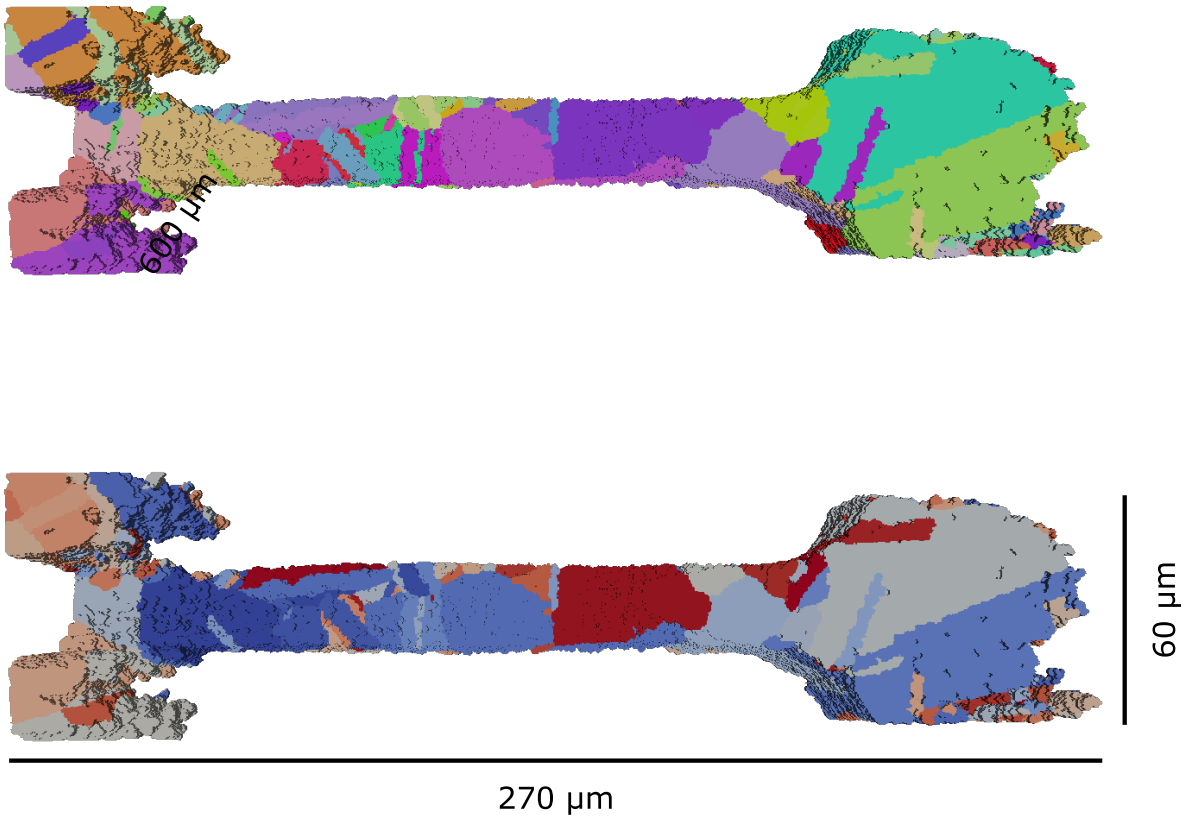

Figure 4.33: The microtensile dataset is rendered using IPF color (top) and random grain ID (bottom).

4.3.5 Nonmetallic Inclusion Dataset

This dataset was collected to investigate the influence of nonmetallic inclusions on local strain fields and the crack initiation process. A double flat fatigue sample provided by General Electric was cut from material intentionally seeded with large alumina seeds before powder consolidation [7]. An inclusion intersecting the surface on a flat was identified and EBSD collected around it. Secondary electron images were collected from the surrounding region for high resolution digital image correlation (DIC) and the sample low cycle fatigued at 400 °C at a frequency of 1 Hz with a peak stress of 965 MPa and an R ratio of -0.5 [142]. Under these loading conditions the fatigue lifetime is fewer than 30000 cycles [142]. Fatigue was interrupted after 1 cycle, 5% of lifetime, 23% of lifetime, and 60% of lifetime. The surface was imaged again during each interruption and the crack path identified. DIC was used to calculate the 2D surface strain field after 1 cycle and 5% of lifetime. The surface crack path, surrounding grain structure, and DIC maps are shown in figure 4.34

A pair of pedestals was cut with 1 centered around the inclusion using wire EDM as shown in figure 4.35. The extra pedestal was used during experiment set up to align the laser beam as closely as possible with the sample surface. The laser was attenuated to 160 mW and 750 nm slices cut with 1500 passes per cut. After each cut the exposed surface was cleaned with a 65 nA Ga^+ FIB with a 30 kV accelerating voltage at a glancing angle of 3°. An example of the resulting exposed surface is shown in figure 4.26. EBSD was collected from a 400 µm × 600 µm area within the cleaned region using a 25 kV electron beam, 8×8 camera binning, and a 550 nm step size. A total volume of 400 µm × 600 µm × 107 µm was collected from 143 ablated slices. Collection of each slice required 27 minutes of instrument time with EBSD accounting for 17 minutes.

Slices were first aligned by maximizing image quality normalized cross correlation. Good voxels were selected by thresholding image quality greater than 7500, grains seg-

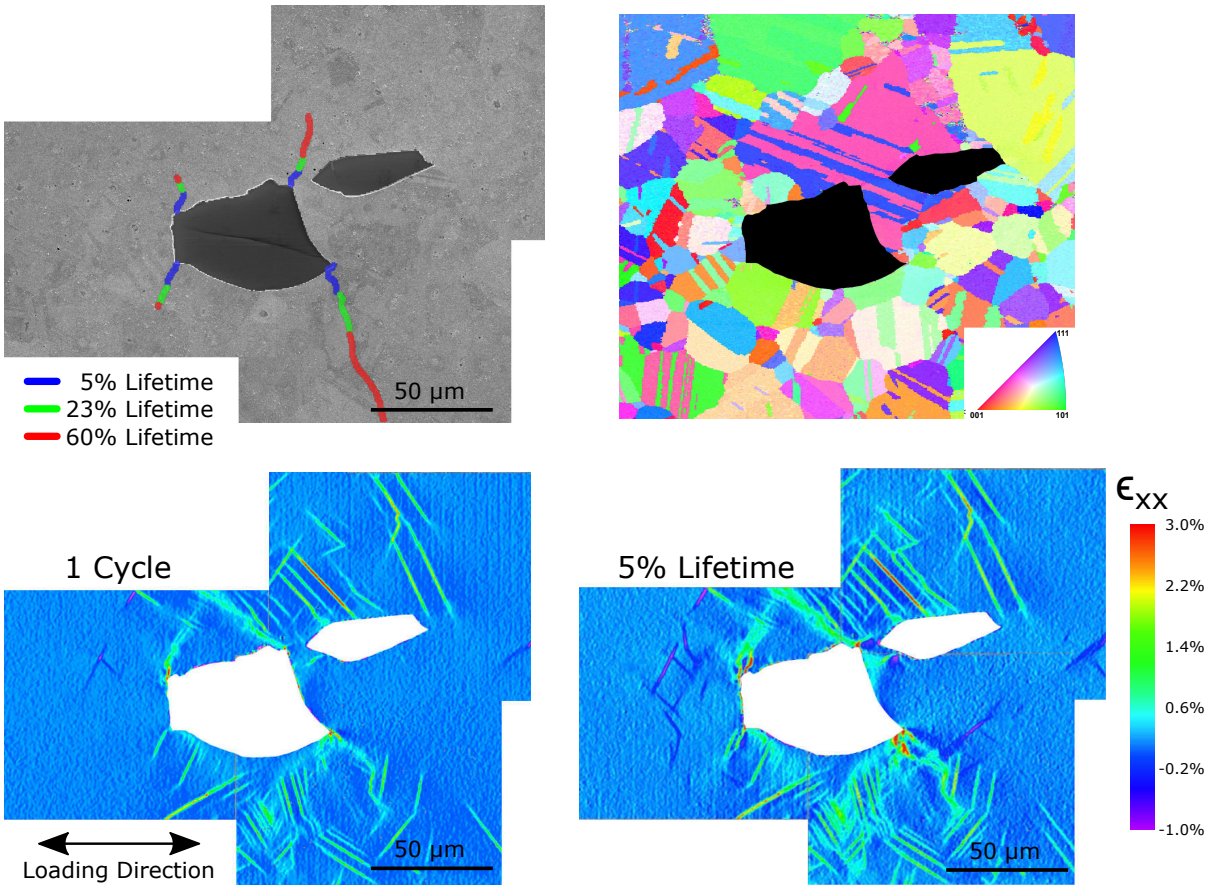

Figure 4.34: The surface beneath which the nonmetallic inclusion was collected is shown before loading with the crack path at several fractions of fatigue life indicated (top left). The grain structure around the crack is IPF colored (top right) and DIC strain maps for the matrix surrounding the inclusion after 1 cycle (bottom left) and 5% of fatigue lifetime (bottom right). Figures reproduced from Stinville et al. [142]. Copyright 2016 by The Minerals, Metals & Materials Society. Used with permission.

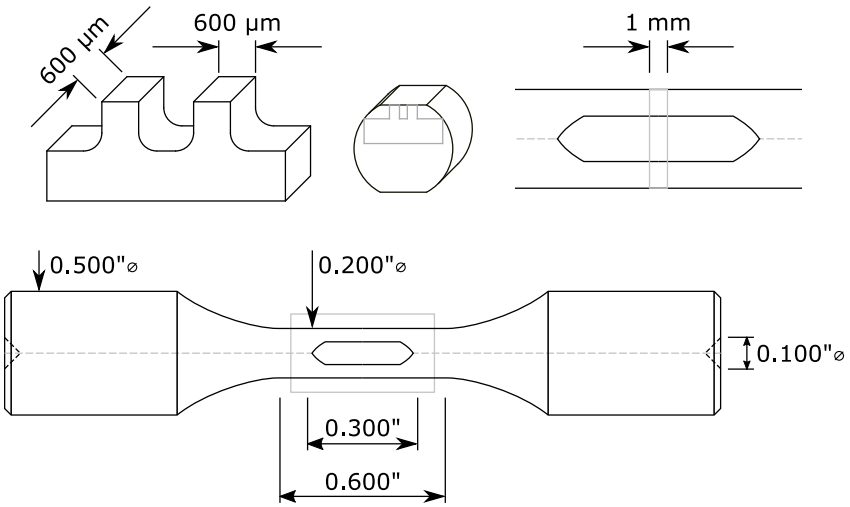

Figure 4.35: A pair of small pedestals (top left) were cut from a disk (top center) cut from the gauge section (top right) of an interrupted fatigue sample (bottom) using wire EDM.

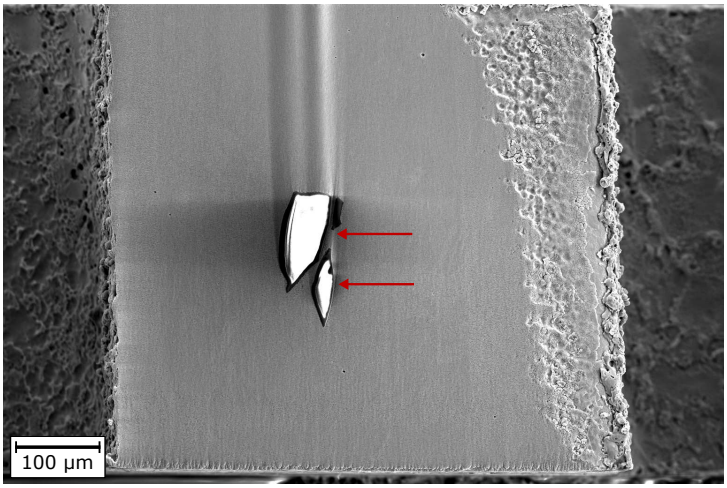

Figure 4.36: A representative exposed surface (slice 25) of the microtensile dataset is shown with arrows indicating the inclusion.

Figure 4.37: The inclusion dataset is rendered using IPF color (left) and random grain ID (center) with 2 non-metallic inclusions shown separately (right).

mented with a 2° tolerance, grains smaller than 27 voxels removed by isotropic neighbor dilation. Twin related domains were grouped with a 5° tolerance on both disorientation axis and disorientation angle and slices aligned using twin related domain centroids. The resulting reconstruction containing 7593 grains and 1781 twin related domains is shown in figure 4.37.

4.3.6 General Observations

Although generating a preliminary dataset reconstruction is trivial with modern software tools, creating a high quality reconstruction is still a significant challenge and required more time than dataset collection for every sample shown. Spending more time to reduce noise or improve data quality was always a good investment. Alignment and segmentation are by far the most difficult tasks. Alignment can be particularly challenging for small datasets where the morphology of a few dominate features dictates shifts computed during registration. Creating sample pedestals small enough to collect data from the entire surface makes alignment significantly easier and recovering the original sample shape provides a simple validation of alignment quality. Orientation gradients and systemic mis-indexing due to pseudo-symmetry are the biggest challenges for segmentation when present. Algorithms to segment orientation gradients [143] and correct pseudo-symmetry

indexing errors [144] exist but are not implemented in 3D.

Chapter 5

Fatigue Crack Initiation

Very high cycle fatigue cracks in the PM disk alloy René 88DT initiate due to strain localization near annealing twin boundaries in large grains that are favorably oriented for slip (possess a high Schmid factor). Accumulation of irreversible, cyclic dislocation slip results in large incompatibility stresses, ultimately nucleating a crack [14]. Surface investigations of interrupted low and very high cycle fatigue tests similarly found that cracks initiate near long twin boundaries in favorably orientated grains with the highest Schmid factor slip system trace parallel to the twin boundary [29]. Twin boundaries have also been observed to play a role in crack initiation in a variety of other FCC material systems including stainless steel and copper [145, 146]. In this chapter new 3D approaches to the characterization of twin boundaries are applied to René 88DT, an improved criterion for strain localization developed, and the frequency of strain localizing microstructural features quantified.

5.1 Twin Boundary Character Measurement

In general, two dimensional planar boundaries, including twin and grain boundaries can be mathematically described by five parameters. Two are needed to define the bound-

ary plane orientation and an additional three are needed to define the disorientation across the boundary [94, 147]. Thus boundaries cannot be fully characterized from a two dimensional cross section, since the sub-surface boundary inclination is generally unknown. The twin scale 3D dataset was used to characterize twin boundary character; this dataset, with a voxel size of $0.1\,\mu m \times 0.1\,\mu m \times 0.5\,\mu m$ represents an appropriate resolution to capture the fine scale annealing twins.

5.1.1 Surface Mesh Generation

Grain boundary character is calculated from 3D datasets using a grain boundary normal and the average orientation of the bounding grains. A surface mesh was generated using a modified version of the multi-material marching cube algorithm [132] to enable measurement of grain boundary plane normals. The algorithm begins by generating edges for each cube face using the multi-material marching squares algorithm [132]. Nodes are inserted at the center of edges connecting two different materials and edges drawn according to the algorithm detailed on page 101 in algorithm 5.1 and depicted in figure 5.1 and figure 5.2. Multi-material marching squares can be efficiently implemented using a lookup table for each of 256 possible configurations (4^4) allowing efficient mesh generation. Multi-material marching cubes has 16777216 possible configurations (8^8) making a lookup table impractically large. An algorithm is used to compute the triangulation of a given material cube is given in algorithm 5.2 with cubes falling into one of 3 categories described in figure 5.3. Since the triangles generated for each cube are independent, mesh generation can be parallelized enabling rapid generation.

In the ambiguous marching square case of 2 materials on opposing diagonals (configuration 0b0101 or 0b1010) the 'higher priority' (lower grain number in this work) pair are connected. This ambiguity can create collapsed channels (figure 5.4) in the originally published algorithm. These channels can cause issues for subsequent mesh operations and an additional clean up step was used to remove them in this work. During mesh

Algorithm 5.1: An algorithm to generate an edge mesh for a square with material labels at each corner is given [132].

Data: Material label at each square corner
Result: Square edge mesh
map labels to [0,3]
if *1 or 2 material labels* **then**
  mesh square as shown in figure 5.1
else
  3 material labels
if *duplicate material adjacent* **then**
  mesh square as shown in center of figure 5.2
else
  mesh square as shown in left of figure 5.2
end
else
  4 material labels
end
mesh square as shown in right of figure 5.2 **return** *mesh nodes, edges*

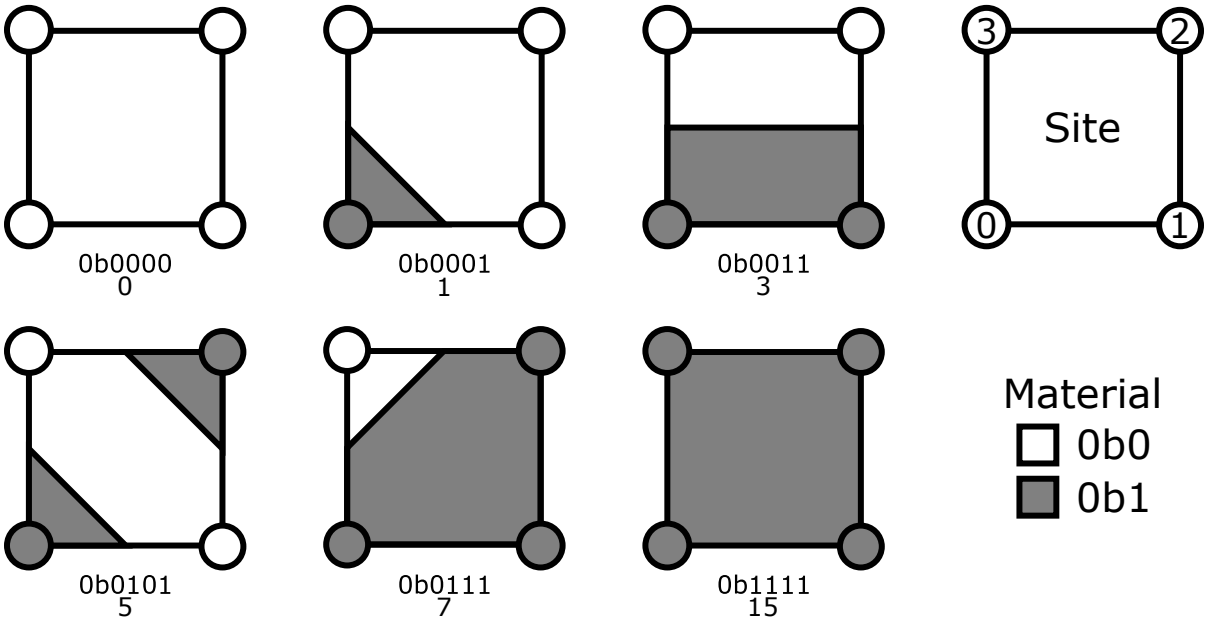

Figure 5.1: The six possible types of marching square edges are shown (the remaining 10 permutations are rotations of depicted configurations).

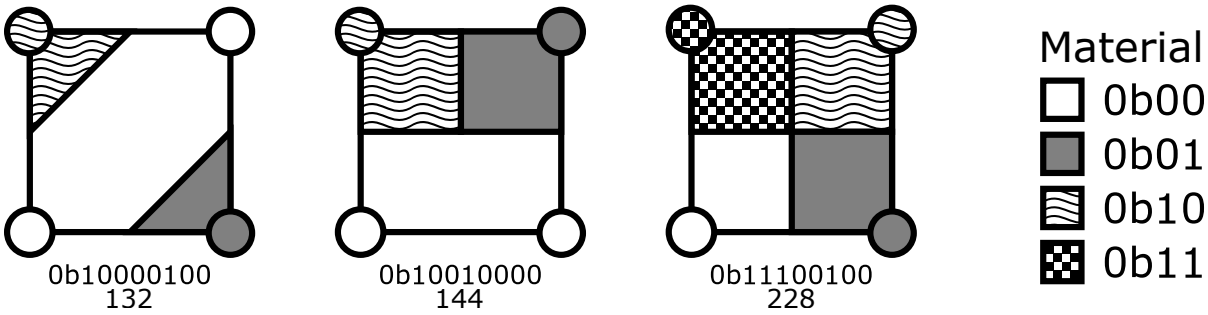

Figure 5.2: The 3 possible types of multiple material marching square edges are shown. The remaining 253 permutations are rotations and relabelings of the configurations shown here or in figure 5.1. Figure based on Wu and Sullivan [132].

Algorithm 5.2: An algorithm to generate a surface mesh for a cube with material labels at each corner is given [132].

Data: Material label at each cube corner
Result: Cube surface mesh
map labels to [0,7]
foreach *cube face* **do**
  face nodes, face edges←`multiMaterialMarchingSquares(`*face*`)`
  edges←{edges, face edges}
  nodes←{nodes, face nodes}
end
if *2 faces have center nodes* **then**
  edges←{edges, edge connecting face center nodes}
else if *3 or more faces have center nodes* **then**
  nodes←nodes, cube center node
  foreach *node* **do**
    if *not cube center node* **then**
      edges←{edges, (node, center node)}
    end
  end
end
foreach *pair of adjacent materials* **do**
  interface triangles←triangulate loop (recursive shortest partitioning diagonal)
  cube triangles←{cube triangles, interface triangles}
end
return *cube nodes, triangles*

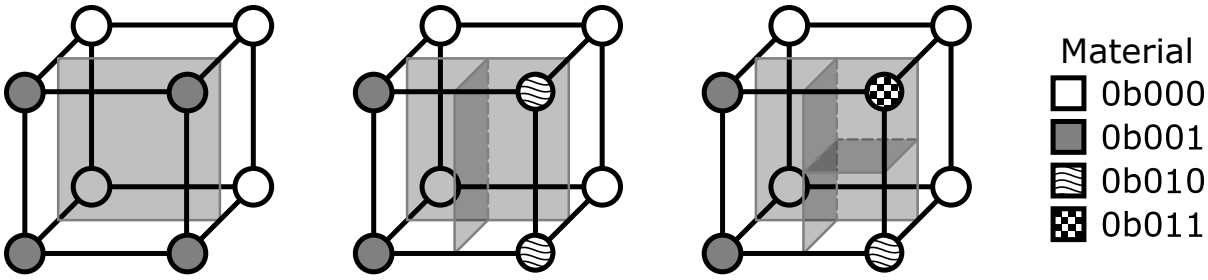

Figure 5.3: The 3 families of multi-material marching cube configurations. Cubes that have no faces with center nodes (left) are meshed by triangulating loops of edges at the interface 2 materials. Cubes that have 2 faces with center nodes (center) have an edge connecting the 2 face centers added and are triangulated as in the first case. Cubes that have 3 or more faces with center nodes (right) have a node added to the center of the cube and a triangle created from each edge with the center node. Figure based on Wu and Sullivan [132].

generation all cases of ambiguous marching squares are noted. After meshing, pairs of cubes sharing an ambiguous face are checked and collapsed channels deleted.

5.1.2 Surface Mesh Smoothing

Surface meshes generated by marching cubes typically require smoothing to remove aliasing artifacts [148]. Since grain boundary surface meshes are non-manifold (contain triple lines and quadruple points) the normal smoothing algorithm is slightly modified by fixing quadrupedal point nodes and restricting movement of nodes on triple lines to one of the two line segments which they define [132]. Laplacian smoothing causes volume shrinkage as shown in figure 5.5 that can be prevented by Laplacian smoothing with an alternating positive and negative parameter to create a low pass filter (algorithm 5.4) [149].

5.1.3 Volume Mesh Generation and Surface Mesh Decimation

Surface meshes enable calculation of boundary character, but most mechanical calculations require a hexahedral or tetrahedral volume mesh as input. Although the voxel grid is already a hexahedral mesh and can be converted to a tetrahedral mesh by splitting each cube into 5 or 6 tetrahedrons, the resulting meshes generally have significantly more

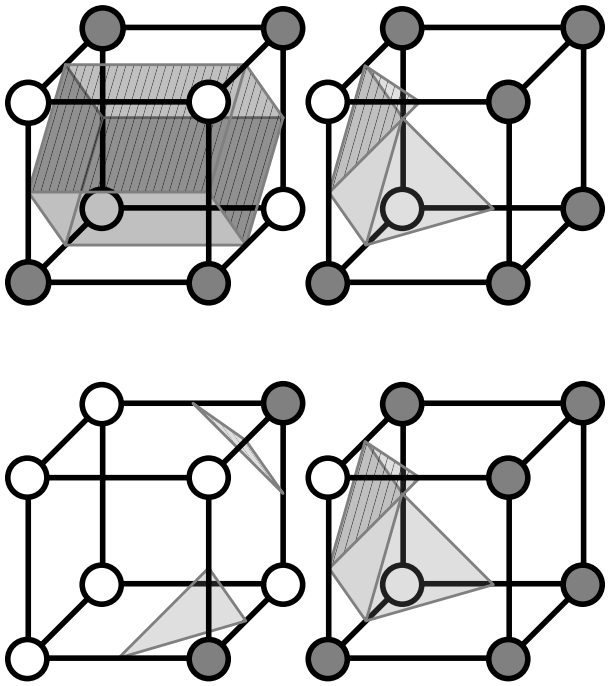

Figure 5.4: The multi-material marching cube algorithm as originally published [132] can create collapsed, zero volume channels (top) that cause issues for subsequent mesh operations. The pair of neighbor cubes shown at top has a collapsed channel connected the higher priority white material. Facets on the cube faces cannot be removed in all cases because holes would be generated in some cases (bottom).

Algorithm 5.3: An algorithm for surface mesh Laplacian smoothing is given [148].

Data: Surface mesh nodes coordinates x, first nearest neighbors, and smoothing parameter λ
Result: Smoothed node coordinates
foreach *node* n **do**
  $\delta_n \leftarrow (0, 0)$
  foreach *neighbor* m **do**
    $\delta_n \leftarrow \delta_n + (x_m - x_n)$
  end
  $\delta_n \leftarrow \frac{\delta_n}{\mathsf{count}(neighbors)}$
end
foreach *node* n **do**
  $x_n \leftarrow x_n + delta_n * \lambda$
end
return x

Algorithm 5.4: An algorithm for Taubin smoothing is given [149].

Data: Surface mesh nodes coordinates x, first nearest neighbors, and smoothing parameters λ and μ ($\mu = -(\lambda + \delta)$))

Result: Smoothed node coordinates

$x \leftarrow$`laplacianSmooth(`x`,`λ`)`

$x \leftarrow$`laplacianSmooth(`x`,`μ`)`

return x

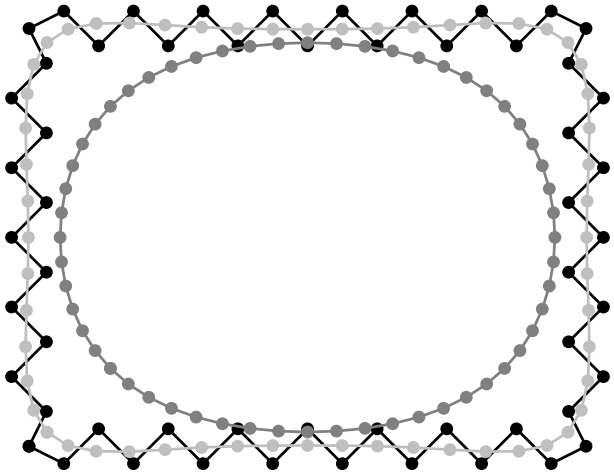

Figure 5.5: A mesh with short range roughness (black) smoothed by 100 iterations of Laplacian smoothing with $\lambda = 0.33$ (dark gray) shows significant volume loss. The same mesh smoothed with 100 iterations of Taubin smoothing with $\lambda = 0.33$ and $\mu = -0.331$ (light gray) retains volume and long wavelength features.

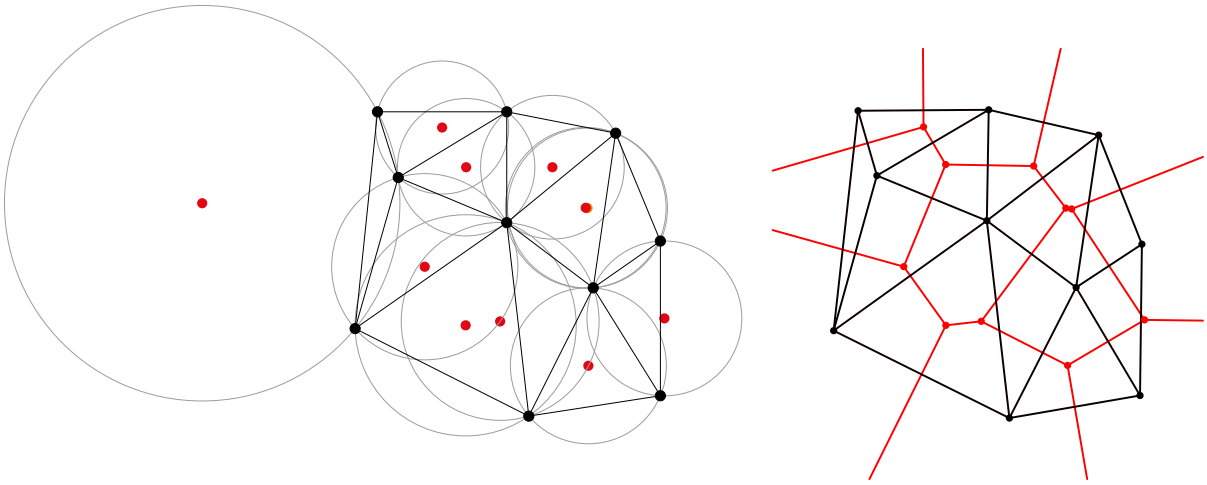

Figure 5.6: No point in a Delaunay triangulation lies within the circumcircle (gray with red centers) of any triangle (left). The Voronoi diagram (red) of a point set is dual to the Delaunay triangulation and can be generated by connecting circumcenters of neighboring simplexes (right). Figures reproduced from Wikimedia Commons [153, 154].

elements than is computationally feasible. The Delaunay triangulation of a 2D point set is the triangulation for which no point lies within the circumcircle of any triangle and is dual to the Voronoi tessellation of the point set as shown in figure 5.6 [150]. Delaunay triangulations have several desirable properties for finite element methods including maximizing the minimum angle of all triangles and algorithms to bound triangle quality by insertion of additional points [150–152].

Constrained Delaunay triangulations are triangulations that are as close as possible to a Delaunay triangulation while containing specified lower dimensional simplexes [151] and may be converted to Delaunay triangulations containing the specified edges by inserting additional points as shown in figure 5.7. Conforming Delaunay triangulations are generalizable to arbitrary dimension [152]. Delaunay tetrahedralizations (Delaunay triangulations in 3D) are the tetrahedralization of a point set such that no point lies within the circumsphere of tetrahedron. The Delaunay tetrahedralization conforming to a surface mesh provides a high quality volume mesh for finite element calculations [155]. The open source library TetGen was used in this work to generate and refine volume meshes from surface meshes [156].

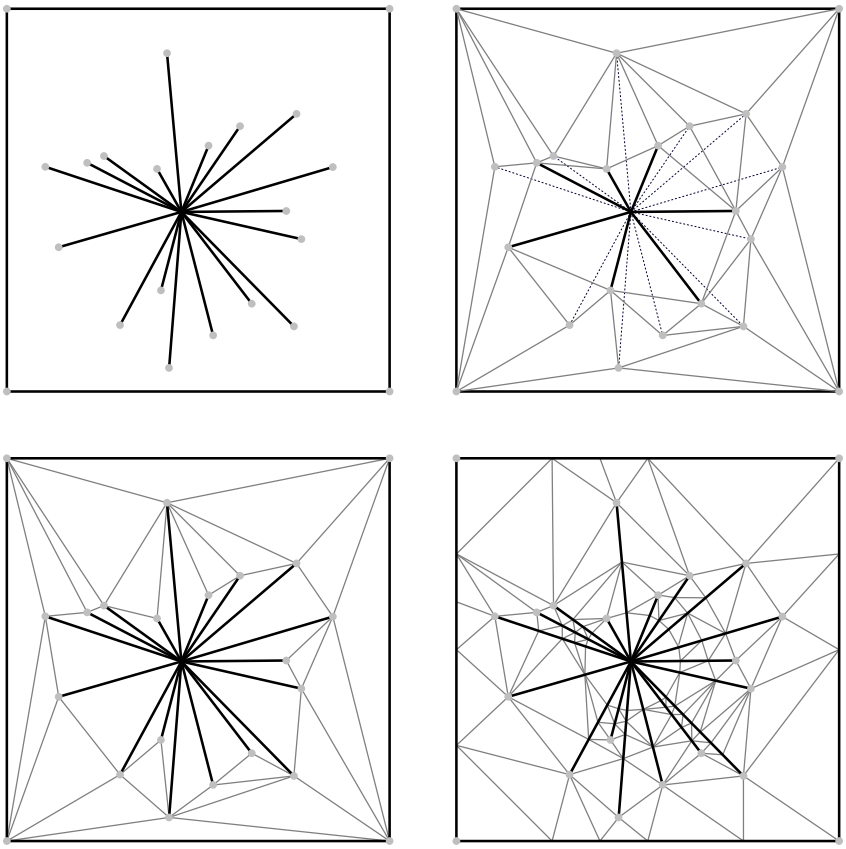

Figure 5.7: A set of points to be triangulated (light gray) and desired edges (black) are shown (top left). The Delaunay triangulation of the point set may not contain the edges (top right). The constrained Delaunay triangulation (bottom left) is as near to the Delaunay triangulation as possible while containing all imposed edges, but may not satisfy the criterion for Delaunay triangulation. Inserting Steiner points or adding points by splitting edges enables construction of a conforming Delaunay triangulation (bottom right). Figures adapted from Shewchuk [152].

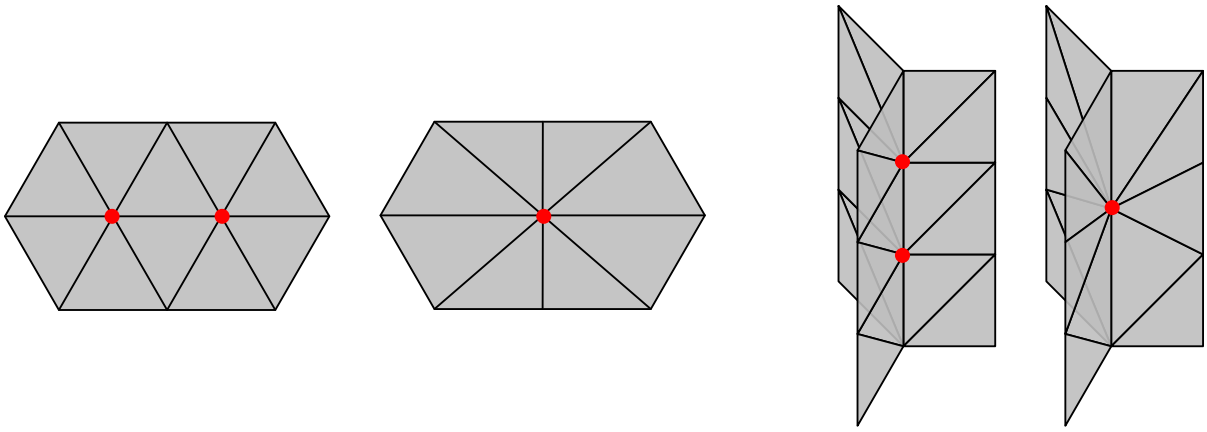

Figure 5.8: Collapsing 2 adjacent nodes on a grain boundary removes 2 triangles from the surface mesh (left). Collapsing 2 adjacent nodes on a triple line removes 3 or 4 triangles (depending on the number of adjacent materials) from the surface mesh (right). All other types of collapse are forbidden to preserve topology.

Generating volume meshes directly from meshed and smoothed datasets generally creates meshes with too many tetrahedrons to be computationally feasible. Quadric error metric based edge collapsing was used to simplify surface meshes [157]. The algorithm to compute error quadrics is given in algorithm 5.5. The lowest error edge is iteratively collapsed as shown in figure 5.8. To preserve topology, mesh nodes are only allowed to combine if they lie on the same grain boundary or triple line and quadruple points are fixed.

Edge collapses may cause triangles to pass through each other, changing grain neighborhoods or causing triangle–triangle intersections. To prevent these issues a Delaunay tetrahedralization is created from the surface mesh and inversion of surrounding tetrahedrons checked for before each edge collapse as described in algorithm 5.6. Collapsing edges may create 'skinny' triangles with a low minimum angle. Volume meshes generated from surface meshes containing skinny triangles can require significant refinement to create tetrahedrons suitable for numerical calculations, offsetting the reduction from decimation. To prevent the creation of skinny triangles, the quality, q,

$$q = \frac{4a\sqrt{3}}{l_1^2 + l_2^2 + l_3^2} \tag{5.1}$$

Algorithm 5.5: An algorithm to compute surface mesh error Quadrics for each node pair [157].

Data: Surface mesh
Result: List of optimum collapse position and associated cost for each mesh edge
foreach *triangle in mesh* **do**
  compute plane $ax + by + cz + d = 0$ defined by triangle
  $K_p \leftarrow \begin{bmatrix} a^2 & ab & ac & ad \\ ab & b^2 & bc & bd \\ ac & bc & c^2 & cd \\ ad & bd & cd & d^2 \end{bmatrix}$
end
foreach *node in mesh* **do**
  $\bar{K} \leftarrow [0]_{4x4}$
  foreach *triangle containing node* **do**
    $\bar{K} \leftarrow \bar{K} + K_p$
  end
  $Q \leftarrow \begin{bmatrix} \bar{k}_{11} & \bar{k}_{12} & \bar{k}_{13} & \bar{k}_{14} \\ \bar{k}_{21} & \bar{k}_{22} & \bar{k}_{23} & \bar{k}_{24} \\ \bar{k}_{31} & \bar{k}_{32} & \bar{k}_{33} & \bar{k}_{34} \\ 0 & 0 & 0 & 1 \end{bmatrix}$
  foreach *neighboring node* **do**
    $\bar{Q} \leftarrow Q + Q_{neighbor}$
    if $\bar{Q}$ *is singular* **then**
      $\bar{v} \leftarrow \{\frac{node+neighbor}{2}, 1\}$
    else
      $\bar{v}_i \leftarrow \bar{Q}_{i4}^{-1}$
    end
    $cost \leftarrow \bar{v}^T \bar{Q} \bar{v}$
    $edges \leftarrow \{edges, edge(node, neighbor, \bar{v}, cost)\}$
  end
end
return *edges*

of each triangle is computed, where a is the triangle area and h_i are the side lengths of the triangle is computed [158]. Equilateral triangles have a quality of 1 and those with a quality greater than 0.6 are considered suitably equiaxed. Skinny triangle formation is optionally prevented by disallowing any edge collapse that creates triangles with a quality below 0.6 (unless the collapse increases the quality of a triangle already below 0.6). The result of generating a volume mesh from an as smoothed and decimated surface mesh is shown in figure 5.9 with the full volume mesh generation procedure shown in figure 5.10.

Algorithm 5.6: An algorithm to simplify a surface mesh (modified from Garland [157]).

```
Data: Surface mesh to decimate
while triangle count > target do
    tetrahedrons←delaunayTetrahedralizaion(surface mesh)
    edges←errorQuadrics(surface mesh) (algorithm 5.5)
    while edges exist do
        inversion←false
        edge←minimum cost edge
        foreach tetrahedron touching edge do
            if volume after edge collapse < 0 then
                inversion←true
            end
        end
        if not inversion then
            collapse edge
            foreach triangle containing new node do
                update K_p
            end
            foreach node in a triangle containing new node do
                update Q
            end
            foreach edge with a node in a triangle containing new node do
                update v̄ and cost
            end
        end
    end
end
```

Volume meshes are easily converted to input for mechanical simulations. The non-metallic inclusion dataset was segmented into matrix and inclusion as a simple test case

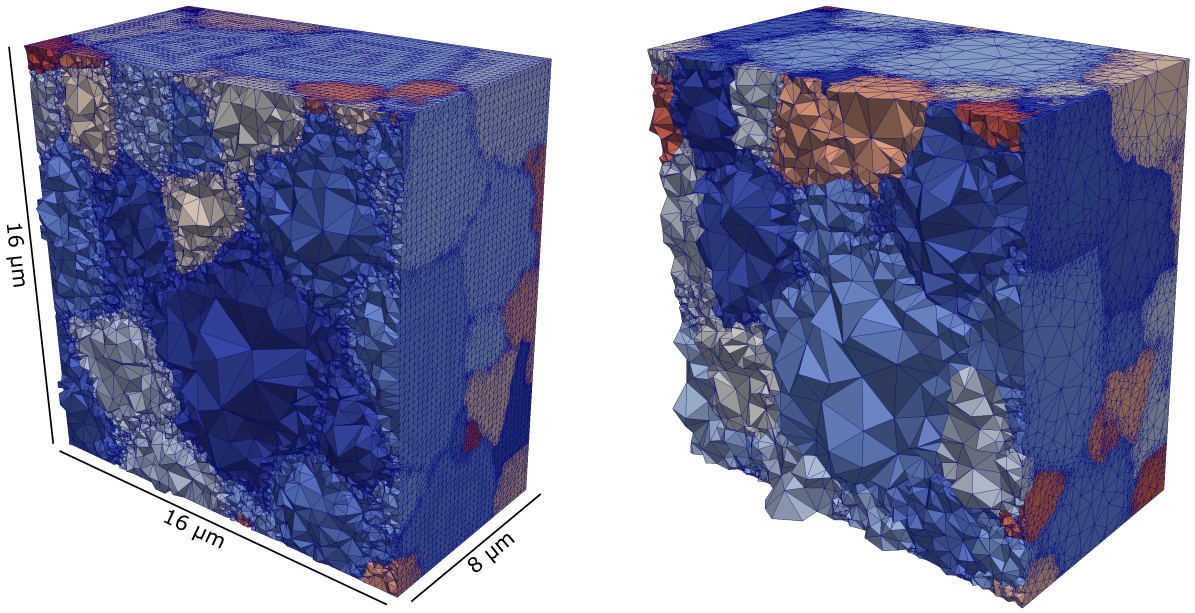

Figure 5.9: Creating a volume mesh from a surface mesh generated by multi-material marching cubes results in a tetrahedral mesh containing too many elements (left). Decimating the surface mesh before volume meshing significantly reduces element count if skinny triangles in the surface mesh are avoided (right). The volume mesh is colored by unique grain ID and was generated from FIB serial sectioned dataset of IN100, courtesy of Michael Uchic [159].

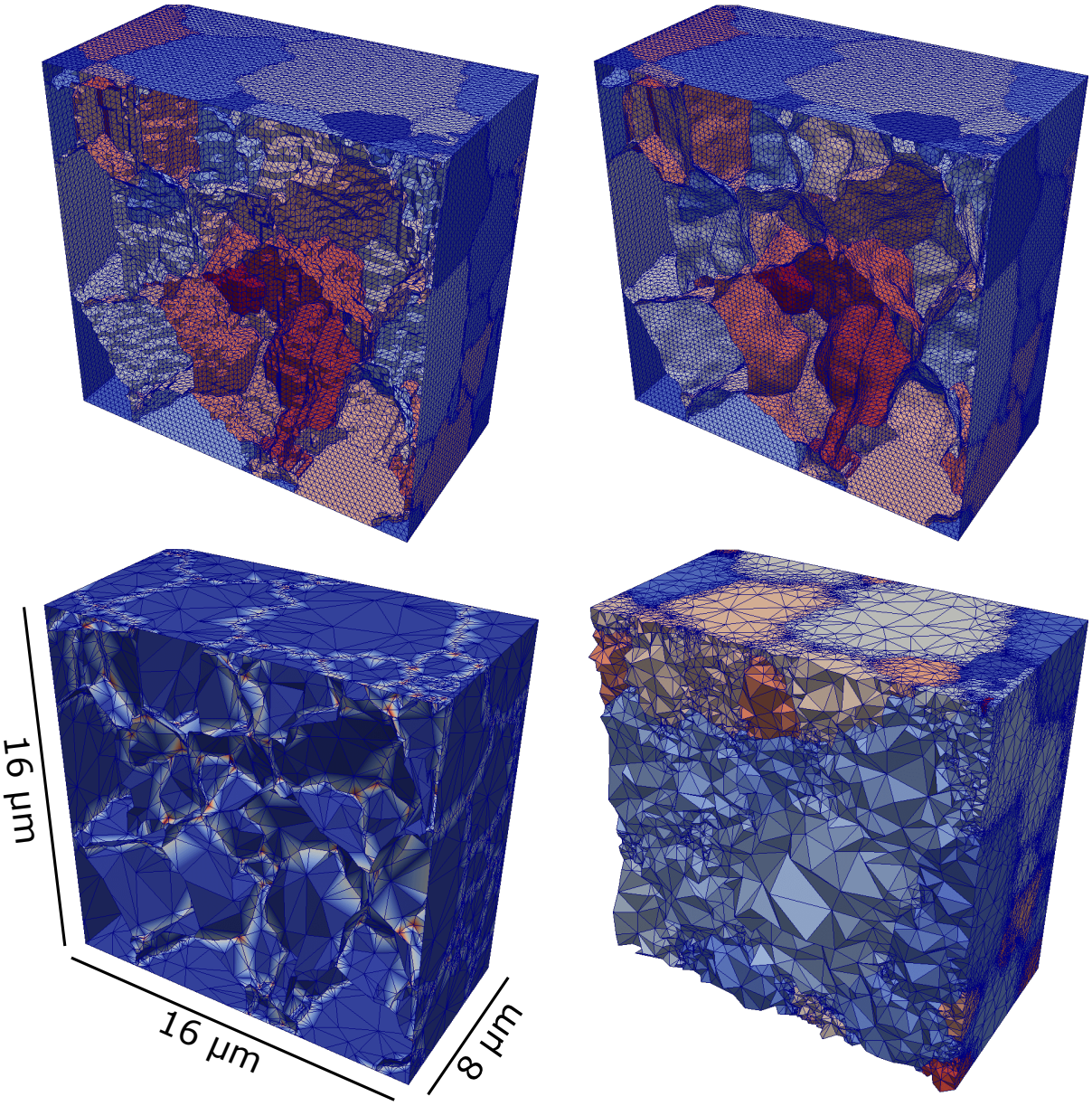

Figure 5.10: The process of generating surface and volume meshes from a segmented dataset is shown. Grain boundaries are meshed using multi-material marching cubes (top left) and smoothed with Laplacian or Taubin smoothing (top right). The surface mesh is decimated without introducing skinny triangles or self intersections (bottom left) and the Delaunay tetrahedralization calculated and refined (bottom right). The surface mesh is colored by unique grain boundary ID in the top row. The decimated surface mesh is colored by node type with grain boundaries in dark blue, triple lines in white, and quadruple points in red. The volume mesh is colored by unique grain ID.

and a volume mesh generated using the procedure described. The mesh was imported into the ABAQUS software package and uniaxial straining in the elastic regime simulated using the polycrystalline elastic properties of nickel for the matrix (E = 176GPa and ν = 0.3) and the polycrystalline elastic properties of alumina for the inclusion (E = 300GPa and ν = 0.3). The simulation was run with interface nodes tied and free, (analogous to a strongly and weakly bonded inclusion respectively) and with loadings of 965 MPa and −482.5 MPa (corresponding to the maximum and minimum applied stresses). The in-plane strain field for the weakly bonded case shows good agreement with the experimental strain field measured by DIC, as shown in figure 5.12. Good qualitative agreement between high elastic stresses and strain localization for the case of a hard isotropic inclusion in an isotropic matrix suggests that non-metallic inclusions do not bear load during tensile phases of fatigue and demonstrates the utility of even simple simulations.

Although considerably more computationally-expensive (due to the larger number of mesh elements), this type of simulation for polycrystalline volumes may provide insights on the character of strain localizing microstructures. An elastically loaded polycrystal without an inclusion is shown in figure 5.13. Volume meshes can be generated for arbitrarily complex microstructures including the typically challenging thin twins of René 88DT as shown in figure 5.14.

5.1.4 Twin Boundary Coherence Measurement

The twin scale 3D dataset was used to characterize twin boundary character since the higher resolution used best captures boundaries from thin annealing twins. Following reconstruction, a grain boundary surface mesh was generated using the modified multi-material marching cube algorithm. The grain surface mesh was smoothed with 100 iterations of Laplacian smoothing with a $\lambda = 0.25$. The resulting surface mesh closely follows grain boundaries in the voxelized dataset with minimal artificial roughness and

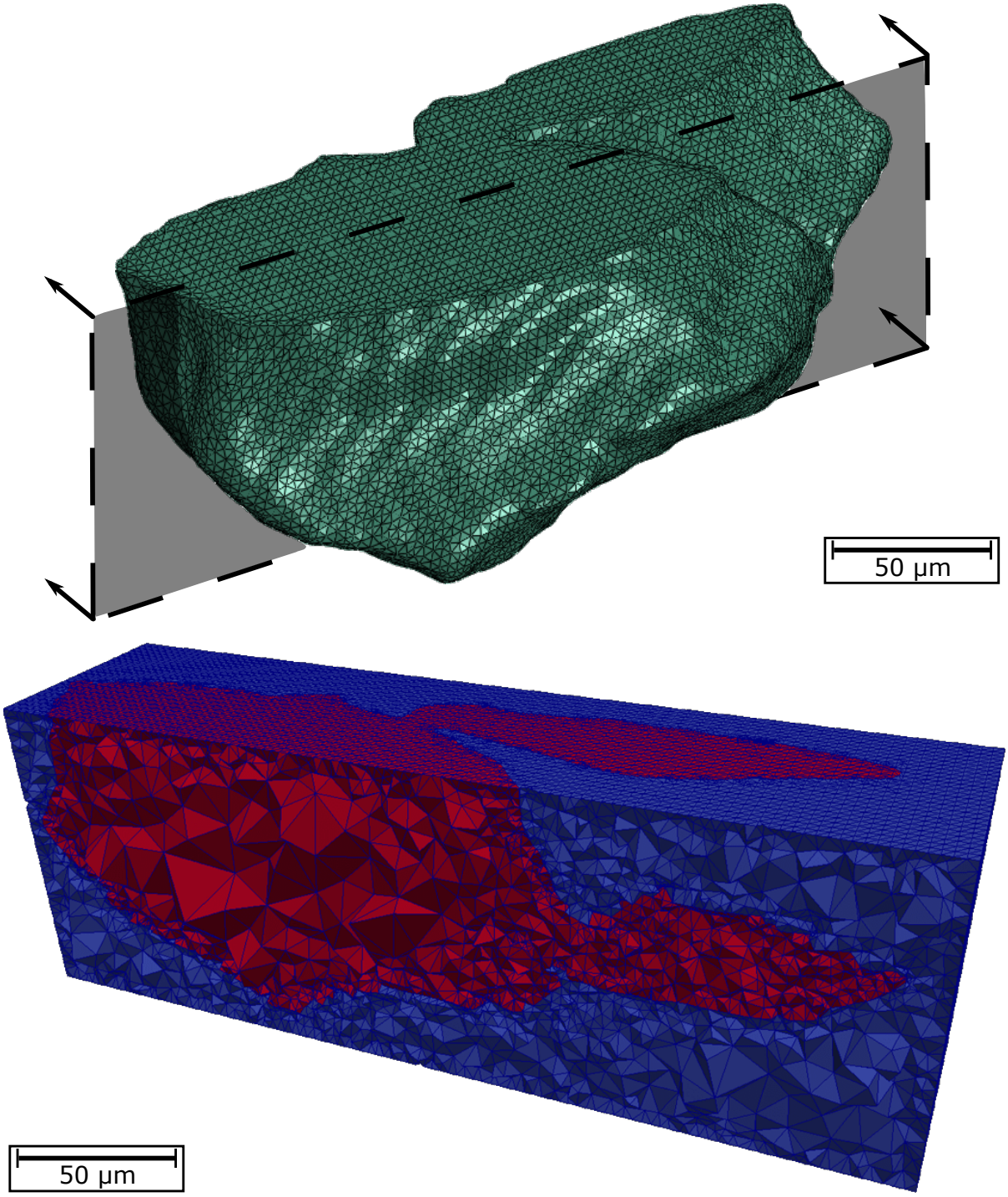

Figure 5.11: The volume mesh of the inclusion is shown with no decimation (top). The inclusion was meshed in a padded box for elastic simulations but is shown meshed in a smaller box (bottom) to show more detail with inclusion elements in red and matrix elements in blue.

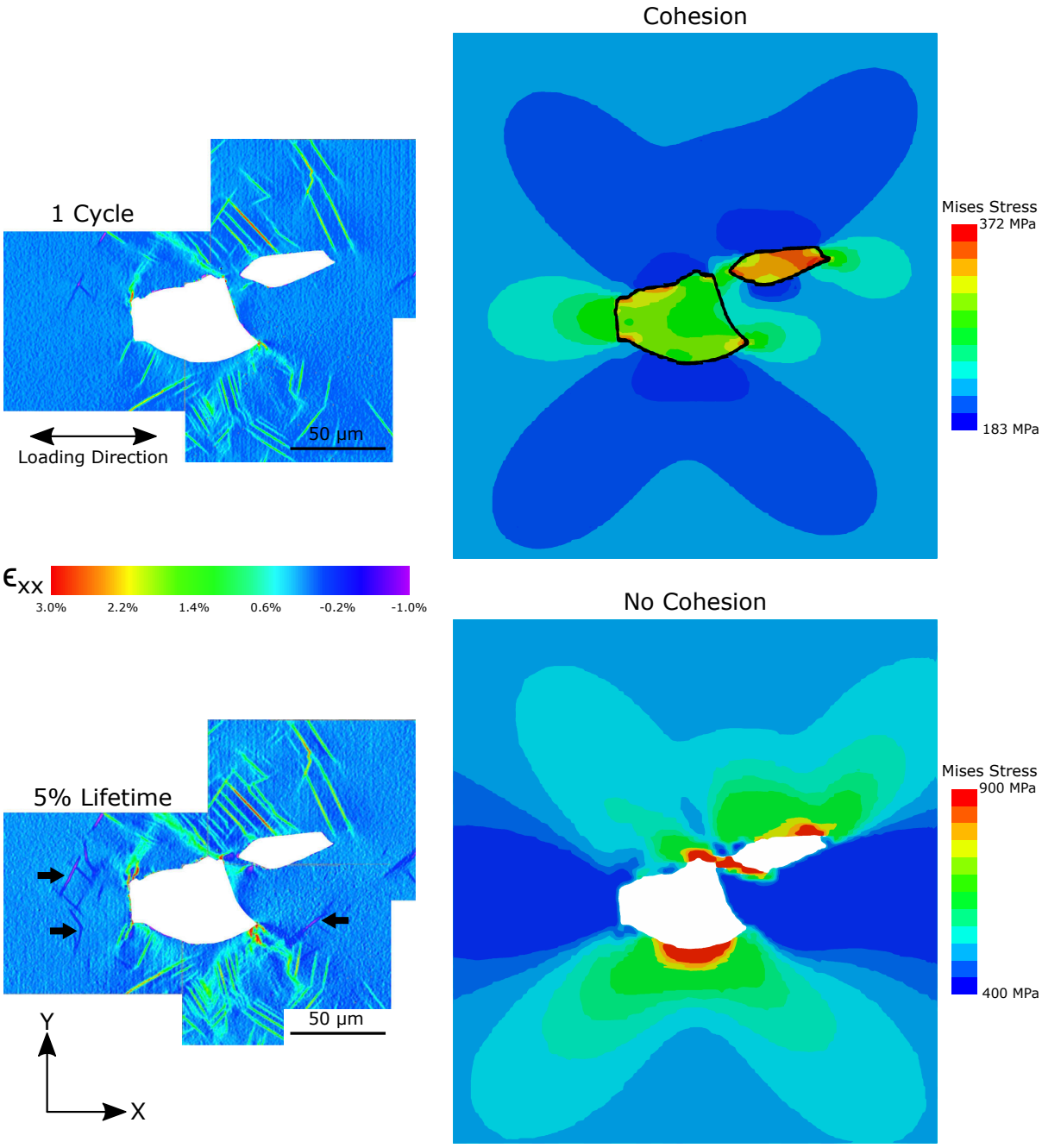

Figure 5.12: The DIC strain map of the inclusion dataset is colored by strain (left) and the surface of an ABAQUS elastic simulation of the 3D inclusion is colored by stress (right) [160]. The weak interface simulation (bottom) has must better agreement with the experimental strain field than the strong interface simulation (top). Figures reproduced from Stinville et al. [142]. Copyright 2016 by The Minerals, Metals & Materials Society. Used with permission.

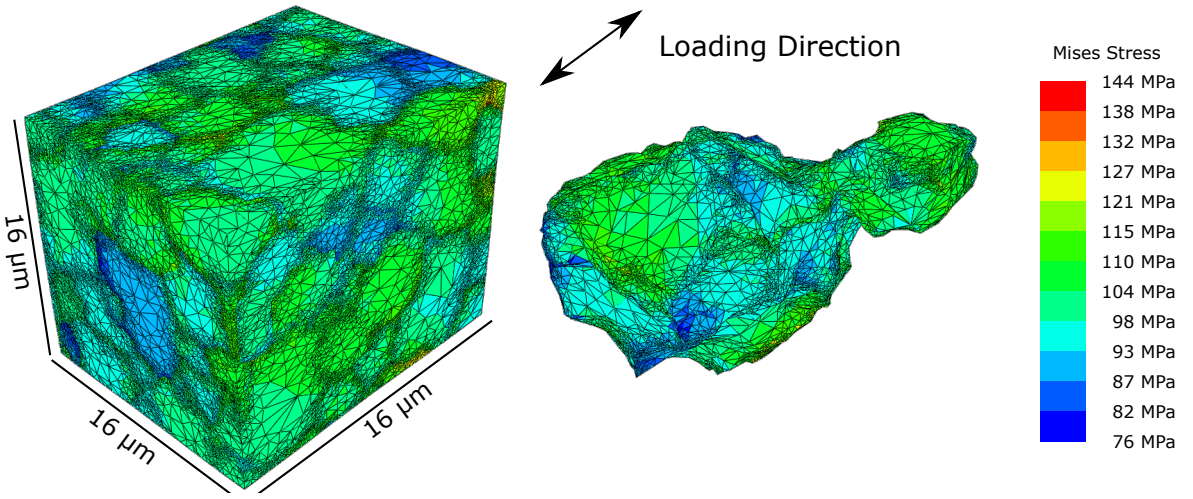

Figure 5.13: 100 MPa uniaxial loading of a perfectly elastic polycrystal using a real 3D microstructure is simulated with the ABAQUS software package and colored by von Mises stress (left) with an internal grain shown (right) [160]. Displacements are exaggerated. The volume mesh was generated from FIB serial sectioned dataset of IN100 courtesy of Michael Uchic [159].

some volume loss for small grains as seen in figure 5.15. The disorientation across each triangle was computed using the average orientations of the two bounding grains.

Triangles with a disorientation angle within 5° of 60° and a disorientation axis within 5° of a {111} normal are defined as twin boundaries, as shown in figure 5.16. A 5° tolerance was selected because the area fraction of twin boundaries exhibits a plateau as shown in figure 5.17 with twin boundaries accounting for 70% of boundary area in the smoothed mesh.

FCC twin boundaries are coherent if the disorientation axis is parallel with the boundary normal. Coherence can be visualized qualitatively using IPF coloring with the triangle normal used as the reference direction as shown in figure 5.18. The incoherence angle can be calculated quantitatively by measuring the angle between the triangle normal and the nearest ⟨111⟩ direction as shown in figure 5.19. The incoherence angle is measured with respect to both bounding orientations and averaged to account for deviations from a perfect twin disorientation.

Computing the incoherence angle for each triangle of the surface mesh shows most

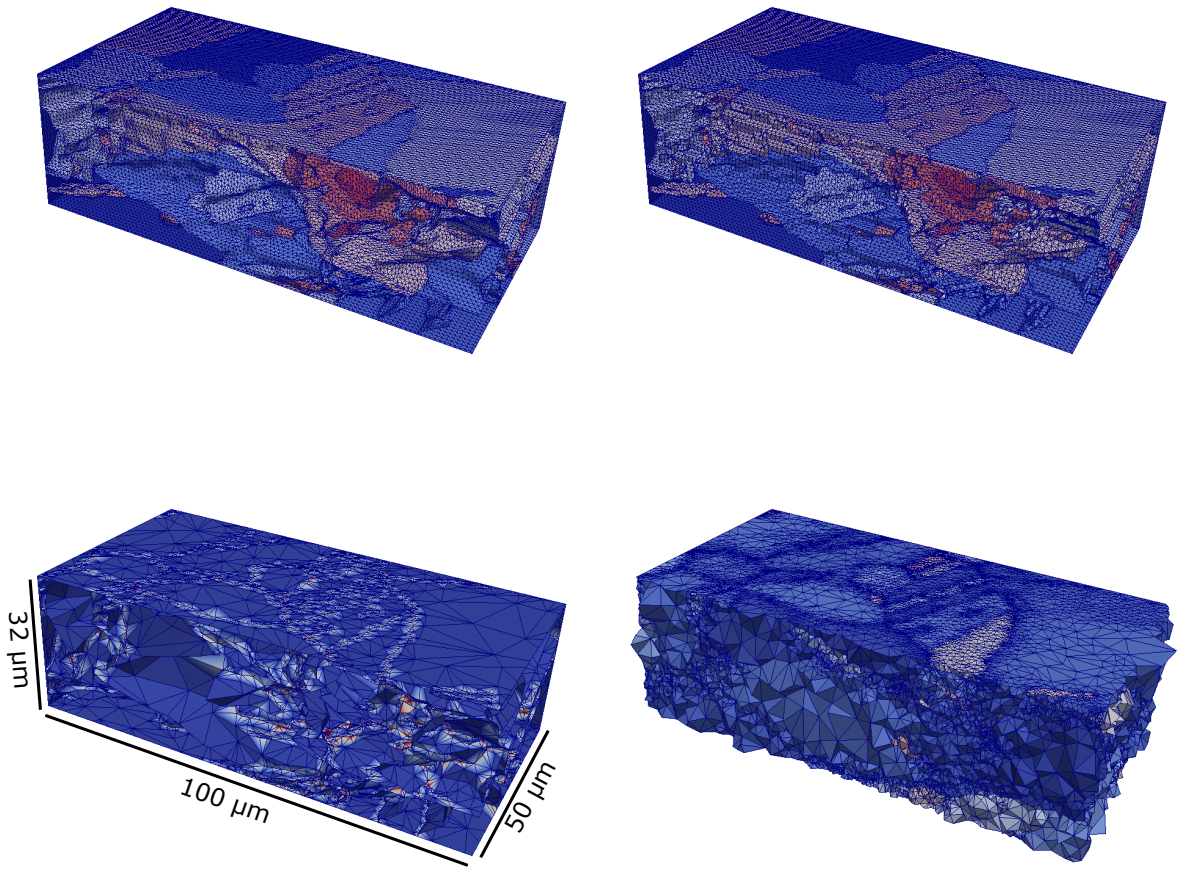

Figure 5.14: The process of generating surface and volume meshes from a segmented polycrystalline dataset is shown for a subset of the inclusion dataset. Meshes are colored as in figure 5.10.

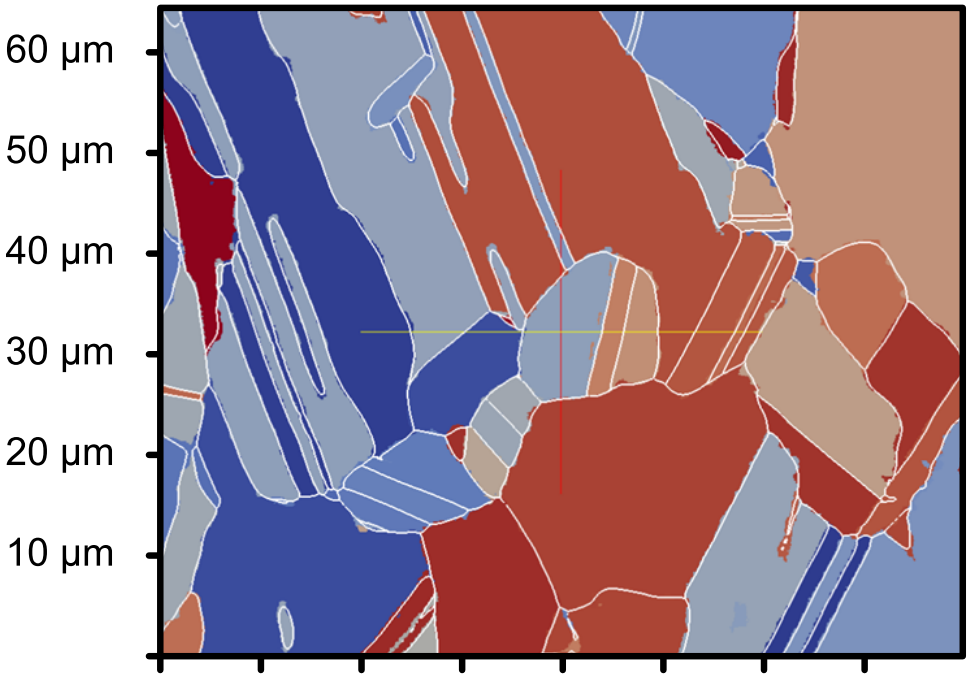

Figure 5.15: A 2D slice of the twin scale dataset is colored by grain ID. The smoothed surface mesh is overlaid in white showing good morphological agreement without aliasing.

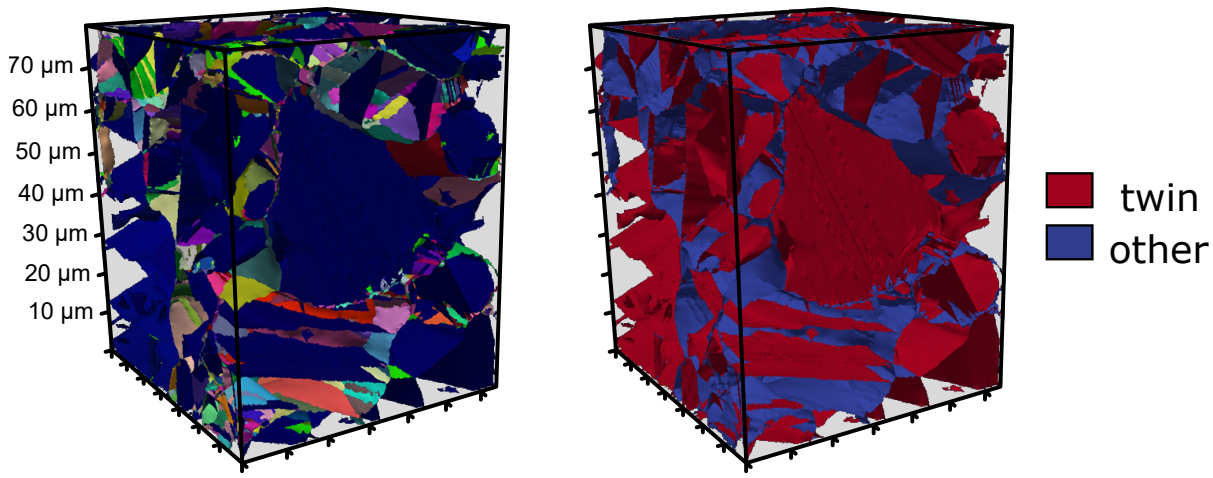

Figure 5.16: All grain boundaries in the twin scale dataset are colored by disorientation (left) with boundaries having a disorientation within 5° of a a twin disorientation flagged (right).

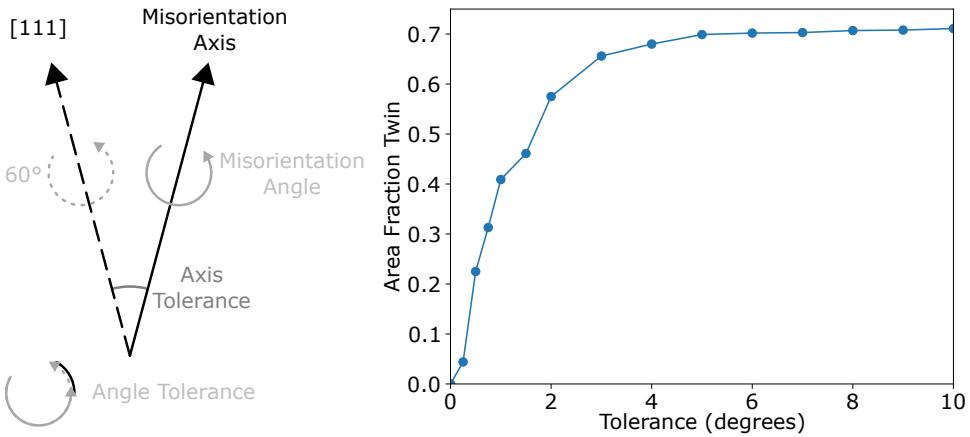

Figure 5.17: Twin boundaries are identified by thresholding on both the angle between the disorientation axis and [111] and the difference between the disorientation angle and 60° (left). A parameter study with both tolerances equal to each other reveals a plateau near 5° (right).

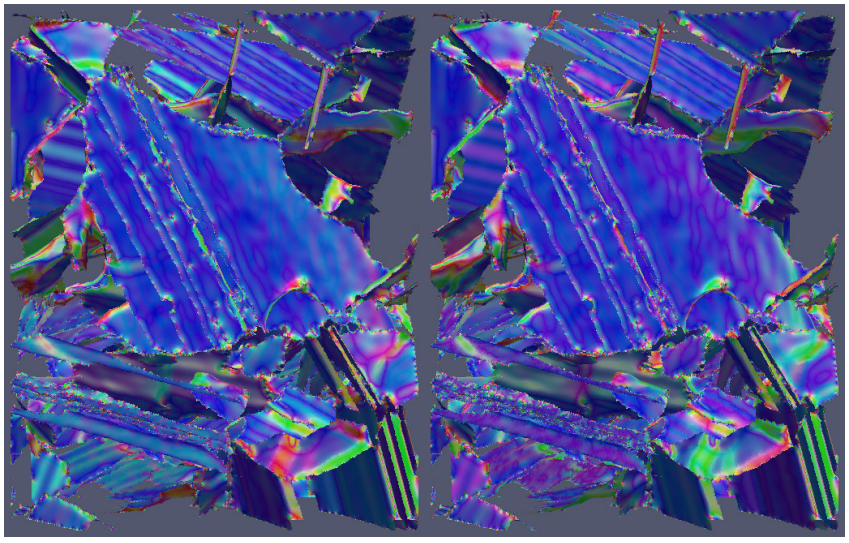

Figure 5.18: Coherence is visualized qualitatively by IPF coloring each triangle using the triangle normal as the reference direction. Triangles are colored by the the orientation of the bounding grain with the lower (left) or higher (right) grain ID.

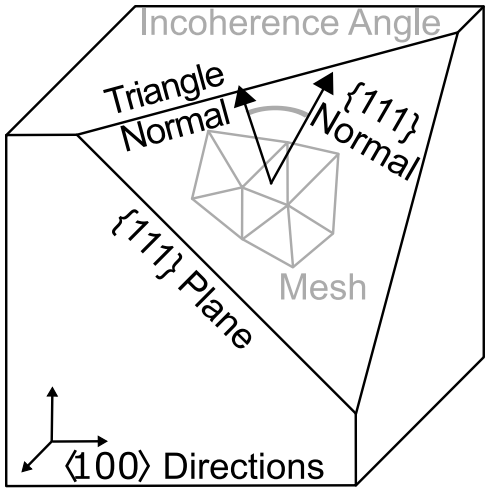

Figure 5.19: The calculation of incoherence angle for a twin boundary face and a single bounding orientation is shown schematically.

grain boundaries are coherent with small incoherent steps or facets (figure 5.20). An area weighted histogram of incoherence angle is shown in figure 5.21. Approximately 80% of the twin boundary area has an incoherence angle less than 20° and 95% has an incoherence angle less than 30°. Artificial roughness introduced to the surface mesh due to the voxelized input causes the mesh faces to deviate from perfect coherence. Laplacian smoothing significantly reduces this artifact but long range, low amplitude ripples persist, adding a finite value to the incoherence angle. Sharp steps have been observed experimentally on twin boundaries in René 88DT [14] and twins frequently terminate within a grain, geometrically requiring regions of incoherent twin boundary area. The coherent direction of a twin related grain pair can be calculated from the twin orientations by identifying the shared {111} type direction as described in algorithm 5.7. Assuming coherence for annealing twin boundaries in René 88DT enables calculation of twin boundary inclination from 2D cross sections, increasing the flexibility of 2D fatigue studies. The ratio of area projected along the coherent twin direction to voxel interface area is shown as a function of coherent direction in the sample reference frame in figure 5.22 and figure 5.23 for the twin and grain scale datasets respectively.

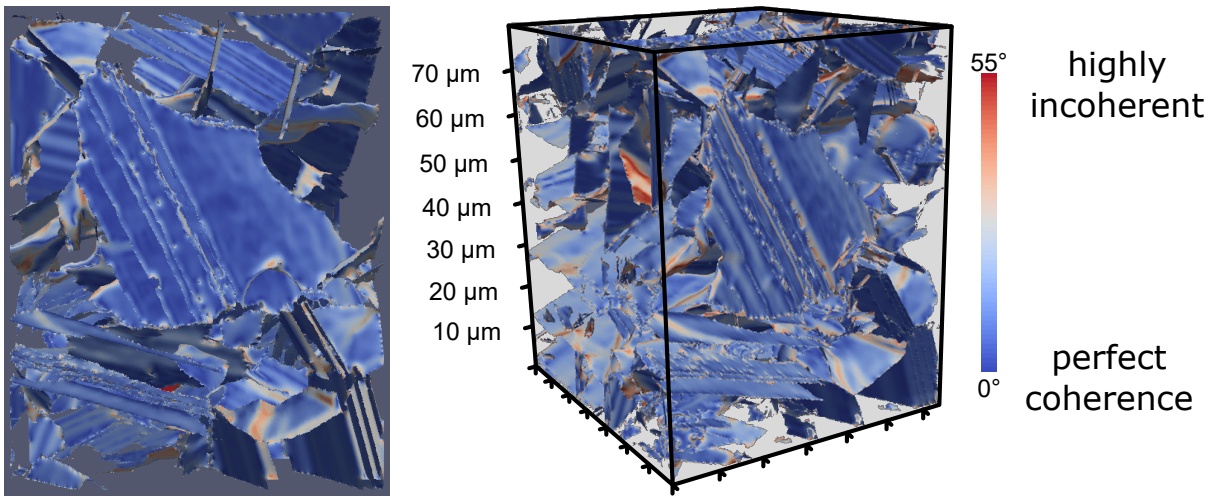

Figure 5.20: The grain boundary mesh of the twin scale dataset is colored by coherence angle.

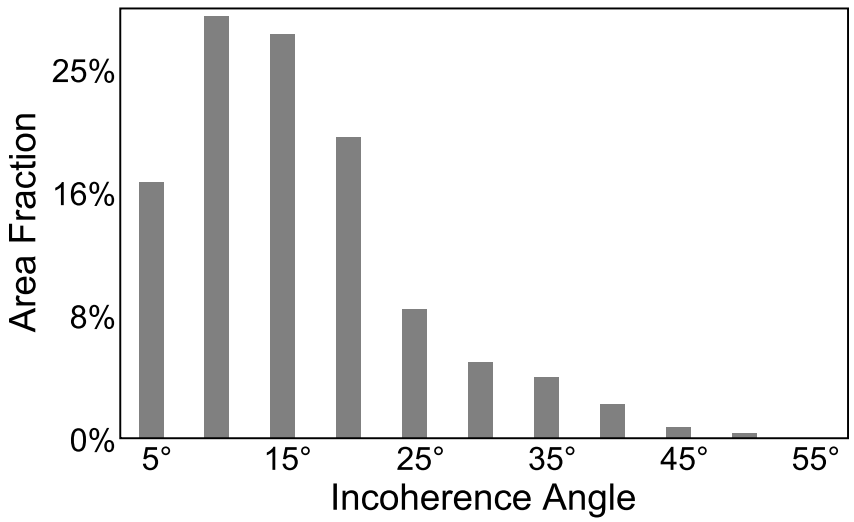

Figure 5.21: An area weighted histogram of twin boundary incoherence angle is shown.

Algorithm 5.7: An algorithm to compute the coherent twin direction is given.

Data: Average orientations of 2 twin related grains a and b
Result: Coherent twin direction in the orientation reference frame
$v_{111} \leftarrow [111], [\bar{1}11], [1\bar{1}1], [11\bar{1}]$
$maxDot \leftarrow 0$
foreach v_i *in* v_{111} **do**
  $v_i \leftarrow$`rotate(`v_i,$a \rightarrow$*orientation reference frame*`)`
  $v_i \leftarrow$`rotate(`v_i,*orientation reference frameb*`)`
  foreach v_j *in* v_{111} **do**
    $dot \leftarrow v_i \cdot v_j$
    if $|dot| > maxDot$ **then**
      $maxDot \leftarrow |dot|$
      if $dot > 0$ **then**
        $\bar{v} \leftarrow v_i + v_j$
      else
        $\bar{v} \leftarrow v_i - v_j$
      end
      $\bar{v} \leftarrow \frac{\bar{v}}{|\bar{v}|}$
    end
  end
end
$\bar{v} \leftarrow$`rotate(`$\bar{v}$,$b \rightarrow$*orientation reference frame*`)`
return $\bar{v}$

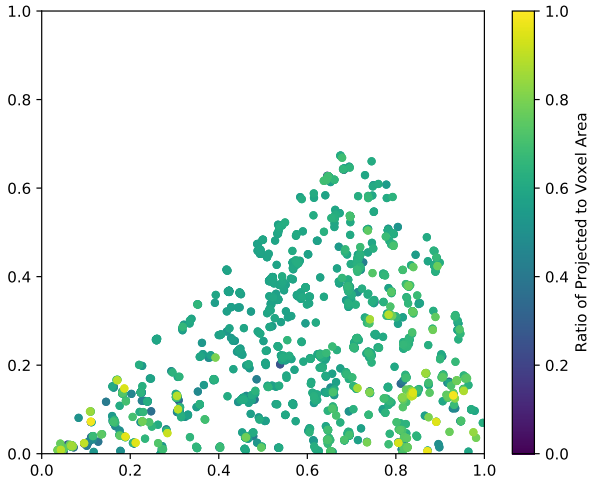

Figure 5.22: Each twin boundary in the twin scale dataset is plotted by coherent direction in the sample reference frame using a Lambert azimuthal equal-area projection with directions moved to the symmetric equivalent position ($z > 0$ and $y \geq x$). Boundaries are colored by the ratio of area projected along the coherent direction to stepped voxel interface area.

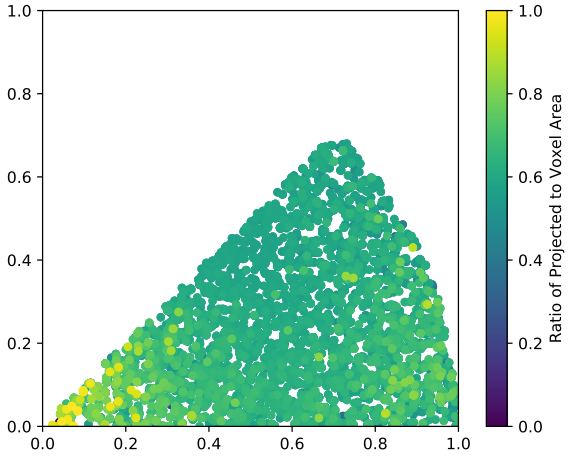

Figure 5.23: Each twin boundary in the grain scale dataset is plotted by coherent direction in the sample reference frame using a Lambert azimuthal equal-area projection with directions moved to the symmetric equivalent position ($z > 0$ and $y \geq x$). Boundaries are colored by the ratio of area projected along the coherent direction to stepped voxel interface area.

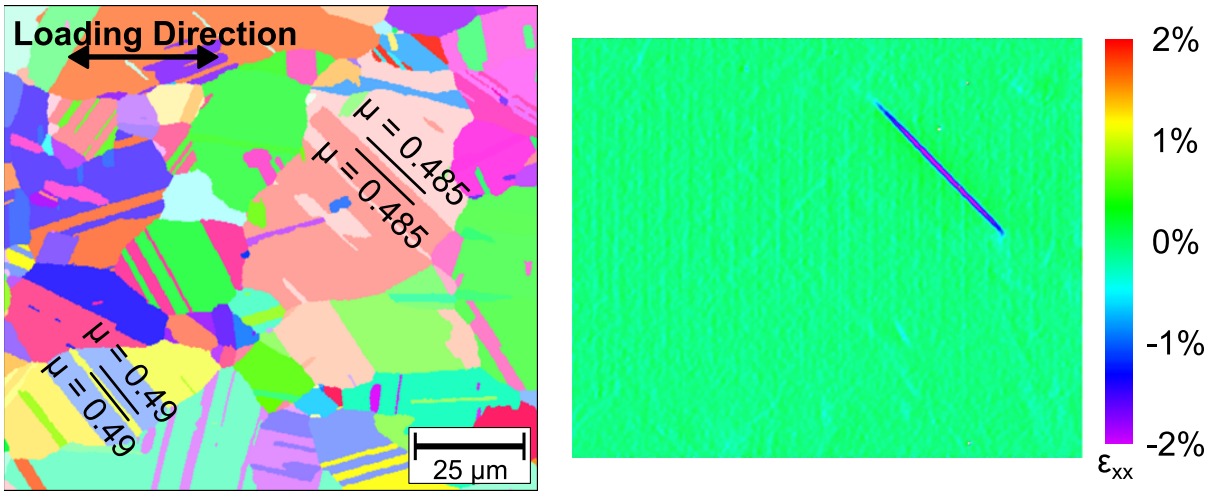

Figure 5.24: Orientation mapping of an unstrained sample (left) and DIC after a single fully reversed cycle of 758 MPa (right) of the same area shows sharp strain localization near a favorably oriented annealing twin boundary. Figure reprinted from Stinville et al., Copyright 2016, with permission from Acta Materialia Inc. [29].

5.2 Strain Localizing Microstructural Features

Fatigue cracks initiate at the sample surface when René 88DT is cycled at room temperature in the low and very high cycle regimes, enabling rapid characterization of significant numbers of fatigue cracks [29]. Surface initiation also enables observations to be coupled with other techniques including DIC and EBSD. Annealing twins bounded by high Schmid factor grains exhibit sharp strain localization even after a single loading cycle as shown in figure 5.24 [29]. For the cycling conditions studied, the strain accumulates with increasing cycle number until a crack is observed at 45% of fatigue lifetime.

EBSD characterization of the neighborhood surrounding cracks reveals that they initiate near twin boundaries bounded by two grains with either a very high Schmid factor or a combination of relatively high Schmid factor and a high elastic modulus mismatch as shown in figure 5.25 [29]. Cracks were only found to initiate near boundaries in which the active (highest Schmid factor) slip system in both twin related grains is parallel to the boundary [29], likely due to compatibility stresses near the twin boundary [14].

Fatigue tests were performed at room temperature with a maximum stress of 758 MPa.

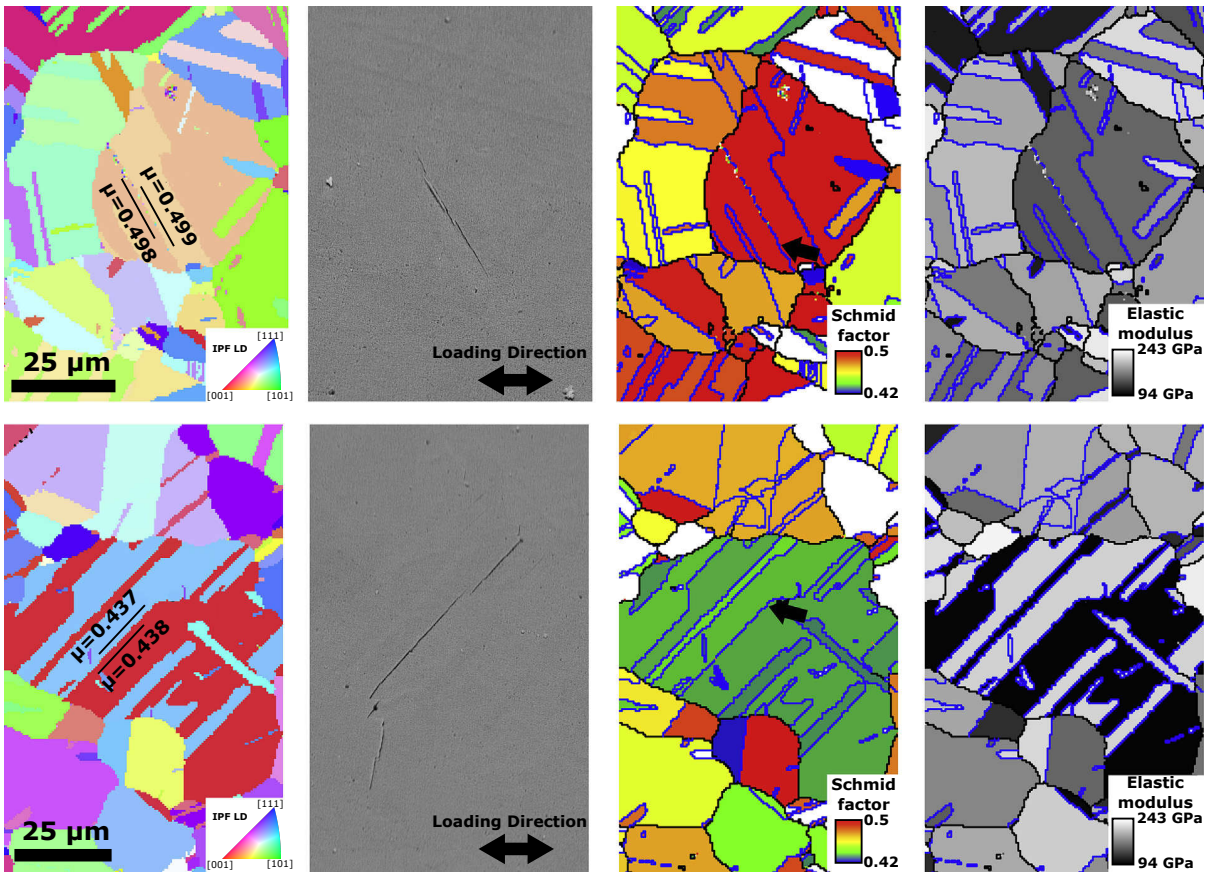

Figure 5.25: Orientation mapping (left) and DIC (right) of the same area shows sharp strain localization near a favorably oriented annealing twin boundary. Figure reprinted from Stinville et al., Copyright 2016, with permission from Acta Materialia Inc. [29].

Low cycle testing was performed on an electromechanical load frame with a R-ratios of -1 and 0.1 and a frequency of 1 Hz. Very high cycle testing was performed using an ultrasonic fatigue system with an R-ratio of -1 and a frequency of 20 kHz. 50 cracks were observed from 10 low cycle samples and 50 cracks observed from 17 very high cycle samples [29]. All cracks were found to initiate near favorably oriented grains with the highest Schmid factor slip system parallel to the twin boundary where characterized to develop a simple criterion for crack initiation as shown in figure 5.26 [29].

The criterion has also been successfully applied to the polycrystalline nickel-base superalloy IN100 with a slightly modified boundary length criterion as shown in figure 5.27. The criterion was subsequently validated by collecting EBSD data from a large 1000 µm × 465 µm surface and identifying candidate sites before fatiguing. After interrupting at 80% of fatigue lifetime, all observed cracks in the scanned area were at previously identified sites, as shown in figure 5.28 and all candidate sites exhibited strain localization [161].

5.3 Fatigue Initiation Property Volume Element

EBSD data were collected from a large 2D area to assess the frequency of strain localizing microstructural features. A sample was cut from a plate of René 88DT and metallographically prepared with 320, 400, 600, 800, and 1200 grit silicon carbide papers. The sample was polished with a 3 µm diamond suspension, vibratory polished in colloidal silica for 12 hours, and a 1.0 x 1.6 mm EBSD scan collected using a 20 kV 0.2 nA electron beam with a 800 nm step size and 4x4 camera binning.

A threshold of 0.1 on confidence index (CI) and 700 on image quality (IQ) was applied to remove any poorly indexed voxels [162]. Grains were defined using a 2° segmentation tolerance and grains smaller than 9 pixels (an equivalent diameter of 2.7 µm) removed by isotropically dilating their neighbors. An IPF map of the dataset and the resulting

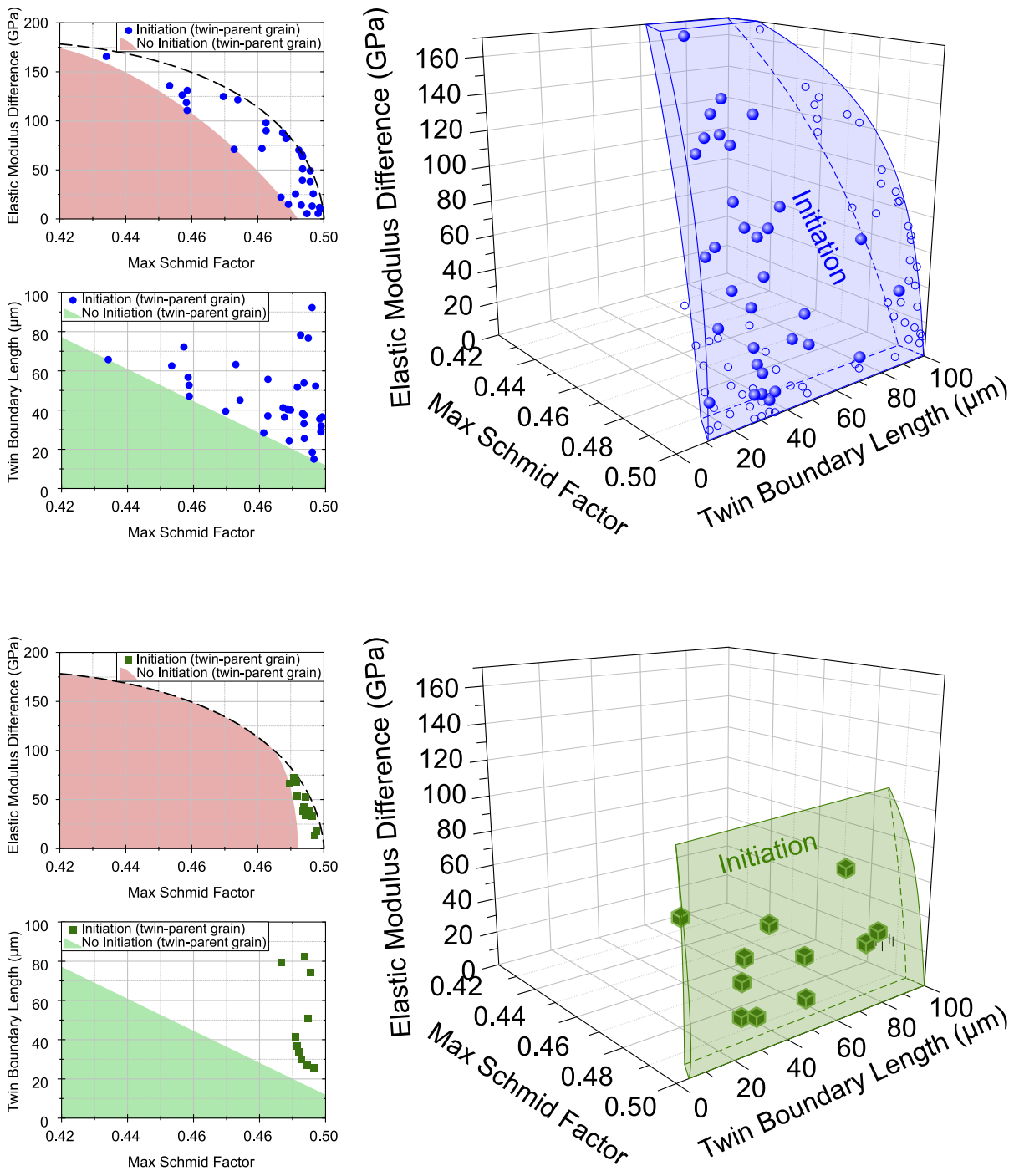

Figure 5.26: The initiation volume in [twin boundary length, max Schmid factor, modulus mismatch] space is shown for the very high and low cycle fatigue regimes (top and bottom respectively). Figure reprinted from Stinville et al., Copyright 2016, with permission from Acta Materialia Inc. [29].

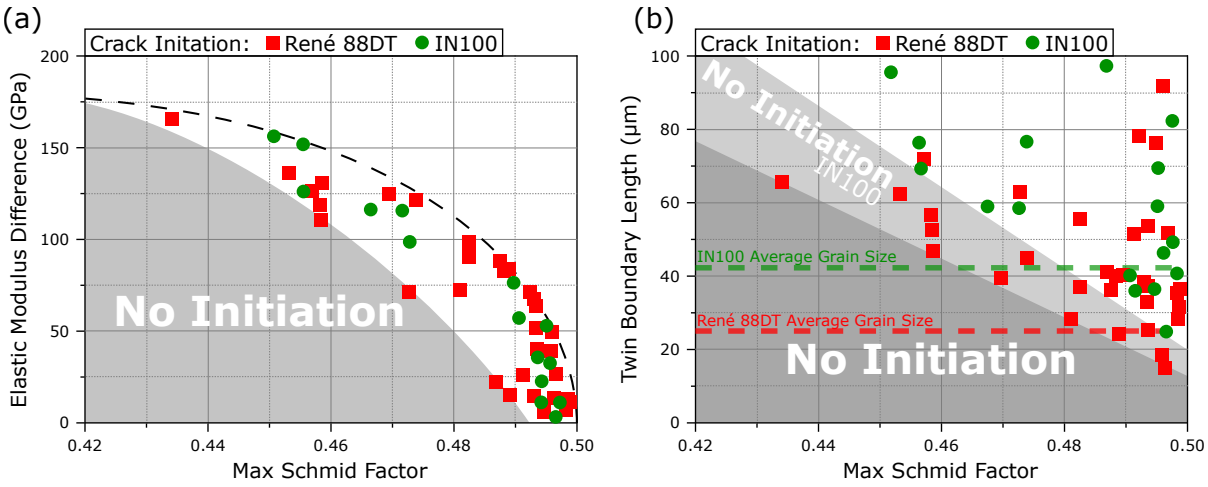

Figure 5.27: The initiation volume in [twin boundary length, max Schmid factor, modulus mismatch space] is shown for both René 88DT and IN100. Figure reproduced from from Stinville et al. [161] with permission of Springer, copyright 2017 Springer Science+Business Media.

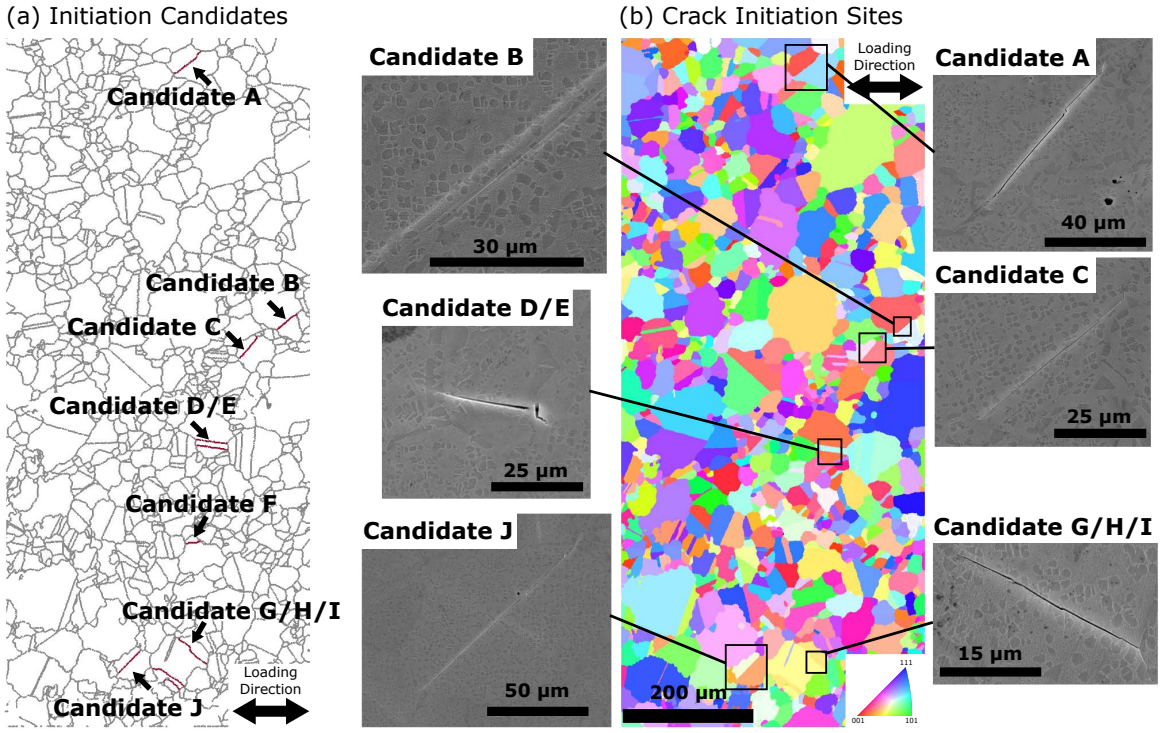

Figure 5.28: Validation of the localization criterion is shown for IN100. Figure reproduced from from Stinville et al. [161] with permission of Springer, copyright 2017 Springer Science+Business Media.

segmentation are shown in figure 5.29.

For each grain the Schmid factor for each slip system and the elastic modulus for [100] loading were computed using the grain average orientation (figure 5.30). Elastic modulus along an arbitrary crystallographic direction $[uvw]$ can be computed as $\frac{1}{s'_{11}}$ for a single crystal compliance matrix rotated to align $[uvw]$ with e_1. Moduli were computed using cubic single crystal elastic stiffnesses

$$\begin{bmatrix} c_{11} & c_{12} & c_{12} & 0 & 0 & 0 \\ c_{12} & c_{11} & c_{12} & 0 & 0 & 0 \\ c_{12} & c_{12} & c_{11} & 0 & 0 & 0 \\ 0 & 0 & 0 & c_{44} & 0 & 0 \\ 0 & 0 & 0 & 0 & c_{44} & 0 \\ 0 & 0 & 0 & 0 & 0 & c_{44} \end{bmatrix}$$

with $c_{11} = 247\,\text{MPa}$, $c_{12} = 153\,\text{MPa}$, $c_{44} = 122\,\text{MPa}$. Stiffnesses and compliances can be rotated with a 6×6 rotation matrix with $C' = KCK^T$ and $S' = K^{-T}SK^{-1}$:

$$K = \begin{bmatrix} K^{(1)} & 2K^{(2)} \\ K^{(3)} & K^{(4)} \end{bmatrix} \tag{5.2}$$

$$K^{-T} = \begin{bmatrix} K^{(1)} & K^{(2)} \\ 2K^{(3)} & K^{(4)} \end{bmatrix} \tag{5.3}$$

$$\begin{aligned} K_{ij}^{(1)} &= \Omega_{ij}^2 \\ K_{ij}^{(2)} &= \Omega_{i \bmod(j+1,3)} \Omega_{i \bmod(j+2,3)} \\ K_{ij}^{(3)} &= \Omega_{\bmod(i+1,3)j} \Omega_{\bmod(i+2,3)j} \\ K_{ij}^{(4)} &= \Omega_{\bmod(i+1,3)\bmod(j+1,3)} \Omega_{\bmod(i+2,3)\bmod(j+2,3)} \\ &+ \Omega_{\bmod(i+1,3)\bmod(j+2,3)} \Omega_{\bmod(i+2,3)\bmod(j+1,3)} \end{aligned} \tag{5.4}$$

$$\Omega = \begin{bmatrix} m_1 \cdot e_1 & m_1 \cdot e_2 & m_1 \cdot e_3 \\ m_2 \cdot e_1 & m_2 \cdot e_2 & m_2 \cdot e_3 \\ m_3 \cdot e_1 & m_3 \cdot e_2 & m_3 \cdot e_3 \end{bmatrix} \tag{5.5}$$

with e_i the basis vectors of the unrotated frame and m_i the basis vectors of the rotated frame [163]. A stiffness tensor rotation can be written compactly in Einstein notation as $C'_{ijkl} = \Omega_{ip}\Omega_{jq}C_{pqrs}\Omega_{kr}\Omega_{ls}$ [163] and a compliance tensor rotation may similarly be written as $S'_{ijkl} = \Omega_{ip}\Omega_{jq}S_{pqrs}\Omega_{kr}\Omega_{ls}$ [164]. Simplifying $1/s_{1111}$ for cubic materials allows directional elastic modulus to be computed directly [165].

$$\frac{1}{E_{hkl}} = s_{11} - 2(s_{11} - s_{12} - \frac{s_{44}}{2})\frac{h^2k^2 + k^2l^2 + l^2h^2}{(h^2 + k^2 + l^2)^2} \tag{5.6}$$

A grain boundary surface mesh was generated, the disorientation of each boundary calculated, and twin boundary and line segments classified using a 5° tolerance on disorientation axis and disorientation angle as shown in figure 5.31. The coherent direction of each twin boundary was computed using algorithm 5.7. Twin related domains were grouped and twin boundaries for which the highest Schmid factor slip system is parallel to the boundary plane identified (assuming coherent boundaries to infer boundary inclination) as shown in figure 5.32. The length of each twin boundary was computed by projecting segment lengths onto the coherent boundary trace and the modulus mismatch across each boundary calculated as shown in figure 5.33. Boundaries meeting the localization criterion for low cycle fatigue (figure 5.26) were identified as shown in figure 5.34. Boundaries were considered to pass the elastic modulus mismatch versus Schmid factor criterion if they satisfied:

$$\Delta E \geq k_m^2 m^2 + k m^1 + k_m^0 \tag{5.7}$$

with ΔE the elastic modulus mismatch across the boundary, m the maximum Schmid factor of either bounding grain, and k_m^2, k_m^1 and k_m^0 constants with values $-21.3\,\mathrm{GPa}$,

17.4 GPa, and −3.39 GPa respectively [29]. Boundaries were considered to pass the length versus Schmid factor criterion if they satisfied:

$$l \geq k_l^1 m + k_l^o \tag{5.8}$$

with l the boundary length and k_l^1 and k_l^0 constants with values −917 µm and 466 µm [29]. Detailed subregions for the entire sequence are shown in figure 5.35.

Of 68545 grain boundaries in the mesh, 146 (0.2%) meet the criterion for strain localization. When considering the mean value of a microstructural feature or a property, along with statistical deviation from the mean value, a proper sampling framework is critical [166]. The relevant feature or property is repeatedly measured with samples of varying size. Volumes small with respect to the relevant characteristic length scale will have high variability with scatter decreasing at larger volumes. If the convergence behavior is well characterized, scatter can be predicted as a function of interrogated volume [166].

The dataset was subsampled to investigate the microstructure volume element size relevant to fatigue crack initiation [166]. Square volume elements with edge lengths ranging from 5–500 µm were used to calculate the frequency of localization sites. At each size, 50 volumes were randomly sampled from the full dataset. The length of all mesh segments falling completely within the volume element were accumulated and the line fraction of boundaries satisfying the localization criterion measured (figure 5.36).

A property volume element (PVE) for fatigue strain localization can defined by examining standard deviation with increasing sample area. The least squares power law curve fit for standard deviation of strain localizing boundary fraction is $1.15 * \text{area}^{-0.5}$. Convergence, defined as a 95% confidence that the population mean is within 10% of the sample average occurs for areas greater than 440 µm × 440 µm. If a more stringent criterion is enforced, e.g. a 99% confidence that the population mean is within 5% of

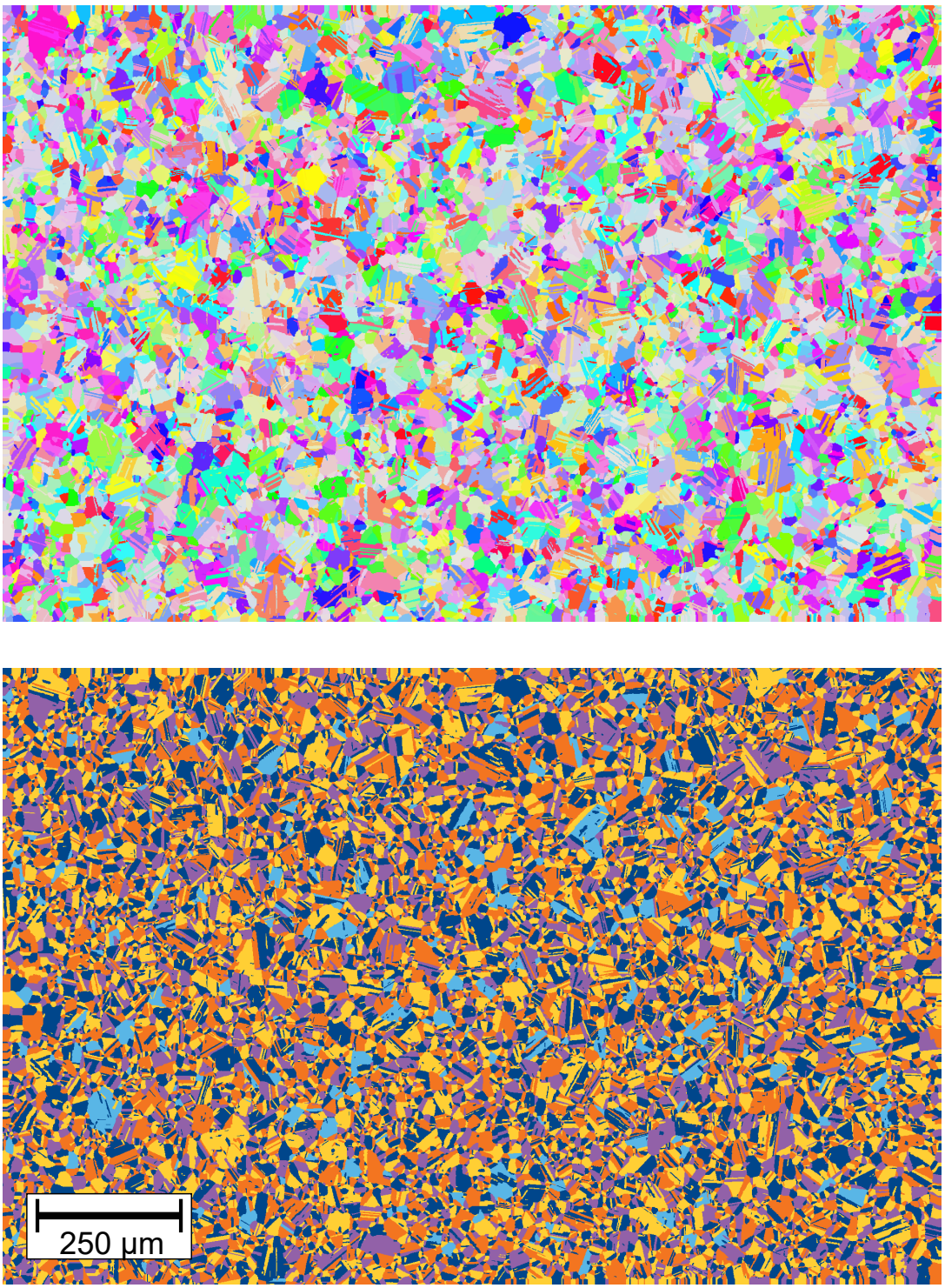

Figure 5.29: A large 2D dataset of René 88DT is shown with IPF color (top) and map colored using grains (bottom).

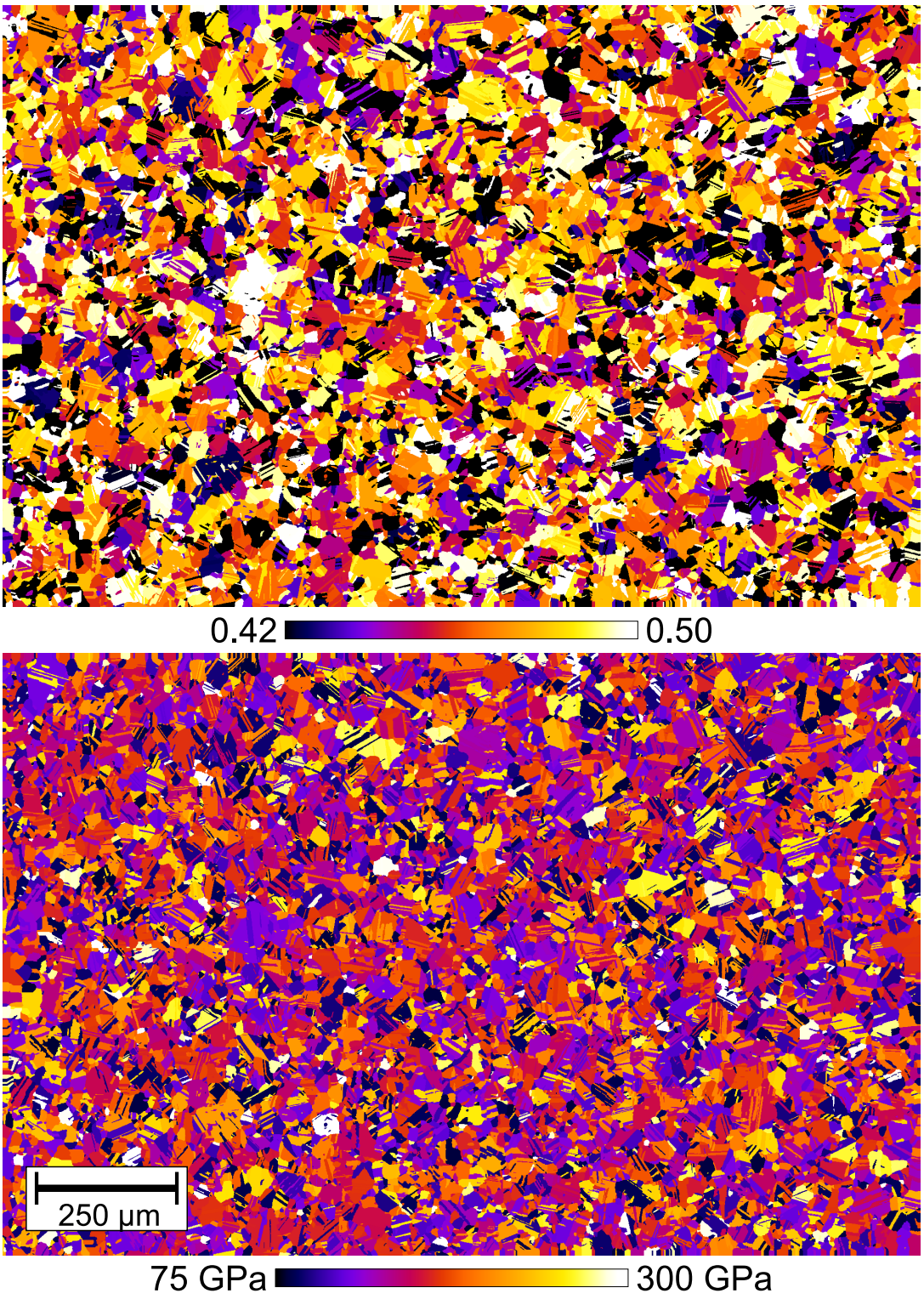

Figure 5.30: A large 2D dataset of René 88DT is colored by Schmid factor (top) and directional elastic modulus (bottom) for loading in the [100] (horizontal) direction.

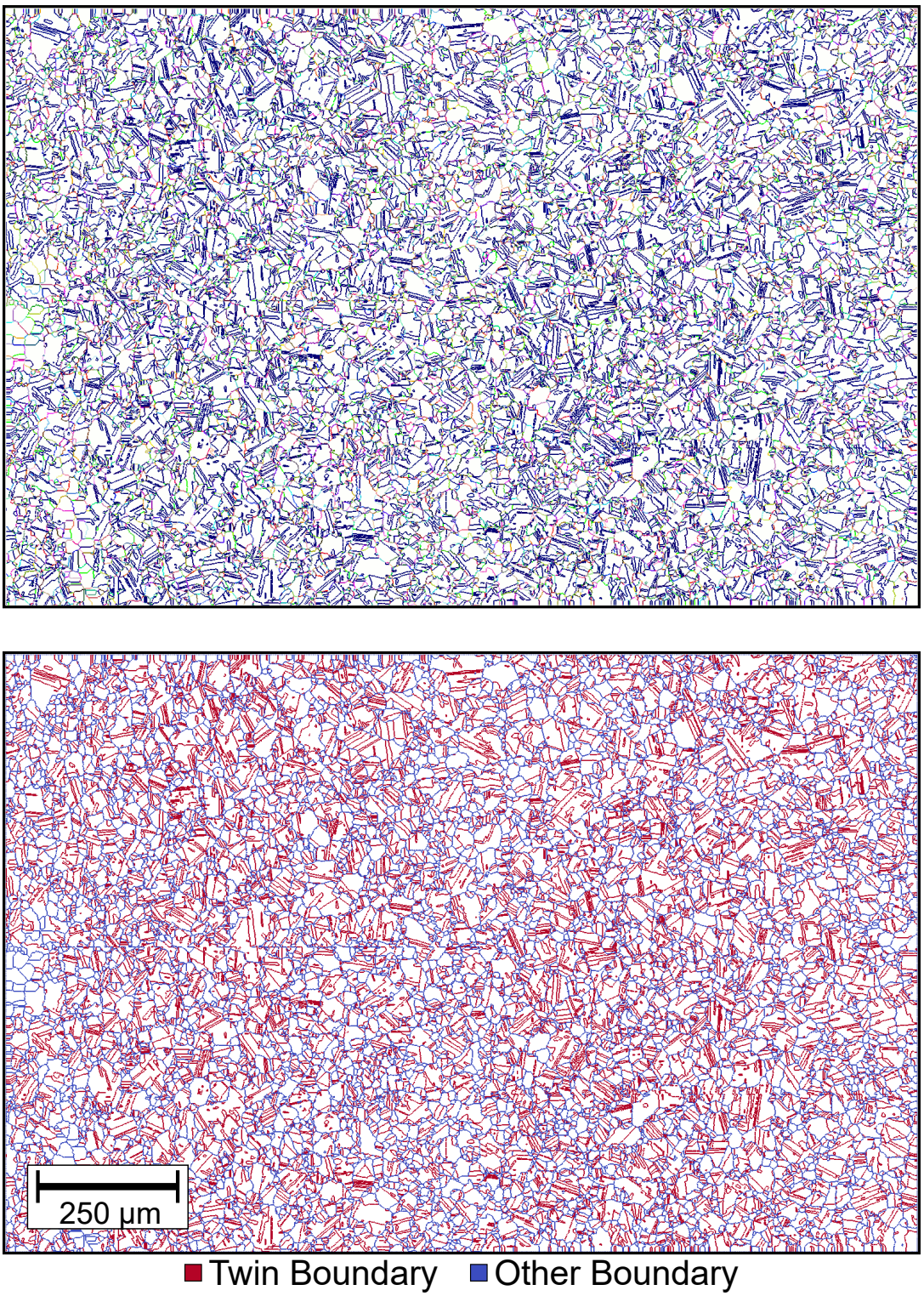

Figure 5.31: A grain boundary mesh of a large 2D dataset of René 88DT is colored by disorientation color (top) and twin boundary flag (bottom). A disorientation coloring legend is available in figure 1.14.

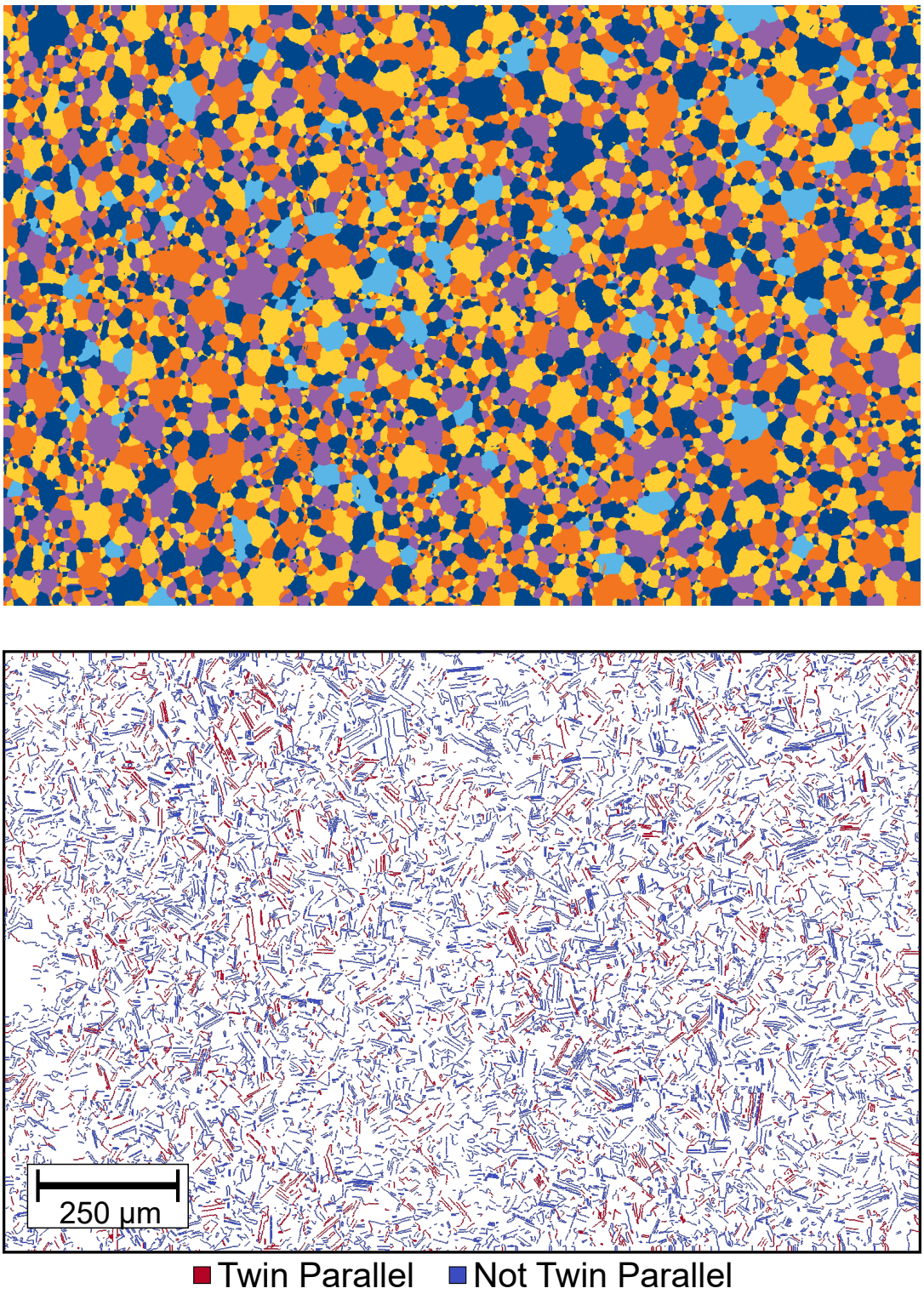

Figure 5.32: A large 2D dataset of René 88DT is map colored using twin related domains (top) and a twin related grain boundaries colored by if the highest Schmid factor slip plane in both bounding grains is parallel the coherent plane (bottom).

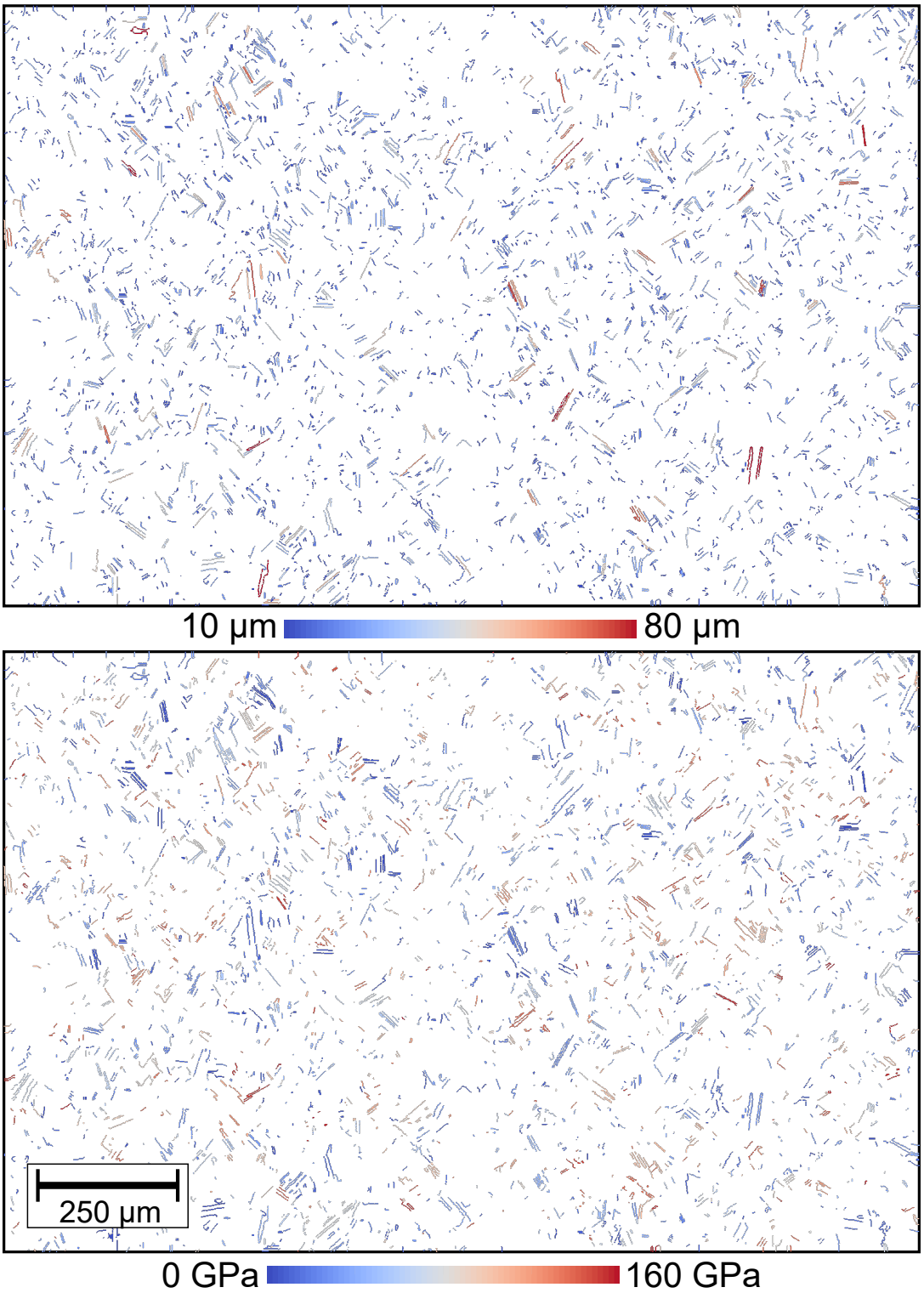

Figure 5.33: Twin related grain boundaries with the highest Schmid factor slip plane parallel to the coherent plane are colored by coherent boundary length (top) and directional elastic modulus mismatch (bottom).

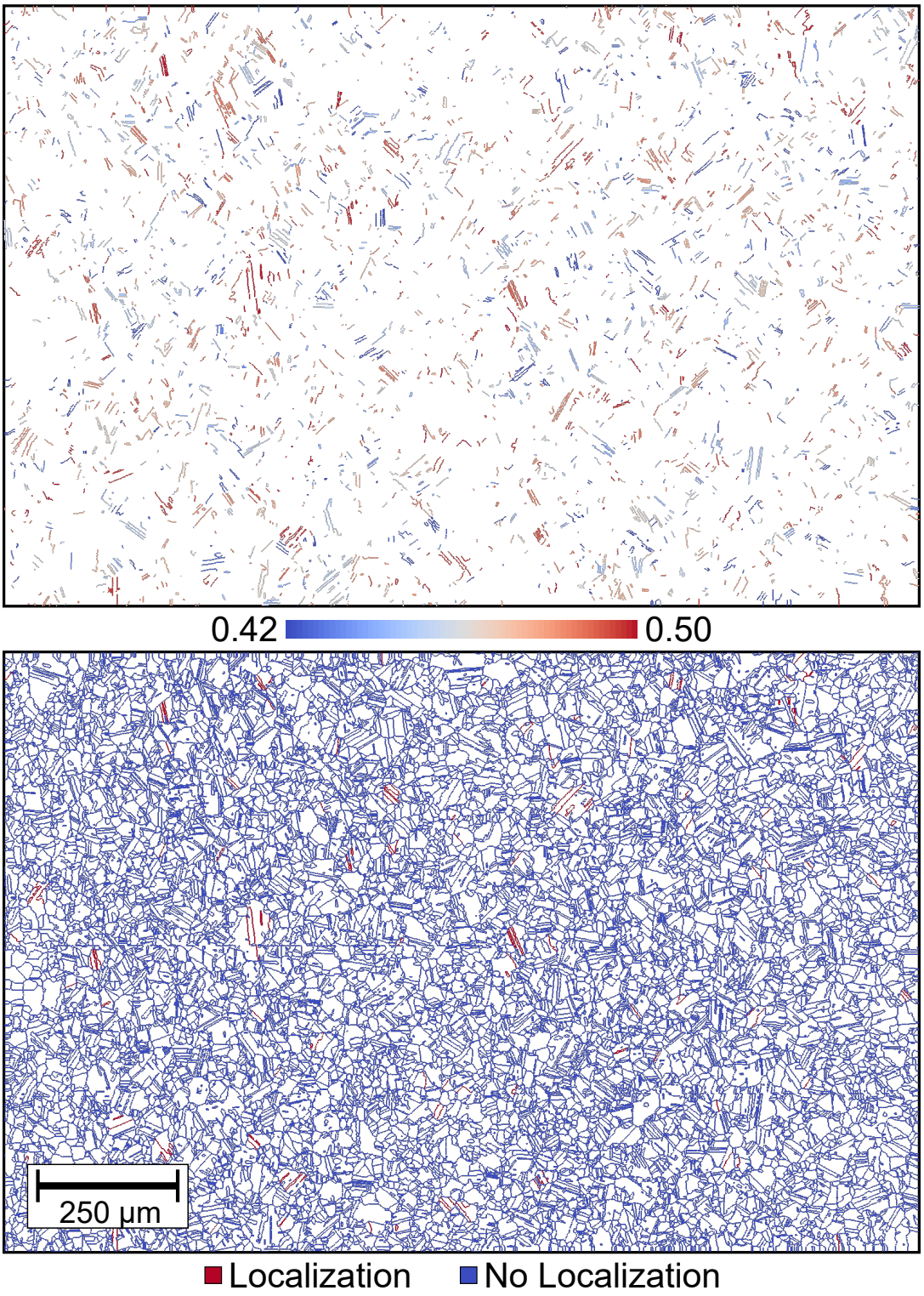

Figure 5.34: Twin related grain boundaries with the highest Schmid factor slip plane parallel to the coherent plane are colored by Schmid factor (top). A grain boundary mesh of a large 2D dataset of René 88DT is colored by if the boundary meets the strain localization criterion (bottom).

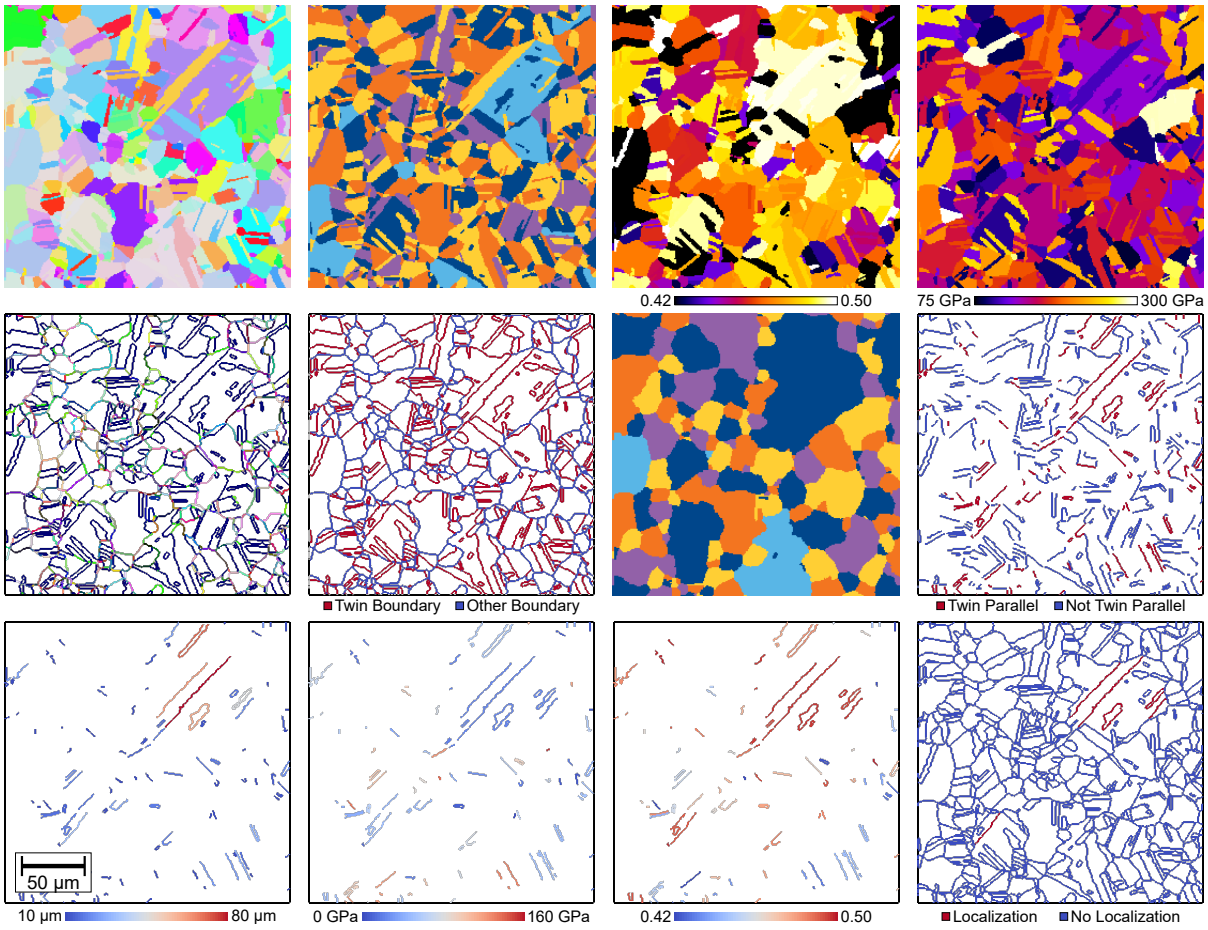

Figure 5.35: The process of identifying localization sites is shown for a small sub region. A raw EBSD scan (top far left) is segmented (top left). Schmid factor (top right) and directional modulus (top far right) are computed for each grain. A grain boundary surface mesh is generated and the disorientation for each boundary computed (middle far left). Twin boundaries are identified (middle left) and twin related domains grouped (middle right). Twin boundaries with the highest Schmid factor slip system parallel to the boundary plane are identified (middle far right) and their length (bottom far left), modulus mismatch (bottom left), and Schmid factor (bottom right) computed. Finally localization sites are identified by a combined threshold (bottom far right).

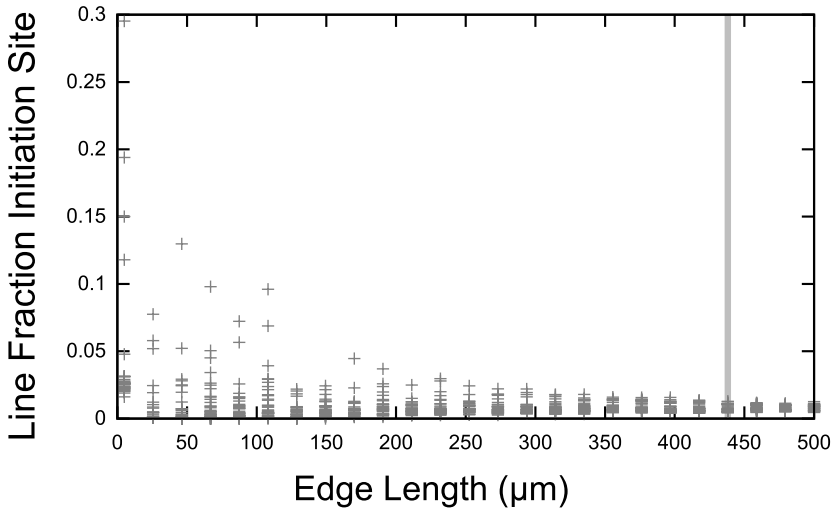

Figure 5.36: The line fraction of fatigue strain localizing boundaries plotted against sampling box size with 15 boxes selected at random for each size. The vertical line indicates 95% confidence convergence to within 5% of the sample mean. Figure reproduced from Lenthe et al. [119].

the sample mean, convergence does not occur for the entire 1.0 mm × 1.6 mm dataset, suggesting the property volume element is larger than the area sampled.

The number density of 265 strain localization sites per mm^2 is roughly an order of magnitude greater than experimentally observed crack densities of 10 per mm^2 [29]. However, twin boundaries that meet the localization criterion are frequently clustered, as shown in figure 5.35. Plasticity within one grain along a twin may reduce the overall level of elastic strain in surrounding grains, artificially increasing the density of candidates. A measurement of twin related domains containing localization sites (figure 5.37) corrects for the overestimation and provides a metric more suitable for direct comparison with experimental observations.

Of a total of 5226 twin related domains, 243 (4.6%) contain at least 1 boundary satisfying the localization criterion with a histogram shown in figure 5.38. The area density of clusters with at least one site meeting the initiation criterion is 146 mm^{-2}. The process of identifying clusters meeting the strain localization criterion was repeated for loading directions between [100] and [$\bar{1}$00] in 0.1° increments over all loading directions.

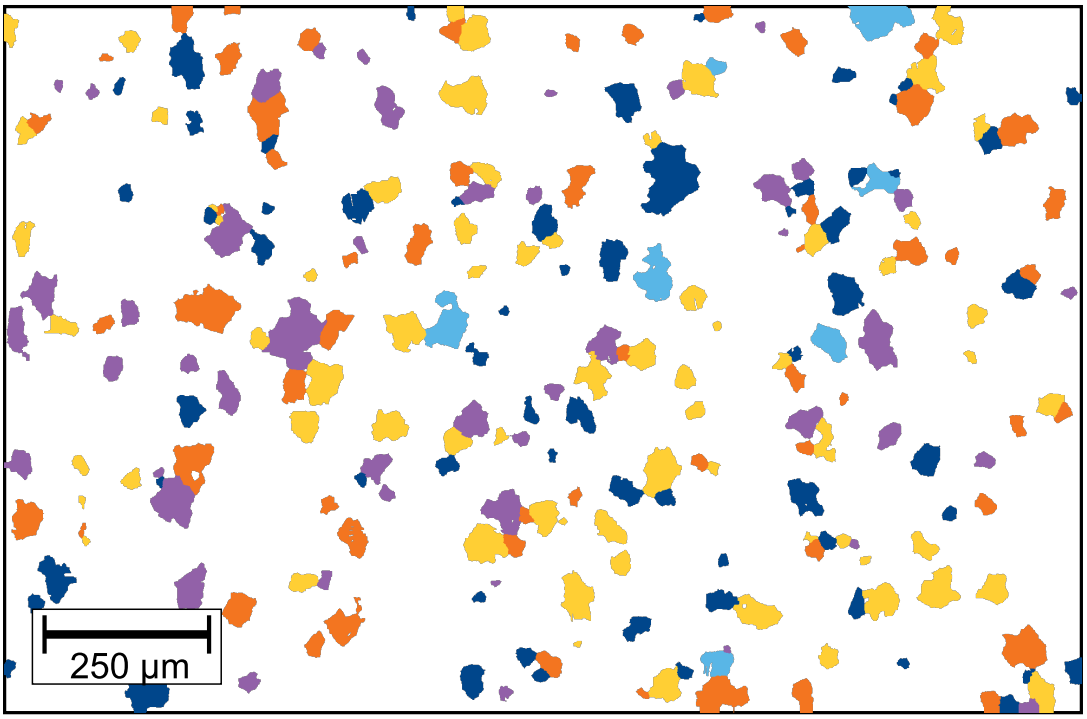

Figure 5.37: Twin related domains containing at least 1 strain localization site are map colored.

231 ± 14 clusters meet the criterion, with the number of sites meeting the localization criterion plotted as a function of loading direction in figure 5.39. The number of initiating clusters falls within 231 ± 38 for all loading directions (2.7 standard deviations).

Figure 5.40 shows each twin related domain colored by the fraction of loading directions for which the domain meets the strain localization criterion. The average domain meets the criterion for 4.4% of directions and the area weighted average for 15%. The fraction of localizing loading directions is plotted discretely against twin related domain equivalent diameter, showing that large domains are more likely to localize strain. The relatively low scatter in localizing domains in conjunction with a low fraction of loading directions meeting the criterion in a given domain suggests a large enough area has been measured for the microstructural feature to converge.

Sub-areas were sampled from the dataset for [100] loading to estimate the fatigue life initiation property volume element. 20 boxes were sampled for each size, using boxes from $4.8\,\mu m \times 4.8\,\mu m$ to $835.2\,\mu m \times 835.2\,\mu m$ in $4.8\,\mu m$ increments. The total number of

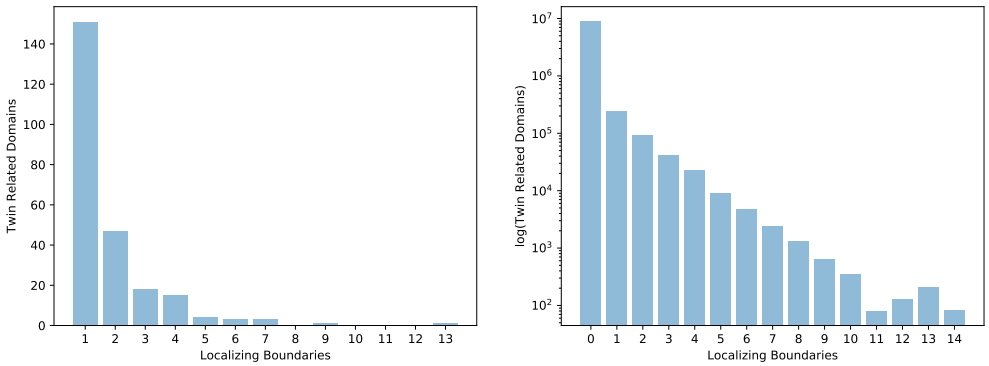

Figure 5.38: A histogram of strain localizing boundaries per twin related domain is shown for [100] loading (left, 4983 domains contain no candidate boundaries). A cumulative histogram for all loading directions (from [100] to $[\bar{1}00]$ in 1° increments) shows a similar trend (right).

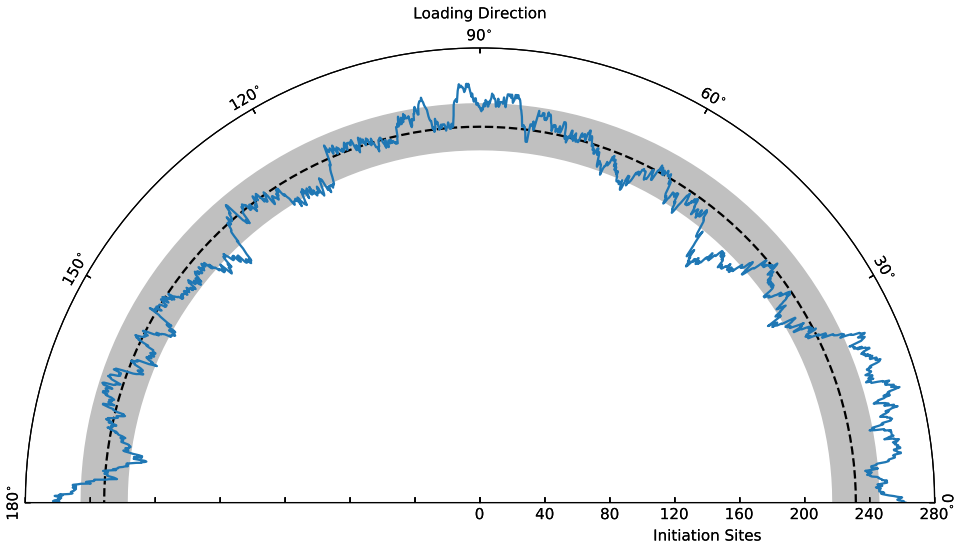

Figure 5.39: The number of twin related domains containing at least one boundary meeting the localization criterion is plotted as a function of loading direction. The dashed line indicates the mean value and the shaded region extends 1 standard deviation in either direction.

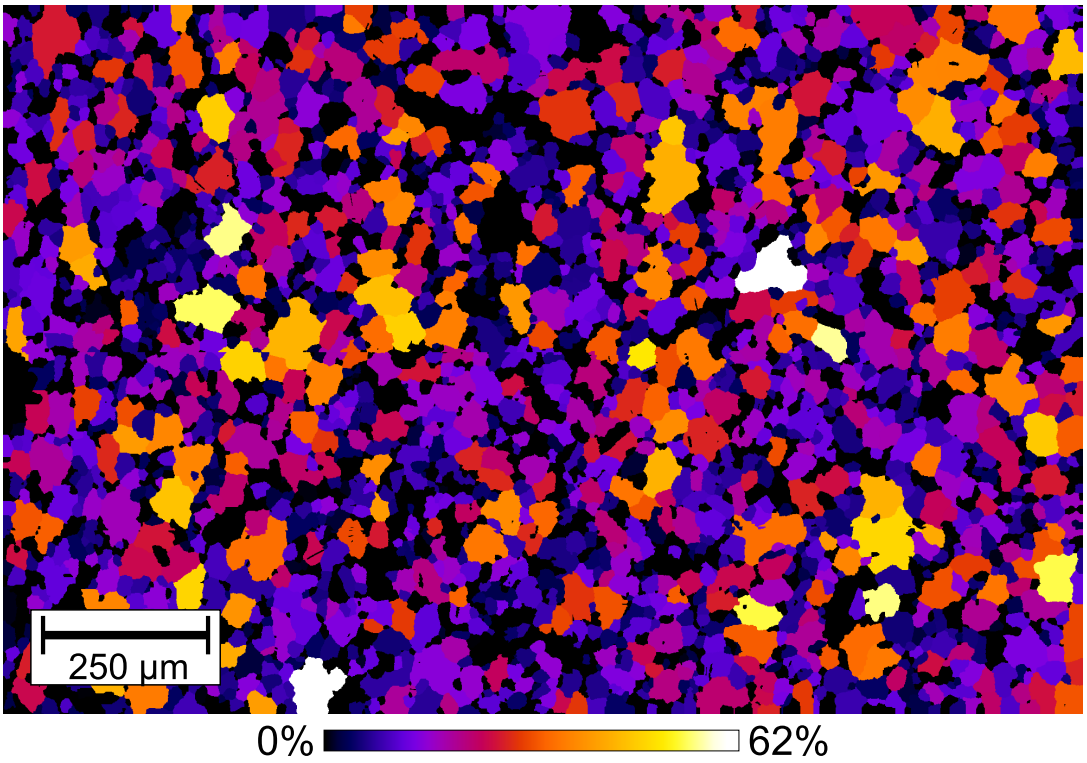

Figure 5.40: Each twin related domain is colored by the fraction of loading directions (from [100] to [$\bar{1}$00] in 1° increments) for which it meets the strain localization criterion.

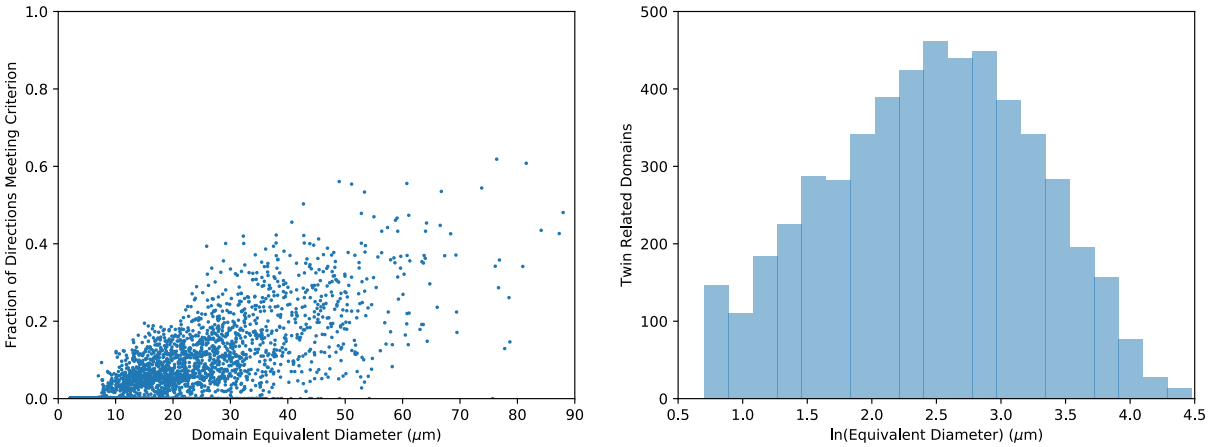

Figure 5.41: Each twin related domain is plotted by the fraction of loading directions (from [100] to [$\bar{1}$00] in 1° increments) for which it meets the strain localization criterion against domain equivalent diameter (left). A histogram of ln(equivalent diameter) shows that domain sizes follow a log-normal distribution (right).

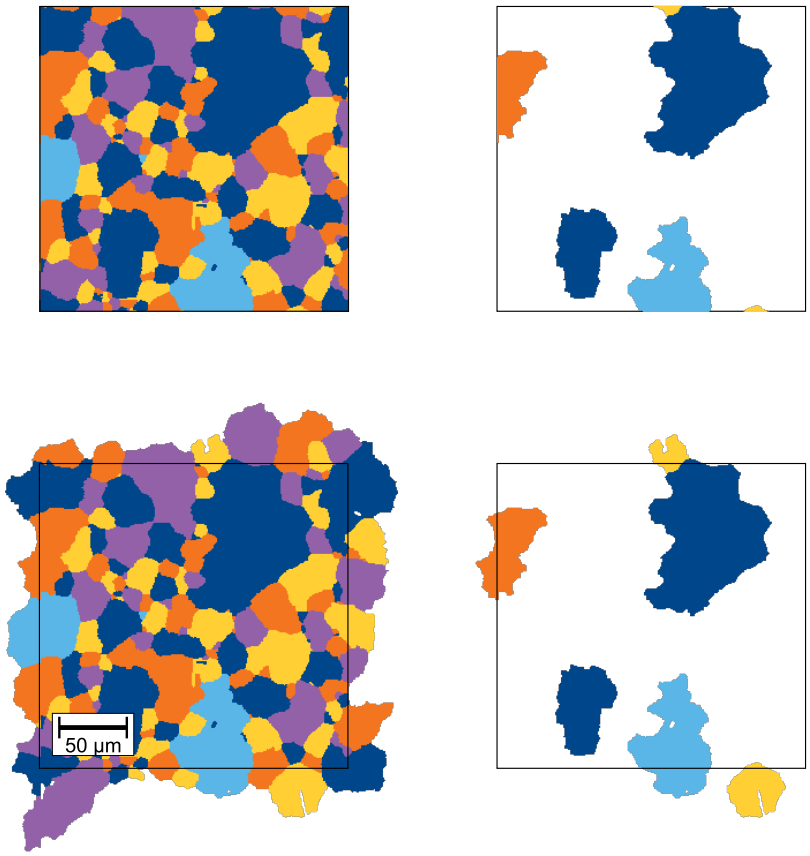

Figure 5.42: A sample box with twin related domains map colored is shown in the top left. Domains meeting the localization criterion may be clipped by box edges (top right). By expanding the sampled region to include only full domains (bottom left) the clipping is avoided when counting localizing domains (bottom right).

twin related domains in each box as well as the number satisfying the strain localization criterion were calculated. The area of the sampled region included the full area of each twin related domain at least partially within the box as shown in figure 5.42 to counting fractions of domains meeting the initiation criterion.

Convergence is checked assuming a Student's t-distribution with convergence assumed when the 95% confidence interval for a population of samples at a given size is fully within $\mu \pm 0.1 * \mu$ where μ is the sample mean as shown in figure 5.45. Convergence of localizing domain density occurs for sampling boxes larger than $730\,\mu m \times 730\,\mu m$ and convergence of fraction localizing domains does not converge within the regions sampled. The large fraction of the scan area required for localization density convergence suggests

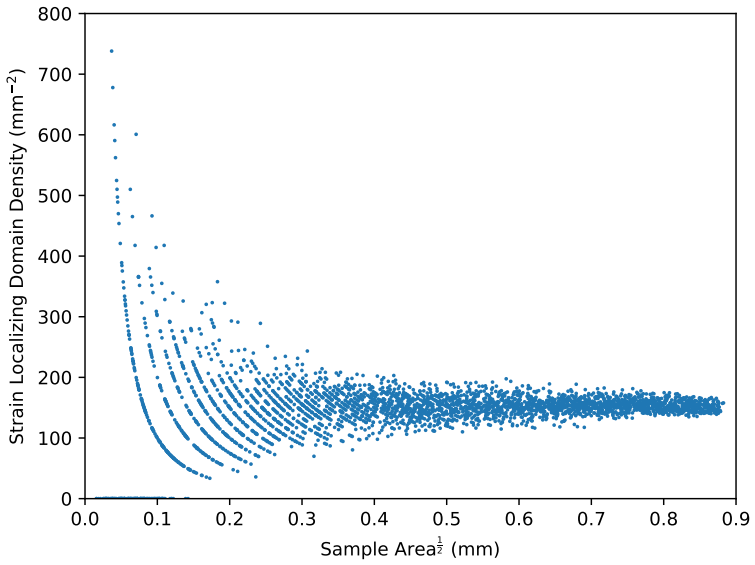

Figure 5.43: Strain localizing twin related domain area density is plotted against sampled area for increasing box size. Discrete lines correspond to {0,1,2,...} domains per region.

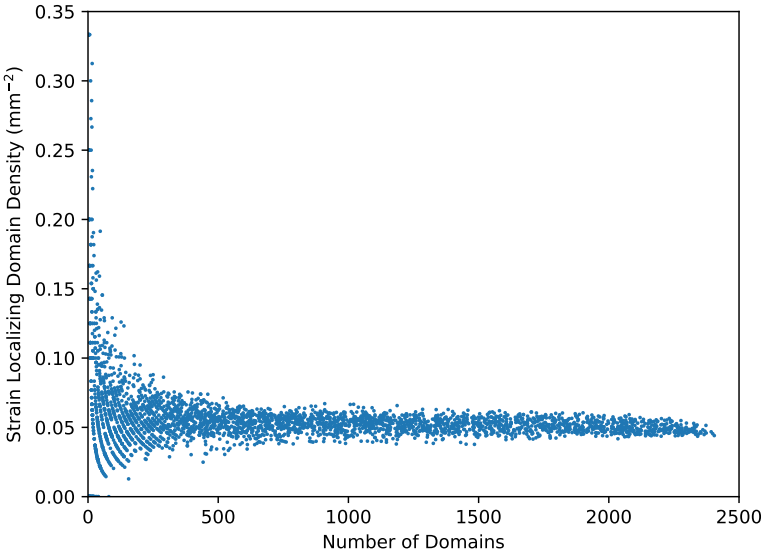

Figure 5.44: Fraction of twin related domains meeting the criterion for strain localization is plotted against number of twin domains sampled for increasing box size. Discrete lines correspond to {0,1,2,...} localizing domains per region.

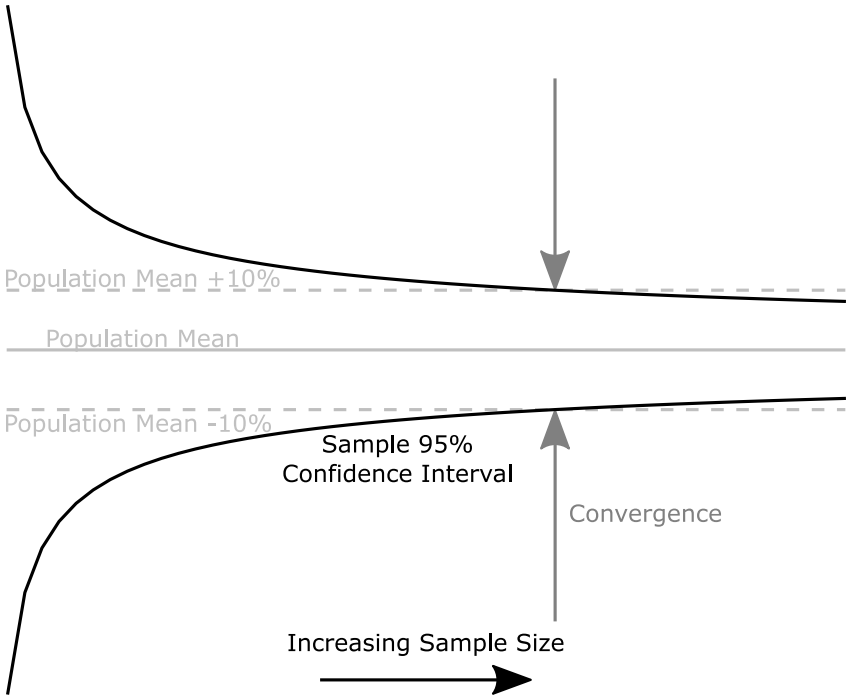

Figure 5.45: The convergence criterion is illustrated schematically.

the true converged area is larger due to a loss of independence between samples. The converged volume is likely on the order of the dataset size based on the small variation in density with loading direction in conjunction with the low fraction of loading directions causing a given twin related domain to meet the convergence criterion. These large converged areas are consistent with highly variable fatigue life, but are insufficient to account for large fatigue life scatter in samples with volumes significantly larger than the region investigated, even accounting for cracks nucleating within only a a fraction of strain localizing domains. In all likelihood the stress concentrations associated with the impingement of the localized band on the adjacent grain will also need to be accounted for via mechanics analysis.

Since small crack growth can also account for a significant fraction of the total fatigue life, a propagation criterion is required to determine the property volume element for fatal cracks. Although simple disorientation criteria exist [15], they are unsuitable for René 88DT, given the complex grain boundaries resulting from high twin density.

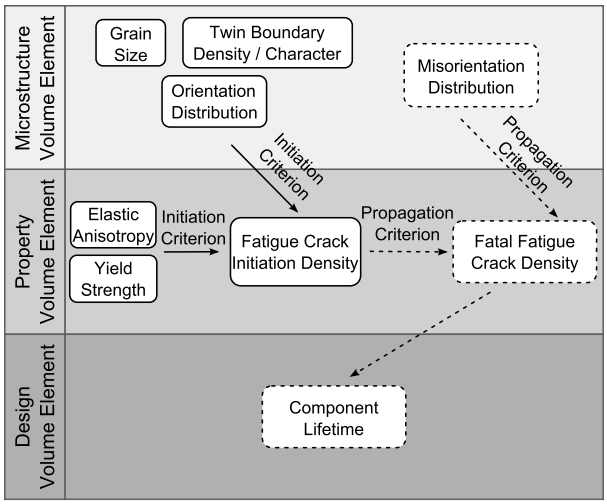

Figure 5.46: The average incidence of initiation sites and variability of fatigue crack initiation density is dependent on the values and variabilities of contributing microstructures and properties through the initiation criterion. A fatal crack density property volume element will be determined in turn by implementing a propagation criterion. Variability in fatal crack density ultimately guides design and predicting component lifetimes.

Development of a propagation criterion will enable measurement of the property volume element for fatal fatigue crack density as shown schematically in figure 5.46, but requires characterization of twin related domain and investigations of specific boundary configurations that arrest or enable crack growth.

Chapter 6

Fatigue Crack Growth

Since small crack growth can also account for a significant fraction of the total fatigue life, a propagation criterion is required to determine the PVE for fatal cracks. High angle boundaries, including twin boundaries, arrest microstructurally short cracks [15]. In this chapter, the neighborhood of the arrested crack from the crack 3D dataset is investigated with boundaries penetrated by and arresting the crack compared.

A variety of slip transmission metrics exist to quantify the likelihood of transferring plasticity across a grain boundary (table 6.1) [167]. In general these are measures of slip system alignment in neighboring grains with some considering twist and tilt angles separately. Geometric and angular threshold metrics are both calculated from slip plane normals, slip directions, and/or boundary plane normal as shown in figure 6.1. Geometric metrics consider alignment continuously while angular threshold metrics postulate a cutoff in transmission beyond some critical angle. Geometric criterion may also be averaged using Schmid factor (m) or accumulated plastic slip (γ).

Only a single grain boundary on the crack path meets the strain localization criterion allowing assumption of the crack nucleation site. $\hat{N}_{\alpha\beta}$, $\hat{N}^{mod}_{\alpha\beta}$, $\hat{M}_{\alpha\beta}$, $\hat{M}^{mod}_{\alpha\beta}$, and m'_m were calculated for each of the grain boundaries the crack encountered in the crack 3D dataset, assuming nucleation in the lower modulus grain next to the grain boundary

Table 6.1: Common slip transmission metrics compiled from Bayerschen et al. [167]. Metrics requiring 3D data (boundary twist angle) are indicated in '3' and those requiring simulation (accumulated slip length) in 'S'.

Category	Metric	3	S
Geometric	$\hat{N}_{\alpha\beta} = (n^A_\alpha \cdot n^B_\beta)(d^A_\alpha \cdot d^B_\beta) + (n^A_\alpha \cdot d^B_\beta)(d^A_\alpha \cdot n^B_\beta)$		
	$\hat{N}^{mod}_{\alpha\beta} = (n^A_\alpha \cdot n^B_\beta)(d^A_\alpha \cdot d^B_\beta)$		
	$\hat{M}_{\alpha\beta} = (l^A_\alpha \cdot l^B_\beta)(d^A_\alpha \cdot d^B_\beta)$	•	
	$\hat{M}^{mod}_{\alpha\beta} = l^A_\alpha \cdot l^B_\beta$	•	
Angular Threshold	$\lambda = \sum_{\alpha,\beta} \cos\left(\frac{\pi}{2\omega_c} \arccos(n^A_\alpha \cdot n^B_\beta)\right) \cos\left(\frac{\pi}{2\kappa_c} \arccos(d^A_\alpha \cdot d^B_\beta)\right)$		
	$\hat{X}_{\alpha\beta} = \cos\left(\frac{\pi}{2\delta_c} \arccos(l^A_\alpha \cdot l^B_\beta)\right) \cos\left(\frac{\pi}{2\kappa_c} \arccos(d^A_\alpha \cdot d^B_\beta)\right)$	•	
Weighted Geometric	$m'_m = \sum_{\alpha,\beta} \hat{N}^{mod}_{\alpha\beta} m^A_\alpha m^B_\beta \Big/ \sum_{\alpha,\beta} m^A_\alpha m^B_\beta$		•
	$s'_\gamma = \sum_{\alpha,\beta} \hat{N}^{mod}_{\alpha\beta} \gamma^A_\alpha \gamma^B_\beta \Big/ \sum_{\alpha,\beta} \gamma^A_\alpha \gamma^B_\beta$		•
	$s'_\gamma = \sum_{\alpha,\beta} \hat{M}^{mod}_{\alpha\beta} \gamma^A_\alpha \gamma^B_\beta \Big/ \sum_{\alpha,\beta} \gamma^A_\alpha \gamma^B_\beta$		•
	$LRB'_\gamma = \sum_{\alpha,\beta} \hat{M}_{\alpha\beta} \gamma^A_\alpha \gamma^B_\beta \Big/ \sum_{\alpha,\beta} \gamma^A_\alpha \gamma^B_\beta$		•

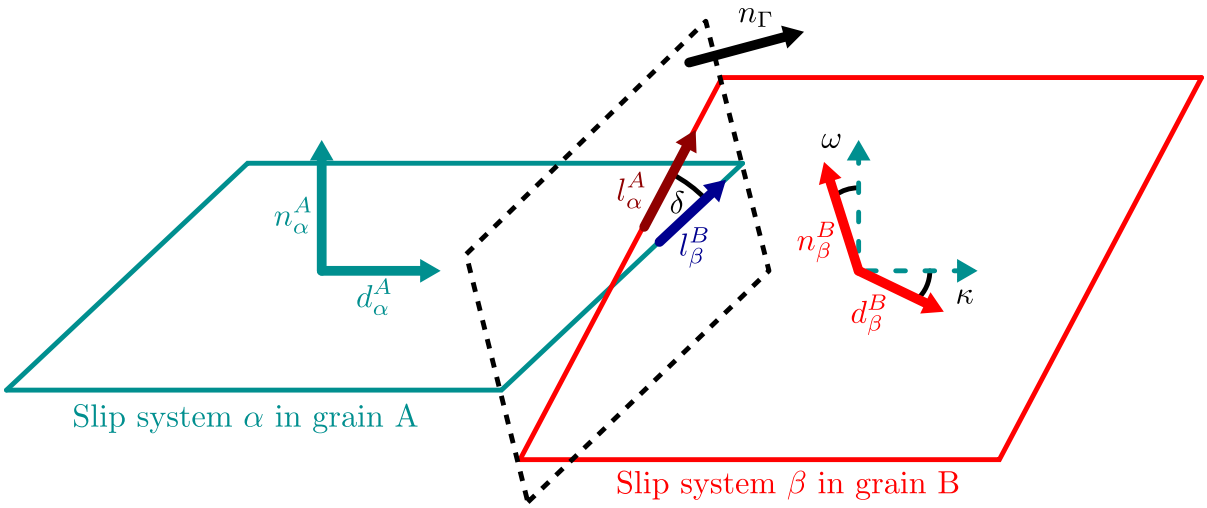

Figure 6.1: Geometric parameters used for calculating slip transmission metrics are shown. Figure based on Bayerschen et al. [167], reproduced with permission of Springer, copyright 2017 Springer Science+Business Media.

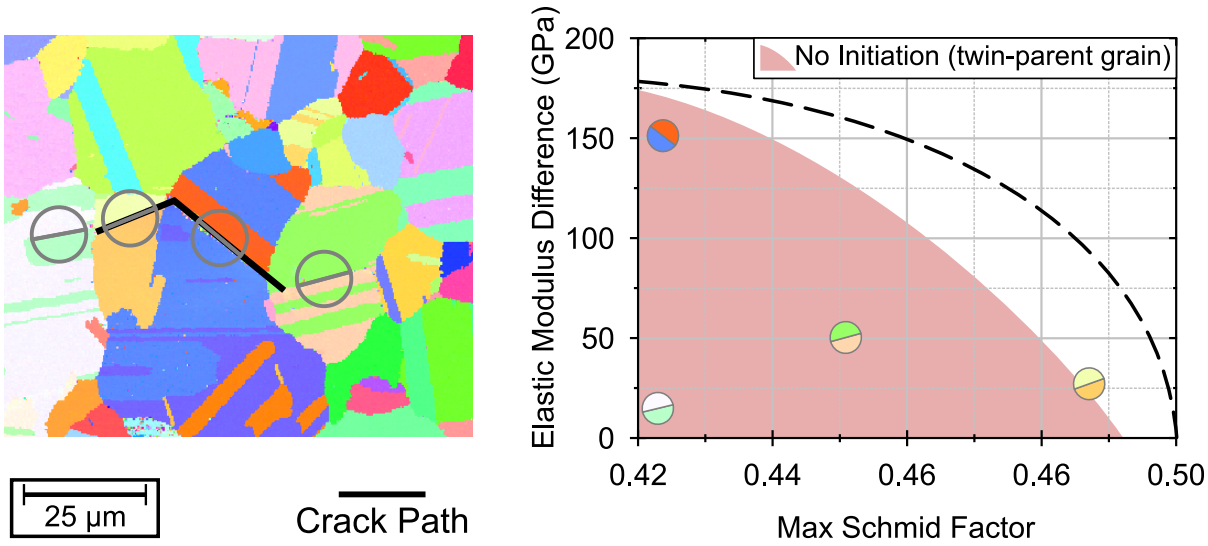

Figure 6.2: The surface of the crack dataset is IPF colored with the crack path indicated in black with twin boundaries on or near the crack path circled (left). The twin boundary between the yellow and orange grains meets the strain localization criterion (right). The crack also propagated along the twin boundary between the red and blue grains which almost meets the localization criterion. The crack was arrested on both ends by boundaries oriented such that they are far from satisfying the localization criterion.

meeting the strain localization criterion. The crack propagated across two boundaries (one twin boundary and one random boundary) and was arrested by a different boundary on each end (also one twin related boundary and one random boundary). None of the metrics calculated showed a strong correlation with crack propagation when computed for each boundary the crack propagated across and was arrested by. Plotting each of the boundaries near the crack by elastic modulus mismatch versus Schmid factor reveals the crack first propagates near a boundary almost meeting the strain localization criterion as shown in figure 6.2. The crack was arrested at each end by twin boundaries far from meeting the strain localization criterion, suggesting that a network of boundaries meeting or nearly meeting the strain localization criterion may promote crack propagation. The first boundary that the crack propagated across is also a twin boundary, emphasizing the importance of twin related domain structure in early fatigue crack growth.

Although twin related domains play critical roles in both fatigue crack initiation and growth, their 3D structure and connectivity is poorly understood. Annealing twins have

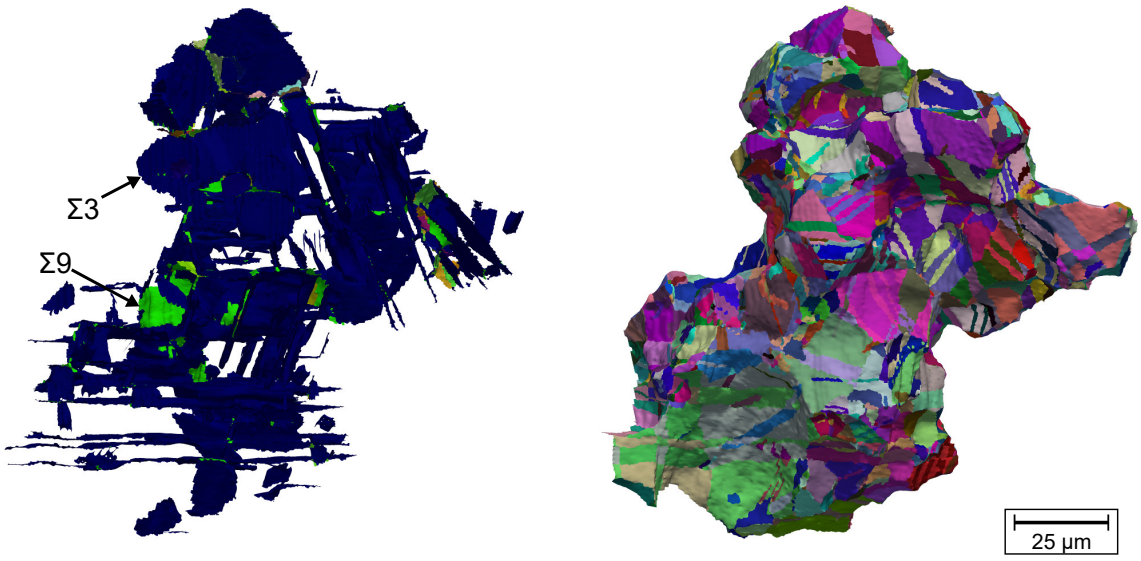

Figure 6.3: The internal boundaries for a single large reconstructed twin related domain are shown with dark blue and green corresponding to Σ3 and Σ9 boundaries, respectively (left). The complex internal twin structure of each individual domain compounds for boundaries with neighboring domains, resulting in a myriad of misorientations (right).

been characterized in 3D for austenitic stainless steel [168] and $NiMn_2$ [85]. Although the morphology of individual twins was qualitatively analyzed, quantitative measures of twin structure are lacking. The high degree of twinning in René 88DT makes even qualitative visual observations challenging, as shown in figure 6.3

6.1 Twin Related Domain Structure

A network interpretation of twin related domain structure allows for more effective qualitative observations and microstructure quantification. Each grain in a twin related domain is represented as a network node and each grain boundary as a network edge (the link between two directly connected nodes). Network nodes are assigned grain traits (e.g. size, centroid, or average orientation) and network edges are assigned boundary traits (e.g. disorientation or surface area) as shown in figure 6.4. Positioning, scaling, and coloring by attributes allows many qualities of a twin related domain to be visual-

ized simultaneously (figure 6.5) and allows better observation of the internal structure compared to volume renderings (figure 6.6).

Twin related domains in René 88DT with relatively few unique orientations may still have many distinct grains from repeated twinning back and forth between two orientations. A simplified orientation space network representation may be created by grouping nodes with the same orientations and grouping edges between the same two orientations. These reduced networks may be plotted in orientation space instead of real space to appreciate the variant structure of the network as shown in the top of figure 6.7. Networks may also be visualized in 2D by sacrificing physical meaning of node position as shown in the bottom of figure 6.7.

6.2 Qualitative Observations

The network representation of twin related domains was constructed for all fully contained grains in the grain scale 3D dataset. 424 of 570 fully contained domains contained more than one orientation. The domains are rendered as a volume and as networks for each domain in figure 6.8. The networks are significantly biased toward smaller and less complicated domains since many twin related domains in the dataset are connected to the exterior through a series of twin relationships.

Qualitatively there are two main populations of twin related domain network morphology. Some domains have one dominant central orientation with many small nodular grains as shown in figure 6.9 while others have a 'backbone' of smaller grains alternating between the same two twin related orientations as shown in figure 6.10. The complexity and number of grain boundaries both within and bounding twin related domains can result in falsely merging two neighboring twin related domains that have a near twin disoriented patch as shown in figure 6.11.

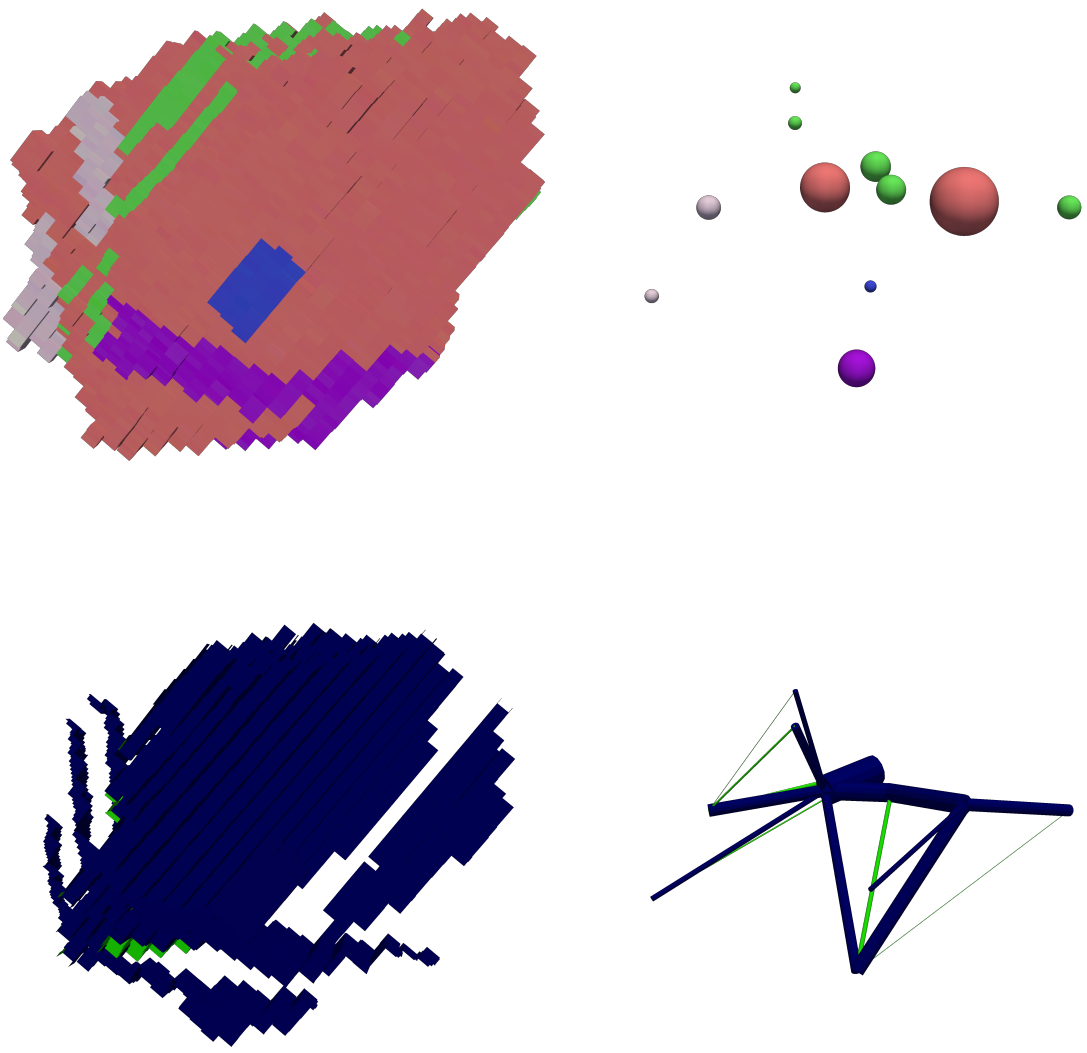

Figure 6.4: Grains of a twin related domain (top left) become nodes (top right) and grain boundaries (bottom left) become edges (bottom right) in the network representation. Grains and nodes are IPF colored. Nodes are positioned at the corresponding grain centroid and scaled by equivalent diameter. Edges are drawn between nodes, colored by boundary disorientation, and scaled by surface area$^{\frac{1}{2}}$.

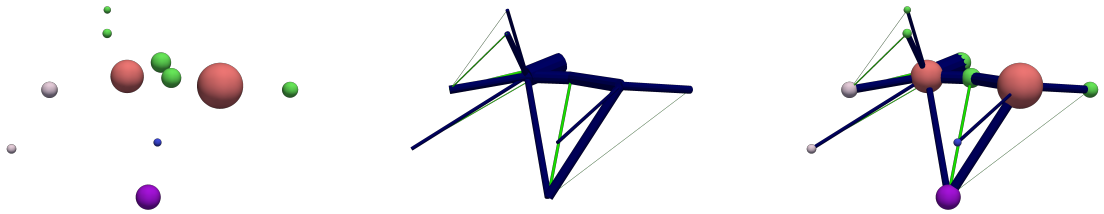

Figure 6.5: Nodes (left) and edges (center) of the network representation of a twin related domain can be visualized simultaneously (right) to appreciate many aspects of domain structure simultaneously.

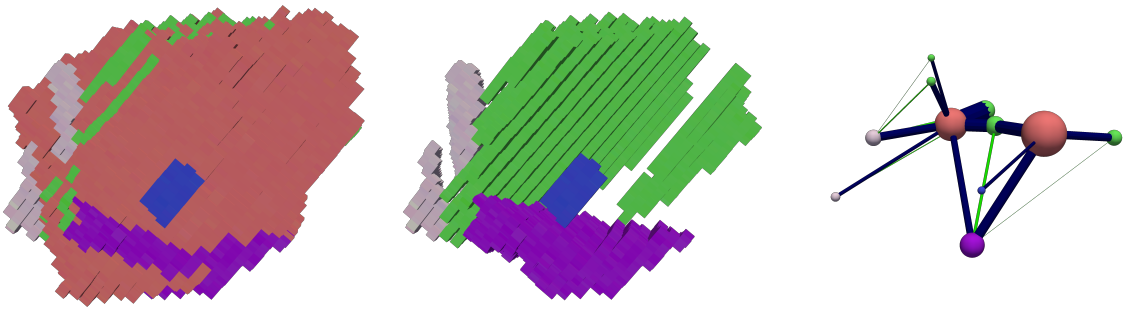

Figure 6.6: Appreciating the internal structure of a twin related domain is challenging with a volume rendering (left). Removing the largest volume fraction variant (center, orange orientation removed) or using a grain boundary mesh helps for simple domains, but a network visualization (right) makes connectivity obvious.

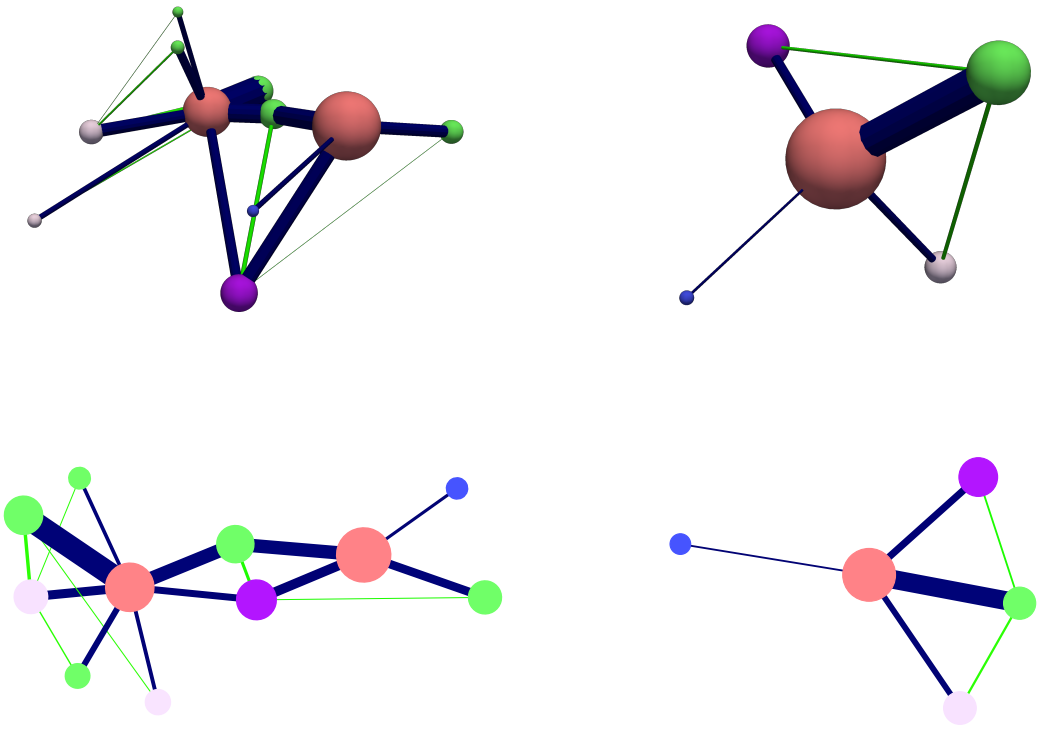

Figure 6.7: The real space network representation of a twin related domain (top left) may be reduced to orientation space (top right) by grouping like nodes and edges. Nodes in the reduced network are colored by the average of each grain orientation averaged with volume weighting, sized by total volume of like grains. Nodes in the reduced network are positioned by orientation in cubochoric space [169] with the largest volume node placed at the symmetric equivalent orientation closest to the origin and the neighboring nodes placed at the symmetric equivalent orientation closest to the corresponding twin misorientation with the largest volume node. A simplified 2D version of real space (bottom left) and orientation reduced (bottom right) networks can be created by sacrificing physical meaning of node positions. 2D positions were determined using a Fruchterman-Reingold force-directed algorithm [170] with eigenvectors of the network Laplacian used as seed positions.

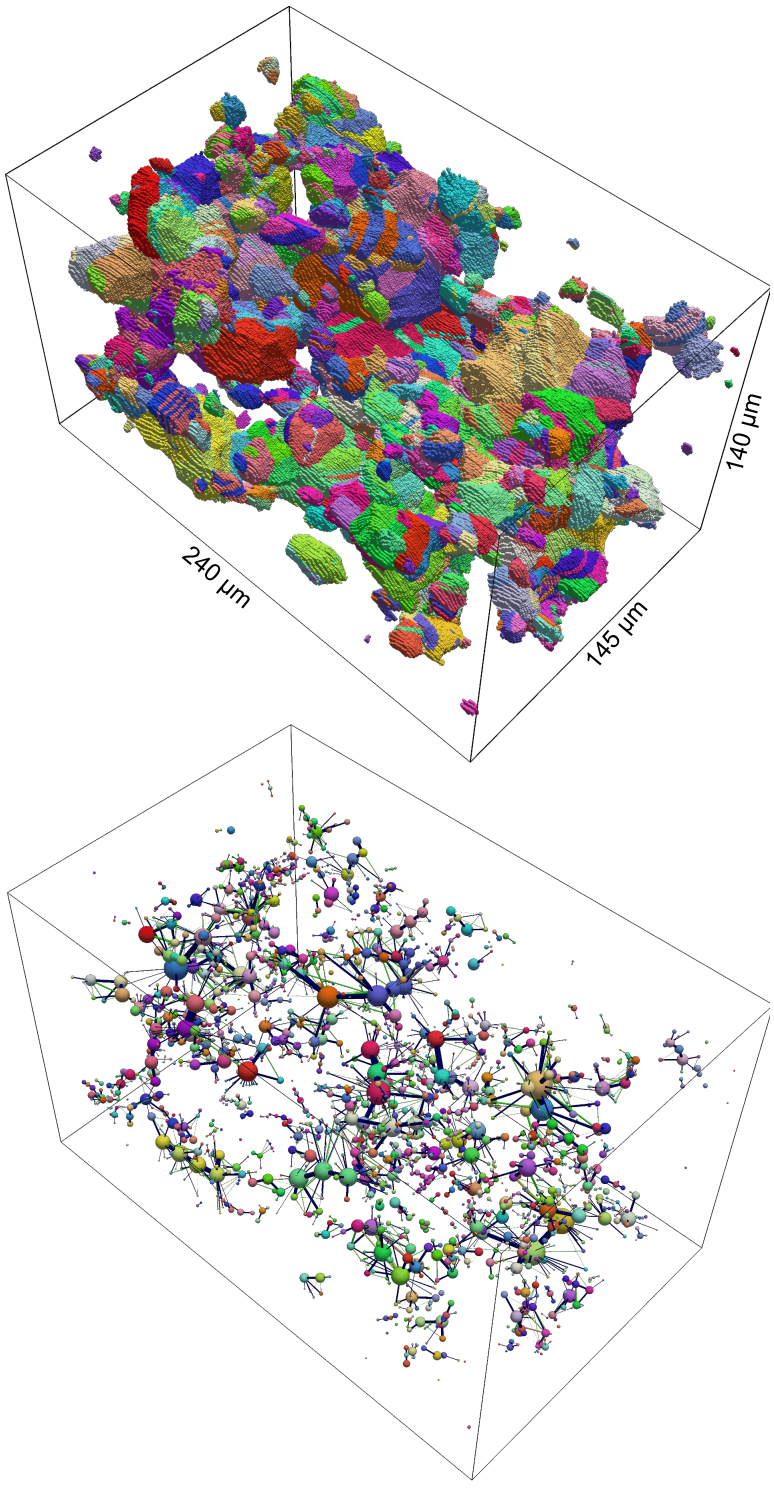

Figure 6.8: All fully contained twin related domains in the grain scale dataset are rendered as volumes (top) and networks (bottom).

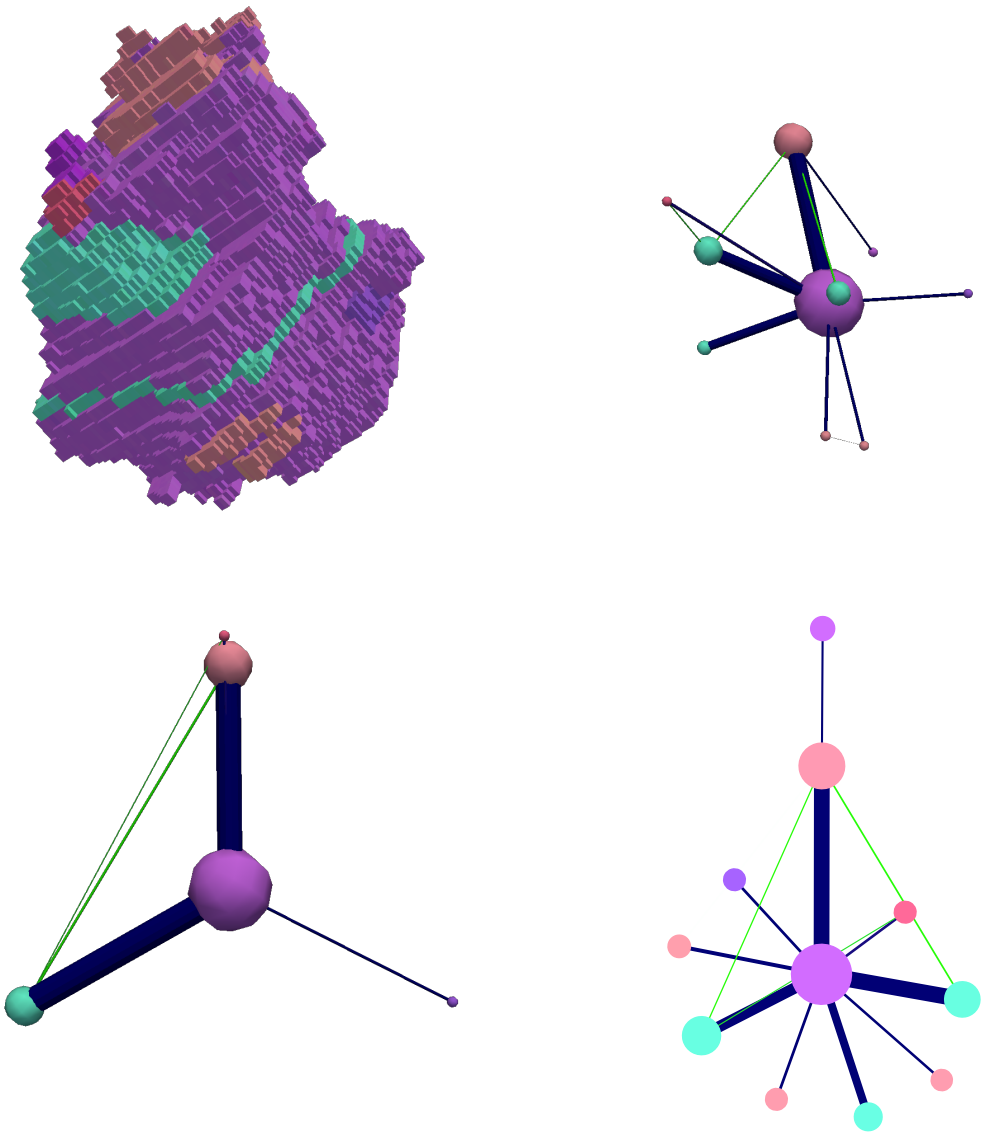

Figure 6.9: An example of a nodular type twin related domain is rendered by volume (top left), as a real space network (top right), as an orientation reduced network (bottom left) and in 2D (bottom right).

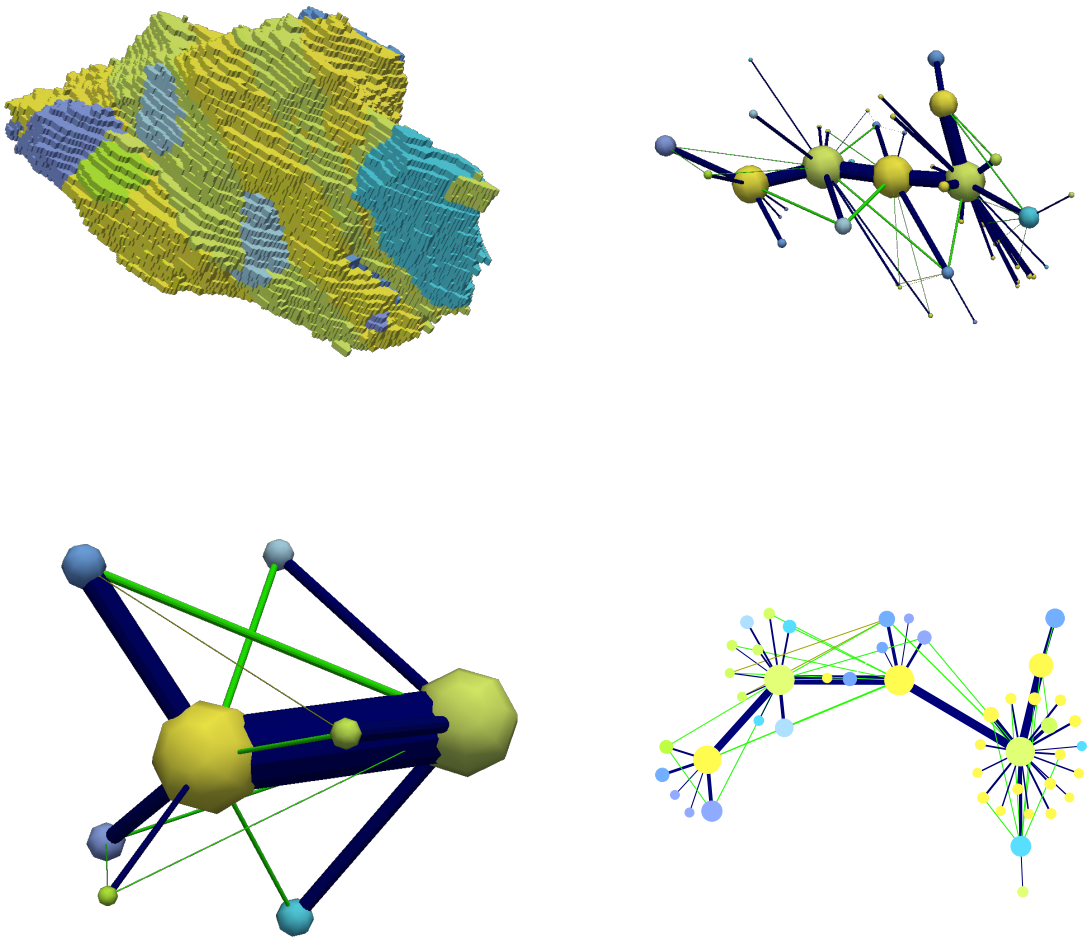

Figure 6.10: An example of a backbone type twin related domain is rendered by volume (top left), as a real space network (top right), as an orientation reduced network (bottom left) and in 2D (bottom right).

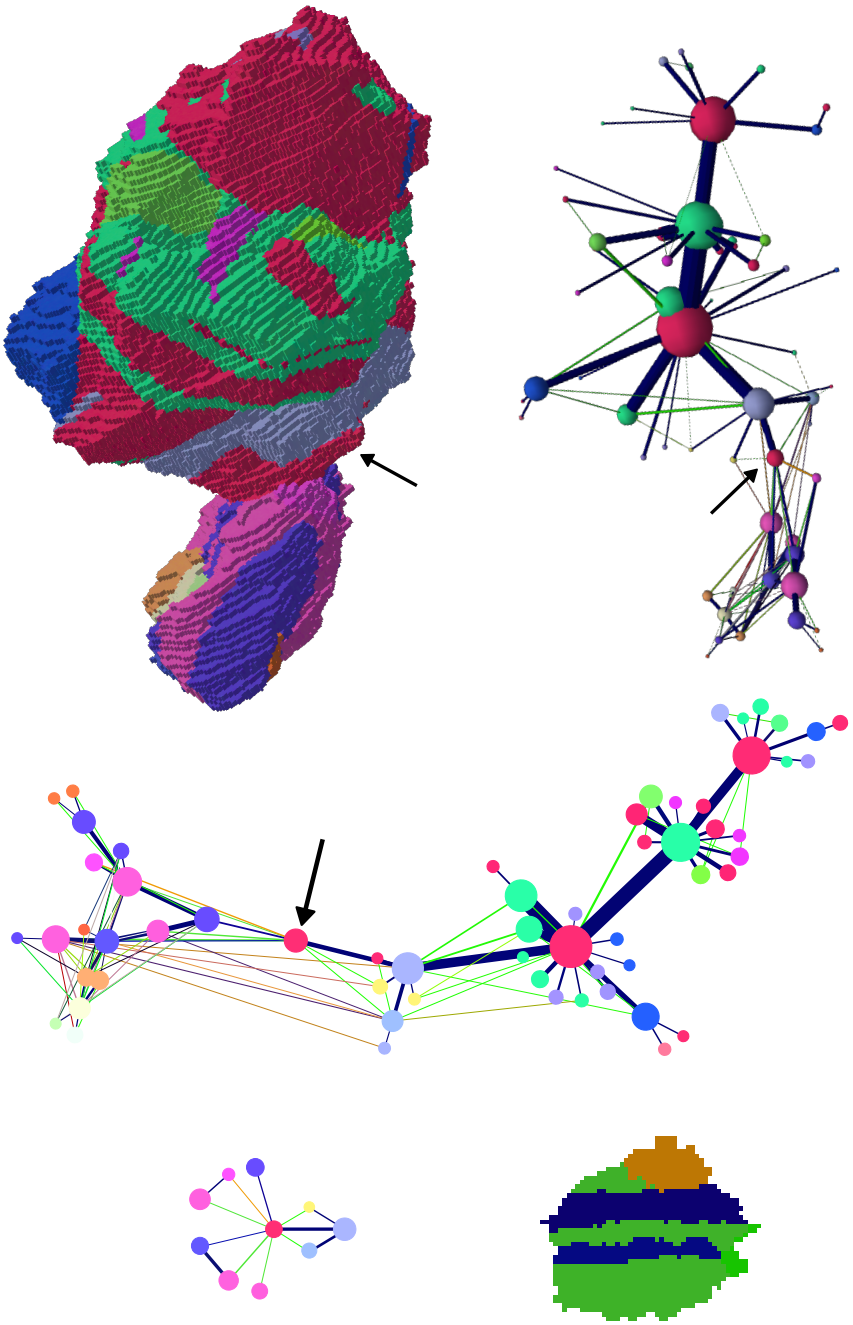

Figure 6.11: Two incorrectly grouped neighboring twin related grains are rendered as a volume (top left), a real space network (top right), and a 2D network (middle). A single grain (node) with two grain boundaries (edges) within the twin misorientation tolerance linking the two concave domains is indicated by the arrow. A sub-network of only nodes adjacent to the choke point grain (bottom left) and the interface between the two domains (bottom right) more clearly show the random grain boundaries within twin tolerance.

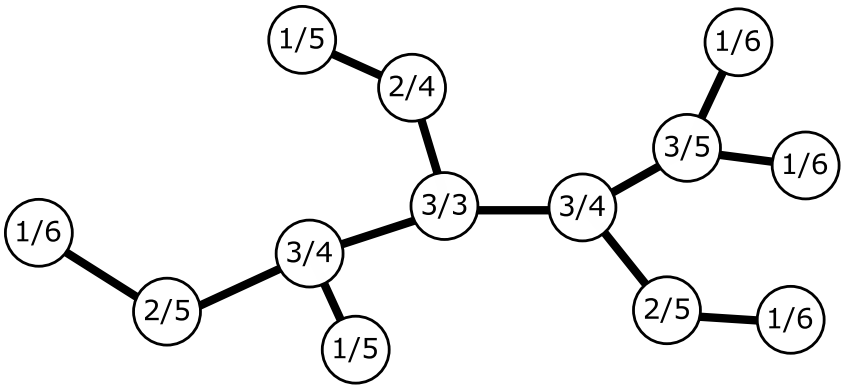

Figure 6.12: A graph is shown with the degree (number of neighboring nodes) and eccentricity (distance to the furthest node in the graph) listed in each node. The graph radius is the minimum eccentricity (3) and the diameter is the maximum eccentricity (6). Nodes with eccentricity equal to the radius are the graph center and those with eccentricity equal to the diameter are the graph periphery.

6.3 Quantitative Measurements

A variety of measures from graph theory have physical meanings for networks of a twin related domain. Node degree (number of neighboring nodes), node eccentricity (distance to the furthest node in the graph), graph radius (minimum node eccentricity), graph diameter (maximum node eccentricity), and center (nodes with eccentricity equal to graph radius) are illustrated in figure 6.12. Network measures are calculated considering only twin related edges in this work, but all edges could be included. The number of nodes in an orientation reduced network corresponds to the number of variants. Node degree corresponds to the number of twin related neighbors or variants in real space and orientation reduced networks respectively. Radius and diameter correspond to lower and upper bounds respectively on the number of twin generations within the twin related domain.

The following values were measured for each of the 570 fully contained twin related domains:

- Surface area

- Twin boundary area (both as meshed and projected along the coherent twin direction)
- Non-twin internal boundary area
- Number of grains
- Number of variants
- Volume and equivalent diameter
- Volume of the largest grain
- Volume of the largest variant
- Number of twin boundaries
- Number of non-twin boundaries
- Graph diameter and radius of the real space network
- Graph diameter and radius of the orientation reduced network
- Distance from real space network graph center to largest grain
- Distance from orientation reduced network graph center to largest variant
- Number of boundaries meeting the strain localization criterion assuming boundary length is equivalent diameter of coherent projected twin surface area

Histograms of graph radius and diameter are shown for the real space networks in figure 6.13 and for the orientation reduced networks in figure 6.14. A histogram of twin related domain equivlant diameter is shown in figure 6.15.

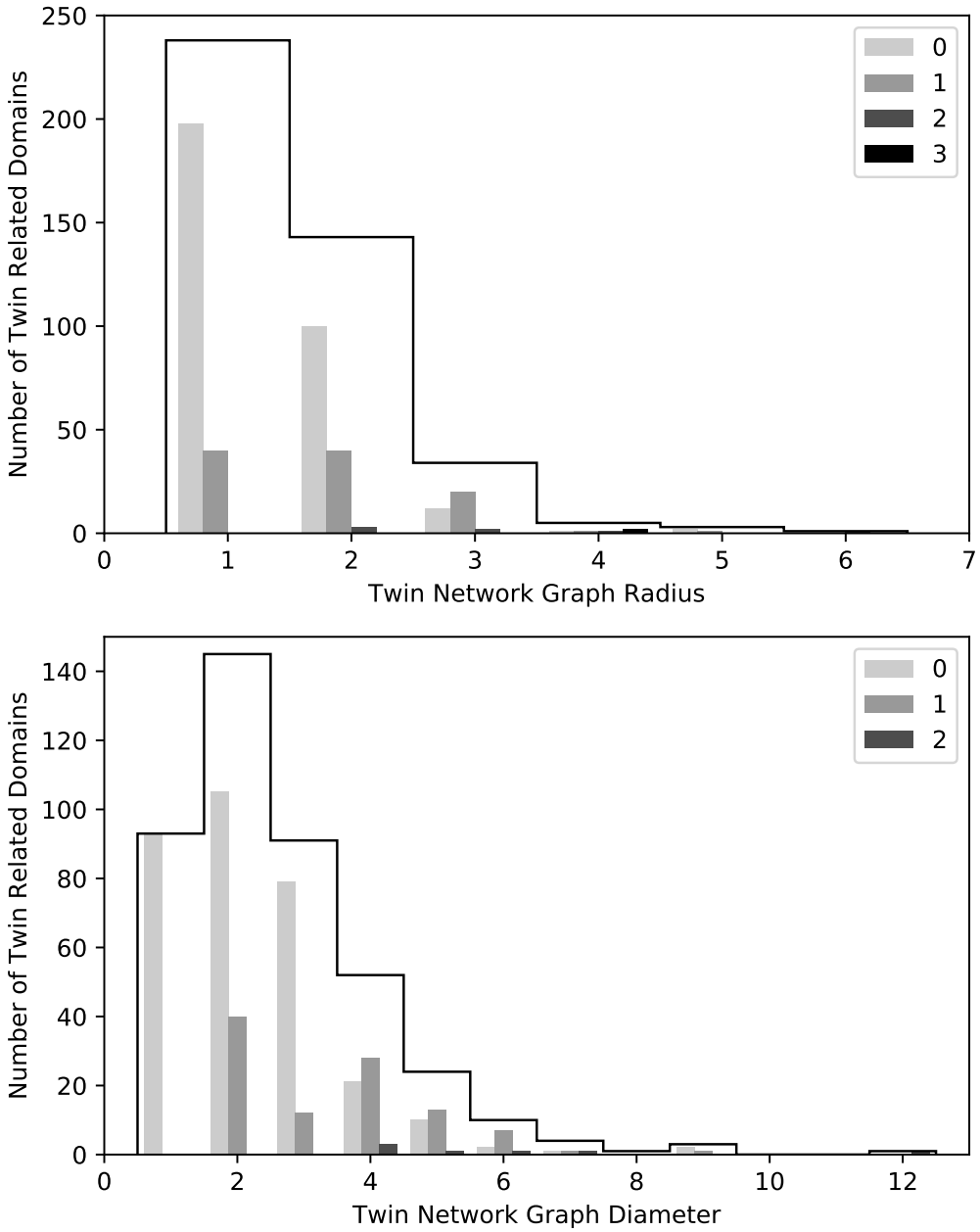

Figure 6.13: Histograms of the graph radius (top) and diameter (bottom) are shown for real space networks of twin related domains with at least two orientations. Domains are split and colored by the distance of the largest node from the network's graph center.

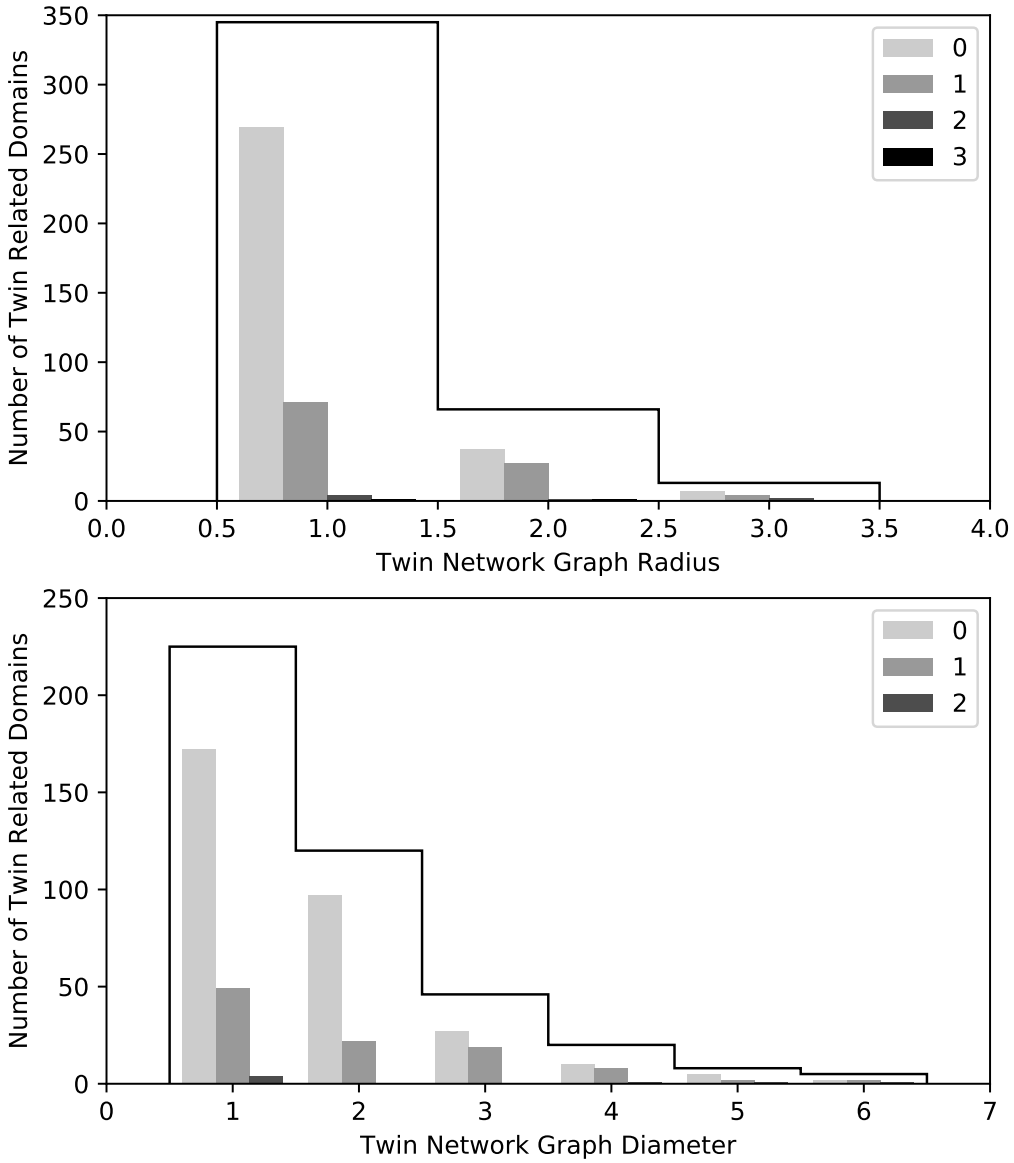

Figure 6.14: Histograms of the graph radius (top) and diameter (bottom) are shown for orientation reduced networks of twin related domains with at least two orientations. Domains are split and colored by the distance of the largest node from the network's graph center.

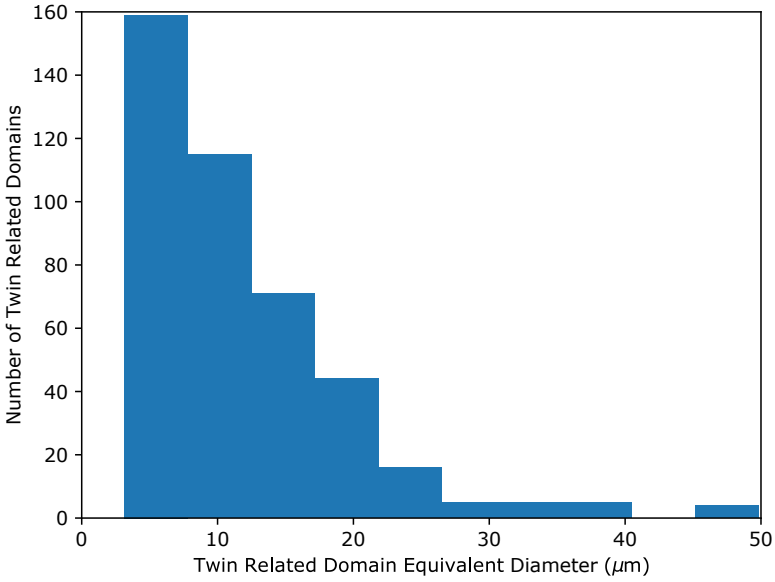

Figure 6.15: A histogram of fully contained twin related domain equivalent diameter is shown. The average grain size for grains within the domains plotted is 6 µm.

6.3.1 Parent Orientation Identification

Commercial software packages can remove twins by filling each twin related domain with the average orientation of the dominant variant (parent orientation) [171]. These algorithms were developed for mechanical twins and are insufficient for the complex annealing twin structure of René 88DT, even when the full 3D structure is known. A histogram of volume fraction of the largest grain and variant is shown in figure 6.16 with domains categorized by the distance from the largest grain or variant to the network's graph center. Even when grains are grouped into variants, the largest orientation is frequently less than half of the domain volume and the largest volume variant may not be the graph center.

Plotting volume fraction of the largest grain against twin related domain equivalent diameter as shown in figure 6.17 reveals that domains with a single dominant orientation are only possible at intermediate sizes. Smaller domains tend towards an even split between two orientations and larger domains have too many variants for a single one to

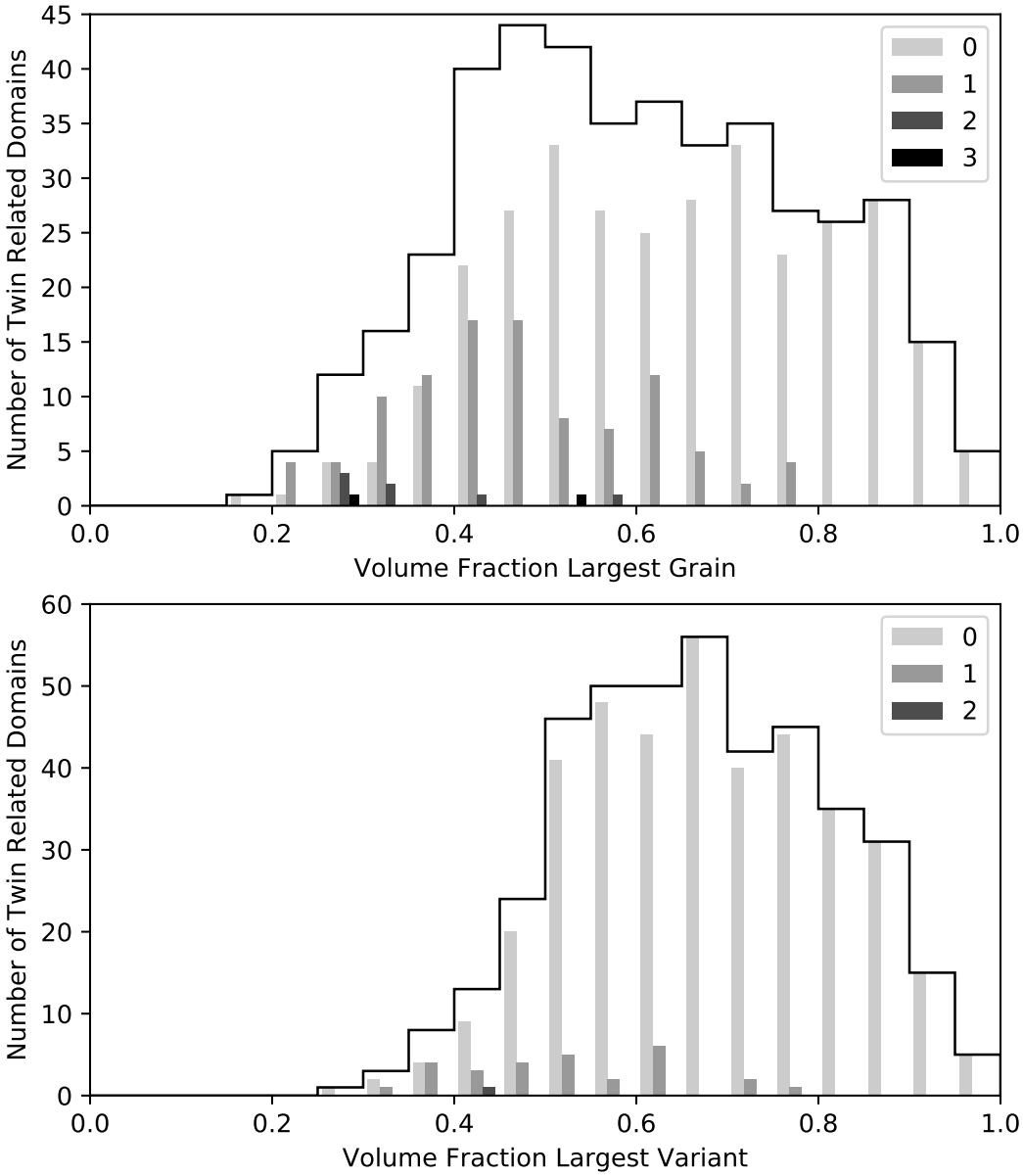

Figure 6.16: Histograms of the volume fraction of the largest single grain (top) and largest single orientation (bottom) are shown for twin related domains with at least two orientations with domains split by the distance of the largest node from the network graph center.

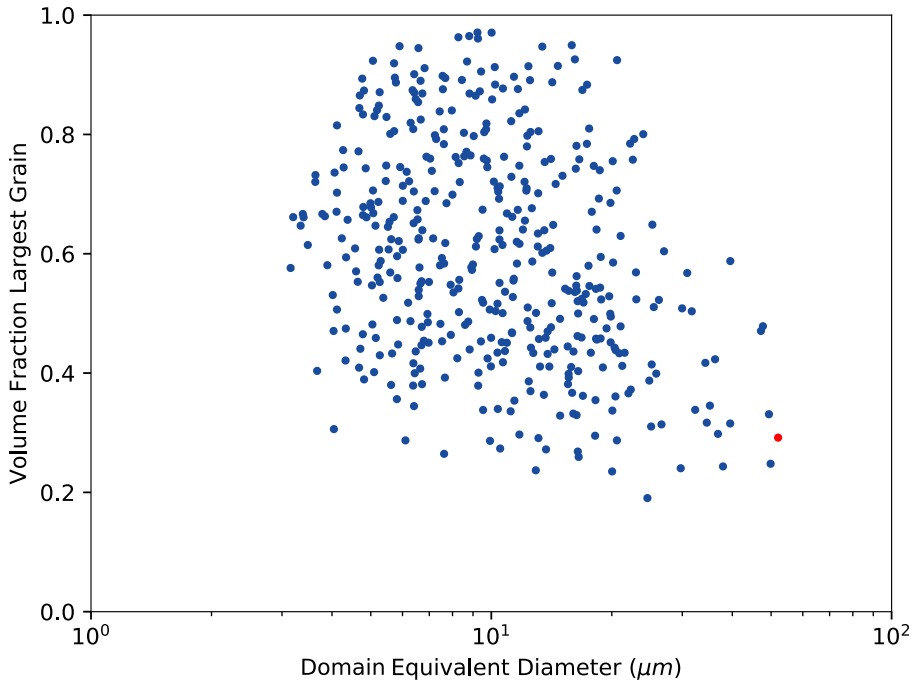

Figure 6.17: Volume fraction of the largest domain cluster is plotted against domain size revealing a single dominate orientation only occurs for intermediate sized domains.

dominate. Based on the data shown in figure 6.13, figure 6.14, figure 6.16, and figure 6.17 the concept of a single parent orientation may not always be appropriate. If an orientation must be selected, the orientation of the central node in the orientation space reduced network appears to be the most robust choice. The concept of a parent orientation is most appropriate when the reduced network has a radius of 1 and the central node has the largest volume fraction.

6.3.2 Annealing Twin Formation

Accurate measurements of twin boundary density are a critical metric for studies of annealing twin formation mechanism. Density is properly measured in 2D experiments by line intercept. Since volume and twin boundary area are measured for each twin related domain, twin boundary density can be measured directly on a per domain basis without the need for stereology. Twin boundary density versus domain size is plotted in figure 6.18 and twin boundary area versus domain size in figure 6.19.

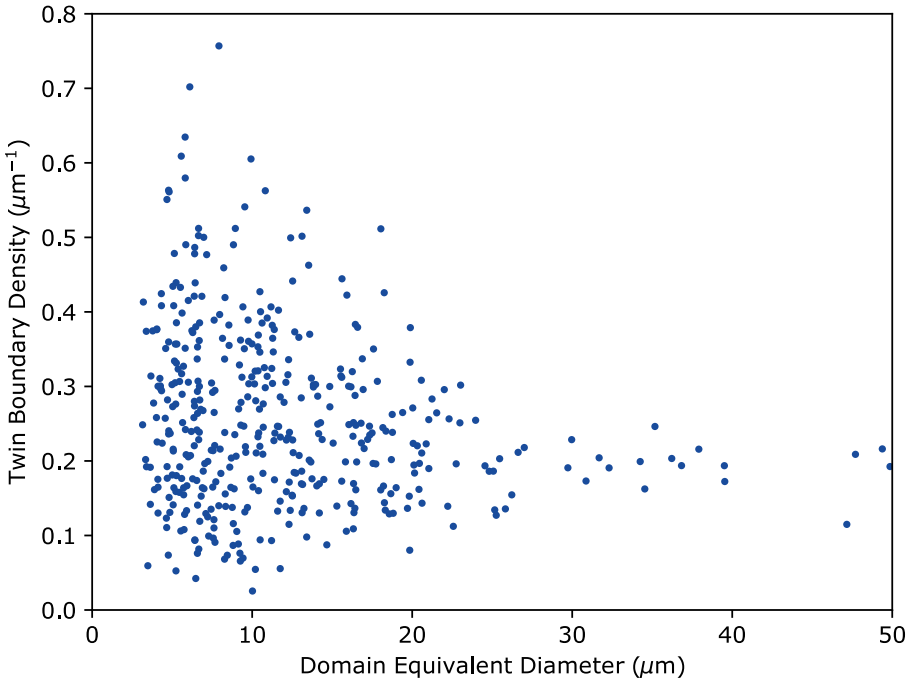

Figure 6.18: Twin boundary density (area per volume) is plotted against domain equivalent diameter for all fully contained twin related domains with at least one twin boundary.

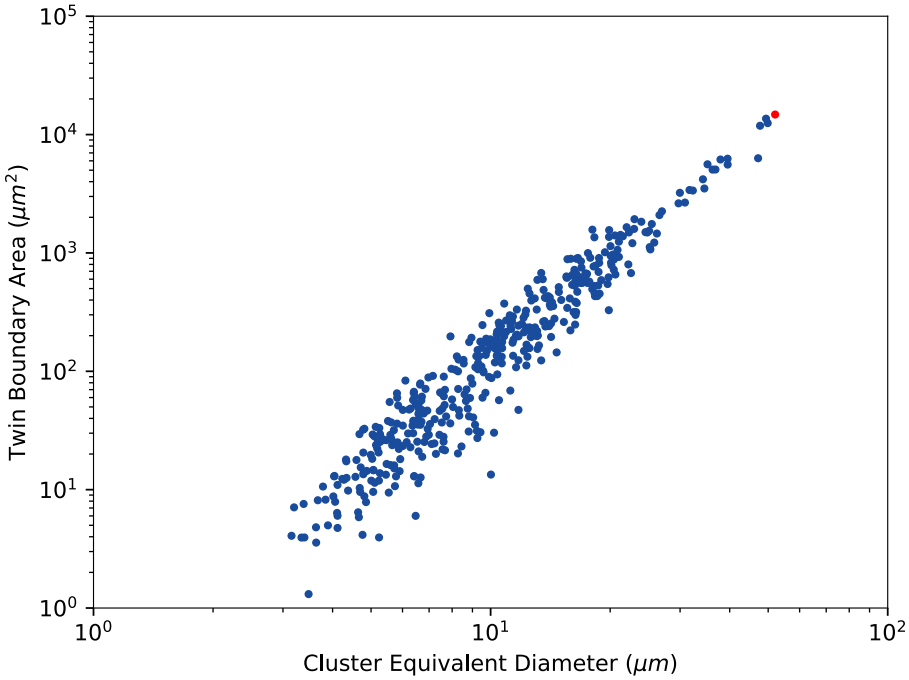

Figure 6.19: Twin boundary area is plotted against domain equivalent diameter for all fully contained twin related domains with at least one twin boundary.

Boundary density appears relatively constant with decreasing scatter as domain size increases. In Gleiter's growth accident model of twin formation the primary microstructural variable controlling twinning probability p is the difference in energy between the growing and the shrinking grains ΔG^o:

$$p = \exp\left\{\left(\frac{Q}{kT} - \ln\left(\frac{\Delta G^o}{kT}\right)\right) \Big/ \left(1 - \frac{\pi\epsilon^2 h^2}{\sigma_z kT\left(\frac{Q}{kT} - \ln\left(\frac{\Delta G^o}{kT}\right)\right)}\right)\right\} \tag{6.1}$$

with more details of the model described in chapter 2. This model of twin formation suggests decreasing twin boundary density with increasing domain size if curvature is the primary driving force for grain boundary migration (ΔG^o). The model predicts a constant twin boundary density with increasing domain size if stored strain energy density is the primary driving force for migration, since the constant driving force results in a constant probability of nucleating a faulted {111} plane. Recrystallized grains consuming deformed grains should have constant twin density and grain growth within a fully recrystallized microstructure should create an inverse relationship between domain size and twin density. The profile of boundary density versus grain size is consistent with a constant twin probability with increased scatter at lower domain sizes consistent with nucleating fewer {111} planes (i.e. a smaller number of samples).

A simple model of spherical grains growing on 8 {111} facets and assuming that a nucleated twin boundary propagates across the full final area of the grain is illustrated in figure 6.20. The twin boundary area a_n created by nucleation of a single faulted {111} plane is:

$$a_n = \pi(r^2 - r_n^2) = \pi h^2(n^2 - n_n^2) \tag{6.2}$$

where r and n are the final grain radius in meters and number of {111} planes respectively, r_n and n_n are the grain radius when the twin boundary nucleates, and h is the {111} plane spacing. The cumulative expected twin boundary area when recrystallized grains

impinge, A, within a domain grown on 8 $\{111\}$ facets is:

$$A = 8\sum_{n_n=1}^{n} pa = 8\sum_{n_n=1}^{n} p\pi h^2(n^2 - n_n^2) = \frac{4}{3}p\pi h^2 n(4n+1)(n-1) \tag{6.3}$$

where p is the probability that a given $\{111\}$ plane nucleus is faulted and computed using Gleiter's model. Assuming $n \gg 1$, a reasonable assumption since even a small 1 µm diameter nickel grain has a radius of 2460 $\{111\}$ planes, enables approximating total twin boundary area with a simpler form:

$$A \approx \frac{16}{3}p\pi h^2 n^3 \tag{6.4}$$

Dividing by the volume of the spherical grain yields an expected density of:

$$density = \frac{4p}{h} \tag{6.5}$$

Working backwards from the observed twin density of $0.2\,\mu m^{-1}$ results in a twinning probability of 0.01. Assuming a forging temperature of 1000 °C and the physical constants shown in table 6.2, the stored strain energy density required for a twinning probability of 0.01 is $383\,MJm^{-3}$. This density corresponds to a plastic strain of 2.5 (250%) for a flow stress of 150 MPa [172].

Table 6.2: Values used for computing ΔG^o from p, after Cahoon et al. [71].

Variable	Value	Units
ϵ	0.497	Jm^{-2}
h	$2.0346 * 10^{-10}$	m
σ_z	0.0336	Jm^{-2}
k	$1.3806 * 10^{-23}$	JK^{-1}
T	1273.215	K
Q	$2 * 10^{-19}$	J

Finally, formation by growth accident or other boundary migration based formation models can only account for five variants if the growth plane normals are fixed because

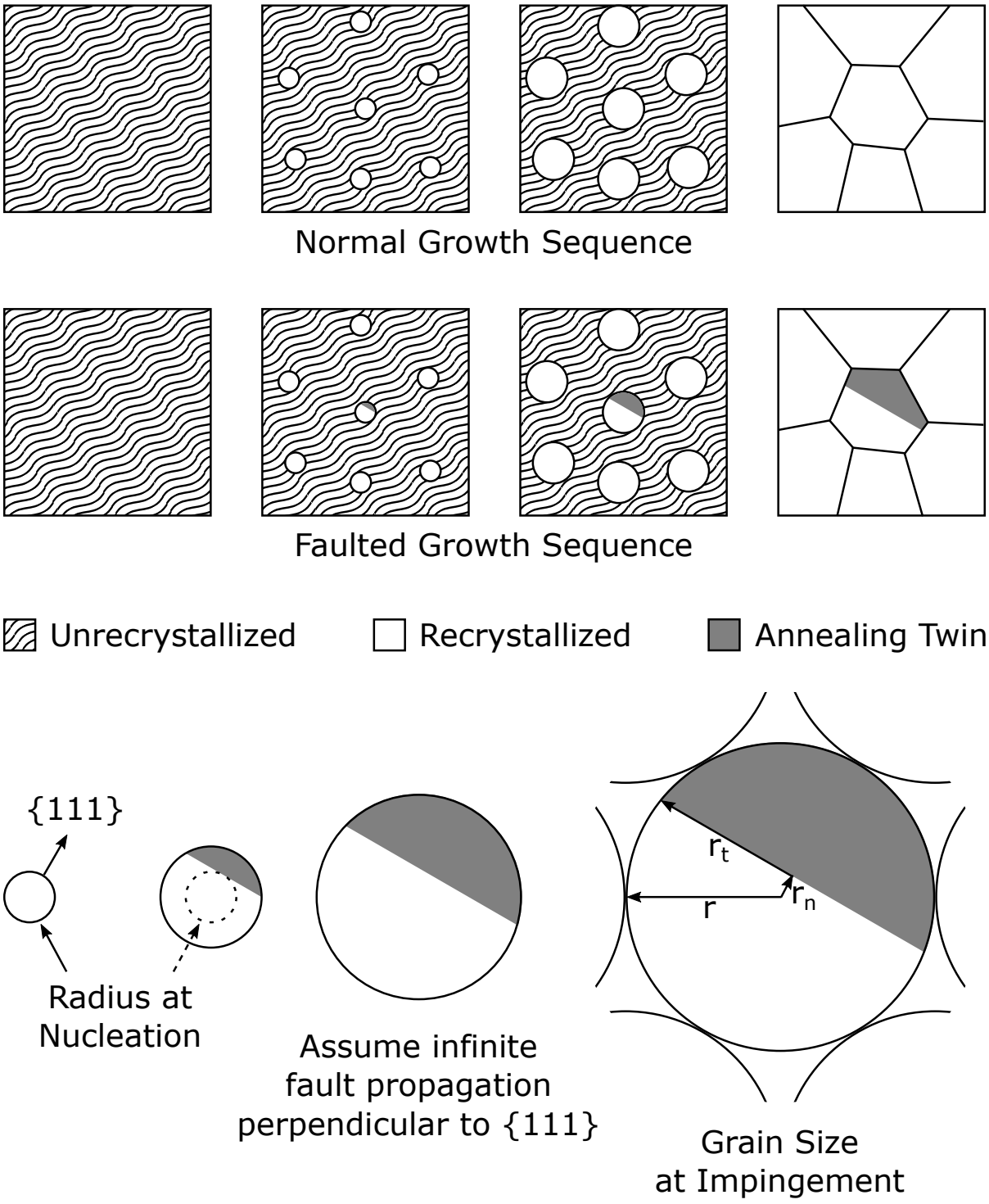

Figure 6.20: A simple model for annealing twin area resulting from a nucleated fault is shown.

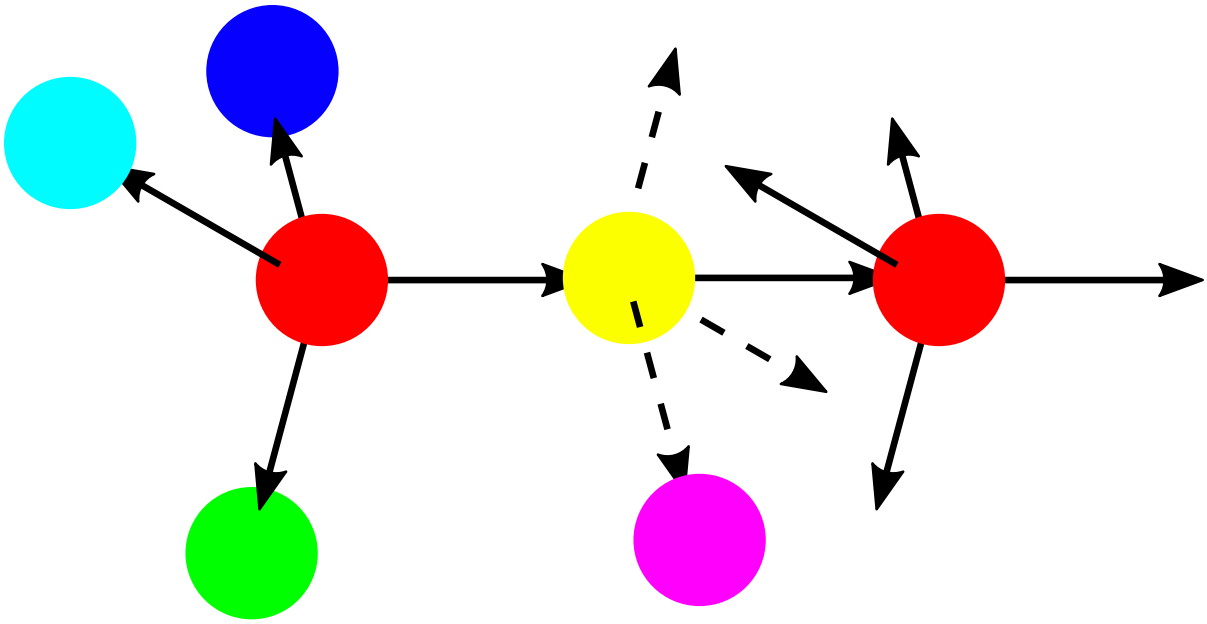

Figure 6.21: Growth restricted to {111} type planes can only account for five orientation variants in a single twin related domain. A grain with the red orientation can twin into 4 different variants (blue, cyan, green, and yellow) by twinning along the 4 different {111} type planes (solid lines). If growth continues along the same {111} direction and a second fault occurs, the same orientation is recovered (red, right). Nucleation of a sixth variant (magenta) requires the growth direction rotate to a new {111} direction after twinning (dashed lines).

repeated twinning along the same growth direction results in alternating between the same two orientations, as shown in figure 6.21. This is consistent with the 'backbone' morphology observed for some twin related domains. However, a significant number of twin related domains contain more than five orientation variants, as shown in figure 6.22. This suggesting a rotation in migrating grain boundary normals, potentially driven by gradients in stored strain energy density.

6.3.3 Fatal Fatigue Crack Sites

The 3D crack path captured in the crack dataset is shown in figure 6.23 along with neighboring grains and grain boundaries. The crack path has two facets with the smaller facet adjacent to the twin meeting the strain localization criterion. The network representation of the two twin related domains surrounding the crack are shown in figure 6.24.

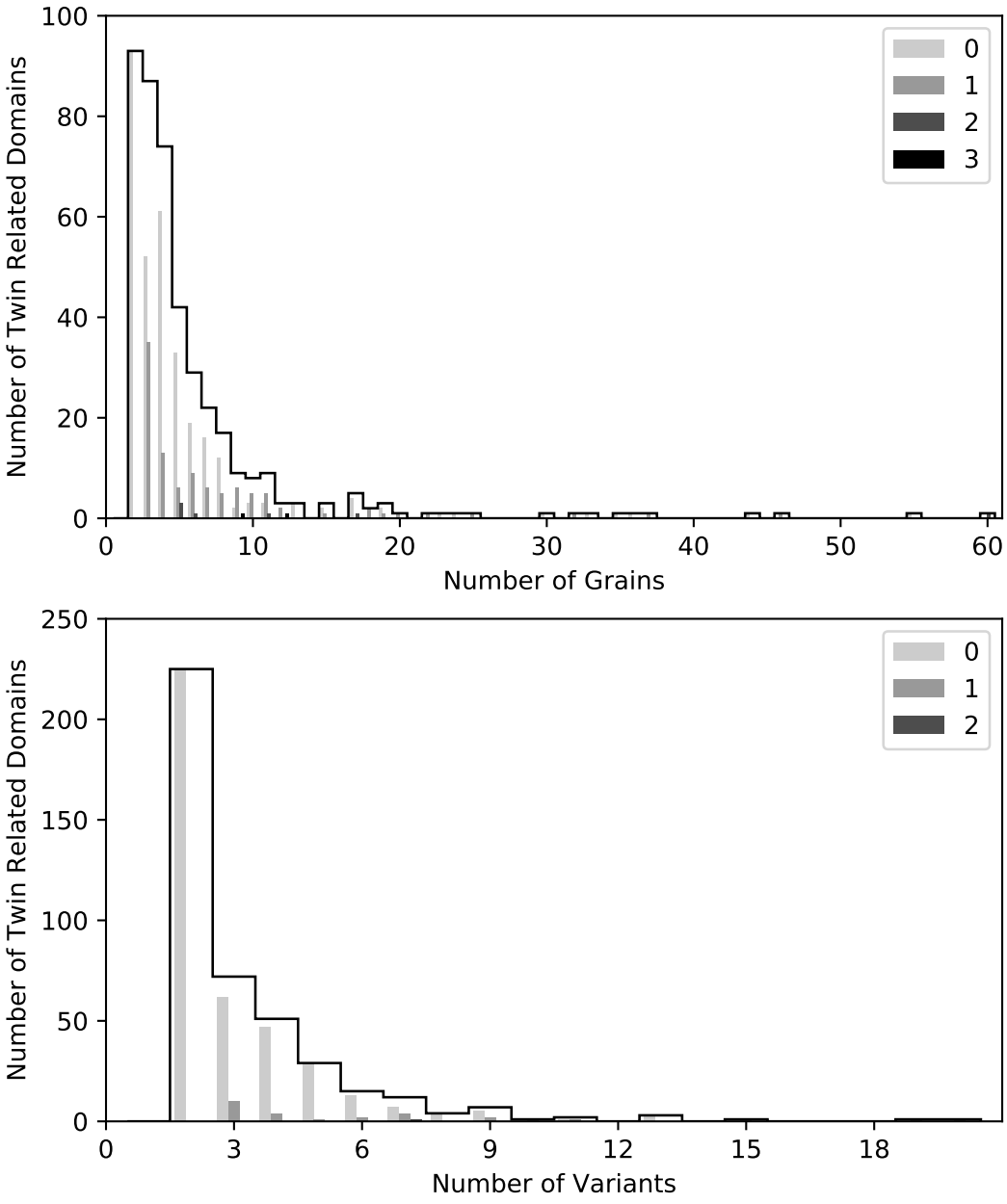

Figure 6.22: Histograms of the number of grains (top) and number of variants (bottom) are shown for twin related domains with at least two orientations with domains split by the distance of the largest node from the network graph center.

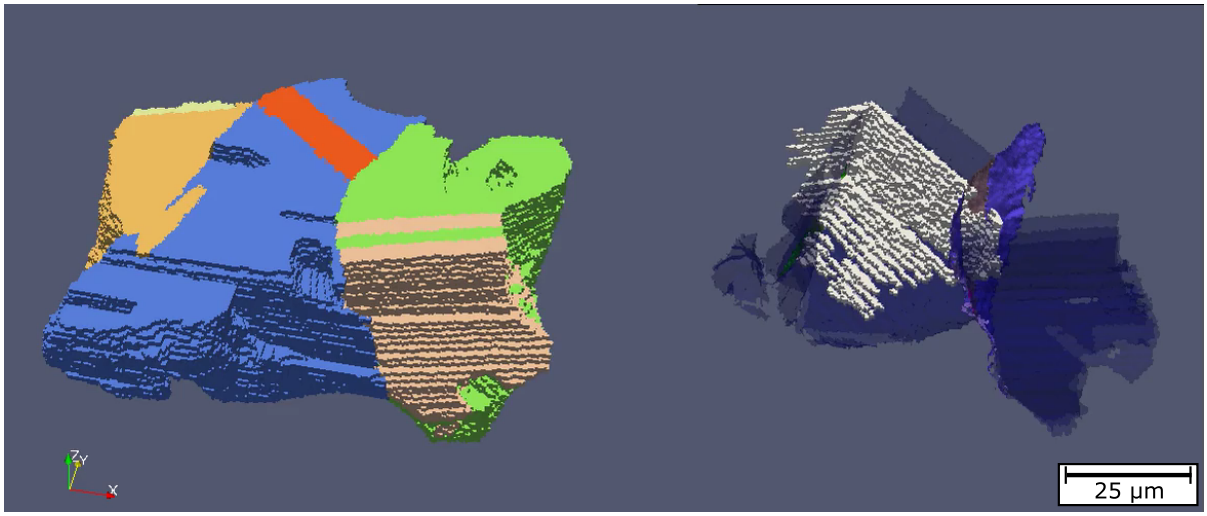

Figure 6.23: Grains touching the crack path are rendered as a volume in IPF color (left) and internal boundaries of those grains are colored by disorientation with twin boundaries slightly transparent (right). The crack path, identified with a threshold on image quality, is rendered as solid white voxels (right). The yellow and orange grain pair meet the strain localization criterion and blue and red pair nearly meet the criterion.

The initiating cluster is larger than all the fully contained clusters captured, and appears to lie at the high end of the tail of most twin related domain distributions, including number of grains (51), number of variants (18), and equivalent diameter (52 µm). This observation is consistent with previous work by Miao et al. suggesting fatal cracks initiate in the large twin or low angle boundary related regions [15]. Although slip transmission metrics don't appear to be correlated with crack arrest or growth across a grain boundary, thresholds on twin related domain descriptors may provide a promising means for developing a criterion for early fatigue crack propagation and fatal crack site identification. Currently statistics for a larger number of twin related domains, both fully capture bulk domains and those containing propagating cracks, are required. Gathering statistics for twin related domains containing cracks and other areas of future work are discussed in chapter 7.

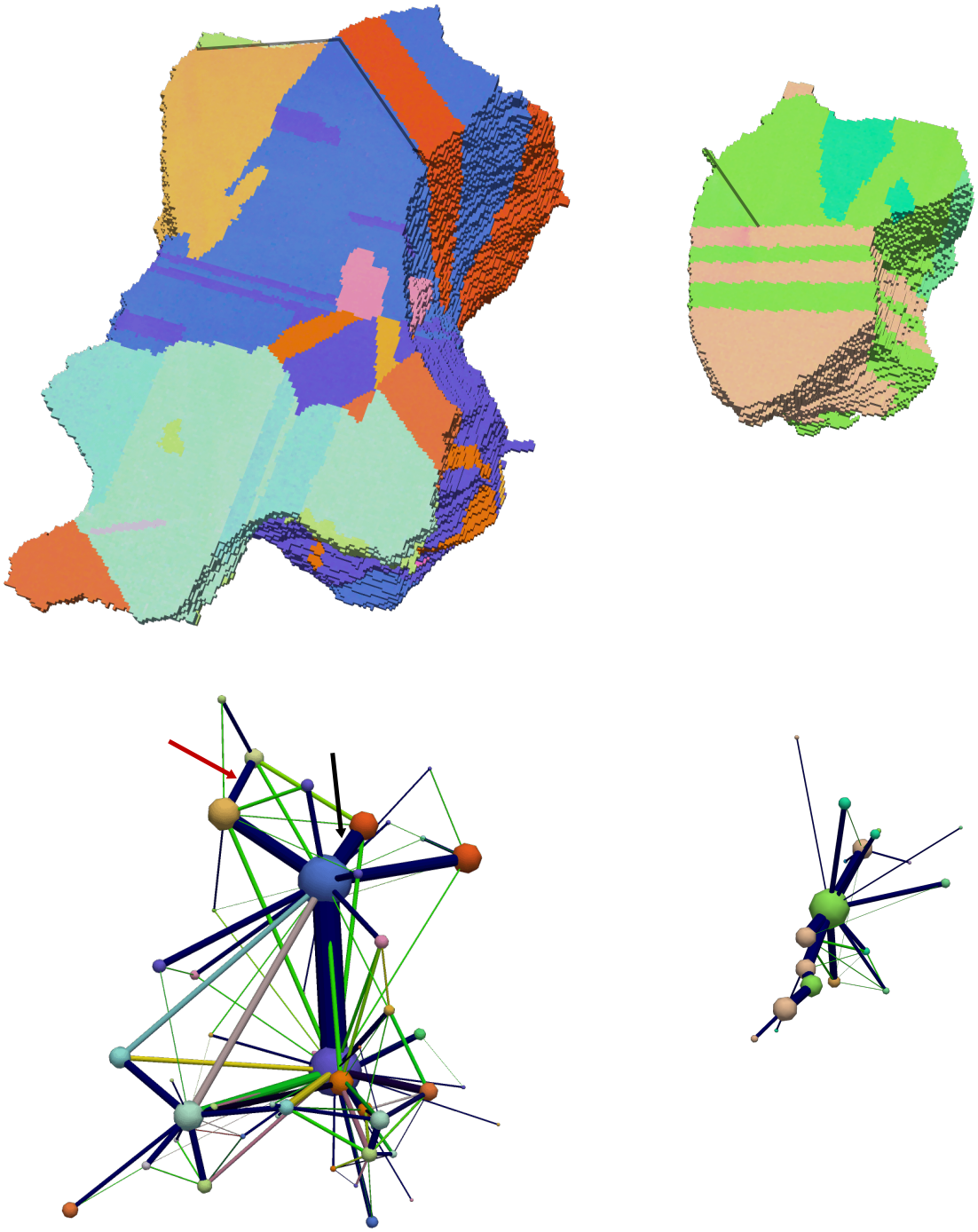

Figure 6.24: The twin related domains where the crack initiated (left) and propagated (right) are rendered as volumes (top) and real space networks (bottom). The black line on the volume renderings shows the crack on the surface and the red and black arrows on the initiating domain network indicated the twin boundaries the crack initiated next to and propagated next to respectively.

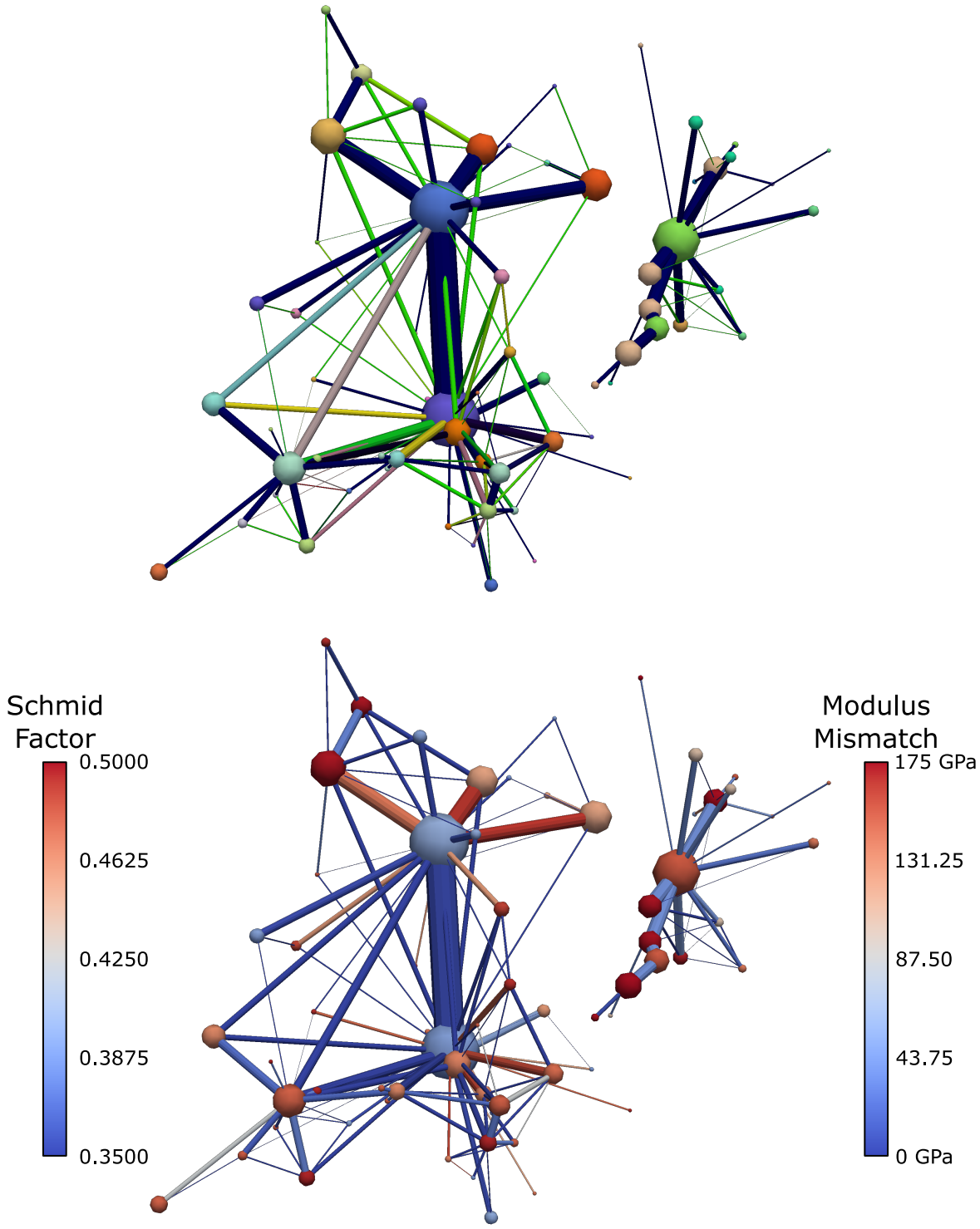

Figure 6.25: The twin related domains where the crack initiated (left) and propagated (right) are rendered as real space networks with nodes colored by IPF color (top) or Schmid factor (bottom) and edges colored by disorientation color (top) or elastic modulus mismatch (bottom).

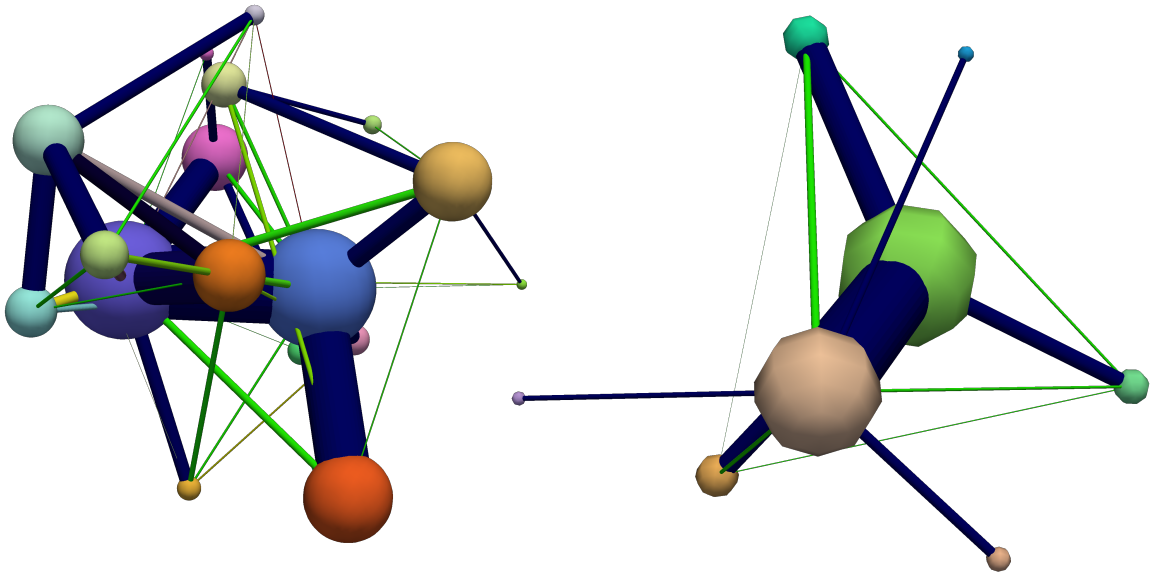

Figure 6.26: The twin related domains where the crack initiated (left) and propagated (right) are rendered as orientation reduced networks.

Chapter 7

Conclusions and Recommendations for Future Work

In this work a property volume element for fatigue crack initiation in polycrystalline nickel-base superalloys has been developed and a potential criterion for fatal fatigue sites identified. The main conclusions from this work are presented in this chapter with suggestions for future research areas discussed.

7.1 Summary and Conclusions

Collecting 3D targeted datasets of René 88DT has enabled characterization of and quantification of microstructural features that cannot be captured from 2D data alone. Insights gained from this work can be leveraged to glean additional information from 2D data in the same or similar material systems. Collecting high quality 3D datasets, producing meaningful reconstructions, and extracting useful quantitative measures requires development and/or implementation of specialized algorithms. Combined, these efforts have refined the criterion for and frequency and spatial location of strain localization events that occur in René 88DT, provided a possible avenue for continued work in mi-

crostructurally short fatigue crack growth, and laid the framework for improved fatigue lifetime predictions. The main individual conclusions are listed below.

1. The TriBeam system enables rapid collection of 3D microstructural data at volumes and resolutions relevant to structural materials problems. Continuing development efforts have improved data quality and made the TriBeam considerably more accessible to new users.

2. Twin boundaries in René 88DT are generally coherent and their density is consistent with the growth accident formation model, assuming stored strain energy density is the primary driving force for boundary migration. Twin boundaries account for 70% of total twin boundary area at the highest resolution measured with a twin boundary density of $0.2\,\mu m^{-1}$ ($2 \times 10^5\,m^{-1}$) for as received material with a 20 µm grain size.

3. A criterion to define convergence of microstructrual and property values has been developed. Comparing the confidence interval of sub-sampled regions to the population mean can be used to define convergence for any scalar value. This method requires accurate measurement of the population mean and independent samples.

4. The property volume element for surface initiation of very high cycle fatigue cracks is at least $440\,\mu m \times 440\,\mu m \times 440\,\mu m$ for René 88DT. The area for convergence may be slightly higher since $440\,\mu m \times 440\,\mu m$ is an appreciable fraction of the area investigated, limiting independence of samples. However, comparison of difference loading directions suggests the property volume element is converged by the 1000 µm × 1600 µm scan area.

5. The network structure of twin related domains cannot be fully understood in 2D and a wide number of metrics can be calculated for twin related domains when their full 3D structure is known. The twin related domains of René 88DT have been

quantified by characterizing distributions of a variety of these measures including grain and variant count, twin area, and graph metrics bounding number of twin generations.

6. Fatigue cracks able to grow beyond the nucleating grain occur in twin related domains on the extremes of microstructural distributions. The twin related domain containing the propagating crack investigated was on the tail of the distribution for grain count, variant count, and domain size.

7.2 Recommendations for Future Work

7.2.1 TriBeam System Development

Development of the TriBeam system has significantly improved the accessibility of femtosecond laser tomography, but considerable room for improvement remains. There are many possibilities for hardware and software improvements including:

1. Chamber and detector contamination would be reinforced by adding a trap to capture ablated material. A pair of biased Faraday cages seems particularly promising given the increased contamination rate observed on the Everhart-Thornley detector scintillator.

2. Modifying the beamline and laser injection geometries could improve the laser field of view and reduce laser distortion by placing the scanning plane closer to the objective lens.

3. A broad ion beam would clean faster and more effectively than the current focused Ga^+ ion beam and could be used for high resolution 3D experiments capturing smaller volumes.

4. Incorporation of an appropriate detector could enable Raman spectroscopy mapping, either with the current laser operating at a lower power or by injecting a second laser with a similar wavelength.

5. Software development to continue the transition from automatic to autonomous operation is crucial to enhanced reliability and ease of use.

7.2.2 Improved Serial Sectioning Dataset Reconstruction

Despite progress on collecting 3D microstructural datasets and analysis to extract quantitative data, comparatively little work has explored improved dataset reconstruction and the parameters required for most algorithms are still frequently selected subjectively. Current algorithms for segmentation, cleanup, and artifact removal are relatively naive with considerable potential available in development of physics informed algorithms. An example particularly relevant to this work is handling twins that are thin with respect to the voxel resolution. Thin twins are segmented into multiple grains if they are not connected. The resulting small grains are likely to be flagged as artifacts, perforating the twin. Prior knowledge about twin morphology and crystallography could be leveraged to group nearby twins, as shown in figure 7.1. Incorporating prior knowledge into reconstruction algorithms may provide significant opportunities to improve dataset fidelity and are likely to have parameters that can be selected quantitatively based on experimental conditions.

7.2.3 Annealing Twin Formation

3D microstructral data of twin related domains offers a powerful tool for studying annealing twin density and formation mechanism since grain size and twin area can be compared on a per domain basis. With 3D data twin density can be measured for individual domains before recrystallization is complete, decoupling recrystallization and

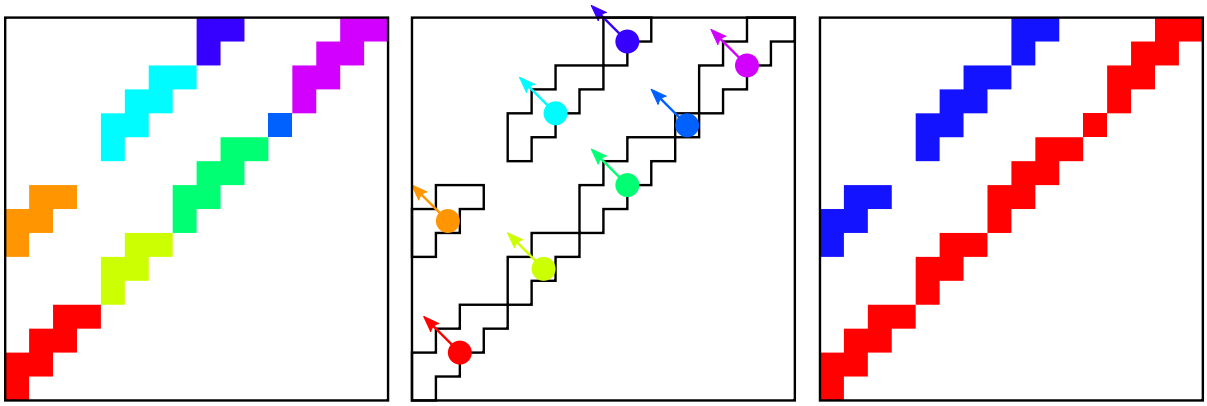

Figure 7.1: Thin twins may be segmented into multiple grains due to resolution (left). A plane can be defined for each small twin using the grain centroid and the coherent normal direction of the largest surface area neighbor (center). Grains of the same variant that define nearly the same plane are grouped (right).

grain growth effects. Brass is a traditional model system for annealing twin formation since the stacking fault of the alpha (FCC solid solution) phase can be tuned by altering composition [64, 76, 77]. Pure zinc has an HCP crystal structure and increasing zinc concentration decreases the stacking fault energy of alpha brass [173]. Measuring twin densities and twin related domain structure over a range of stored strain energy densities and twin boundary energies would provide valuable data for comparison to formation models.

7.2.4 Twin Related Domain Quantification

Although a large variety of metrics were calculated for twin related domains, there are many more possible. Most of the measures computed in this work have easily interpretable physical meanings but are discrete (e.g. number of grains, number of variants, or number of twin generations). There is signficant room to develop continuous twin related domain network based metrics that are still physically meaningful for example 'weighted' number of generations through a network flow type measure. Another major omission in this work is identification of higher order $\Sigma 3^n$ type boundaries. All internal boundaries of a twin related domain have a $\Sigma 3^n$ type disorientation [174], with disorien-

tation relationships for values of n up to 6 given in table 7.1. Consideration of higher order boundaries may provide important additional insights into annealing twin formation mechanism. Finally although 424 fully contained twin related domains were quantified, the removal of surface domains introduces a slight bias towards smaller domains. Capturing a larger microstructural volume can reduce the bias and provide statistics for a greater number of twin related domains.

7.2.5 Propagating Crack Statistics

Developing a rigorous criterion for fatal crack sites and assessing their frequency requires investigation of significantly more interrupted cracks. A fatigue experiment interrupted at a high fraction of lifetime has two crack populations as shown in figure 7.2. Many cracks initiate and are arrested within one grain while others have grown through several grains. Collecting a 3D dataset across a large surface of an interrupted sample will capture multiple cracks and allow comparison of the two populations. The current TriBeam configuration is not suitable for collection across such a large surface area, but mechanical serial sectioning is well suited. Dr. Michael Uchic and Dr. Michael Chapman are working to collect a dataset from an interrupted fatigue sample of René 88DT on the LEROY system at the Air Force Research Laboratory. An example slice is shown in figure 7.3. Collection, reconstruction, and analysis of the dataset is a major challenge but could provide crucial data for improved understanding of microstructurally short crack growth behavior.

7.2.6 Synthetic Microstructures

Although real 3D microstructures can provide input to crystal plasticity and other physics based models, mesh generation is a major challenge, particularly if the number of elements is computationally constrained. Periodic boundary conditions or other requirements may also preclude the use of real experimental microstructures. 3D synthetic

Table 7.1: Cubic coincidence site lattices of the type $\Sigma 3^n$ are given as axis angle pairs (θ about $\langle uvw \rangle$) and Rodrigues vectors (r_x, r_y, r_z). CSL values were calculated using the method described by Ranganathan [47].

Σ	n ($\Sigma 3^n$)	θ	u	v	w	r_x	r_y	r_z
3	1	60.00	1	1	1	$\frac{1}{3}$	$\frac{1}{3}$	$\frac{1}{3}$
9	2	38.94	1	1	0	$\frac{1}{4}$	$\frac{1}{4}$	0
27a	3	31.59	1	1	0	$\frac{1}{5}$	$\frac{1}{5}$	0
27b	3	35.43	2	1	0	$\frac{2}{7}$	$\frac{1}{7}$	0
81a	4	38.38	5	3	1	$\frac{5}{17}$	$\frac{3}{17}$	$\frac{1}{17}$
81b	4	38.94	4	1	1	$\frac{1}{3}$	$\frac{1}{12}$	$\frac{1}{12}$
81c	4	54.53	3	2	2	$\frac{3}{8}$	$\frac{1}{4}$	$\frac{1}{4}$
81d	4	60.41	4	4	3	$\frac{4}{11}$	$\frac{4}{11}$	$\frac{3}{11}$
243a	5	7.36	1	1	0	$\frac{1}{22}$	$\frac{1}{22}$	0
243b	5	12.21	3	1	1	$\frac{3}{31}$	$\frac{1}{31}$	$\frac{1}{31}$
243c	5	31.59	4	1	1	$\frac{4}{15}$	$\frac{1}{15}$	$\frac{1}{15}$
243d	5	35.43	5	4	2	$\frac{5}{21}$	$\frac{4}{21}$	$\frac{2}{21}$
243e	5	43.08	9	5	5	$\frac{9}{29}$	$\frac{5}{29}$	$\frac{5}{29}$
243f	5	43.08	9	7	1	$\frac{9}{29}$	$\frac{7}{29}$	$\frac{1}{29}$
243g	5	43.08	11	3	1	$\frac{11}{29}$	$\frac{3}{29}$	$\frac{1}{29}$
243h	5	49.75	6	5	5	$\frac{3}{10}$	$\frac{1}{4}$	$\frac{1}{4}$
243i	5	49.75	7	6	1	$\frac{7}{20}$	$\frac{3}{10}$	$\frac{1}{20}$
243j	5	60.00	11	11	1	$\frac{11}{27}$	$\frac{11}{27}$	$\frac{1}{27}$
729a	6	11.25	3	2	1	$\frac{3}{38}$	$\frac{1}{19}$	$\frac{1}{38}$
729b	6	22.09	7	7	3	$\frac{7}{53}$	$\frac{7}{53}$	$\frac{3}{53}$
729c	6	22.09	9	5	1	$\frac{9}{53}$	$\frac{5}{53}$	$\frac{1}{53}$
729d	6	28.61	7	6	2	$\frac{7}{37}$	$\frac{6}{37}$	$\frac{2}{37}$
729e	6	28.61	8	4	3	$\frac{8}{37}$	$\frac{4}{37}$	$\frac{3}{37}$
729f	6	28.61	8	5	0	$\frac{8}{37}$	$\frac{5}{37}$	0
729g	6	28.61	9	2	2	$\frac{9}{37}$	$\frac{2}{37}$	$\frac{2}{37}$
729h	6	31.28	6	4	1	$\frac{3}{13}$	$\frac{2}{13}$	$\frac{1}{26}$
729i	6	31.28	7	2	0	$\frac{7}{26}$	$\frac{1}{13}$	0
729j	6	38.38	17	5	1	$\frac{1}{3}$	$\frac{5}{51}$	$\frac{1}{51}$
729k	6	38.38	13	11	5	$\frac{13}{51}$	$\frac{11}{51}$	$\frac{5}{51}$
729l	6	38.94	8	7	7	$\frac{2}{9}$	$\frac{7}{36}$	$\frac{7}{36}$
729m	6	38.94	11	5	4	$\frac{11}{36}$	$\frac{5}{36}$	$\frac{1}{9}$
729n	6	44.38	4	3	1	$\frac{8}{25}$	$\frac{6}{25}$	$\frac{2}{25}$
729o	6	44.38	5	1	0	$\frac{2}{5}$	$\frac{2}{25}$	0
729p	6	47.13	12	8	5	$\frac{12}{35}$	$\frac{8}{35}$	$\frac{1}{7}$
729q	6	47.13	13	8	0	$\frac{13}{35}$	$\frac{8}{35}$	0
729r	6	47.13	14	6	1	$\frac{2}{5}$	$\frac{6}{35}$	$\frac{1}{35}$
729s	6	49.70	15	13	11	$\frac{15}{49}$	$\frac{13}{49}$	$\frac{11}{49}$
729t	6	49.70	17	15	1	$\frac{17}{49}$	$\frac{15}{49}$	$\frac{1}{49}$
729u	6	54.15	11	10	9	$\frac{11}{34}$	$\frac{5}{17}$	$\frac{9}{34}$
729v	6	54.15	14	9	5	$\frac{7}{17}$	$\frac{9}{34}$	$\frac{5}{34}$
729w	6	54.53	8	8	5	$\frac{1}{3}$	$\frac{1}{3}$	$\frac{5}{24}$
729x	6	59.00	19	15	11	$\frac{19}{47}$	$\frac{15}{47}$	$\frac{11}{47}$
729y	6	60.41	13	10	10	$\frac{13}{33}$	$\frac{10}{33}$	$\frac{10}{33}$

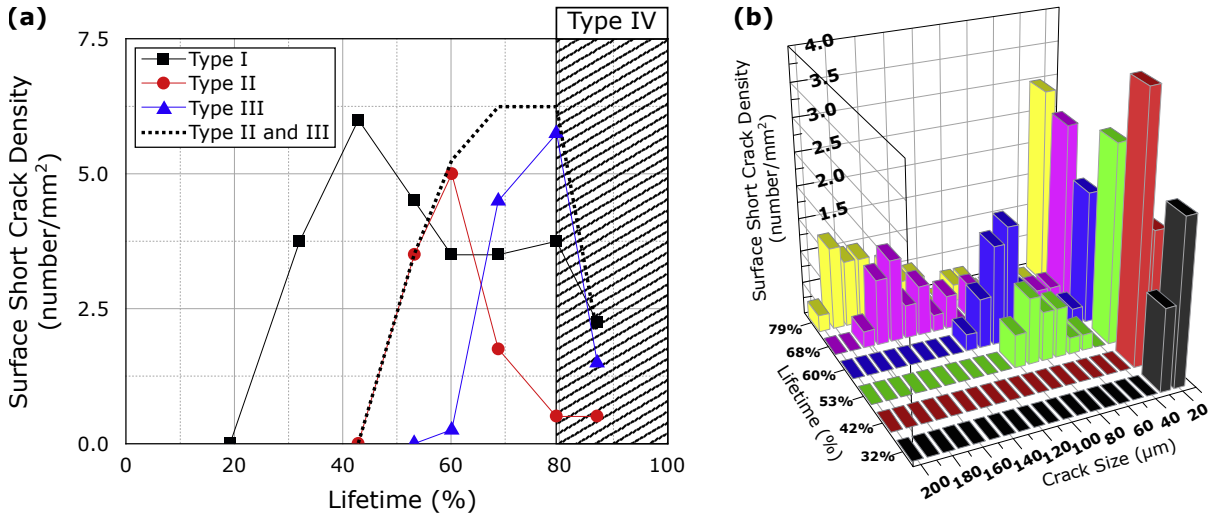

Figure 7.2: The surface density of cracks is shown with cracks split into type I (contained within a single grain), type II (1–3 grains), and type III (3–10 grains) (left). Histogram of crack length are also shown for increasing cycles with a bimodal distribution apparent above 50% of fatigue lifetime. Figure reprinted from Stinville et al., Copyright 2016, with permission from Acta Materialia Inc. [29].

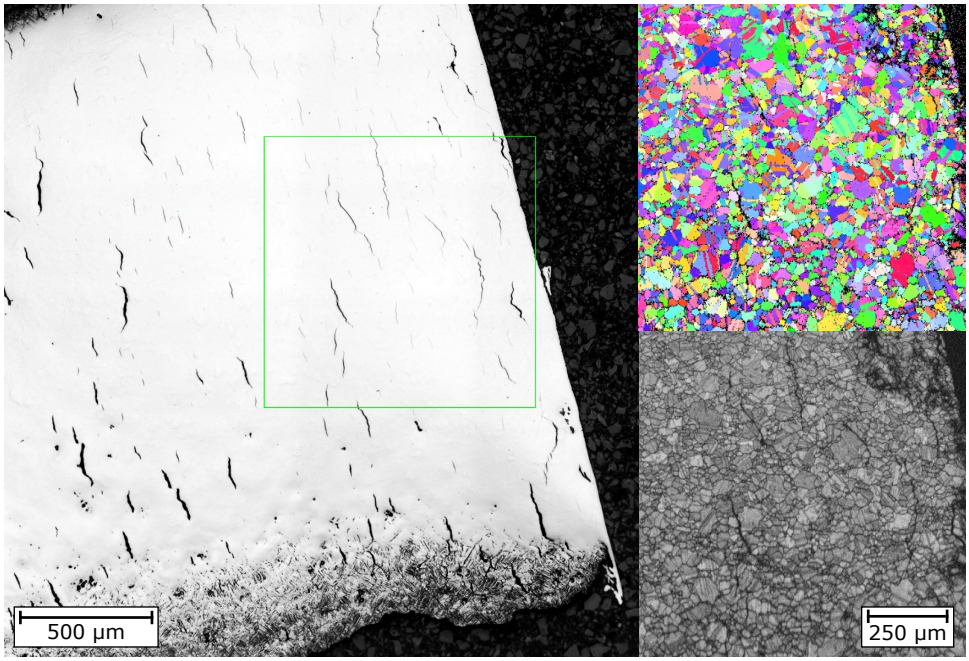

Figure 7.3: An optical micrograph (left) of a large exposed surface captured on the LEROY system at Air Force Research Laboratory by Dr. Michael Uchic and Dr. Michael Chapman shows a region of interest. EBSD data from the region of interest are colored by IPF coloring (top right) and indexing confidence (bottom right).

microstructures for nearly equiaxed microstructures can be produced by sampling from geometric and crystallographic distributions of real materials [175, 176]. Algorithms to generate realistic annealing twin microstructures do not currently exist, in part due to a lack of appropriate statistical distributions to sample from. Network measures provide a method to benchmark procedural or physics based synthetic generation algorithms, providing new opportunities for algorithm development. Generation of high quality twinned microstructures could be used to parametrically study the influence of grain size, twin related domain structure, and other microstructural features on the frequency of strain localizing sites, providing an important link for an integrated computational materials engineering approach to new alloy design.

Bibliography

[1] T. M. Pollock and S. Tin. "Nickel-Based Superalloys for Advanced Turbine Engines: Chemistry, Microstructure and Properties". *Journal of Propulsion and Power* 22.2 (2006), pp. 361–374.

[2] R. C. Reed. *The Superalloys: Fundamentals and Applications*. Cambridge university press, 2008.

[3] M. J. Donachie and S. J. Donachie. *Superalloys: A Technical Guide*. ASM international, 2002.

[4] H. Okamoto. "Al-Ni (Aluminum-Nickel)". *Journal of Phase Equilibria* 14.2 (1993), pp. 257–259.

[5] H. C. Fiedler et al. "The Spray Forming of Superalloys". *JOM* 39.8 (1987), pp. 28–33.

[6] D. Furrer and H. Fecht. "Ni-Based Superalloys for Turbine Discs". *JOM* 51.1 (1999), pp. 14–17.

[7] E. S. Huron and P. G. Roth. "The Influence of Inclusions on Low Cycle Fatigue Life in a P/M Nickel-Base Disk Superalloy". In: *Superalloys 1996: Proceedings of the 8th Intenational Symposium of Superalloys*. John Wiley & Sons, Inc. 1996, pp. 359–368.

[8] G. H. Gessinger. *Powder Metallurgy of Superalloys*. Butterworth Publishers, Stoneham, MA, 1984.

[9] D. Chang, D. Krueger, and R. Sprague. "Superalloy Powder Processing, Properties and Turbine Disk Applications". In: *Superalloys 1984, Proceedings of the Fifth International Symposium on Superalloys*. 1984, pp. 245–273.

[10] G. Gessinger and M. Bomford. "Powder Metallurgy of Superalloys". *International Metallurgical Reviews* 19.1 (1974), pp. 51–76.

[11] R. Menzies, J. Edington, and G. Davies. "Superplastic Behaviour of Powder-Consolidated Nickel-Base Superalloy IN-100". *Metal Science* 15.5 (1981), pp. 210–216.

[12] S. Reichman and J. Smythe. "Superplasticity in P/M IN-100 Alloy". *International Journal of Powder Metallurgy* 6 (1970).

[13] J. A. Immarigeon and P. Floyd. "Microstructural Instabilities During Superplastic Forging of a Nickel-Base Superalloy Compact". *Metallurgical Transactions A* 12.7 (1981), pp. 1177–1186.

[14] J. Miao, T. M. Pollock, and J. W. Jones. "Crystallographic Fatigue Crack Initiation in Nickel-Based Superalloy René 88DT at Elevated Temperature". *Acta Materialia* 57.20 (2009), pp. 5964–5974.

[15] J. Miao, T. M. Pollock, and J. W. Jones. "Microstructural Extremes and the Transition From Fatigue Crack Initiation to Small Crack Growth in a Polycrystalline Nickel-Base Superalloy". *Acta Materialia* 60.6–7 (2012), pp. 2840–2854.

[16] R. Kozar et al. "Strengthening Mechanisms in Polycrystalline Multimodal Nickel-Base Superalloys". *Metallurgical and Materials Transactions A* 40.7 (2009), pp. 1588–1603.

[17] J. M. Hyzak and I. M. Bernstein. "The Effect of Defects on the Fatigue Crack Initiation Process in Two P/M Superalloys: Part I. Fatigue Origins". *Metallurgical Transactions A* 13.1 (1982), pp. 33–43.

[18] B. A. Lerch, N. Jayaraman, and S. D. Antolovich. "A Study of Fatigue Damage Mechanisms in Waspaloy From 25 to 800°C". *Materials Science and Engineering* 66.2 (1984), pp. 151–166.

[19] A. Pineau and S. D. Antolovich. "High Temperature Fatigue of Nickel-Base Superalloys–A Review With Special Emphasis on Deformation Modes and Oxidation". *Engineering Failure Analysis* 16.8 (2009), pp. 2668–2697.

[20] H. F. Merrick. "The Low Cycle Fatigue of Three Wrought Nickel-Base Alloys". *Metallurgical Transactions* 5.4 (1974), pp. 891–897.

[21] D. Kalderon. "Steam Turbine Failure at Hinkley Point 'A'". *Proceedings of the Institution of Mechanical Engineers* 186.1 (1972), pp. 341–377.

[22] L. Witek. "Failure Analysis of Turbine Disc of an Aero Engine". *Engineering Failure Analysis* 13.1 (2006), pp. 9–17.

[23] J. Gayda and R. V. Miner. "Fatigue Crack Initiation and Propagation in Several Nickel-Base Superalloys at 650°C". *International Journal of Fatigue* 5.3 (1983), pp. 135–143.

[24] D. Eylon and J. Hyzak. "An Investigation of Fatigue Origins in Superalloy Powder Compacts". *Metallurgical Transactions A* 9.1 (1978), pp. 127–129.

[25] A. Shyam et al. "Development of Ultrasonic Fatigue for Rapid, High Temperature Fatigue Studies in Turbine Engine Materials". In: *Superalloys 2004*. Ed. by K. A. Green et al. Warrendale, PA: The Minerals, Metals & Materials Society, 2004, pp. 19–23.

[26] B. A. Cowles. "High Cycle Fatigue in Aircraft Gas Turbines—An Industry Perspective". *International Journal of Fracture* 80.2–3 (1989), pp. 147–163.

[27] C. Bathias. "There is No Infinite Fatigue Life in Metallic Materials". *Fatigue & Fracture of Engineering Materials & Structures* 22.7 (1999), pp. 559–565.

[28] A. Kumar et al. "In situ Characterization of Fatigue Damage Evolution in a Cast Al Alloy via Nonlinear Ultrasonic Measurements". *Acta Materialia* 58.6 (2010), pp. 2143–2154.

[29] J. C. Stinville et al. “A Combined Grain Scale Elastic-Plastic Criterion for Identification of Fatigue Crack Initiation Sites in a Twin Containing Polycrystalline nickel-base superalloy”. *Acta Materialia* 103 (2016), pp. 461–473.

[30] S. D. Antolovich, S. Liu, and R. Baur. “Low Cycle Fatigue Behavior of René 80 at Elevated Temperature”. *Metallurgical Transactions A* 12.3 (1981), pp. 473–481.

[31] T. Wu, J. Ni, and C. Bathias. “An Automatic Ultrasonic Fatigue Testing System for Studying Low Crack Growth at Room and High Temperatures”. In: *Automation in Fatigue and Fracture: Testing and Analysis*. ASTM International, 1994.

[32] A. Kumar et al. “Nonlinear Ultrasonics for in situ Damage Detection During High Frequency Fatigue”. *Journal of Applied Physics* 106.2 (2009).

[33] J. Z. Yi et al. “Ultrasonic Fatigue of a Single Crystal Ni-Base Superalloy at 1000 C”. *Materials Science and Engineering: A* 443.1 (2007), pp. 142–149.

[34] A. Shyam et al. “Development of Ultrasonic Fatigue for Rapid, High Temperature Fatigue Studies in Turbine Engine Materials”. In: *10th International Symposium on Superalloys, Champion, PA, September*. 2004, pp. 19–23.

[35] D. J. Morrison and V. Chopra. “Cyclic Stress-Strain Response of Polycrystalline Nickel”. *Materials Science and Engineering: A* 177.1–2 (1994), pp. 29–42.

[36] A. Hunsche and P. Neumann. “Quantitative Measurement of Persistent Slip Band Profiles and Crack Initiation”. *Acta Metallurgica* 34.2 (1986), pp. 207–217.

[37] T. Mura. “A Theory of Fatigue Crack Initiation”. *Materials Science and Engineering: A* 176.1–2 (1994), pp. 61–70.

[38] A. Weidner et al. “Half-Cycle Slip Activity of Persistent Slip Bands at Different Stages of Fatigue Life of Polycrystalline Nickel”. *Materials Science and Engineering: A* 492.1–2 (2008), pp. 118–127.

[39] H. Mughrabi et al. “Fatigue Crack Initiation by Cyclic Slip Irreversibilities in High-Cycle Fatigue”. *Fatigue Mechanisms: Advances in Quantitative Measurment of Physical Damage* (1983), p. 1.

[40] H. Mughrabi. “Cyclic Slip Irreversibilities and the Evolution of Fatigue Damage”. *Metallurgical and Materials Transactions B* 40.4 (2009), pp. 431–453.

[41] K. Tanaka and T. Mura. “A Dislocation Model for Fatigue Crack Initiation”. *Journal of Applied Mechanics* 48.1 (1981), pp. 97–103.

[42] R. E. Stoltz and A. G. Pineau. “Dislocation-Precipitate Interaction and Cyclic Stress-Strain Behavior of a γ' Strengthened Superalloy”. *Materials Science and Engineering* 34.3 (1978), pp. 275–284.

[43] M. Yamashita and K. Kakehi. “Tension/compression Asymmetry in Yield and Creep Strengths of Ni-Based Superalloy With a High Amount of Tantalum”. *Scripta materialia* 55.2 (2006), pp. 139–142.

[44] J. Larsen et al. “Reducing Uncertainty in Fatigue Life Limits of Turbine Engine Alloys”. *International Journal of Fatigue* 57 (2013), pp. 103–112.

[45] G. Nolze and R. Hielscher. "Orientations–Perfectly Colored". *Journal of Applied Crystallography* 49.5 (2016), pp. 1786–1802.

[46] S. Patala, J. K. Mason, and C. A. Schuh. "Improved Representations of Misorientation Information for Grain Boundary Science and Engineering". *Progress in Materials Science* 57.8 (2012), pp. 1383–1425.

[47] S. Ranganathan. "On the Geometry of Coincidence-Site Lattices". *Acta Crystallographica* 21.2 (1966), pp. 197–199.

[48] D. Warrington and P. Bufalini. "The Coincidence Site Lattice and Grain Boundaries". *Scripta Metallurgica* 5.9 (1971), pp. 771–776.

[49] G. Palumbo, E. M. Lehockey, and P. Lin. "Applications for Grain Boundary Engineered Materials". *JOM* 50.2 (1998), pp. 40–43.

[50] F. J. Humphreys and M. Hatherly. *Recrystallization and Related Annealing Phenomena*. Elsevier, 2004.

[51] A. Berger et al. "On the Generation of New Orientations During Recrystallization: Recent Results on the Recrystallization of Tensile-Deformed fcc Single Crystals". *Progress in Materials Science* 32.1 (1988), pp. 1–95.

[52] G. Gottstein. "Annealing Texture Development by Multiple Twinning in f.c.c. Crystals". *Acta Metallurgica* 32.7 (1984), pp. 1117–1138.

[53] D. P. Field et al. "The Role of Annealing Twins During Recrystallization of Cu". *Acta Materialia* 55.12 (2007), pp. 4233–4241.

[54] T. Baudin, A. L. Etter, and R. Penelle. "Annealing Twin Formation and Recrystallization Study Of Cold-Drawn Copper Wires From EBSD Measurements". *Materials Characterization* 58.10 (2007), pp. 947–952.

[55] M. A. Meyers and C. McCowan. "The Formation of Annealing Twins: Overview and New Thoughts". *International Symposium on Interface Migration and Control of Microstructure* 8408–037 (1984), pp. 99–123.

[56] J. W. Christian and S. Mahajan. "Deformation Twinning". *Progress in Materials Science* 39.1–2 (1995), pp. 1–157.

[57] J. Wang, I. Beyerlein, and C. Tomé. "An Atomic and Probabilistic Perspective on Twin Nucleation in Mg". *Scripta Materialia* 63.7 (2010), pp. 741–746.

[58] G. Gindraux and W. Form. "New Concepts of Annealing-Twin Formation in Face-Centered Cubic Metals". *The Journal of the Institute of Metals* 101 (1973). www.tandfonline.com, pp. 85–93.

[59] S. Mahajan. "Critique of Mechanisms of Formation of Deformation, Annealing and Growth Twins: Face-Centered Cubic Metals and Alloys". *Scripta Materialia* 68.2 (2013), pp. 95–99.

[60] W. G. Burgers. "'Stimulation Crystals' and Twin Formation in Recrystallized Aluminium". *Nature* 157 (1946), pp. 76–77.

[61] J. P. Nielsen. "The Origin of Annealing Twins". *Acta Metallurgica* 15.6 (1967), pp. 1083–1085.

[62] K. J. Kurzydlowski. "On the Formation of Twin Grains as a Result of Grain Encounters During the Process of Recrystallization and Grain Growth". *Scripta Metallurgica et Materialia* 25.5 (1991), pp. 1099–1102.

[63] H. Gleiter. "The Formation of Annealing Twins". *Acta Metallurgica* 17.12 (1969), pp. 1421–1428.

[64] C. S. Pande, M. A. Imam, and B. B. Rath. "Study of Annealing Twins in fcc Metals and Alloys". *Metallurgical Transactions A* 21.11 (1990), pp. 2891–2896.

[65] S. Mahajan et al. "Formation of Annealing Twins in f.c.c. Crystals". *Acta Materialia* 45.6 (1997), pp. 2633–2638.

[66] M. A. Meyers and L. E. Murr. "A Model for the Formation of Annealing Twins in F.C.C. Metals and Alloys". *Acta Metallurgica* 26.6 (1978), pp. 951–962.

[67] P. J. Goodhew. "Annealing Twin Formation by Boundary Dissociation". *Metal Science* 13.3–1 (1979), pp. 108–112.

[68] S. Dash and N. Brown. "An Investigation of the Origin and Growth of Annealing Twins". *Acta Metallurgica* 11.9 (1963), pp. 1067–1075.

[69] H. C. H. Carpenter and S. Tamura. "The Formation of Twinned Metallic Crystals". *Proceedings of the Royals Society of London. Series A, Containing Papers of a Mathematical and Physical Character* 113.763 (1926), pp. 161–182.

[70] R. L. Fullman and J. C. Fisher. "Formation of Annealing Twins During Grain Growth". *Journal of Applied Physics* 22.11 (1951), pp. 1350–1355.

[71] J. R. Cahoon, Q. Li, and N. L. Richards. "Microstructural and Processing Factors Influencing the Formation of Annealing Twins". *Materials Science and Engineering: A* 526.1–2 (2009), pp. 56–61.

[72] Q. Li, J. R. Cahoon, and N. L. Richards. "On the Calculation of Annealing Twin Density". *Scripta Materialia* 55.12 (2006), pp. 1155–1158.

[73] A. Garbacz and M. W. Grabski. "Modelling of CSL Boundaries Distribution in Polycrystals". *Scripta Metallurgica* 23.8 (1989), pp. 1369–1374.

[74] C. B. Thomson and V. Randle. "A Study of Twinning in Nickel". *Scripta Materialia* 35.3 (1996), pp. 385–390.

[75] C. S. Pande and M. A. Imam. "Grain Growth and Twin Formation in Boron-Doped Nickel Polycrystals". *Materials Science and Engineering: A* 512.1–2 (2009), pp. 82–86.

[76] H. Hu and C. S. Smith. "The Formation of Low-Energy Interfaces During Grain Growth in Alpha and Alpha-Beta Brasses". *Acta Metallurgica* 4.6 (1956), pp. 638–646.

[77] G. Baro and H. Gleiter. "The Formation of Annealing Twins". *Zeitschrift fuer Metallkunde* 63 (1972), pp. 661–663.

[78] R. A. Varin and J. Kruszynska. "Control of Annealing Twins in Type 316 Austenitic Stainless Steel". *Acta Metallurgica* 35.7 (1987), pp. 1767–1774.

[79] D. Horton, C. B. Thomson, and V. Randle. "Aspects of Twinning and Grain Growth in High Purity and Commercially Pure Nickel". *Materials Science and Engineering: A* 203.1–2 (1995), pp. 408–414.

[80] V. Randle, P. R. Rios, and Y. Hu. "Grain Growth and Twinning in Nickel". *Scripta Materialia* 58.2 (2008), pp. 130–133.

[81] W. Charnock and J. Nutting. "The Factors Determing the Freuquency of Occurance of Annealing Twins". *Metal Science* 1.1 (1967), pp. 78–83.

[82] W. Form, G. Gindraux, and V. Mlyncar. "Density of Annealing Twins". *Metal Science* 14.1 (1980), pp. 16–20.

[83] N. Bozzolo, N. Souaï, and R. E. Logé. "Evolution of Microstructure and Twin Density During Thermomechanical Processing in a γ-γ' Nickel-Based Superalloy". *Acta Materialia* 60.13–14 (2012), pp. 5056–5066.

[84] J. Bystrzycki and W. Przetakiewicz. "3 - Dimensional Reconstruction of Annealing Twins Shape in FCC Metals by Serial Sectioning". *Scripta Metallurgica et Materialia* 27.7 (1992), pp. 893–896.

[85] J. Bystrzycki, W. Przetakiewicz, and K. J. Kurzydłowski. "Study of Annealing Twins and Island Grains in F.C.C. Alloy". *Acta Metallurgica et Materialia* 41.9 (1993), pp. 2639–2649.

[86] J. Gastaldi and C. Jourdan. "Observation of the Annealing Twin Growth by Synchrotron Radiation X-Ray Topography". *Physica Status Solidi (A)* 52.1 (1979), pp. 139–148.

[87] D. P. Field, R. C. Eames, and T. M. Lillo. "The Role of Shear Stress in the Formation of Annealing Twin Boundaries in Copper". *Scripta Materialia* 54.6 (2006), pp. 983–986.

[88] K. H. Song, Y. B. Chun, and S. K. Hwang. "Direct Observation of Annealing Twin Formation in a Pb-Base Alloy". *Materials Science and Engineering: A* 454.0 (2007), pp. 629–636.

[89] D. Farkas, E. Bringa, and A. Caro. "Annealing Twins in Nanocrystalline Fcc Metals: A Molecular Dynamics Simulation". *Physical Review B* 75 (18 2007), p. 184111.

[90] E. M. Bringa et al. "Fivefold Twin Formation During Annealing of Nanocrystalline Cu". *Scripta Materialia* 59.12 (2008), pp. 1267–1270.

[91] T. L. Wolfsdorf, W. H. Bender, and P. W. Voorhees. "The Morphology of High Volume Fraction Solid-Liquid Mixtures: An Application of Microstructural Tomography". *Acta Materialia* 45.6 (1997), pp. 2279–2295.

[92] E. E. Underwood. "The Mathematical Foundations of Quantitative Stereology". In: *Stereology and Quantitative Metallography*. ASTM International, 1972.

[93] R. T. DeHoff. "Quantitative Serial Sectioning Analysis: Preview". *Journal of Microscopy* 131.3 (1983), pp. 259–263.

[94] C.-S. Kim, A. D. Rollett, and G. S. Rohrer. "Grain Boundary Planes: New Dimensions in the Grain Boundary Character Distribution". *Scripta Materialia* 54.6 (2006), pp. 1005–1009.

[95] M. V. Kral et al. "Three-Dimensional Analysis of Microstructures". *Materials Characterization* 45.1 (2000), pp. 17–23.

[96] J. E. Spowart. "Automated Serial Sectioning for 3-D Analysis of Microstructures". *Scripta Materialia* 55.1 (2006), pp. 5–10.

[97] J. V. Smith. "Tutorial Review. Synchrotron X-Ray Sources: Instrumental Characteristics. New Applications in Microanalysis, Tomography, Absorption Spectroscopy and Diffraction". *Analyst* 120.5 (1995), pp. 1231–1245.

[98] J. H. Kinney and M. C. Nichols. "X-Ray Tomographic Microscopy (XTM) Using Synchrotron Radiation". *Annual Review of Materials Science* 22.1 (1992), pp. 121–152.

[99] G. Johnson et al. "X-Ray Diffraction Contrast Tomography: A Novel Technique for Three-Dimensional Grain Mapping of Polycrystals. II. The Combined Case". *Journal of Applied Crystallography* 41.2 (2008), pp. 310–318.

[100] W. Ludwig et al. "X-Ray Diffraction Contrast Tomography: A Novel Technique for Three-Dimensional Grain Mapping of Polycrystals. I. Direct Beam Case". *Journal of Applied Crystallography* 41.2 (2008), pp. 302–309.

[101] R. Suter et al. "Forward Modeling Method for Microstructure Reconstruction Using X-Ray Diffraction Microscopy: Single-Crystal Verification". *Review of Scientific Instruments* 77.12 (2006), p. 123905.

[102] W. Ludwig et al. "Three-Dimensional Grain Mapping by X-Ray Diffraction Contrast Tomography and the Use of Friedel Pairs in Diffraction Data Analysis". *Review of Scientific Instruments* 80.3 (2009).

[103] M. D. Uchic, M. A. Groeber, and A. D. Rollett. "Automated Serial Sectioning Methods for Rapid Collection of 3-D Microstructure Data". *JOM* 63.3 (2011), pp. 25–29.

[104] M. A. Groeber et al. "3D Reconstruction and Characterization of Polycrystalline Microstructures Using a FIB-SEM System". *Materials Characterization* 57.4–5 (2006), pp. 259–273.

[105] M. Uchic et al. *An Automated Multi-Modal Serial Sectioning System for Characterization of Grain-Scale Microstructures in Engineering Materials (Preprint).* Tech. rep. DTIC Document, 2012.

[106] M. P. Echlin et al. "A New TriBeam System for Three-Dimensional Multimodal Materials Analysis". *Review of Scientific Instruments* 83.2 (2012), p. 023701.

[107] M. P. Echlin et al. "TriBeam Tomography of Ti6-4 for Plasticity Characterization". In: *TMS Annual Meeting*. TMS. Warrendale, PA, 2014.

[108] M. D. Uchic et al. "Three-Dimensional Microstructural Characterization Using Focused Ion Beam Tomography". *MRS Bulletin* 32.5 (2007), pp. 408–416.

[109] M. P. Echlin et al. “The TriBeam System: Femtosecond Laser Ablation in situ SEM”. *Materials Characterization* 100 (2015), pp. 1–12.

[110] G. Spanos. “Foreword: Scripta Materialia Viewpoint Set on 3D Characterization and Analysis of Materials”. *Scripta Materialia* 55.1 (2006), p. 3.

[111] M. De Graef, M. V. Kral, and M. Hillert. “A Modern 3-D View of an “old” Pearlite Colony”. *JOM* 58.12 (2006), pp. 25–28.

[112] M. V. Kral and G. Spanos. “Three-Dimensional Analysis of Proeutectoid Cementite Precipitates”. *Acta Materialia* 47.2 (1999), pp. 711–724.

[113] M. Uchic. “3-D Microstructural Characterization: Methods, Analysis, and Applications”. *JOM* 58.12 (2006), pp. 24–24.

[114] M. A. Groeber and M. Jackson. “DREAM.3D: A Digital Representation Environment for the Analysis of Microstructure in 3D”. *Integrating Materials and Manufacturing Innovation* 3.1 (2014), pp. 1–17.

[115] M. Groeber et al. “A Framework for Automated Analysis and Simulation of 3D Polycrystalline Microstructures.: Part 1: Statistical Characterization”. *Acta Materialia* 56 (2008), pp. 1257–1273.

[116] M. P. Echlin et al. “Three-Dimensional Characterization of the Permeability of W–Cu Composites Using a New “TriBeam” technique”. *Acta Materialia* 64.0 (2014), pp. 307–315.

[117] W. C. Lenthe et al. “Quantitative Voxel-To-Voxel Comparison of TriBeam and DCT Strontium Titanate Three-Dimensional Data Sets”. *Journal of Applied Crystallography* 48.4 (2015), pp. 1034–1046.

[118] J. E. Douglas et al. “Three-Dimensional Multimodal Imaging and Analysis of Biphasic Microstructure in a Ti–Ni–Sn Thermoelectric Material”. *APL Materials* 3.9 (2015), p. 096107.

[119] W. C. Lenthe et al. “Statistical Assessment of Fatigue-Initiating Microstructural Features in a Polycrystalline Disk Alloy”. In: *Superalloys 2016: Proceedings of the 13th Intenational Symposium of Superalloys*. John Wiley & Sons, Inc. 2016, pp. 569–577.

[120] M. S. Titus et al. “Dislocation Injection in Strontium Titanate by Femtosecond Laser Pulses”. *Journal of Applied Physics* 118.7 (2015).

[121] M. P. Echlin et al. “Materials Response to Glancing Incidence Femtosecond Laser Ablation”. *Acta Materialia* 124 (2017), pp. 37–46.

[122] J. Ready. *Effects of High-Power Laser Radiation*. Elsevier, 2012.

[123] The HDF Group. *Hierarchical Data Format, Version 5*. 1997. URL: `http://www.hdfgroup.org/HDF5/`.

[124] L. N. Brewer and J. R. Michael. “Risks of “Cleaning” Electron Backscatter Diffraction Data”. *Microscopy Today* 18.2 (2010), pp. 10–15.

[125] M. Syha et al. “Three-Dimensional Grain Structure of Sintered Bulk Strontium Titanate From X-Ray Diffraction Contrast Tomography”. *Scripta Materialia* 66.1 (2012), pp. 1–4.

[126] M. Syha et al. “Combining X-Ray Diffraction Contrast Tomography and Mesoscale Grain Growth Simulations in Strontium Titanate: An Integrated Approach for the Investigation of Microstructure Evolution”. In: *Developments in Strategic Materials and Computational Design III*. John Wiley & Sons, Inc., 2012, pp. 127–137.

[127] M. Bäurer et al. “Grain Growth Anomaly in Strontium Titanate”. *Scripta Materialia* 61.6 (2009), pp. 584–587.

[128] M. Bäurer, H. Kungl, and M. J. Hoffmann. “Influence of Sr/Ti Stoichiometry on the Densification Behavior of Strontium Titanate”. *Journal of the American Ceramic Society* 92.3 (2009), pp. 601–606.

[129] A. C. Kak et al. *Principles of Computerized Tomographic Imaging*. IEEE Press, 1987.

[130] M. Syha et al. “Validation of Three-Dimensional Diffraction Contrast Tomography Reconstructions by Means of Electron Backscatter Diffraction Characterization”. *Journal of Applied Crystallography* 46.Pt 4 (2013), pp. 1145–1150.

[131] S. I. Wright and M. M. Nowell. “EBSD Image Quality Mapping”. *Microscopy and Microanalysis* 12 (01 2006), pp. 72–84.

[132] Z. Wu and J. M. Sullivan. “Multiple Material Marching Cubes Algorithm”. *International Journal for Numerical Methods in Engineering* 58.2 (2003), pp. 189–207.

[133] J. C. Gower and G. B. Dijksterhuis. *Procrustes Problems*. Oxford University Press, 2004.

[134] P. Jaccard. “The Distribution of the Flora in the Alpine Zone”. *New Phytologist* 11.2 (1912), pp. 37–50.

[135] A. H. Cheetham and J. E. Hazel. “Binary (Presence-Absence) Similarity Coefficients”. *Journal of Paleontology* (1969), pp. 1130–1136.

[136] T. Sørensen. “A Method of Establishing Groups of Equal Amplitude in Plant Sociology Based on Similarity of Species Content and its Application to Analyses of the Vegetation on Danish Commons”. *Biologiske Skrifter* 5 (1948), pp. 1–34.

[137] L. R. Dice. “Measures of the Amount of Ecologic Association Between Species”. *Ecology* 26.3 (1945), pp. 297–302.

[138] H. W. Kuhn. “The Hungarian Method for the Assignment Problem”. *Naval Research Logistics Quarterly* 2.1–2 (1955), pp. 83–97.

[139] J. Munkres. “Algorithms for the Assignment and Transportation Problems”. *Journal of the Society for Industrial and Applied Mathematics* 5.1 (1957), pp. 32–38.

[140] D. W. Eastman et al. “Benchmarking Crystal Plasticity Models With Microtensile Evaluation and 3D Characterization of René 88DT”. In: *Superalloys 2016: Proceedings of the 13th Intenational Symposium of Superalloys*. John Wiley & Sons, Inc. 2016, pp. 811–820.

[141] S. Ghosh, G. Weber, and S. Keshavarz. “Multiscale Modeling of Polycrystalline Nickel-Based Superalloys Accounting for Subgrain Microstructures”. *Mechanics Research Communications* 78.Part B (2016), pp. 34–46.

[142] J. C. Stinville, V. M. Miller, and T. M. Pollock. “Effect of Non-Metallic Ceramic Inclusions on Strain Localization During Low Cycle Fatigue of a Polycrystalline Superalloy”. In: *Superalloys 2016: Proceedings of the 13th Intenational Symposium of Superalloys*. John Wiley & Sons, Inc. 2016, pp. 897–905.

[143] C. McMahon et al. “Boundary Identification in EBSD Data With a Generalization of Fast Multiscale Clustering”. *Ultramicroscopy* 133 (2013), pp. 16–25.

[144] G. Nolze, A. Winkelmann, and A. P. Boyle. “Pattern Matching Approach to Pseudosymmetry Problems in Electron Backscatter Diffraction”. *Ultramicroscopy* 160.Supplement C (2016), pp. 146–154.

[145] M. Mineur, P. Villechaise, and J. Mendez. “Influence of the Crystalline Texture on the Fatigue Behavior of a 316L Austenitic Stainless Steel”. *Materials Science and Engineering: A* 286.2 (2000), pp. 257–268.

[146] R. C. Boettner, A. J. McEvily Jr, and Y. C. Liu. “On the Formation of Fatigue Cracks at Twin Boundaries”. *Philosophical Magazine* 10.103 (1964), pp. 95–106.

[147] A. Morawiec and K. L. Merkle. “Symmetries of Grain Boundary Distributions”. In: *Proceedings of the Third International Conference on Grain Growth*. Ed. by H. Weiland, B. L. Adams, and A. D. Rollet. Warrendale, PA: The Minerals, Metals & Materials Society, 1998, p. 509.

[148] D. A. Field. “Laplacian Smoothing and Delaunay Triangulations”. *Communications in Applied Numerical Methods* 4.6 (1988), pp. 709–712.

[149] G. Taubin. “Curve and Surface Smoothing Without Shrinkage”. In: *Computer Vision, 1995. Proceedings., Fifth International Conference On*. IEEE. 1995, pp. 852–857.

[150] C. L. Lawson. “Properties of N-Dimensional Triangulations”. *Computer Aided Geometric Design* 3.4 (1986), pp. 231–246.

[151] L. P. Chew. “Constrained Delaunay Triangulations”. *Algorithmica* 4.1–4 (1989), pp. 97–108.

[152] J. R. Shewchuk. “General-Dimensional Constrained Delaunay and Constrained Regular Triangulations, I: Combinatorial Properties”. *Discrete & Computational Geometry* 39.1 (2008), pp. 580–637.

[153] M. Kopsch. *The Delaunay Triangulation With All the Circumcircles and Their Centers*. 2012. URL: `https://commons.wikimedia.org/wiki/File:Delaunay_circumcircles_centers.svg`.

[154] Hferee. *A Delaunay Triangulation and its Voronoi Diagram*. 2011. URL: https://commons.wikimedia.org/wiki/File:Delaunay_Voronoi.svg.

[155] D. Shenton and Z. Cendes. "Three-Dimensional Finite Element Mesh Generation Using Delaunay Tesselation". *IEEE Transactions on Magnetics* 21.6 (1985), pp. 2535–2538.

[156] H. Si. "TetGen, a Delaunay-Based Quality Tetrahedral Mesh Generator". *ACM Transactions on Mathematical Software* 41.2 (2015), p. 11.

[157] M. Garland and P. S. Heckbert. "Surface Simplification Using Quadric Error Metrics". In: *Proceedings of the 24th Annual Conference on Computer Graphics and Interactive Techniques*. ACM Press/Addison-Wesley Publishing Co. 1997, pp. 209–216.

[158] R. E. Bank. *Pltmg: A Software Package for Solving Elliptic Partial Differential Equations: Users' Guide 8.0*. SIAM, 1998.

[159] M. D. Uchic et al. "3D Microstructural Characterization of Nickel Superalloys via Serial-Sectioning Using a Dual Beam FIB-SEM". *Scripta Materialia* 55.1 (2006), pp. 23–28.

[160] Hibbitt, Karlsson, and Sorensen. *ABAQUS/Standard User's Manual*. Vol. 1. Hibbitt, Karlsson & Sorensen, 2001.

[161] J. C. Stinville et al. "Microstructural Statistics for Fatigue Crack Initiation in Polycrystalline Nickel-Base Superalloys". *International Journal of Fracture* (2017).

[162] S. I. Wright and M. M. Nowell. "EBSD Image Quality Mapping". *Microscopy and Microanalysis* 12 (01 2006), pp. 72–84.

[163] A. F. Bower. *Applied Mechanics of Solids*. CRC press, 2009.

[164] J. F. Nye and R. Lindsay. "Physical Properties of Crystals". *Physics Today* 10 (1957), p. 26.

[165] M. A. Meyers and K. K. Chawla. *Mechanical Behavior of Materials*. Prentice Hall, 1999.

[166] M. P. Echlin, W. C. Lenthe, and T. M. Pollock. "Three-Dimensional Sampling of Material Structure for Property Modeling and Design". *Integrating Materials and Manufacturing Innovation* 3.1 (2014).

[167] E. Bayerschen et al. "Review on Slip Transmission Criteria in Experiments and Crystal Plasticity Models". *Journal of Materials Science* 51.5 (2016), pp. 2243–2258.

[168] A. C. Lewis et al. "Two- and Three-Dimensional Microstructural Characterization of a Super-Austenitic Stainless Steel". *Materials Science and Engineering: A* 418.1 (2006), pp. 11–18.

[169] D. Roşca, A. Morawiec, and M. De Graef. "A New Method of Constructing a Grid in the Space of 3D Rotations and its Applications to Texture Analysis". *Modelling and Simulation in Materials Science and Engineering* 22.7 (2014), p. 075013.

[170] T. M. Fruchterman and E. M. Reingold. "Graph Drawing by Force-Directed Placement". *Software: Practice and Experience* 21.11 (1991), pp. 1129–1164.

[171] B. Henrie, T. Mason, and B. Hansen. "A Semiautomated Electron Backscatter Diffraction Technique for Extracting Reliable Twin Statistics". *Metallurgical and Materials Transactions A* 35.12 (2004), pp. 3745–3751.

[172] W. J. Tu. "Deformation Mechanisms and Strain Storage During Forging of Powder-Metallurgy Nickel-Base Turbine Disk Alloy". PhD thesis. The University of Michigan, 2010.

[173] X. Wu et al. "Effect of Stacking Fault Energy on Mechanical Behavior of Cold-Forging Cu and Cu Alloys". *Materials & Design* 47 (2013), pp. 372–376.

[174] B. W. Reed and M. Kumar. "Mathematical Methods for Analyzing Highly-Twinned Grain Boundary Networks". *Scripta Materialia* 54.6 (2006), pp. 1029–1033.

[175] M. Groeber et al. "A Framework for Automated Analysis and Simulation of 3D Polycrystalline Microstructures.: Part 1: Statistical Characterization". *Acta Materialia* 56.6 (2008), pp. 1257–1273.

[176] M. Groeber et al. "A Framework for Automated Analysis and Simulation of 3D Polycrystalline Microstructures. Part 2: Synthetic Structure Generation". *Acta Materialia* 56.6 (2008), pp. 1274–1287.